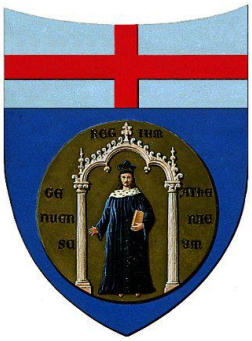

UNIVERSITA' DEGLI STUDI DI GENOVA

Scuola di Dottorato in Scienze e Tecnologie della Chimica e dei Materiali

Corso di Dottorato in Scienze e Tecnologie Chimiche

XXX CICLO

OUT-OF-EQUILIBRIUM BEHAVIOUR OF COPPER-BASED ALLOYS IN INDUSTRIAL, ARTISTIC AND HISTORICAL GRAVITY CASTING PROCESSES

Justine Marie Vernet

Tutor	Prof. Paolo Piccardo
Thesis Defense	March 2018

“To cast a molten metal in a mould and let the melt solidify and cool there does not seem to be a very complicated process. It would be reasonable to assume that casting is a fairly simple business.

However, this conclusion does not at all agree with reality.”

Fredriksson and Åkerlind, 2006

TABLE OF CONTENTS

ABSTRACT

Copper alloys and casting practices are of major importance in both fields of archaeometry and material sciences. Universally recognized as key technologies in humankind history, they have known a continuous use through times and still are intensively applied in our modern industry.

However, a considerable part of the actual knowledge on the non-equilibrium behaviour of ancient copper alloys during casting processes, like bronze and brass, comes from empirical traditions more than from scientific researches. Furthermore, from an archaeological point of view, technological investigations are often limited by the fact that as-cast artefacts and metallurgical structures (moulds, furnaces, etc.) are rarely discovered on the same site.

This Ph.D. research investigates the impact of different cooling conditions on the microstructural and mechanical features of as-cast copper-based alloys with industrial and archaeological interest in the aim to 1) better predict the characteristic of copper-based alloys after undergoing common casting processes, 2) better understand archaeological corpus in as-cast state in order to make hypothesis about the parameters of casting process.

The present thesis is organized in 5 main parts:

- The 1st chapter consists of an overview highlighting the importance of casting technology in both ancient and modern times. We will also present copper-based alloys as a key materials in several fields, form archaeological sciences to modern industry and artistic production.

- The 2nd chapter presents the main mechanisms of solidification. Phase diagrams as well as a state of the art about the gathered knowledge on out-of-equilibrium curves for the considered copper based alloys are presented;

- The 3rd chapter describes the methodology applied, as well as the materials investigated and the techniques used. The work is separated in two parts.

  The first one consists in gathering quantitative data on the solidification of experimental as-cast alloys (bronze, brass, gunmetal and leaded alloys) in order to find correlations between cooling conditions and final characteristics (macro and microstructure, macrohardness). A multi-technical methodology based on a multivariate approach (DoE, PCA) was built in order to study different scales of cooling rate (i.e. medium and near rapid), and the impact of different variables of process (i.e. alloy composition, superheat, mould material).

The second part is based on the metallographic study of the archaeological corpus of Loyettes (France). The assemblage is composed by 69 as-cast axe-ingots coming from a Bronze Age deposit and presenting similar macroscopic characteristics. A reduced corpus of 20 objects have been selected and investigated in the intent to determine their microstructural features and some process parameters (composition of the alloy, assumptions on the mould material, etc.).

- The 4th chapter presents the results obtained during the experimental casting tests and the archaeometrical investigation. A particular attention is paid on the filing of the model of experimental design and the application of these results assuming the casting technology applied on the Loyettes corpus as a reference.

- The 5th chapter displays the final conclusions of the achieved works with some considerations for further studies.

This study includes working collaborations with:

- Prof. Roberto CABELLA,
  DISTAV – Università degli Studi di Genova, Italy

- Prof. Cristina CARBONE,
  DISTAV – Università degli Studi di Genova, Italy

- Dr. Fabien DELRIEU,
  DRAC Auvergne-Rhône-Alpes,
  Ministère de la Culture et de la Communication, France

- Ph.D. Maréva GABILLOT,
  UMR 6298 ARTEHIS – Université de Bourgogne, France

- Prof. Riccardo LEARDI,
  DIFAR – Università degli Studi di Genova, Italy

- Dr. Daniel MACCIÒ,
  DCCI – Università degli Studi di Genova, Italy

- Ph.D. Lorenzo MONTESANO,
  DIMI – Università degli Studi di Brescia, Italy

- Dr. Eng. Marialaura TOCCI,
  DIMI – Università degli Studi di Brescia, Italy

- Prof. Massimo VERDOYA,
  DISTAV – Università degli Studi di Genova, Italy

INTRODUCTION

Transforming and shaping the matter is a major issue for humankind. From the dawn of history, with the first carved shells to our modern times, with more efficient and high-tech devices, materials have always been an excellent ground for human societies to emerge, grow and express itself.

According to this vision, casting technology and copper materials are hardly dissociable since both are universally recognized as true *trait d'union* between times and civilizations.

On one side, copper has been manufactured either by casting or plastic deformation in a continuous way during almost 10 millennia, first from native copper and unintentional alloys, then from intentional alloys produced with arsenic-rich ores and tin-rich ores. Thanks to alloying, new mechanical and visual features have been reached. After the first industrial revolution at the end of the 18^{th} century, ferrous alloys – and later new industrial materials like aluminium – progressively substituted copper in many applications where their production became too expensive. Nevertheless, copper-based alloys have continued to play a significant role in specific fields, like artistic artwork, steam installations or electronic devices, where the cheapest materials would not be efficient enough.

On the other side, casting is one of the most important technologies used since ancient times, deriving from both stone and glass manufacturing. Casting still continues to be predominant in modern economy, in particular in transport industry and in artistic fields.

In each casting process, solidification is the common step that has to be taken into account. Either for forming of finished artworks or producing of semi-finished materials, the transition from liquid to solid state is a fundamental stage conditioning the final object's features.

From the point of view of materials science, phase diagrams can predict the thermodynamic behaviour of materials with respect to variations of temperature, composition or pressure. However, when dealing with real casting processes and conditions of very rapid phase transition, kinetics laws drive the solidification phenomena and new models have to be applied for the systems description.

The interest for non-equilibrium conditions of process and metastable structure appears in contemporary researches during the 1960s but the behaviour of alloys under rapid solidification has been particularly explored during the 1990s.

In 2001, Jones presents the status and the potential of theses manufacturing methods in modern industry. He concludes with the presentation of three priority research axes for future investigations:

1) the development of new predictive models for the formation of non-equilibrium phases and microstructures in different alloys and for different process conditions;
2) the identification of the effects of constitution and microstructure on properties during processing and the exploration of new variants of production processes or combinations of such processes;
3) the identification of the factors that have led to successful applications of Rapid Solidification (RS) and Non Equilibrium Processing (NEP) and have to search for further applications (Jones, 2001).

For ferrous materials, the development of Time-Temperature-Transformation (TTT) and Continuous-Cooling-Curves (CCC) diagrams for the description of non-equilibrium manufacturing conditions have allowed a better understanding of the overall processes, in particular regarding the formation of metastable phases.

However, for non-ferrous alloys, and particularly copper-based alloys, the non-equilibrium behaviour in casting conditions is rather coming from empirical skills of foundrymen, able to adapt the cast materials to the applied process, rather than on scientific researches.

In particular, as highlighted by Martorano and Capocchi (Martorano and Capocchi, 2000), the obtainment of high quality castings is only possible by gathering quantitative information on the influence of processing variables on casting features. Therefore, investigating the correlations between the process parameters and both macro and microstructures of metallic materials on one hand, and the relationships between casting structures and physical, chemical and mechanical properties on the other hand, is of major interest in industrial field.

In the archaeometric domain, gathering data on the emergence and spread of manufacturing technologies also provides precious proofs on the first human organizations, the construction and transformations of cities into states and societies.

Therefore, numerous researches involving archaeology and material science are still ongoing in order to improve our understanding of the technological transitions that occurred through time and across civilisations. Understanding the long-term behaviour of materials also permits to anticipate further alteration of modern materials.

The great majority of phenomena investigated in science and chemistry are complexes and depend on a large number of parameters. The validity of univariate methodologies, also called *OVAT* (One Variable at A Time) or *COST* (Change One Single variable at a Time), only depends on the total independence of the optimized variables taken into account. Such reasoning can then appear limited and do not guarantee the complete resolution of the definite issue.

Chemometrics is a field of chemistry, which applies multivariate mathematical and statistical methods to resolve specific issues. By simultaneously considering multiple variables, this methodology allows for the acquisition of a maximum of information from a chemical data set with a reduced number of experiments. This methodology can be applied in two different steps in the scientific procedure: before the experiment, by designing and selecting the optimal procedures or sets of experiments (Design of Experiment - DoE); after the experiment, to identify patterns in the chemical data set (similarities, differences, evolutions) by compressing the number of variables (Principal Component Analysis - PCA).

In the field of metallurgy, some examples of multivariate methodologies, in particular the use of design of experiment, are present in literature. Becker has performed mixture models in order to build correlations between properties and quantity of various components of the alloy (Becker, 1978). Experimental designs are also used in the industrial field for the analysis of casting quality since they allow to take into consideration several levels of different variables and quantify their respective impact (Viquar Mohiuddin et al., 2014; Dabade and Bhedasgainkar, 2013; Verran et al, 2008). However, to our knowledge, no design of experiment has been performed yet with the aim to investigate as-cast copper-based alloys, and in particular the impact of both mixture parameters and process variables. Regarding the PCA, it is more used in the extraction field for the interpretation of trace elements in alloys, and in archaeometric investigations for tracing object's provenance (Guissani et al., 2007).

Resuming, several problematic can be raised from this general panorama:

- What are the microstructural features of copper-based alloys of historical, artistic and industrial interest when submitted to non-equilibrium cooling rates characteristic of casting processes by gravity? Can they be predicted?
- Which archaeological information can be obtained from the metallographic analysis of as-cast products? What about immaterial culture of the society who produced these artefacts?
- Can multivariate thinking be applied in the investigation of as-cast materials in order to explore both composition effects and impact of process parameters?

CHAPTER 1.

CASTING TECHNOLOGY AND COPPER-BASED ALLOYS:

BRIDGES BETWEEN TIMES

1.1) The technology of casting by gravity

1.1.1) Generalities on metal casting

Metal casting technology consists in ancestral and modern manufacturing practices that allow the direct production of metallic pieces by pouring of a molten material into a mould made of a definite material containing a negative shape of the cast product (ASM Handbook, 1992).

This artefact can already be a finished product or a semi-finished product, which can be subjected to further thermomechanical treatments like annealing, quenching or mechanical deformation, in order to model more precisely its features. It could also be an ingot of specific composition, which would be remelt in later foundry processes.

A wide panel of casting processes is available to the metalworker, and numerous foundries and research centres are repeatedly working on more and more effective new casting processes. Figure 1 is displaying a classification of industrial casting processes according to the mould characteristics.

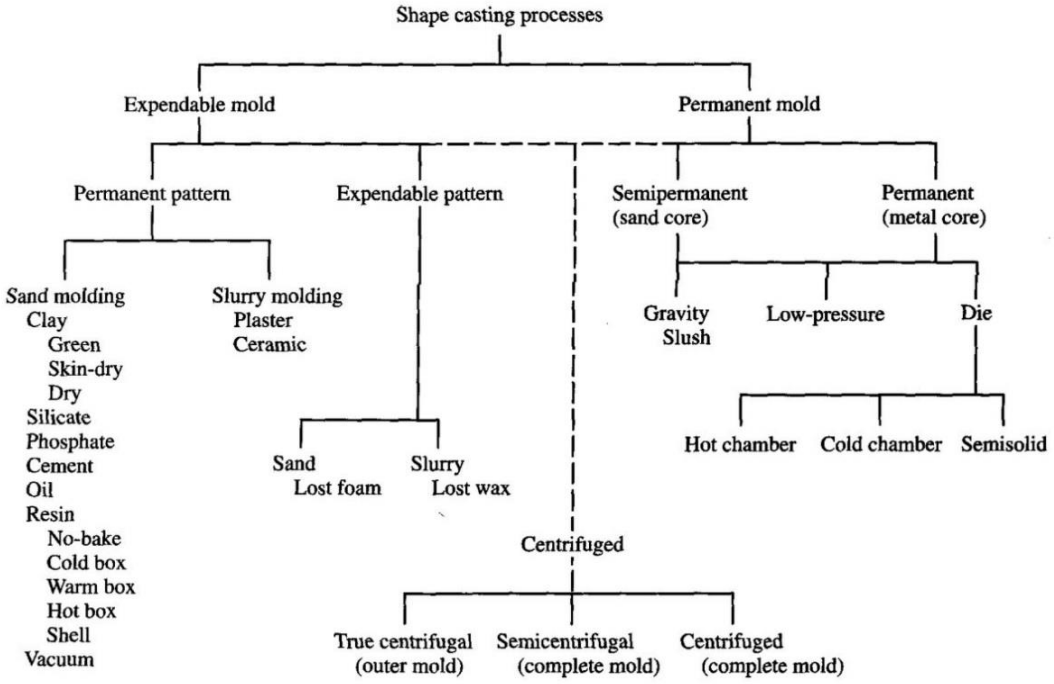

Figure 1: Metal casting processes (Schey, 2000)

Every process can be fragmented into a succession of elementary operations whose parameters are specific to the considered technique. The technical choices will have a strong influence on the quality and the features of the resulting cast product.

The first steps consist in the realisation of a pattern that is a positive model of the piece to cast from which the mould will be constructed. According to the purpose, several materials can be chosen for the pattern construction: metals (aluminium, brass), wood, resin or plaster. Both pattern and mould could be either expendable (i.e. consumed or broken during the process for the cast removal) or permanent and reusable for further castings. A particular attention should be paid to this stage in order to improve the filling of the mould by the melt and hence the quality of the product. Phenomena occurring during the pouring and the solidification of the metal are indeed deeply related to the mould characteristics and should be taken into account for an accurately prediction of the piece final features, as discussed in section 2.1. Numerical methods exist for the conception and drawing of casting models and sprue, as well as the position of pouring channels and vents in order to optimize this step (Campbell, 2004).

In further stages, the cast material is either prepared by using pre-manufactured ingots or is made by melting every alloying elements in adequate furnaces. In modern industry, these pure alloying metals come from ores smelting. Since its properties deeply depend on the amount of alloying elements, the presence of impurities may have a decisive impact on the final product. Furthermore, not all processes are suitable for every casting alloys and it is therefore important to choose the casting process with due regard to the casting alloy. This material is heated up to the pouring temperature. At this stage, a certain level of superheating over the melting temperature could be applied in order to increase the fluidity of the cast alloy.

Eventually the material is poured into the chosen mould. Different forces, such as gravity, pressure or centrifugal effect, can be involved in the mould filling. The atmosphere of casting is also an important parameter, since it is conditioning the interactions with the molten metal. Casting could be achieved either in ambient atmosphere, under vacuum or under inert atmosphere like helium or argon.

Unlike other manufacturing methods such as forging, pressing or metal joining, the metal casting technology has the advantages of enabling the series production of identical objects with a great precision, even for complex geometries. It also presents cost advantages over materials that are fabricated by other processing techniques (Hurst, 1996).

1.1.2) Main techniques of casting by gravity

The gravity casting is the simplest and oldest way of pouring a molten metal using gravity. During the process, the thermal energy of the alloy is transferred to the mould by conduction.

❖ **Sand casting**

Sand casting is widely used for its low costs of production. It offers to produce large amount of articles of great dimensions.

Various techniques might be applied for the mould construction according to the complexity of the casting piece design and to the way of production (one-off jobs or series production), from simple floor moulding, described in the archaeological section, to more complex protocols implying cores, inserts or hollow shapes (Hurst, 1996).

The most common technique is the two-box moulding in which a pair of matching segments (an upper and a lower part respectively called cope and drag) are accurately joined (Figure 2).

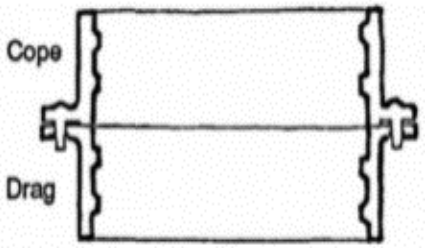

Figure 2 Sketch of the two moulding box in overturned position for sand casting (Hurst, 1996)

This cavity is produced with a pattern, commonly made of wood or metal, which gives the final shape of the piece. If the pattern has a flat surface, the technique is called flat-back moulding (Figure 3a), while the technique applied for a non-flat pattern is called odd-side moulding (Figure 3b).

In both techniques, the drag is first filled by rammed sand in overturned position. Once the drag turned right way up, the pattern is positioned on its surface and the cope is assembled over the drag. The gating system might be placed during this step. In turn, the cope is filled by rammed sand. Eventually, the pattern is carefully removed from the mould.

A large quantity of moulding sands can be chosen by the craftsmen. They are varying in term of moisture content, permeability and compression strength according to their mineralogical composition, grain morphology and granulometry. They are either called *natural*, if they are directly suitable for mould making in the extraction state, or *synthetic*, if a further mix with bounding agents or additives is needed.

The oldest and most basic form of sand casting is green sand moulding. The terminology green refers to the non-artificial nature of the materials used as binding agent. Hence natural moulding sand may be any colour from yellow to red due to the ferric minerals, and might even turn black or grey after few days of use.

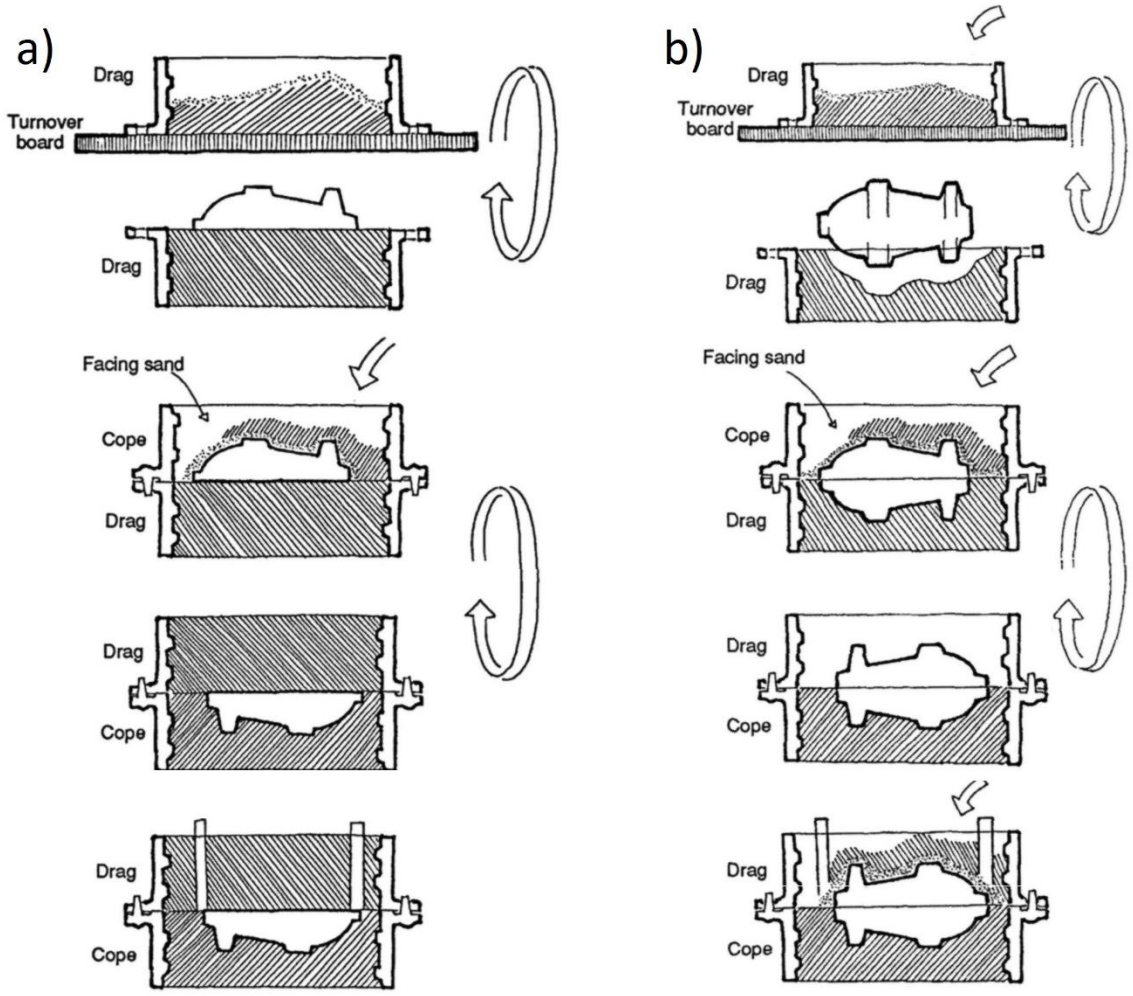

Figure 3: Two-box moulding technique (Hurst, 1996): a) flat-back moulding, b) odd-side moulding

❖ **Permanent-mould and chill casting**

Techniques involving non-expandable moulds are die, centrifugal and chill castings. Die and centrifugal castings are actually similar to permanent-mould casting, except that pressure and centrifugal force are respectively employed to fill the mould instead of gravity forces. Chill casting is widely used in industry for the large production of big and heavy section castings, as well as for the manufacturing of non-ferrous alloys (Flemings, 1991).

Before pouring, the mould is often preheated in order to limit the thermal shock between the molten material and the cold metallic surface. This way, the metal flow is favoured and the probability of thermal damages to the casting is reduced.

Refractory coatings, called washes (ceramic slurry) are often used in permanent mould- castings to intentionally decrease the heat transfer coefficient. This way, the mould filling is eased and the solidification-shrinkage cavities in the casting can be reduced. On the

other hand, washes also prevent the casting from sticking to the mould, and then prolong the mould life. Several studies have been performed in order to search for the optimum conditions of use, in order to improve the mould life (West and Grubach, 2004).

Since the mould has been manufactured with the hollow shape of the casting piece, cores installed inside the mould are not fundamental. The mould consists of two halves generally made of cast iron or steel. Other metallic and non- metallic materials could also be used like steel, bronze or graphite. An example of permanent mould is presented in Figure 4. Once closed, the molten metal could be poured inside the gating cavity and removed once solidified.

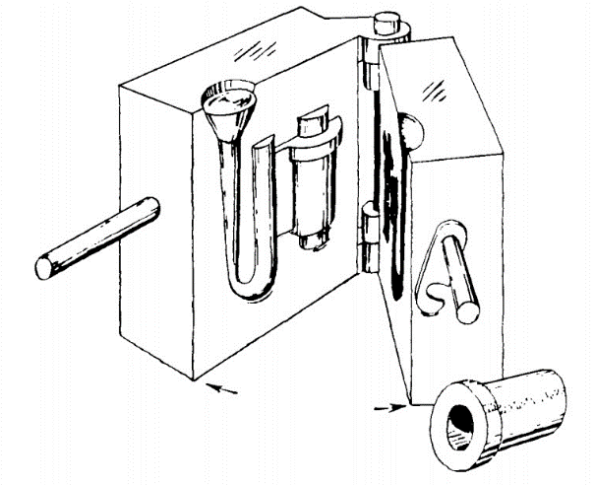

Figure 4: Permanent-mould casting (Taylor and al., 1959)

To overcome the absence of physical element in the mould design, which could compensate for metal shrinkage, the model dimensions are slightly oversized according to the tabulated contraction value of the corresponding cast metal. This way, the cast object can be further worked to reach the desired dimensions. A riser could also be inserted on the top of the piece in order to limit shrinkage defects on the casting. Vent holes are carved on the contact surface between the two halves in order to allow gas evacuation during the pouring stage, without leakage of the molten metal.

❖ Investment casting and lost-wax techniques

These processes are of particular interest for both industrial and artistic fields because of their ability to produce complex and precise geometry products with accuracy, repeatability and integrity using a large variety of metals or high-performance alloys. Therefore, this technique also presents higher costs of production than other processes.

These technologies are based on the use of clay materials as casting mould and on an expendable pattern made of wax, resin or plastics. Although similar, these two processes present nevertheless some technical differences.

Historically, this technique was essentially called lost-wax casting, for which two main methods might be applied (direct or indirect), as illustrated in Figure 5.

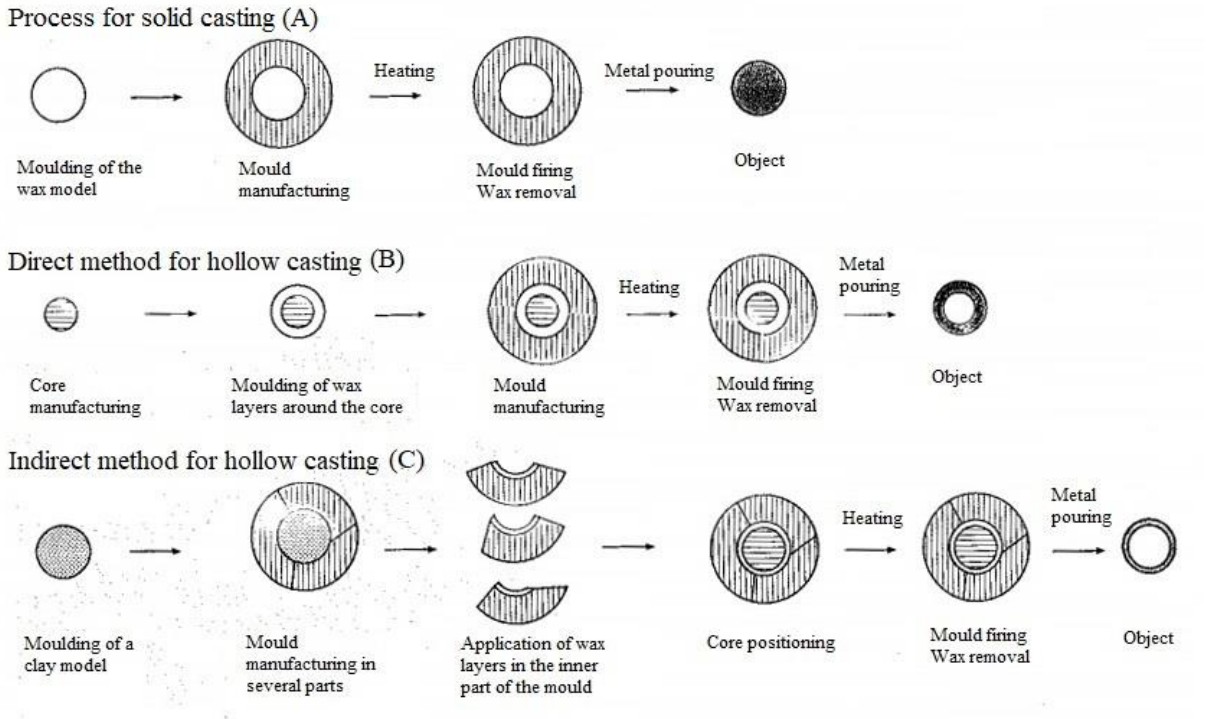

Figure 5: Lost-wax casting methods (Rolley, 2003, photo by B.Mille)

1. In the direct method, a positive wax pattern is made (A), possibly around a refractory core or a framework (B) and is connected by a network of gating channels made of wax as visible in the engraving of Wuttig (1814) presented in Figure 6. The model is then covered with several layers of wet clay and fibres. The addition of the core allows the achievement of hollow casting.

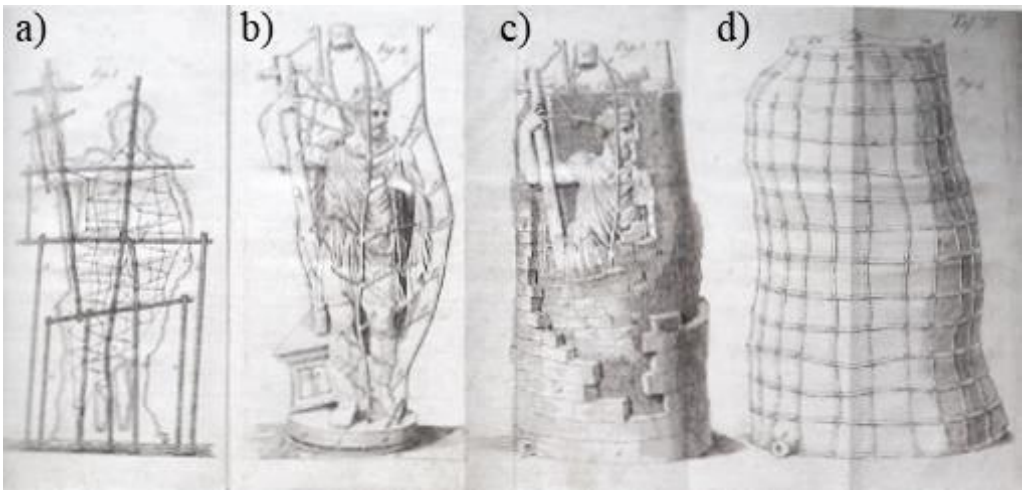

Figure 6: Preparation of the mould for lost-wax casting (Beentjes, 2014): a) construction of the framework, b) assembling of the wax gating channels, c) and d) construction of the refractory mould.

2. In the indirect method (C), a model of the piece is crafted and covered by mould fragments that are formed by clay layers (or plaster for modern applications). Once

disassembled and the model removed, the inner surface of mould fragments is recovered by several wax layers: first with molten wax in order to reproduce the finest details on the model's surface, and then by a thicker layer. The total thickness of the wax layers corresponds to the final casting metal layer. After having assembled back every mould fragments, the cavity is eventually filled with rammed refractory materials which will act as a core.

Subsequently, for both methods, the moulds are baked at high temperature in overturned position in order for the wax to melt, drip out or even volatilize along with moisture in the mould.

The great changes that occurred in the industry development during the mid-20th century made lost-wax casting evolve as investment casting for which series production becomes possible (Hurst, 1996).

In this new shell-investment-casting process, visible in Figure 7, several patterns of small dimensions are formed and assembled around the wax-gating axe. This pattern is then immersed in a slurry and in a fluidized bed of fine particulate material until a shell with a desired thickness is built up. Afterwards, the mould is dewaxed and fired in a similar way of lost-wax moulds. Once the metal is poured, the mould is broken, and pieces are separated from each other.

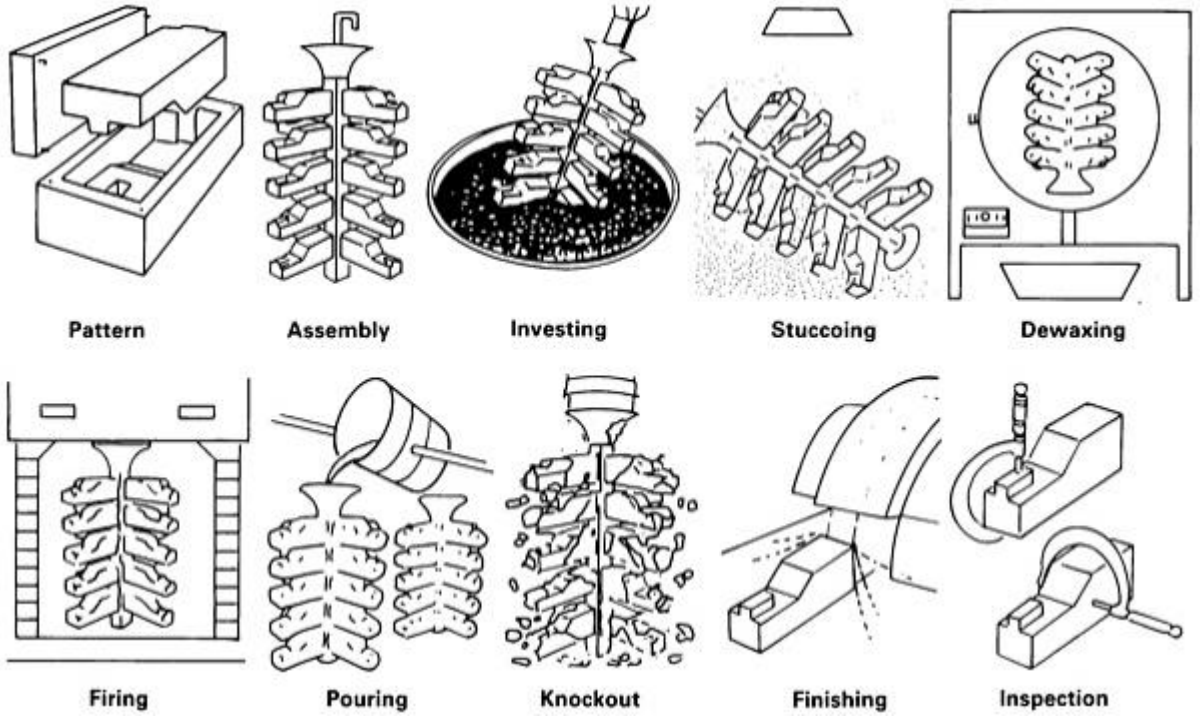

Figure 7: Investment casting process (Horton, 2004)

The major advantages of investment-casting processes, compared to sand castings, are the greater complexity, thinner sections, better dimensional accuracy and the final surface that can be obtained (Flemings, 1991). These techniques also appear to be complementary to other techniques: such as in the case of lost wax casting applied for ornaments or lettering on the surface of sand cast artefacts like cannon or bells (Hurst, 1996).

However, investment castings require long times of production in comparison with other techniques, involving high costs of production.

1.1.3) Some archaeological and historical keys for Western Europe

- **About early practices in Prehistorical and Classic Periods**

According to the actual state of knowledge, the development of stone tools is associated to the Palaeolithic Era, while the mastering of ceramic technology rather appeared during the Neolithic Era along with the beginnings of agriculture and sedentariness.

The discovery of native metals around the 10th millennium BC in different parts of the world, and their gradual use as a substitute for lithic tools in the successive millenniums correspond to the emergence of a new kind of hierarchical organizations (Tylecote, 1992). On one hand, metal working requires indeed a high level of specialization from the craftsmen, and on the other hand allows the production of lustrous non-perishable goods. It is therefore reasonable to assume that the appearance of metallurgy could only occur in highly structured societies (Pernot, 2006).

Later, the emergence of more complex metallurgical practices (the metal extraction from ores, melting and casting into artefacts) allows the design of new materials and consequently further progresses of civilization. Such processes are well detailed on ancient Egyptian tombs paintings of the 16th and 15th centuries BC (Gnesin, 2013).

In particular, the natural ability of metals in the molten state to fill cavities laid the basis for developing various casting techniques, which can be investigated in archaeological contexts through the examination of crucibles, moulds, ingots or furnace fragments.

The earliest evidences of casting techniques are originated from India and Mesopotamia, around the 4th-3rd millennium BC, in which open moulds made of insulating material (stone, clay or sand) were used for flat object manufacturing (De Ryck et al., 2005; Tylecote, 1991). Some moulds discovered by archaeologists even present the peculiarity of being multifaceted, i.e. rectangular block of stone in which each side is carved (Figure 8a) (Ashkenazi et al. 2016). No archaeological evidence for floor casting has been discovered for early periods yet. However, for obvious practical reasons of material availability and ease of use, this practice

cannot be questioned. Furthermore, foundries in many parts of Africa or India still use this method (Hurst**,** 1996).

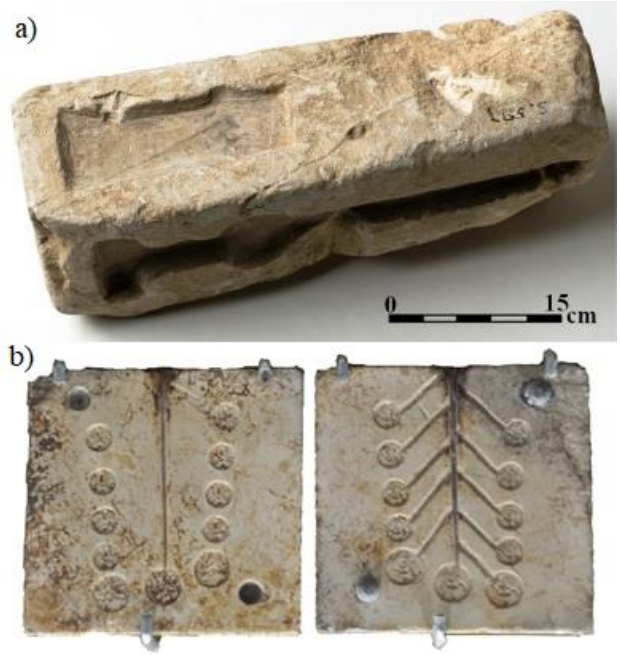

Figure 8: a) ***Four-sidded open stone mould for casting bronze*** *(Gezer, Israel, 13th-12th centuries BC) (Israel Antiquities Authority, photo by M. Suchowolski)(Ashkenazi et al. 2016);*

b) ***Bivavle mould in marble for lead casting*** *(1st-3rd centuries AC) (Vatican Museum, photo by P.Vernet)*

Later bivalve moulds or non-expandable moulds, in stone or metals, were manufactured to allow series productions, like arrowheads and spears (Figure 8b), while more complex techniques like lost-wax or sand casting were developed to produce greater size articles.

In their latest investigations, Webley and Adams have reviewed moulds made of bronze during the Later Bronze Age in Britain. They highlighted the fact that moulds were generally produced in leaded tin bronze; moulds were not only seen as raw tools but were sometimes finely decorated (Webley and Adams, 2016). Other studies on moulds from different period and areas are also known (Cert, 2000; Caparros et al., 2010).

The modalities of development of metallurgy and metallurgical practices, and their spread, along with consumption patterns of specific alloying elements still remain an important issue in archaeometallurgy. Several theories and models have been elaborated to figure it out (Berthoud et al., 1982; Roberts et al, 2009; Radivojević et al, 2013; Bray and Pollard, 2012; El Morr and Pernot, 2011).

The question of recycling in ancient casting practices is also a thorny issue among archaeologists, even if the latest studies showed some advancements thanks to new approaches in data interpretation (Pollard et al., 2015). Instead of giving importance to the exact chemical composition of alloys with assumptions about intentional or unintentional alloying process, they have rather observed trends for alloys ubiquity in a large number of archaeological sets from Britain. In this way, they were able to notice major changes in casting practices and metal circulation, particularly during the first millennium AC.

During Classical Era, the Greek and Roman civilizations are particularly recognised for their mastering of casting techniques in great and colossal statuary production.

Earliest known written sources allow to gather further technical information besides archaeometrical analysis. Hence, Pliny the Elder described the use of lost-wax technique with core on separate elements, and the burial of the whole mould in order to ease the metal pouring. According to the current knowledge, the technical progress from direct method to indirect method in lost-wax casting for great statuary is situated around the Vth century BC in Greece (Rolley, 2003).

The polychromic aspect of antic bronzes is also now well accepted and among patination finishing, elaborated separated-fusion processes could also be applied. For example, Formigli assumed that red lips made of copper could have been first cast (Figure 9a) and inserted in the lost-wax model of the head in order to be associated to the whole statue (Figure 9b). This way, a strong polychromic effect is obtained between the red colour of copper for lips and the goldish colour of bronze for the rest of the face (Figure 9c) (Formigli, 2013).

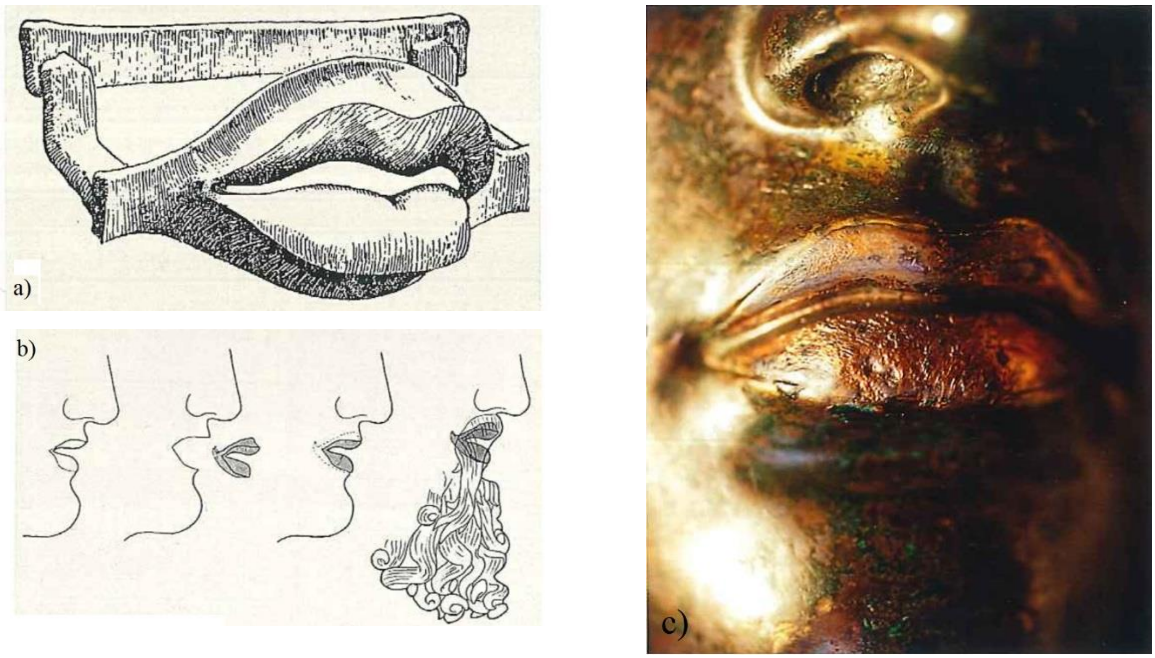

Figure 9: Examples of insert for bronze polychromy (Formigli, 2013): a) ***Graphic reconstruction of the Antikythera's Ephebos lips****, b)* ***Proposition of insert (Riace Bronze A)****, c)* ***Polychromic effect on the Ephebos of Via dell'Abbondanza (Pompei)***

- **From medieval era to European Renaissance**

After the decline of the Roman Empire during the first part of 1st millennium AC, and under the influence of western invaders, the metallurgy of ferrous materials knew technical improvements all along the medieval era in Western Europe. This phenomenon lead to an increased use of materials like wrought iron and steel for agricultural tools and military items.

However the metallurgy of non-ferrous materials remains obscure during the post-Roman period (Tylecote, 1992), even if written sources from alchemists or other authors like Theophilus during the early 12th still transmit encyclopaedic visions on the techniques at that time.

Regarding casting practices, the main foundry activities of this period focused on the fabrication of bells, cannons and cauldrons in copper-based alloys (Tylecote, 1992). Copper cauldrons will furthermore be precious goods for exchanges with Amerindian tribes during the 17th century (Moreau, 2017). Sand moulding is probably used for the creation of simple solid castings in both open and two-part moulds, while lost-wax casting technique were likely performed for more complex objects (Beentjes, 2014).

During the Renaissance, the keen interest of architects, poets and philosopher for ancient Greek and Roman civilizations is noticeable across the whole occidental Europe. This phenomenon leads to a revival of casting technology and new technological innovations focused on the development of processes allowing the reproduction of great size artworks.

The relationships between masters and apprentices induce a deep change in the structure of the society and the development of an international founders network across Europe based on skill diffusion (Chevillot, 2014). Dańko and Holtzer also highlighted the fact that the invention of printing by Gutenberg during the 15th century certainly played a role in the development of low-melting non-ferrous metal casting (Dańko and Holtzer, 2006).

Hence, large single castings were attempted from Italy to Holland with the techniques of lost wax casting (Chevillot, 2014; Beentjes, 2014). In this connected area that is the western Europe, the identification of national patterns in the casting process for the French production have been explored by Castelle et al. through archaemetrical investigation of the core (Castelle et al., 2015).

Among this great statuary production, an other kind of arteworks inspired by the Roman tradition have flourished during the 16th century: the small lifelike sculptures. These productions, that was often higher-prized than hand-sculpted artworks, feature very fine details and were manufactured from real life animals or plants with a combined technique of sand moulding and lost-wax casting (Figure 10) (Smith and Beentjes, 2010).

Figure 10:Life-cast lizard (lead)and plants, (silver), attributed to Wenzel Jamnitzer (ca. 1540) (Smith and Beentjes, 2010, picture Germanisches Nationalmuseum)

Eventually, according to Tylecote this post-medieval period laid the foundations for the Industrial Revolution which started in Western Europe with the use of coal for metallurgical processes around 1700 (Tylecote, 1992).

- **Modern industrial progresses**

Beentjes argues that, at the beginning of the 19th century, almost all bronze and iron sculptures were mainly cast using lost-wax technique and different materials as mould (loam and plaster) as noted in the technical literature of this time (Beentjes, 2014).

In addition, foundry men were highly specialized in either lost-wax casting or sand casting, since these two technologies often appeared as competitive (Dubos, 2003).

From the 19th century and during the first part of the 20th century, industrial revolutions and world wars have propelled metallurgical activities and deeply modified metallurgical practices. The fast evolutions of innovation brought different techniques that, instead of being opposite, are found to be complementary, unlike historical opposition between lost-wax and sand casting (Dubos, 2003).

Lost wax casting knew particular innovations thanks to contemporary materials evolution and development of first gelatine, and then silicon and plaster, for the model surface reproduction (Dubos, 2003; Hurst, 1996).

Sand moulding practices are widespread across Europe between 1810 and 1960, and began to be particularly used for great statuary. For instance, important performance has been realized for the civil statuary in Paris. The arrival of new synthetic materials like mould bounding also facilitates the process and permits to significantly reduce time of fabrication (Beentjes, 2014; Dubos, 2003).

Later, aeronautic and automobile fields played a fundamental role in the second half of the 20th century for the development of new casting techniques for aluminium and light alloys.

Nowadays the foundry industry still stand worldwide in a predominant position and cast products represent 90 percent of manufactured goods and equipment. A large number of industrial sectors is covered worldwide by foundry products applications, from critical component for aircraft and automobiles to home appliances and surgical equipment (Kanicki, 2004).

1.2) Copper and its alloys

1.2.1) Classification of copper-based alloys

Over 400 copper-based alloys are referenced for industrial applications according to specific standards like the Unified Numbering System (UNS) from the American Society for Testing and Materials (ASTM). These standards have been developed with the concern to produce a global designation system to describe the chemical composition and the metallurgical state of alloys. Figure 11 presents a general overview of the different copper-based alloys families, classified on the basis of their main alloying elements.

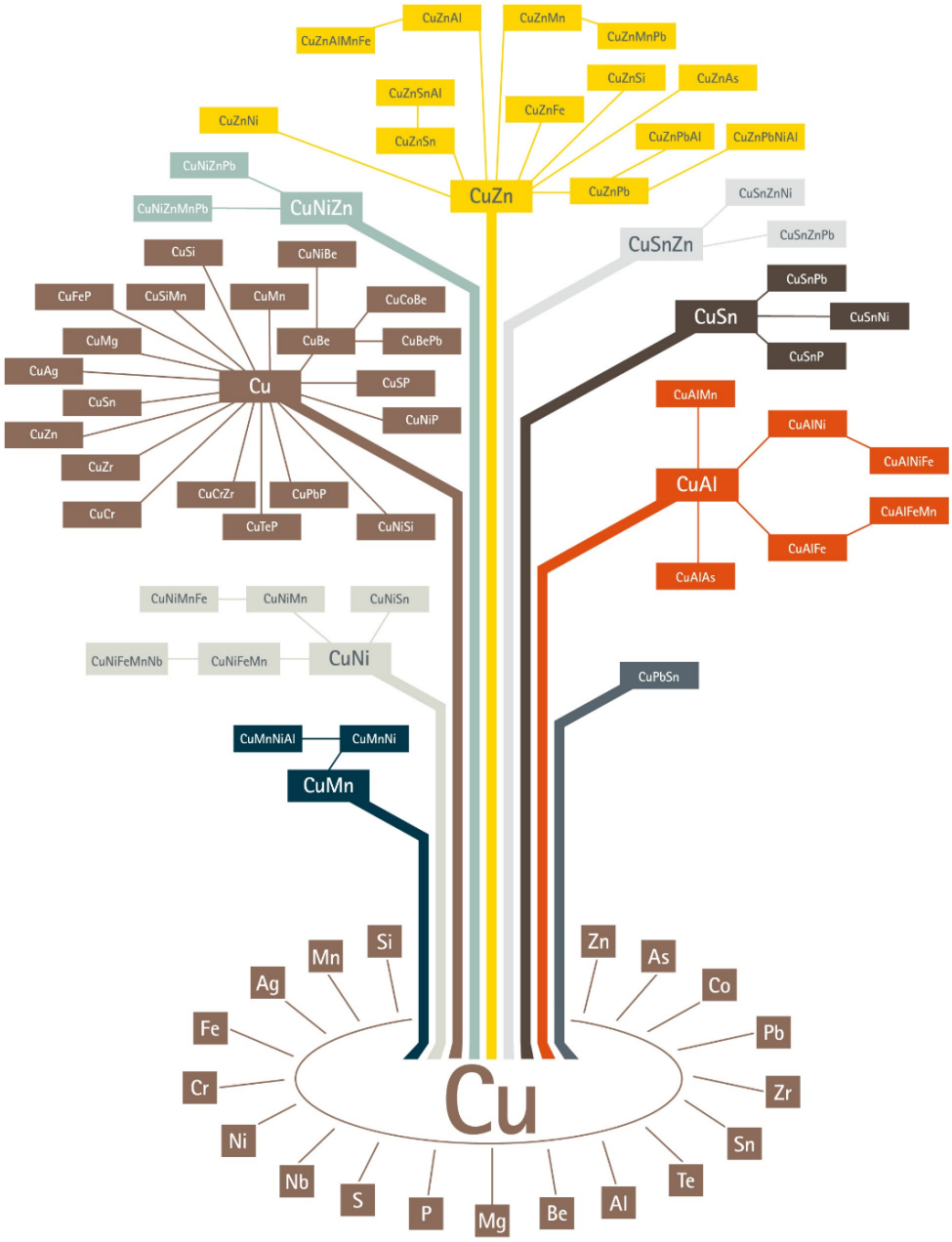

Figure 11: Copper-based alloys families (International Copper Association)

These materials are separated in two main categories: wrought copper alloys (C16000 to C79999) for applications involving plastic deformation and cast copper alloys (C81300 to C99999), which are used in foundry processes.

The nominal compositions of these alloys are detailed in reference Handbook (Schmidt and Schmidt, 2000). They are classified according to the relative standard ASTM, in relation with their main application or manufacturing process.

Table 1 details the main families of industrial cast copper alloys, with particular attention to alloys containing tin (Sn), zinc (Zn) or lead (Pb) as main alloying elements. Other alloys containing iron (Fe), aluminium (Al), manganese (Mn), nickel (Ni), phosphorus (P), silicon (Si) and niobium (Nb), are also widely used by industries but are not taken into consideration in this study.

Common name	*UNS numbers*	*Composition*	*ASTM Standard*
Coppers	**C80100-C81100**	**>99% Cu**	
High-copper alloys	**C81300-C82800**	**>94% Cu**	
Red and leaded alloys	**C83300-C85800**	**Cu-Zn-Sn-Pb (75-89% Cu)**	
Leaded red brass	C83600	Cu Sn5 Pb5 Zn5	ASTM B 62
Leaded red brass	C83600	Cu Sn5 Pb5 Zn5	ASTM B 584
Leaded red brass	C83800	Cu Sn4 Pb6 Zn7	ASTM B 584
Leaded semired brass	C84400	Cu Sn3 Pb7 Zn9	ASTM B 584
Leaded semired brass	C84800	Cu Sn3 Pb6 Zn15	ASTM B 584
Yellow and leaded alloys	**C85200-C85800**	**Cu-Zn-Sn-Pb (57-74% Cu)**	
Yellow brass	C85700	Cu Sn1 Pb1 Zn37	ASTM B 176
Yellow brass	C85800	Cu Sn1 Pb1 Zn40	ASTM B 176
Leaded yellow brass	C85200	Cu Sn1 Pb3 Zn24	ASTM B 584
Leaded yellow brass	C85400	Cu Sn1 Pb3 Zn29	ASTM B 584
Leaded naval brass	C85700	Cu Sn1 Pb1 Zn37	ASTM B 584
Mangenese bronzes and leaded alloys	**C86100-C86800**	**Cu-Zn-Mn-Fe-Pb**	
Silicon bronzes, silicon brasses	**C87300-C87900**	**Cu-Zn-Si**	
Tin bronzes and leaded alloys	**C90200-C94500**	**Cu-Sn-Zn-Pb**	
Tin bronze	C90500	Cu Sn10 Zn2	ASTM B 22
Tin bronze	C91100	Cu Sn16	ASTM B 22
Tin bronze	C91300	Cu Sn19	ASTM B 22
Valve bronze	C92200	Cu Sn6 Pb1.5 Zn4	ASTM B 61
High-lead tin bronze	C93800	Cu Sn7 Pb15	ASTM B 66
High-lead tin bronze	C94300	Cu Sn5 Pb25	ASTM B 66
High-lead tin bronze	C94500	Cu Sn7 Pb19 Zn1	ASTM B 66
High-lead tin bronze	C94100	Cu Sn5.5 Pb20	ASTM B 67
Modified G bronze	C90300	Cu Sn8 Zn4	ASTM B 584
G bronze	C90500	Cu Sn10 Zn2	ASTM B 584
Navy M	C92200	Cu Sn6 Pb1.5 Zn1.5	ASTM B 584
Leaded tin bronze	C92300	Cu Sn8 Pb1 Zn4	ASTM B 584
Leaded tin bronze	C92500	Cu Sn10 Pb1 Zn2	ASTM B 584
High-leaded tin bronze	C93200	Cu Sn7 Pb7 Zn3	ASTM B 584
High-leaded tin bronze	C93500	Cu Sn5 Pb9 Zn1	ASTM B 584
High-leaded tin bronze	C93700	Cu Sn10 Pb10	ASTM B 584
High-leaded tin bronze	C93800	Cu Sn7 Pb15	ASTM B 584
High-leaded tin bronze	C94300	Cu Sn5 Pb25	ASTM B 584

Common name	*UNS numbers*	*Composition*	*ASTM Standard*
Nickel-tin bronzes	**C94700-C94900**	**Cu-Ni-Sn-Zn-Pb**	
Aluminium bronzes	**C95522-C95810**	**Cu-Al-Fe-Ni**	
Copper-nickels	**C96200-C96800**	**Cu-Ni-Fe**	
Nickel silvers	**C97300-C97800**	**Cu-Ni-Zn-Pb-Sn**	
Leaded coppers	**C98200-C98800**	**Cu-Pb**	
Special alloys	**C99300-C99750**	**Ni, Fe, Al, Co, Si, Zn, Mn, Pb**	

Table 1: Generic classification of copper alloys (Tyler, 2000).
ASTM B 22 - Standard Specification for Bronze Castings for Bridges and Turntables;
ASTM B 61 - Standard Specification for Steam or Valve Bronze Castings;
ASTM B 62 - Standard Specification for Composition Bronze or Ounce Metal Castings;
ASTM B66 - Standard Specification for Bronze Castings for Steam Locomotive Wearing Parts;
ASTM B 67 - Standard Specification for Car and Tender Journal Bearings, Lined;
ASTM B 176 - Standard Specification for Copper-Alloy Die Castings;
ASTM B 584 - Standard Specification for Copper Alloy Sand Castings for General Applications.

Casting copper alloys can be further subdivided into three subgroups according to their solidification typology. Indeed, unlike pure metals, which solidify at a single temperature, the solidification of alloys occurs in a specific range of temperatures, whose boundaries are called liquidus and solidus. The particular case of alloy compositions leading to solidification with an invariant transformation (eutectic, peritectic, monotectic), and then an unique temperature of fusion, will be discussed later.

The group I, II and III feature a narrow interval of solidification (50°C), an intermediate solidification range (50-110°C) and a wide freezing range (over 110°C), respectively. The corresponding alloys are visible Table 2. Specific conditions of casting and recommendation would be applied to the different groups, based on empiric experience (Schmidt et al., 2004).

Group I	*Group II*	*Group III*
Copper	Beryllium-coppers	Leaded red brasses
Chromium-copper	Silicon bronzes	Semi-red brasses
Yellow brasses	Silicon brasses	Tin bronzes
Manganese bronzes	Copper-Nickel	Leaded tin bronzes
Aluminium bronzes		High-leaded tin bronzes
Nickel bronzes		
Nickel silvers		
Manganese brasses		

Table 2: Casting groups for copper-based alloys (Schmidt et al., 2004)

The particular combination of chemical and physical properties such as strength, conductivity, corrosion resistance, machinability and ductility make copper and its alloys suitable for a wide range of applications:

- Their high electrical and thermal conductivities make them respectively used as conducting materials in electrical devices, and for heat exchangers, coolers, radiators or chemical construction.

- Their ease to form makes them adequate materials for the manufacture of wires, strips, pots or plates.
- Their good chemical resistance, as well as corrosion resistance, are leveraged for chemical apparatus, overhead cables or rain gutters and specific applications for seawater environment.
- The non-magnetic features are optimal for the manufacture of magnets or coils.
- The colour features of copper alloys are particularly useful in jewellery and artworks.

All these properties can be further enhanced, depending on the composition and manufacturing methods (Heller, 2006). The applications for cast copper and cast copper alloys are detailed in reference Handbooks (Tyler, 2000).

1.2.2) Alloys of interest for the study

❖ **Pure copper and low-alloyed copper**

The copper and high copper alloys are found either wrought or cast and respectively contain a minimum copper content of 99.3 wt.% and 96.0 wt.%, with different proportions of beryllium, cobalt, chrome, silver, nickel and silicon.

When forming processes are involving copper in liquid state, oxygen can be easily dissolved in the metallic matrix. Pure copper and high copper alloys may then contain small oxygen contents, leading to the formation of detrimental oxides for the material characteristics. Several electrolytic or thermal procedures exist and can be applied to refine these materials (Schmidt et al., 2004).

Pure copper is mainly used for electrical and thermal conductors, as well as in applications requiring a particular resistance to corrosion and oxidation.

Depending on the alloy composition and the nature of the main alloying elements, the application field of high-copper alloys cover from high-hardness electrical and thermal conductors, to bearings, safety tools, pump parts and moulds for plastic manufacturing (Tyler, 2000).

❖ **Brass**

From a chemical point of view, the term *brass* refers to alloys of copper and zinc. The industrial reality is actually more complex and a large number of alloys families exists according to zinc content and the nature of secondary alloying elements.

When the zinc content is low (5 – 20wt.%), the material is called *redbrass* or *semired brass*, and might contain tin and lead up to 5 and 7 wt.% respectively. For these alloys, the colour varies between the typical-red of copper rich alloys to a goldish tint. When the zinc content is higher (20 – 36 wt.%), the alloy is said *yellow* and might contain tin and lead up to 1 and 3 wt.% respectively.

Nonetheless, other designations exist. Hence, brasses with a zinc content between 3 and 33 wt.% is also called *tombac*, and quaternary alloys Cu-Sn-Pb-Zn are also known under the american term of *gunmetal*. Other than tin and lead, brasses might also contain iron, aluminium, nickel or silicon in various quantities.

Brasses are appreciated for their workability features as well as their resistance to both saline and freshwater since the addition of zinc also bring an improvement of some properties (e.g. excellent deformability on a large interval of composition, better ductility). Therefore brasses are among the most important copper alloys in terms of industrial applications and are widely used in the field of valves, pipe systems for the carriage of drinkable water**,** coins, air conditioning systems or contact surfaces.

Beyond those improvements, zinc also presents the advantage of being less expensive than other metals, reducing the costs of production. Furthermore, the addition of zinc brings a colour change of the copper matrix, from typical red to different shades of yellow.

Ancient brass artefacts have been sporadically discovered in archaeological assemblages from India, Middle East and Greece under the form of very small items and ornaments. Despite an early appearance from 3^{rd}-1^{st} millennium BC (Thornton, 2007), the manufacturing of brasses have not be carried out by direct fusion of copper and zinc due to the evaporation of this latter in the range of temperatures of the reduction process.

The casting of copper-zinc alloys from pure element became only possible with the discovery of the cementation process performed by Romans around the 1^{st} century BC (Tylecote, 1987). During the Greek-Roman period, Plato has reported that brass alloys were called *orichalcum* and were considered, with gold, as the most precious metal because of their shiny appearance and yellow colour (Gnesin, 2013). Consequently, this particular metallic material has given during the 17^{th} century in Italy a singular status to artisans who worked it: the *ottonari* from *ottone*, the italian designation for brass (Lamouche, 2013).

However, this material acquired a lower prestige with respect to bronze, confining it to the production of smaller artefacts, mainly for ornaments or everyday life objects. This aspect has also been noted in the funeral statuary at the Monumental Cemetery of Staglieno in Genoa, Italy (Bongiorno et al, 2017) where brass alloys were widely used for small ornamental objects.

For handcrafted and traditional artworks, brasses might be preferred by craftsmen because less brittle than bronze, easier to work during the finishing stages of manufacture and for its capacity to better reproduce finer superficial details (Friedman, 2001).

- **Bronzes**

Originally referring to materials containing tin as main alloying element, the term *bronze* currently refers to copper-rich materials in which the major alloying element is different from zinc or nickel. Except for the manganese bronze family that actually are included in brasses. Cupro-aluminium alloys (Cu-Al) are also called aluminium bronzes.

Tin bronzes are the oldest alloys that are still in use in our contemporary society and their usages are intimately associated with the gradual evolution of humankind from Stone Age to the modern periods, as described by Chevillot (Chevillot, 2014). Thanks to its aesthetic properties and the experience accumulated through time for its casting, the bronze is still considered as a noble material and continue to be used for great artworks like statuary.

Apart from the high academic interest, this versatile material gets numerous applications in industrial field for its mechanical, electrical and chemical properties. For example the binary alloy is widely present in lead-free soldering, since tin is the main component of most of solder materials and copper is the most frequently used contact material.

First appearances of tin bronzes are documented in Mesopotamia from the end of the 4^{th} millennium BC and in both Anatolia and Central Europe from the early 3^{rd} millennium BC (De Ryck et al., 2005). Technologically, tin bronzes are well known as a substitute to first arsenical bronzes (Lechtman, 1996).

Through times, the chemical composition of ancient bronzes significantly differs according to the region and the period in which they were produced (Ingo et al., 2006; Ashkenazi et al., 2016; Gouda et al., 2012). Later, their composition varied between 8 and 12wt.% since this composition range allow the material to reach optimal properties for their fabrication and uses (Piccardo and Pernot, 1997).

Despite their fragility and high hardness, high tin bronzes were used for the manufacturing of mirrors since they present an optimal resistance to scratch (Park et al., 2009; Meeks, 1986).

According to a long tradition, high tin bronzes are still in use in the artistic manufacturing of bells and musical instruments for the specific acoustic properties of the delta phase (Debut et al., 2016). In his PhD work, Lamouche reported that according to Biringuccio, during the 16th century in Italy, a distinction was made between bronzes with low and intermediate tin content, and with high-tin bronzes. While the first alloys was called "*bronzo*", the latest ones were called "*metallo*" even if no assimilation to two different materials was made (Lamouche, 2013).

- **Leaded Copper alloys**

Lead is commonly added to copper alloys in order to improve their workability and castability.

Indeed, according to traditional skills, lead might improve the fluidity of copper alloys. Investigations aiming to demonstrate this phenomenon have been performed by Piccardo et al. but no clear relationship between lead content and fluidity have been found yet (Piccardo et al. 2009).

Ternary leaded tin bronze are known from the Middle Bronze Age (c. 1500-1000 BC) in Great Britain and from the 8th century BC in Central Europe (Tylecote, 1992).

In the continuity of Bronze Age, ternary Cu-Sn-Pb alloys are widely used in great statuary. Furthermore, a large variety of objects in high-leaded bronzes has been found in China (vessel, mirror, coins, etc..) (Quaranta et al, 2014).

In industrial classification, leaded copper alloys are a category of casting copper alloys that contain 20 wt.% or more lead. A small amount of silver may also be present, but without tin or zinc. This category should not be confused with the leaded version of previous alloys in which lead remains present at lower contents.

1.2.3) New challenges for copper and its alloys

In the last decades, researches pushing the boundaries of current applications of copper-based alloys have been carried on, aiming at promoting the use of copper-based material to solve global issues such as energy, climate change or health. Some structures, like the Copper Alliance, have created a worldwide network of copper centres spread over the five continents, in the interest of bringing together all the actors working with this material. This organization also gather and diffuse a large documentation on copper and copper-based alloys.

For instance, Frütauer et al. argue that tin bronzes could be an interesting material for the substitution of graphite anodes in lithium ion batteries, since their intermetallic compounds could enhance the storage capacity of the cells and hence improve their cycling stability (Frütauer et al, 2013). The intermetallic compounds of the Cu-Sn system are also of particular interest for electronic packaging and microeletronic applications as conducting substrates (Sang et al., 2009).

Copper alloys of different nature (CuSn, CuZn, CuZnSiP, CuZnPbAl, CuZnSi) tend to be used for their antibacterial features in order to avoid epidemic hazard, particularly in public places, like hospitals for instance or for structures and tools (Efstathiou et al., 2013).

For environment issues, copper-based alloys have been developed for fishing nets (UR30®: CuZnSnAl) because of their antifouling properties and their stability in corrosive and marine atmosphere (Ayer et al., 2016).

CHAPTER 2.

SOLIDIFICATION OF SOME COPPER BASED ALLOYS: FROM PHASE DIAGRAMS TO NONEQUILIBRIUM BEHAVIOUR

2.1) Solidification of casting and ingots

2.1.1) Principles of solidification

Solidification involves the transformation of a molten metal back into the solid state through an exothermic transition. The freezing of materials is conducted by two main mechanisms: nucleation and growth. These phenomena are correlated together by the Gibbs free energy at the interface between the primary and the newly formed phases.

Detailed thermodynamic and kinetics descriptions of these two phenomena, as well as mathematic description of each mechanism, can be found in referential books (Biloni and Boettinger, 1996; Flemings, 1991; Fredriksson and Åkerlind, 2006; Perepezko, 2004; Lesoult, 2004).

Nucleation

Nucleation is a very large concept, which can actually be extent to the other phase transformations like condensation (formation of liquid droplets in saturated vapour), vaporisation (formation of gaseous bubbles) or solid-state transformations (nucleation of clusters in solid materials).

During the cooling of a metallic melt, when the system temperature reaches the melting temperature, first nuclei of a new phase can form. These aggregates feature extremely small dimensions and are not necessarily spherical, according to the interface features. The relative stability of the system could not be guaranteed for equilibrium condition. Indeed, when the system is hold at the melting temperature, there are statistically as many formed nuclei, that dissolved nuclei, since the activation energy for the transition state cannot be reached.

If the temperature of the system is rapidly decreased, the energetic barrier can be lowered, as well as the critical radius value necessary to the nuclei stabilization. This departure from equilibrium temperature is fundamental for crystallization. This phenomenon is called *undercooling*.

When the cooling of the system continues, these nuclei get bigger and become clusters. Once the nucleation is started, and if the temperature decrease is constantly held, nucleation rate raises and the nucleation becomes faster.

The apparition of these extremely small aggregates can occur spontaneously and randomly from the primary phase (*homogeneous nucleation*, Figure 12a) or from solid substrates already present in the medium like inclusions (*heterogeneous nucleation*, Figure 12b).

This last mechanism is thermodynamically favoured, since the presence of nucleation sites permits to decrease the nuclei critical volume, as well as the activation energy.

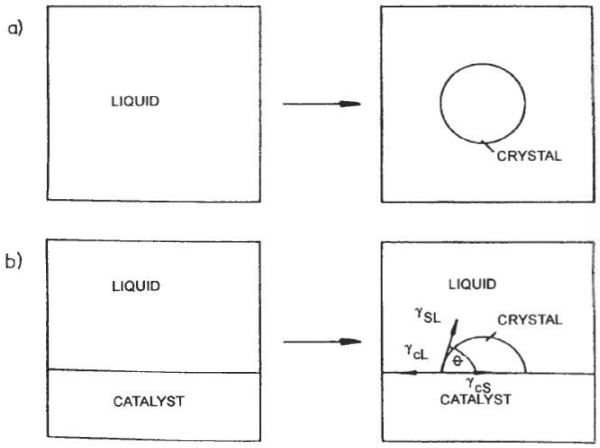

Figure 12: Schematic representation of nucleation mechanisms: a) homogeneous nucleation, b) heterogeneous nucleation (Biloni and Boettiger, 1996)

Growth

Once nuclei are formed and thermodynamically stable, the energy of the system further decreases by their growth through a mechanism of atoms aggregation. The phase transformation of metallurgical interest can be distinguished between those depending on diffusional phenomena and those, which don't. While the first kind corresponds to transformations without any change in the number and composition of phases, the others are transformation providing the formation of metastable phases (e.g. martensite in ferrous materials).

In metallic materials, the growth of grains is generally achieved in the direction of maximal crystallographic density, which brings, for FCC lattices, to the formation of dendritic patterns along the [100] direction.

The growth mechanisms depends on the kinetics conditions and the interface features between the liquid phase and the solid: if the phenomenon is fast, the aggregation of atoms will be coarse, while slower growth rate will bring more defined structures.

2.1.2) Heat transfers during solidification

When hot melt is poured into a mould with a lower temperature, the solidification is driven by the removal of heat along the directions of temperature gradients. A schematic illustration of thermal transfers during solidification is presented Figure 13 for simple geometry casting.

When alloys with large solidification range are considered, the interface between the liquid and the newly formed solid is characterized by the presence of a *mushy zone* (Flemings, 1991).

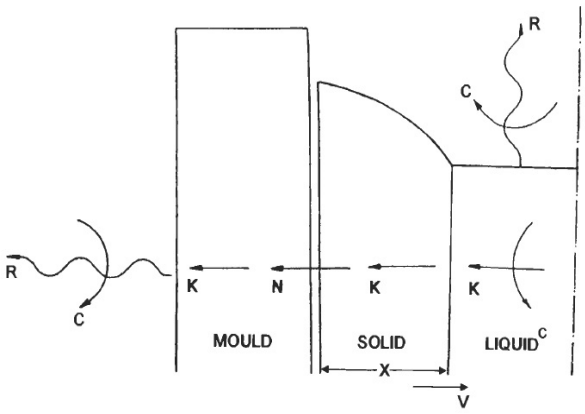

Figure 13: Thermal conditions for solidification of pure superheated liquid metal. R = radiation, C = convection, K = conduction, N = Newtonian heat transfer (Biloni and Boettinger, 1996)

The heat transfer is limited by a series of resistances, which mathematically lead to the heat transfer problem. Generally, the heat flow is limited by the metal-mould thermal resistance, quantified by the Heat Transfer Coefficient (HTC, hi). Many engineering investigations aim the determination of the heat transfer coefficient at the metal-mould interface during specific casting process conditions (Ho and Pehlke, 1985; Silva et al, 2011; Konrad et al., 2011). In particular, some predictions are performed by numerical simulation (Diao and Tsai, 1993; Bonollo and Gramegna; Bencomo et al., 2008).

A great number of casting processes employ mould materials with relatively insulating properties compared to the metal being cast. In this case, the temperature profile inside the mould regularly decreases (Figure 14a). If the process implies the use of metallic permanent mould, the gap is considered discontinuous (Figure 14b).

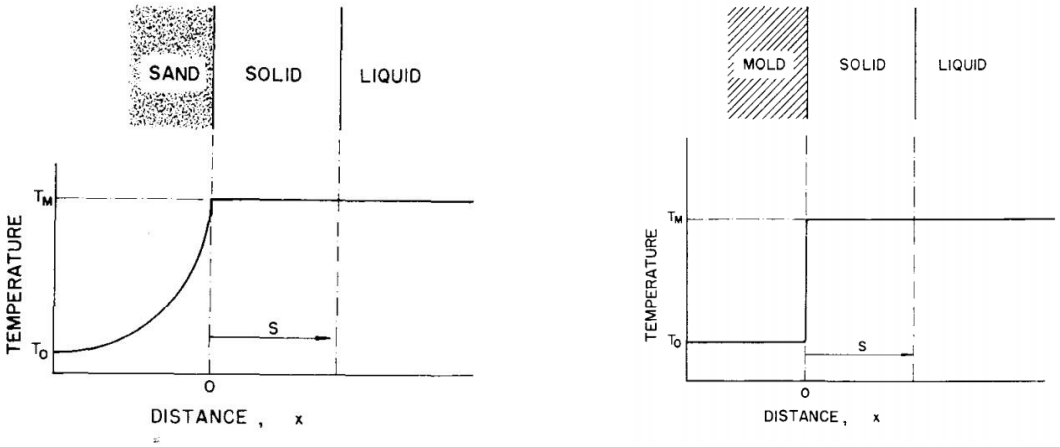

Figure 14: Temperature profiles during casting: a) in insulating mould, b) in permanent mould (Flemings, 1991)

2.1.3) Structure of ingots

During the cooling of a metallic melt poured in a casting mould, the formation of the solid material follows the mechanisms of crystal nucleation and growth previously detailed. It is of interest to examine the metallographic grain formation and growth patterns occurring during this solidification process (Figure 15).

In the area in direct contact with the mould, the undercooling of the melt is particularly high, as well as the cooling rate. Immediately after pouring, the interface at the mould walls acts as substrate for the heterogeneou***s*** nucleation, a large quantity of nuclei is formed, which leads to the formation of a thin skin of solid metal composed by small equiaxed crystals. This zone is called chill zone.

Progressively, as cooling continues, the skin thickness increases to from a shell around the molten metal as heat is transferred through the mould to the ambient environment and solidification, at the contrary, progresses toward the mould cavity centre.

Eventually, the solute concentration increases and the mode of solidification changes from growth of columnar grains to the formation of either equiaxed or columnar dendrites. Dendritic is the most common crystallization mechanism in copper-based alloys. The transition from columnar to equiaxed zones (CET) is defined by a competition between columnar and equiaxed grain growth. Some mechanism has been proposed in literature (Flood and Hunt, 2004).

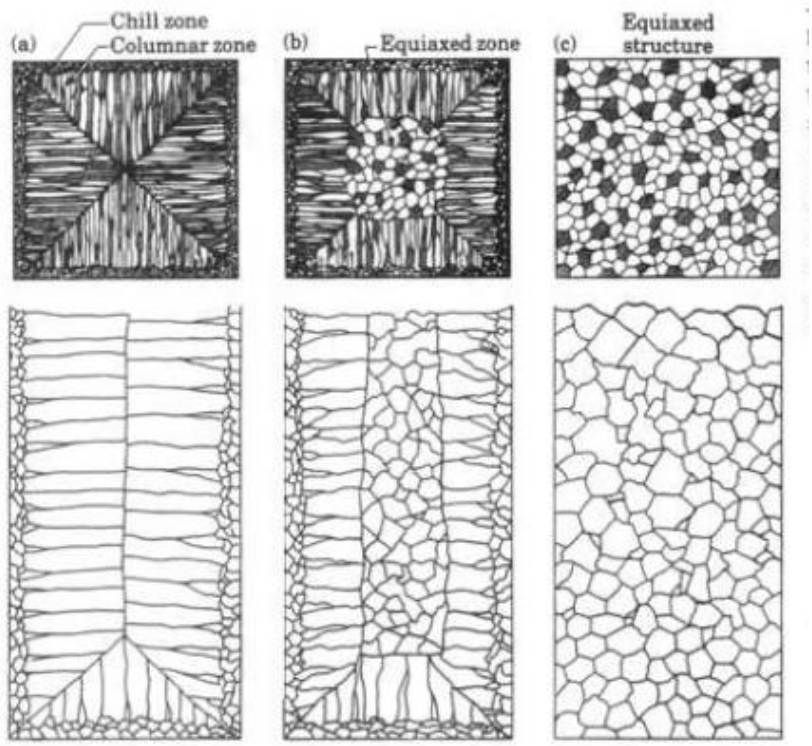

Figure 15: Cast structures of metals solidified in a square mould: a) pure metals, b) solid-solution alloys, c) case of heterogeneous nucleation of grains using nucleating agents (Form and Wallace, 1960)

2.2) The equilibrium prediction

During variations of temperature or composition, phase diagrams allow for the prediction of the alloys behaviour, i.e. the microstructural changes that arise in the material. In these isobaric representations, both liquid-solid and solid-solid transformations are thermodynamically investigated by considering infinitely slow reaction rates. These ones can be assimilated to thermodynamic equilibria.

In this section, only ranges of composition having an interest for this research will be considered: tin, zinc and lead contents respectively up to 20, 40 and 20 wt.%.

2.2.1) Peritectic alloys: bronzes, brasses and gunmetals

2.2.1.1) The peritectic solidification

The peritectic solidification provides for the formation, at the peritectic temperature, of a solid phase (β) called *peritectic*, by the reaction of the liquid phase (L) with a previously formed solid phase (α).

The peritectic solidification can be shortened as: $L + \alpha \rightarrow \beta$, in which the α and β phases might be either solid solutions or intermetallic compounds (Stefanescu and Ruxana, 2004)

In contrast to other invariant transformations (eutectic or monotectic), an interval of solidification exists in the peritectic solidification and may involve a congruent melting. Figure 16 displays the three typologies of peritectic representation in phase diagrams. These classes differ in the shape of the peritectic domain, delimited by the β/ (α+β) solvus and the β solidus.

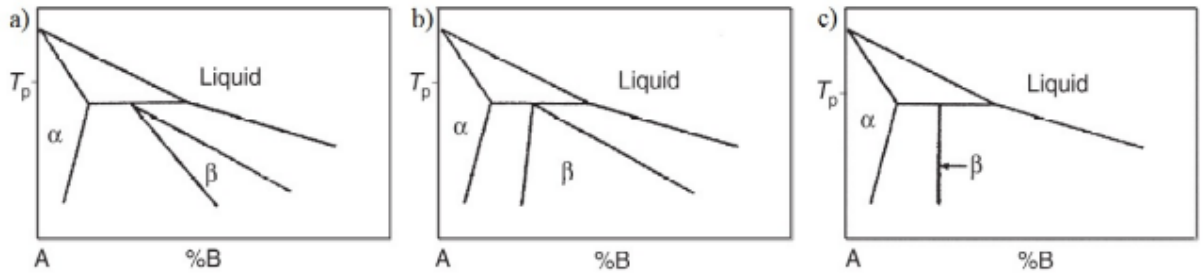

Figure 16: Types of peritectic solidification: a) slopes of the same sign, b) slopes of opposite signs, c) the β phase is an intermetallic compound (Invariant Transformation Structures, Metallography and Microstruc-tures, Vol 9, ASM Handbook, ASM International)

Despite being very common in metallic alloys, the mechanisms of this transformation are complex. In literature, four solidification steps have been highlighted (Hillert, 1979).

Solidification of the primary phase

The solidification first begins when the system reaches temperatures below the solidus and allows the formation of a α-properitectic phase. At every instant, the compositions of the liquid and α-phase could be read respectively on the liquidus and solidus curves; under equilibrium conditions, the volume fraction of each phase is also obtainable by the lever rule.

The peritectic reaction

The peritectic reaction takes place when the three phases (i.e. α, β and the liquid) are in contact with each other.

The β-phase tends to form along the α-grains, using them as heterogeneous germs. Generally, there is dissolution of the α-phase at the interface α/L which causes the formation of a slight low (Figure 17). The atoms of A in excess diffuse through the liquid to the new-formed β-phase. Meanwhile, the B atoms diffuse in the opposite sense. The phenomenon occurs from diffusion of short-range. Because the three phases are coexisting in one triple point, an equilibrium condition of superficial tension have to be respected.

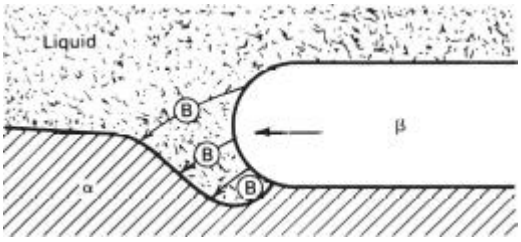

Figure 17: Mechanism of the peritectic reaction by lateral growth of a beta layer along the α - liquid interface (Hillert, 1979)

The peritectic reaction is considered over once the primary phase is completely overlaid by the peritectic product.

The peritectic transformation

Once the peritectic reaction complete, the α-grains are isolated from the liquid by a strip of β-phase. The peritectic transformation can begin by interdiffusion of both atoms of A and B through the newly-formed β-phase. The system behaves as two equilibria β/L and β/α, coupled by interdiffusion. Because the diffusion occurs through the β-phase, it is clear that the driving force is the concentration gradient. Figure 18 displays the diffusion direction of the species A and B.

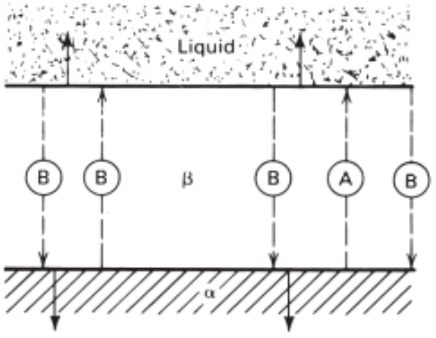

Figure 18: Mechanism of the peritectic transformation by thickening of the beta layer. Solid arrows: growth direction of beta; Dashed arrows: diffusion direction of the atomic species (Hillert, 1979)

The direct solidification of the β-phase

When the superheat of the L/β front become too high, the β-phase grows by its own way. The kinetics of the phenomenon follow laws similar to those of diluted alloy as if the α-phase does not exist. A description might be obtained by prolongation of the liquidus and solidus β-phase.

2.2.1.2) The Cu-Sn system

The phase diagram of binary bronzes Cu-Sn has been the subject of many investigations, reviewed by Hansen and Pell-Walpole (Hansen and Pell-Walpole, 1951).

The diagram generally presented (Figure 19) provides for the formation of a number of ordered and intermetallic phases through a series of peritectic reactions.

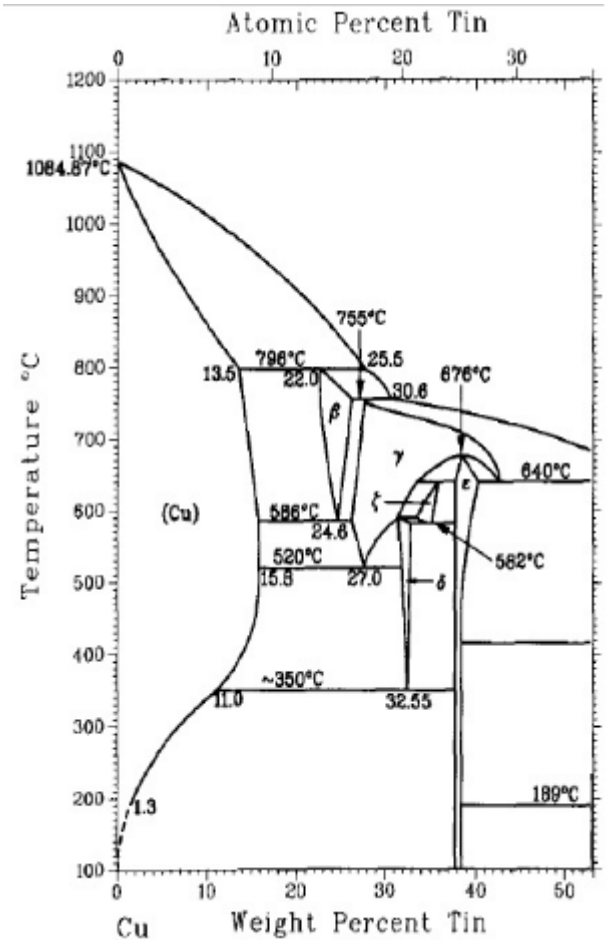

Figure 19: Phase diagram of the Cu-Sn system (Saunders and Miodownik, 1990)

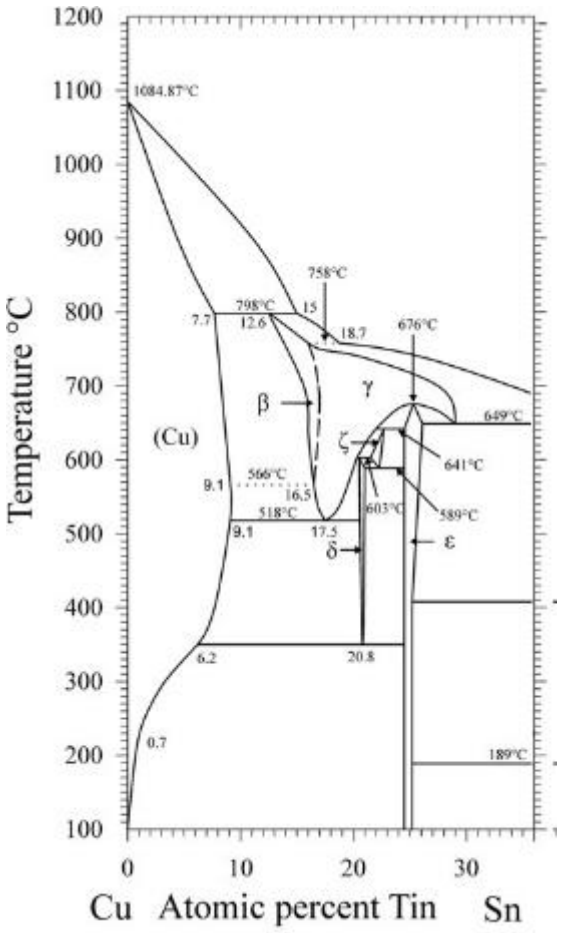

Figure 20: Revised phase diagram (Fürtauer et al., 2013)

More recently, Fürtauer et al have investigated 20 compositions of the copper-tin system, from 11 at.% to 48 at.% Sn, through a methodology based on thermal analysis, metallographic and crystallographic examinations.

They concluded that the presence of the biphasic (β + γ) domain could not be confirmed and they proposed that the transformation β → γ rather corresponds to a disordered-ordered transition visible in Figure 20 (Fürtauer et al, 2013).

For the compositions of interest, the phase diagram provides for:

- Alloys with a tin content lower than 13,5 wt.%: there is crystallization of a primary α-solid solution when the temperature falls into the fusion range (from around 1085-970°C for the liquidus to around1085-796°C for the solidus, according to the tin content). After a slight increase of tin solubility in the α-phase with the lowering of the temperature, the tin solubility strongly falls around 400°C and the ε-phase precipitates.

- Alloys with a tin content between 13,5 and 22 wt.%: the first crystals of primary α-solid solution form from the liquidus temperature (from around 970-870°C to 796°C according to the tin content). At 796°C, the formation of a β-peritectic phase occurs from the reaction of the liquid and the primary α-phase. Hence, from 796°C to 586°C, the material is biphasic and composed by the remaining α phase and the new-formed β-phase. At 586°C, the β-phase decomposes and forms an (α + γ) eutectoid component. Once again, at 520°C a new eutectoid reaction provides for the decomposition of the eutectoid γ into a (α + δ) eutectoid and at around 350°C, the last δ-eutectoic transforms into an (α + ε) eutectoid.

The crystallographic features of the different phases are presented in Table 3.

Phase	*Structure*	*Composition (at.% Sn)*	*Prototype*
α or (Cu)	fcc (cF4)	0 to 9.1	Cu
β	bcc (cI2)	13.1 to 16.5	W
γ	bcc (D03, cF16)	15.5 to 27.5	BiF3
δ	Cubic (cF416)	20 to 21	Cu41Sn11
ε	Orthorhombic (oC80)	24.5 to 25.9	Cu3Sn

Table 3: Crystallographic features of the stable phases (Hansen and Well-Walpole, 1951; Saunders and Miodownik, 1990)

2.2.1.3) The Cu-Zn system

In the same way that tin bronzes, the phase diagram of binary brasses is the results of numerous studies which particularly focused on the phase boundaries and the polymorphism of certain phases (Figure 21) (Miodownik, 1994; Turchi et al. 1991). The latest thermodynamic simulations have confirmed the assessed diagram (Liang et al., 2015). These alloys are characterized by the presence of a very narrow solidification interval as well as a wide copper-rich α-solid solution.

Furthermore, information is not available below 200°C since the extrapolations could not be reliable due to the sluggish kinetics and to a potential ordering in the α phase for those temperatures (Miodownik, 1994).

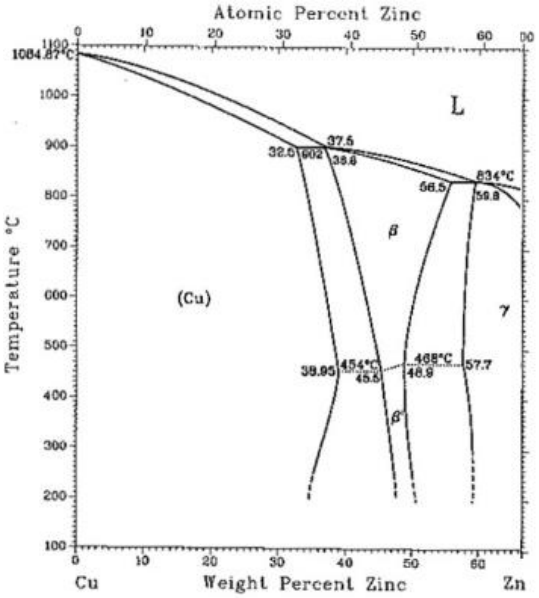

Figure 21: Copper-rich corner of the phase diagram of the binary Cu-Zn system (Miodownik, 1994)

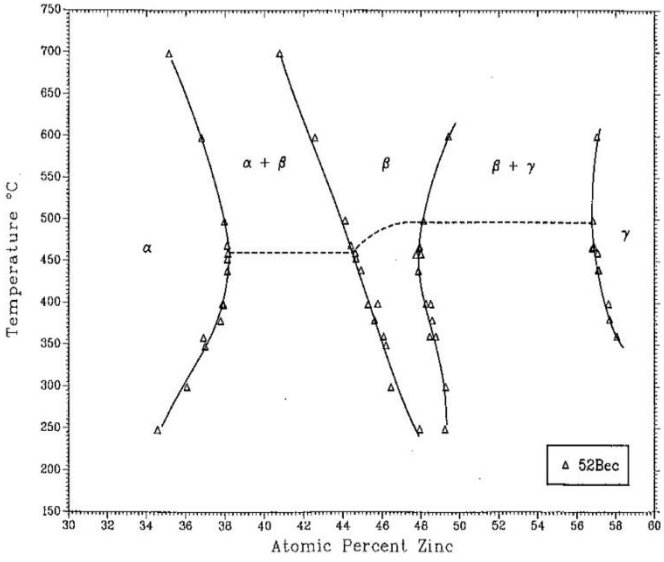

Figure 22: Phase diagram in the composition range between 30 and 60 at.% Zn (Miodownik, 1994)

For the compositions of interest, the phase diagram provides for:

- Alloys with a zinc content up to 32.5 wt.%: the primary α-solid solution forms at temperatures between 1084 °C and c. 930°C for the liquidus according to the zinc content. The last liquid solidifies at temperatures between 1084 °C and 902 °C. The final material is called *monophasic brass* and according to the zinc content, could be either *red brass* (from 5 to 20 wt.% Zn) or *yellow brass* (from 20 to 36 wt.% Zn).

- Alloys with a zinc content between 32.5 to 37.5 wt.%: the first crystals of primary α-solid solution form from the liquidus temperature (from around 970-870 °C to the peritectic temperature 902°C according to the tin content). At 902 °C, the peritectic solidification occurs with the formation of the β-peritectic component from the reaction of the liquid and the primary α-phase.

According to the general composition of the alloy, zinc present in the β-phase might diffuse toward the α primary phase whose solubility slightly increase around 454°C and the final material will be monophasic (Hansen and Pell-Walpole, 1951). Otherwise, an ordering reaction might occur for the β-phase to a β'-phase (Figure 22).

- Alloys with a zinc content over 37.5 wt.%: the primary phase to be formed is not the α-solid solution anymore but the peritectic β-phase around 900 °C. The solidification interval is extremely narrow and the liquid is entirely solidified in β. With the lowering of temperature, the zinc solubility into the primary phase also decreases and re-organized in the α-solid solution. This phenomenon is displayed Figure 23 (Troiani and Baruj, 2007). At 454 °C the disordered-ordered transition of the β phase takes place.

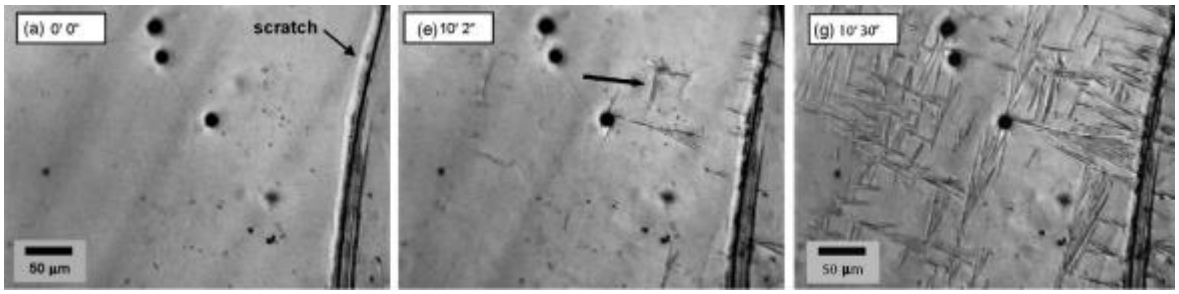

Figure 23: Microscopic observation of the dezinfication phenomenon through the crystallization of the α grains (Troiani and Baruj, 2007)

The crystallographic features of the different phases are presented in Table 4.

Phase	*Structure*	*Composition (at.% Sn)*	*Prototype*
α or (Cu)	fcc (cF4)	0 – 38.3	Cu
β	bcc (cI2)	36.1 – 59.1	W
γ	cP2	44.7 – 48.2	CsCl

Table 4: Crystallographic features of the stable phases (Miodownik, 1994)

2.2.1.4) The Cu-Sn-Zn system

The phase diagram of the ternary Cu-Sn-Zn system has been investigated since the early 20th century by Samuel L. Hoyt, who first mapped the full ternary diagram (Figure 24), as well as the liquidus projection.

Later he published with Tammann[1] the revised liquidus boundaries of those alloys (Figure 25).

Further investigations have studied this system from both experimental and thermodynamic approaches (Jantzen and Spencer, 1998; Vilarinho et al, 2004; Huang et al., 2009).

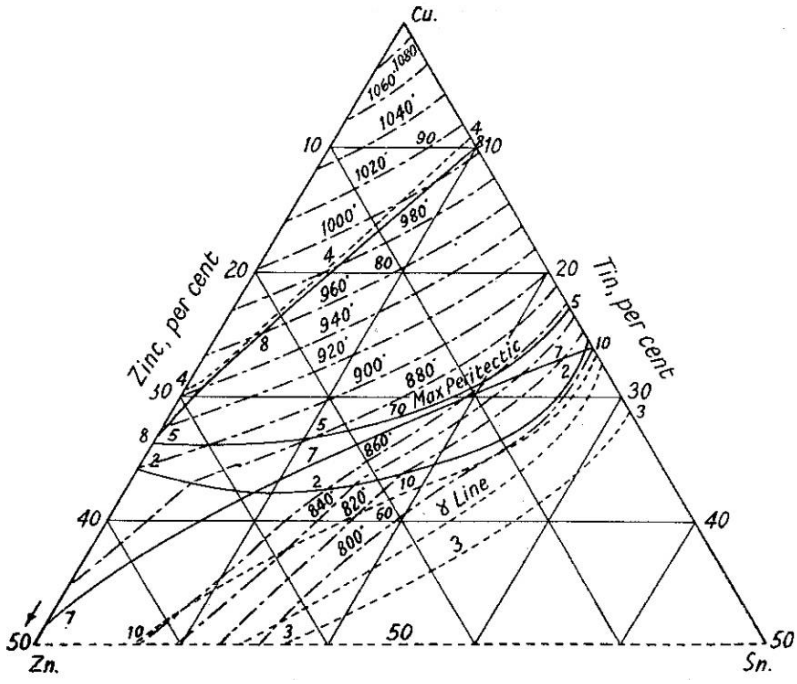

Figure 24: Phase diagram of the ternary Cu-Sn-Zn system according to Hoyt's work (Hansen and Pell-Walpole, 1951)

[1] G. Tammann and M.Hansen, "Uber das ternare System Kupfer-Zinn-Zink", Zeitschrift fuer norganische und allgemine Chemie, 138 (1924), pp. 137 – 161.

The liquidus surface projection (line 2 in Figure 24 and Figure 25) determines the formation of the primary α phase in both Cu-Sn and Cu-Zn systems.

This surface lightly decreases with the increase of tin or zinc contents from the pure copper melting temperature (1084°C) to the respective inflections of the peritectic reaction in the hyperperitectic region (798°C for bronzes with 25.5 wt.% Sn and 902°C for brasses with 37.5 wt.% Zn).

Thus, the liquidus extends across the diagram from the copper-zinc face to the copper-tin face (Hansen and Pell-Walpole, 1951).

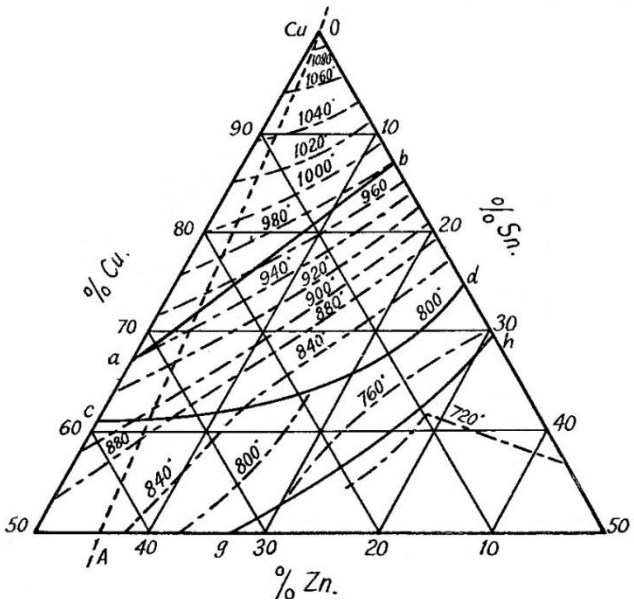

Figure 25: Liquidus projection, according to Tammann and Hansen works (Hansen and Pell-Walpole, 1951)

The peritectic points (line 5 in Figure 24) correspond to the origin of the β phase for every compositions.

Since the peritectic transformation occurs for higher temperatures in the copper-zinc system (902°C) than for the copper-tin system (798°C), Hoyt stated that the peritectic surface rapidly decreases from the brasses face and then goes almost horizontally to the bronze face but he did not provide for any detailed diagrams, or for the α-solidus surface.

This last one has been proposed later by Bauer and Hansen[2] and is visible in the line a-b, even if no further accurate estimation has been made yet (Hansen and Pell-Walpole, 1951).

The limits of solubility for the α phase from solidus to room temperature (range between the lines 4 and 8 in Figure 24) are:

- from 13.5 wt.% Sn at 798°C to less than 10 wt.% at room temperature for bronzes,
- from 31.9 at.% Zn at 902°C to less than 30wt.% Zn at room temperature for brasses.

However these projections might lack some accuracy due to the respective limits of each binary system for low temperatures. Nevertheless it has been proposed that the α solubility limit should decrease in the same manner as for binary tin bronzes (Hansen and Pell-Walpole, 1951).

[2] O.Bauer, M. Hansen, "Der Einfluss von dritten Metallen auf die Konstitution der Messinglegierungen. III. Der Einfluyss von Zinn:", Zeitschrift fuer Metallkundem 22, (1930), pp. 405 – 411.

The two β phases of both binary systems form a continuous series of solid solutions with each other, as the γ phase of the Cu-Zn system does with the δ of the Cu-Sn one.

Hence, the corresponding eutectoid reaction (β → α + γ) occurring at c. 580°C for tin bronzes is continuous with the ordering reaction (β → β') occurring at around 450°C for brasses. This surface transition is visible in Figure 26.

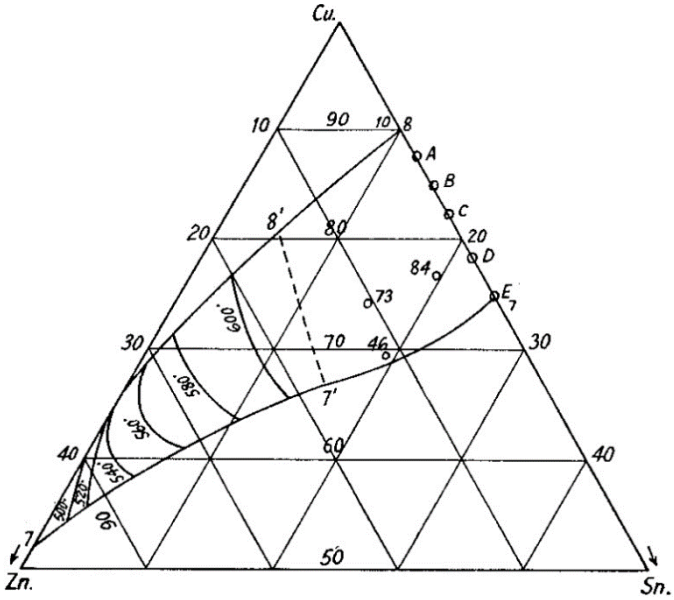

Figure 26: Eutectoid Surface from Hoyt and Brinton works (Hansen and Pell-Walpole, 1951)

For a zinc content below 15 wt.%, the transition corresponds to the eutectoid transformation; beyond this composition, the ordering reaction is predominant and the temperature of the transformation rapidly falls to the corresponding temperature in the binary Cu-Zn system. However, the exact mechanisms these transitions are connected to remain unclear (Hansen and Pell-Walpole, 1951).

For high tin contents, an eutectoid transformation occurs, providing for the formation of a hard phase called γ1 through the reaction β → α + γ1 (Vilarinho et al, 2004).

2.2.2) Monotectic alloys: leaded copper

2.2.2.1) The monotectic solidification

In some metallic systems, the liquid might separates in two immiscible liquids for certain ranges of compositions and temperatures.

These two fields are separated by a dome-shape domain within which the two liquids mix. The maximum temperature of this domain of miscibility is called *critical temperature* (Tc) and corresponds to *limit of liquid miscibility*.

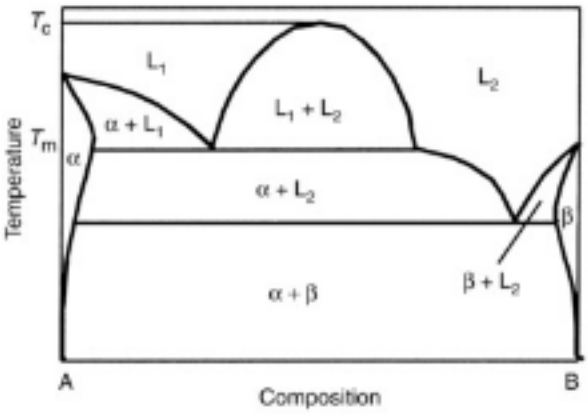

Figure 27: Schema of monotectic system

The monotectic solidification occurs when the liquid (L1) decomposes at the monotectic temperature Tm into a solid (α) and a new liquid phase (L2). The reaction can be represented as L1 → α + L2, as displayed in Figure 27.

Two types of monotectic alloys are identified:

- high-dome alloys, with a ratio Tm/Tc < 0.9 which means a difference of temperature between the critical and monotectic points of hundreds of degree Celsius;
- low-dome alloys, with a ratio Tm/Tc > 0.9, which corresponds to a difference of temperature between the critical and monotectic points of tens of degree Celsius.

2.2.2.2) The Cu – Pb system

The copper-lead system appears much simpler than the two other binary systems investigated. It presents a monotectic point at 955°C for a lead content of around 37.5 wt.% (low-dome alloy).

Since copper and lead respectively have very different melting points, the full diagram is mainly constituted by a biphasic domain which itself contains copper phase and a lead-rich liquid (Figure 28). Studies on this system have been reviewed by Chakrabarti and Laughlin (Chakrabarti and Laughlin, 1984).

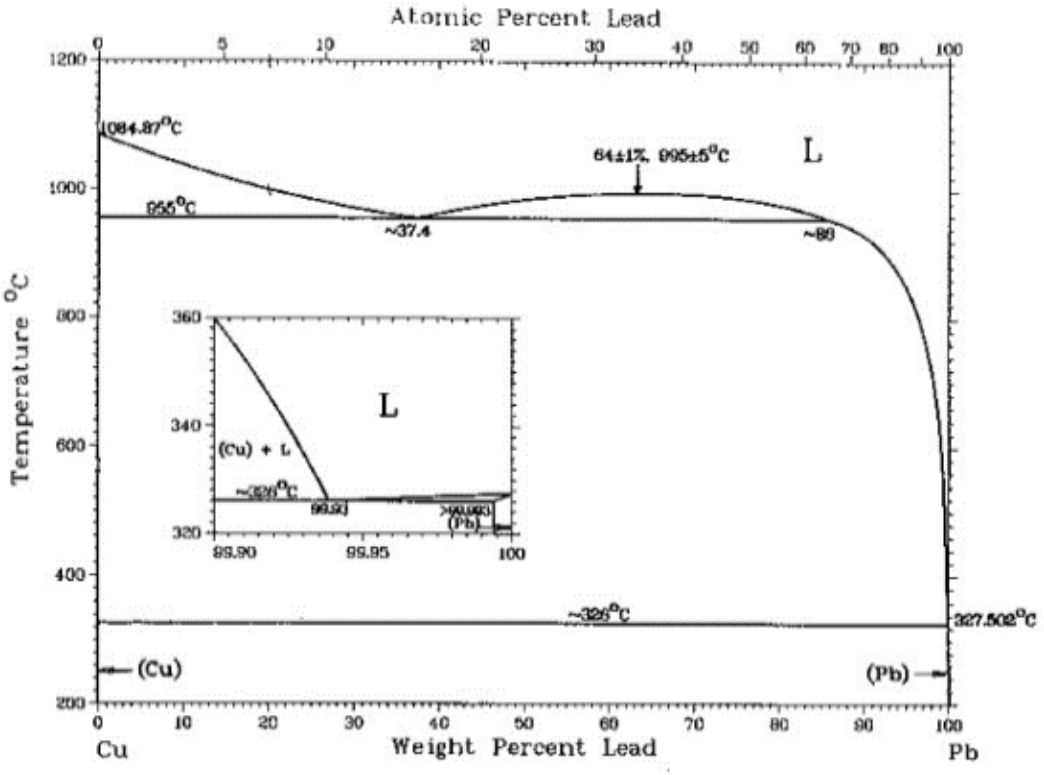

Figure 28: The Cu-Pb phase diagram (Chakrabarti and Laughlin, 1984)

For alloys containing lead up to 20 wt.%, the first copper crystals appear within the lead-rich liquid L1 once the temperature becomes lower than the liquidus (from 1084 °C to around 1000 °C, according to the lead content).

With the lowering of temperature, the proportion of copper crystals increases while the remaining liquid gets richer in lead. At 955 °C, the monotectic reaction occurs and the liquid L1 transform into copper and a new liquid L2. The latter is richer in lead than the former L1. The alloy cools down and the last liquid L2 solidifies at 327 °C. Lead has a solubility in copper-matrix almost null and the final material is composed by primary copper crystal and lead nodule in the interstitial spaces.

The crystallographic features of the different phases are presented in Table 5.

Phase	*Structure*	*Composition (wt.% Pb)*	*Prototype*
(Cu)	fcc (cF4)	0	Cu
(Pb)	fcc (cF4)	100	Cu

Table 5: Crystallographic features of the stable phases (Chakrabarti and Laughlin, 1984)

2.2.2.3) The Cu – Pb – Sn system

The phase diagram was assessed on the basis of published data relating to phase equilibria of the three binary systems Cu-Sn, Cu-Pb and Sn-Pb (Hansen and Pell-Walpole, 1951; Miettinen et al., 2010a; Chang et al., 1979a; Chattopadhyay and Srikanth, 1994).

The liquidus projection is displayed Figure 29.

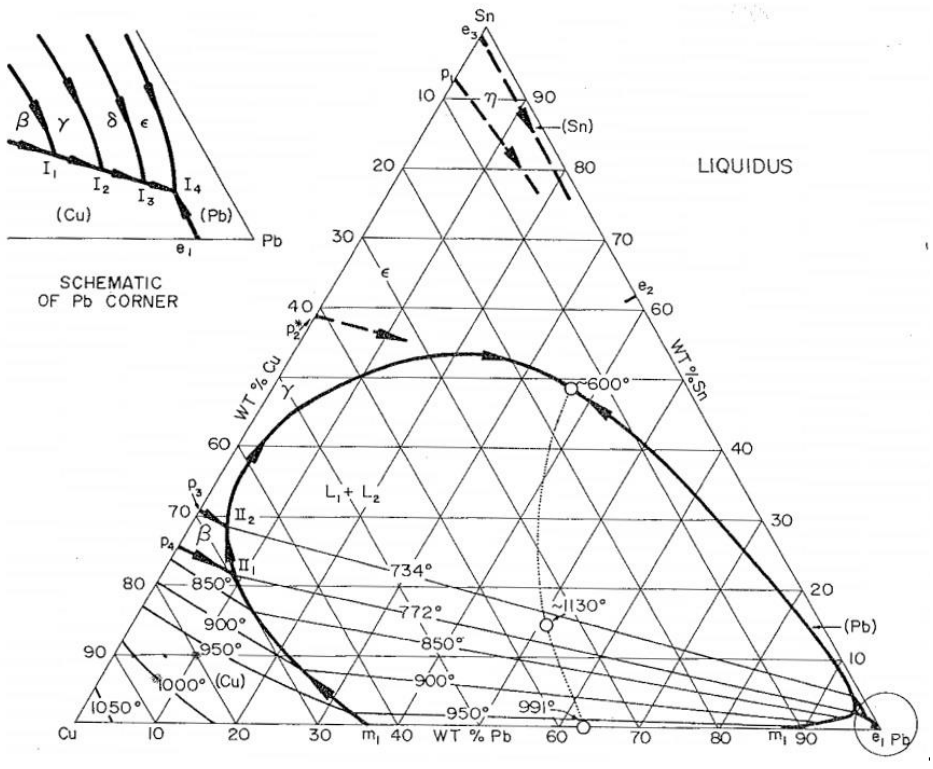

Figure 29: Liquidus projection for the ternary Cu-Pb-Sn system (Chang et al. 1979)

The most important feature of this system is the extension of the miscibility gap with respect to the binary Cu-Pb system. This limit is shown in Figure 29 by the dark line and in Figure 30 at various temperatures.

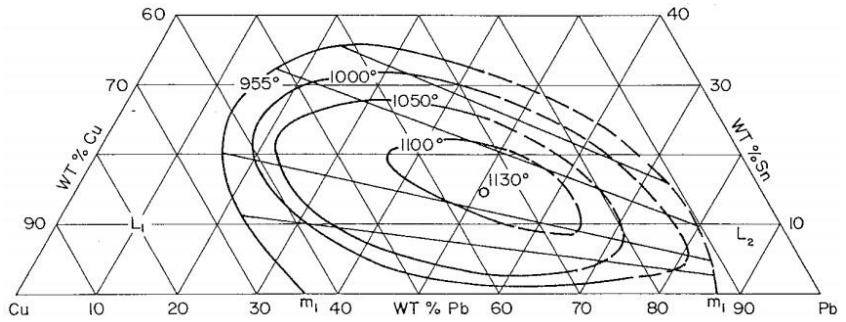

Figure 30: Extension of the miscibility gap at various temperatures (Chang et al. 1979)

In the copper-rich corner (from 36 wt.% of lead in the Cu-Pb system) it decreases almost linearly to the composition of 21 wt% lead and 10 wt% tin, and eventually reaches 2% lead and 40% tin.

Furthermore, the critical point occurs at higher temperatures (between 1130 and 1140 °C) and consists of a composition of 60 wt.% copper and 14 wt.% tin.

It has been reported that at the constant temperature of 772 °C a transition occurs, represented as: α + Liquid (copper) → β + Liquid (lead). This transformation derives from the surface intersection between the peritectic reaction in the Cu-Sn system and the separation transition in the Cu-Pb system (Hansen and Pell-Walpole, 1951).

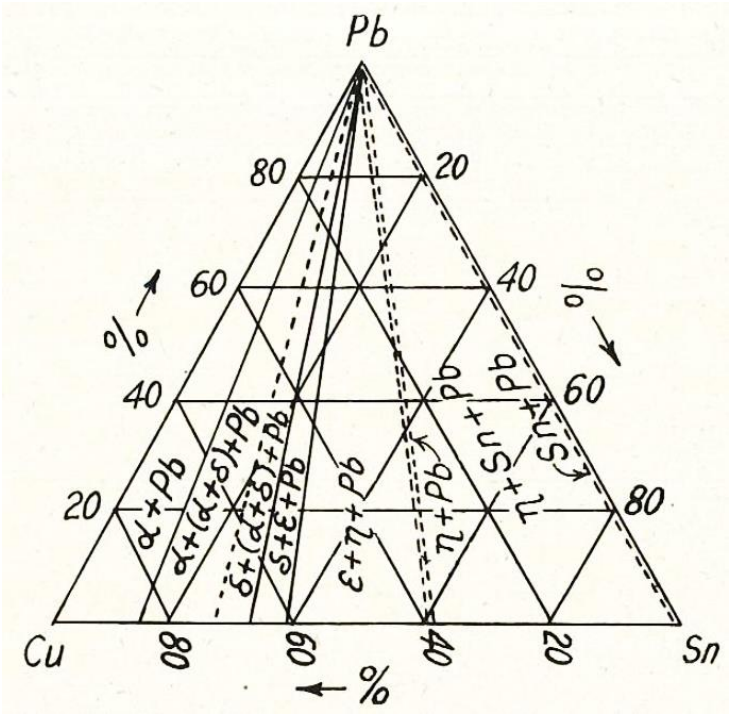

The constitution of such system at room temperature has also been plotted. As displays in Figure 31, each phase field consists of an addition of metallic lead to the corresponding phase combination of the copper-tin system. Indeed, no further ternary stable or metastable phase has been reported (Hansen and Pell-Walpole, 1951).

Figure 31: Phase diagram at room temperature (Hansen and Pell-Walpole, 1951)

2.2.2.4) The Cu – Pb – Zn system

Like the aforementioned ternary system, the Cu – Pb – Zn system displays a large miscibility gap in the liquid phase which extends from the binary systems Cu – Pb and Pb – Zn.

The liquidus surface and the miscibility gap in the system have been studied by different authors with both experimental and numerical methods (Figure 32) (Villars et al., 1997; Miettinen et al., 2010b; Jantzen and Spencer, 1998; Chang et al., 1979b). Once again, no ternary phases have been found.

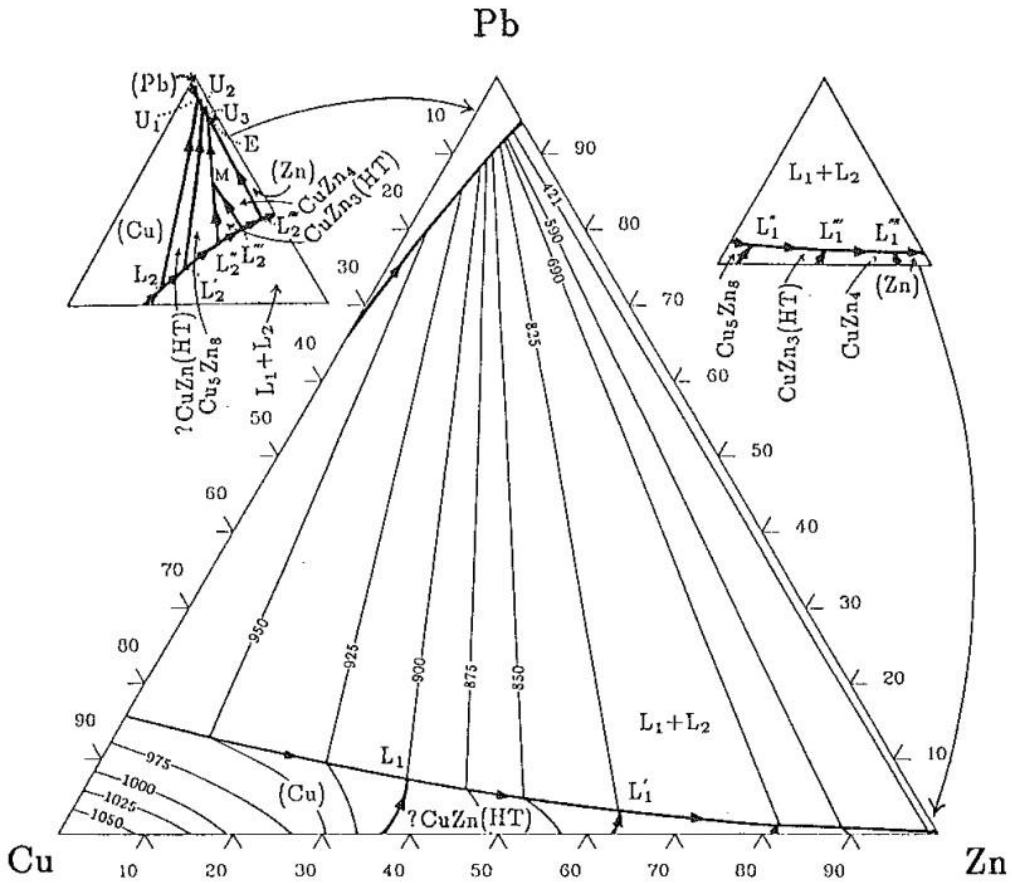

Figure 32: Liquid projection of the ternary Cu-Pb-Zn system (Chang et al., 1979)

2.2.2.5) The Cu – Pb – Sn – Zn system

To our knowledge, no studies have been conducted that describe this quaternary system phase diagram.

However, in the light of the aforementioned ternary systems, it can be reasonably assumed that no particular phase is formed from the interaction between the ternary Cu-Sn-Zn system with lead, due to its insolubility in copper-matrices.

2.3) Out-of-equilibrium curves of copper-based alloys

Any process of solidification can occur at ideal equilibrium conditions and different degrees of departure from equilibrium have been stabilized as a function of the cooling rate increase. In this work, the nomenclature explicated by Flemings has been used (Table 6).

Range of cooling rate		Production process	Dendrite arm spacing (μm)
$K.s^{-1}$	Designation		
10^{-4} to 10^{-2}	Slow	Large castings and ingots	5000 to 200
10^{-2} to 1	Medium	Small sand castings and ingots Billet and bar continuous castings	200 to 50
1 to 10^{3}	Near-rapid	Strip casting; Die casting; coarse powder atomization; "Premium Quality" casting	50 to 5
10^{3} to 10^{9}	Rapid	Melt spinning; fine powder atomization; thin strip casting; electron beam or laser surface melting	5 to 0.05

Table 6: Range of cooling rates in solidification process (Flemings, 1991)

2.3.1) Cooling curves

While the isothermal non-equilibrium curves (TTT) and continuous cooling curves (CCC) have been widely developed for ferrous materials, non-ferrous alloys has been less studied.

VanderVoort has published at the beginning of the 1990s an atlas wich lists the works carried out in the determination of time-temperature diagrams for non-ferrous materials (VanderVoort, 1991). The majority of investigations are focused on light alloys like aluminium and magnesium

The determination of the cooling rate in real casting experiment is a delicate issue and several methodologies can be applied. In cooling curve thermal analysis technique, the value of the cooling rate can be assessed by calculating the slope of cooling curve above the liquidus temperature. However Hosseini et al. have shown that for high cooling rates processes, this technique is limitated in recording temperature variation of the sample, and thus in the cooling rate determination (Hosseini et al., 2013).

2.3.2) Impact on microstructure and properties

The correlations existing between cooling conditions and microstructure on one hand and between cooling conditions and mechanical properties on an other hand, are extensively investigated for different alloying systems. It is agreed that both thermal conditions and alloy content affect the structure of cast alloys.

The effect of cooling rate and different crystal growth velocities on alloys microstructure is often estimated through the primary dendritic arm spacing (PDAS - $\lambda 1$) and secondary dendritic arm spacing (SDAS - $\lambda 2$). According to empirical analysis, it is generally

known that increasing the cooling rate reduces both the primary and secondary dendrite arm spacing.

Flemings has presented an equation (Eq. 1) able to rely the SDAS with the cooling rate value as a function of the alloy system since the constants *a* and *b* are characteristic of the material (Flemings, 1991).

$$SDAS = a\ CR^{-b} \qquad \text{(Eq. 1)}$$

For ferrous materials, studies have been done to develop simple expressions able to predict dendritic arm spacing as a function of carbon content and thermal conditions of low alloys steel in the range of cooling rate occurring in steel casting processes (Cicutti and Boeri, 2001) . As instance, El-Bealy and Thomas have highlighted the role of different solidification modes, in particular the peritectic solidification, in the variations of PDAS. This one first steeply decreases with carbon content in the hypoperitectic areas, then increases in the hyperperitectic region for near-peritectic compositions. For higher carbon content, the PDAS gradually decreases. The SDAS however regularly decreases with carbon content (El-Bealy and Thomas, 1996).

For non-ferrous alloys, research has been particularly focused on aluminium alloys, as shown by the wide literature (Hosseini et al, 2013; Dolić et al., 2012; Zhang et al, 2008).

Copper-based alloys however have been studied in a more limited measure:

Martorano and Capocchi have pointed out that only few empirical equations have been developed for tin bronzes, without any experimental confirmation. Therefore, they have investigated through the application of an experiment design the unidirectional solidification of a binary tin bronze (CuSn 8wt.%) in a cylindrical insulating mould (mullite based material) and for different cooling conditions. They reported measurements of dendrite arm spacing, related to the local solidification time and to the cooling rate (Martorano and Capocchi, 2000a). They proposed two equations correlating dendrite arm spacing (µm) and cooling rates (°C/min), verified by other experimental results.

$$PDAS = 1230\ R^{-0.45} \qquad \text{(Eq. 2)}$$

$$SDAS = 184\ R^{-0.36} \qquad \text{(Eq. 3)}$$

In another paper, they analysed the microsegregation induced by directionally solidification of the same alloy (Martorano and Capocchi, 2000b). They observed a decrease of microsegregation along the longitudinal axis and that columnar zone have a lower degree of microsegregation than in the equiaxed area. They gathered several microstructural parameters.

Taşliçukur et al. have investigated a binary bronze alloy (CuSn 10) cast in different moulds (sand and investment mould) with microstructural comparison and measurement of macrohardness of the cast specimen. They found that both samples are composed by a dendritic structure of primary solid-solution and (α+δ) eutectoid constituents, and that the matrix produced by sand casting was finer than the other. No quantitative estimation of the volume percentage of secondary phase formed has been done but they note that a lower quantity of secondary phase in the sand-cast specimen (Taşliçukur et al., 2012).

Ventura et al have focused on the impact of different growth rates (from 2 to 100 $\mu m.s^{-1}$) on the microstructure of lead-free Sn-Cu solders alloys in the near-eutectic composition ranges. They showed that different morphology of eutectic can be obtained by varying the growing rate, which also deeply influence the interdendritical space (Ventura et al., 2011).

However, these observations have to be incorporated into wider heat flow models in order to quantitatively predict macroscopic and microscopic behaviours during casting processes, especially defects formation such as inclusions and cracks, which are strongly associated with the microstructure evolution. Different analytical expressions have been to correlate the PDAS and SDAS with growth rate, temperature gradient, cooling rate, and local solidification time.

Miettinen has adapted the IDS-model (InterDendritic Solidification) initially developed for the simulation of steel solidification, to the solidiifcation of some binary copper-based alloys (Miettienen, 2001). The CASBOA model (Copper Alloy Solidification for Binary One-solid phase Alloys) can simulated the fcc solidification of CuAg, CuAl, CuNi, CuP, CuSn and CuZn systems. On one hand, this model allows the determination of the fractions and compositions of both liquid and solid phase at any temperature during solidification. On a second hand, thermophysical properties (i.e. enthalpy, specific heat, thermal conductivity, density and viscosity) can be determined.

Furthermore, micro and macrostructure has a major effect on main mechanical properties. The fineness of the dendritic structure affects microsegregation and inclusion formation, which leads to a deterioration in mechanical properties.

The impact of alloying elements (Al, Si, Mn, Zn, Ni and As) on the properties of copper and tin bronzes (CuSn 6wt.%) have been investigated by Ri and al. (Ri and al., 2014).

They found that hardness is slightly increased by zinc content through the mechanism of solid solution hardening and that the effect is major in tin bronzes than low-alloyed copper.

CHAPTER 3.

METHODOLOGY, MATERIALS AND TECHNIQUES

3.1) Objective and general methodology

This doctoral work proposes **to investigate the influence of cooling rate on the solidification of some copper-based alloys of industrial and archaeological interest**.

The global methodology is separated in two parts: an experimental and an archaeometric part:

- The experimental part aims to understand the correlations between the parameters of the process and the structural features of the as-cast material (i.e. micro and macrostructure, defects), and to connect them to some mechanical properties (e.g. hardness).

  For this purpose, two ranges of cooling rate are investigated:

  – *the near-equilibrium domain* (medium cooling rates from 5.10^{-2} to 50.10^{-2} $K.s^{-1}$)[3], in which the first steps of solidification of the two main binary systems (Cu-Sn and Cu-Zn) are monitored by thermal analysis. The tin content has been chosen between 3 and 20 wt.%, while the zinc content is between 5 and 40 wt.%, in order to investigate the transition between the monophasic phase (α) and biphasic domain (α+β) for both systems.

  – *near-rapid cooling rate range* (from 1 to 10^3 $K.s^{-1}$), in which the impact of cooling rate produced in real casting conditions on binary, ternary and quaternary copper-based alloys is investigated. Experimental design (D-Optimal Design) which provides the construction of models able to describe any material feature as a function of definite variables with a reduced number of experiment, is performed in order to compare the multivariate approach with traditional statistical analysis in the field of casting metallurgy.

    Tests are also performed in order to estimate the cooling rate applied to the melt by the different moulds, by mounting K-type thermocouples in different positions inside the mould and by comparing their thermal evolution with Numerical Simulation. First results are visible in Appendix 9.

  For every system, a metallographic study, and hardness measurements are performed on the samples in order to compare the theoretical lever rules with the composition of the samples induced by the non-equilibrium cooling rate.

[3] from 3 $K.min^{-1}$ to 30$K.min^{-1}$

The methodology for the experimental part is detailed in Table 7.

Cooling rate scale	*Analytical Technique*	*Investigated systems*	*Measured response*
Medium (10^{-2} – 1 $K.s^{-1}$)	Differential Thermal Analysis (DTA)	Cu – Sn; Cu – Zn	Cooling curves Metallography
Near - rapid ($1 – 10^{3}$ $K.s^{-1}$)	D – Optimal Design (D-Opt) Thermal monitoring Numerical Simulation	Cu – Sn; Cu – Zn Cu – Sn – Pb; Cu – Zn – Pb; Cu – Sn – Zn; Cu – Sn – Zn – Pb	Cooling curves Metallography Hardness

Table 7: Experimental methodology

- The archaeometric part focuses on the study of a Bronze Age assemblage of as-cast axe-ingots, more accurately described in Section 3.2.3.

A complete metallographic investigation is carried out in order to determine the composition of the alloys, the present phases and their relative proportions. Measurements are also performed with the aim to describe the samples microsegregation.

On the basis of the results obtained in the previous experimental part, correlations between structural features and casting process are done in order to propose some elements for the reconstruction of the *chaine opératoire*.

3.2) Materials

3.2.1) Experimental alloys

In the way to gather reproducible data for both metallurgical industry and archaeometric fields, specific copper-based alloys have been selected.

Chemical names relative to the alloying systems are used, instead of industrial specifications, which sometimes might be confusing (Table 8 with relative figure).

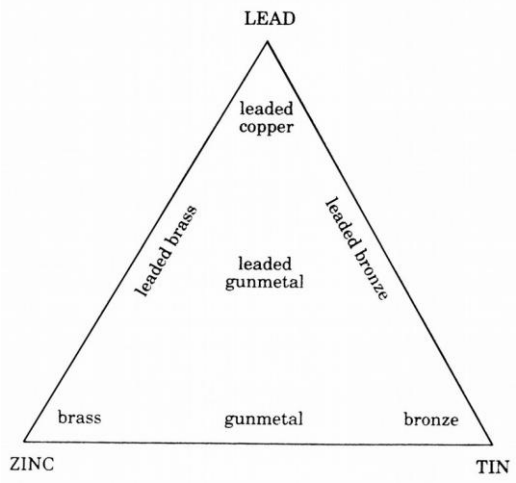

Denomination	*Chemical System*
Tin bronze	Cu – Sn
Brass	Cu – Zn
Leaded copper	Cu – Pb
Gunmetal	Cu – Sn – Zn
Leaded tin bronze	Cu – Sn – Pb
Leaded brass	Cu – Zn – Pb
Leaded gunmetal	Cu – Sn – Zn – Pb

Table 8: Selected copper-based alloys

Samples of thermal analysis (medium cooling rates)

For the thermal analysis, the two main binary systems Cu-Sn and Cu-Zn are studied.

Compositions allowing the investigation of both monophasic (α) and biphasic (α+β) fields have been selected (Table 9). The composition CuSn10 is performed twice (I and II) in order to observe the influence of two different cooling rates.

Binary tin bronzes		*Binary brasses*	
CuSn3	3 wt.% Sn	**CuZn5**	5 wt.% Zn
CuSn5	5 wt.% Sn	**CuZn10**	10 wt.% Zn
CuSn8	8 wt.% Sn	**CuZn20**	20 wt.% Zn
CuSn10	10 wt.% Sn	**CuZn30**	30 wt.% Zn
CuSn12	12 wt.% Sn	**CuZn40**	40 wt.% Zn
CuSn14	14 wt.% Sn		
CuSn20	20 wt.% Sn		

Table 9: DTA - samples

Samples of casting experiments (near-rapid cooling rates)

Five metallic systems are examined (Cu-Sn, Cu-Zn, Cu-Sn-Zn, Cu-Pb-Sn, Cu-Pb-Zn and Cu-Pb-Sn-Zn). Each of them could be represented by a quaternary system where the amounts of tin, zinc and lead are varying in the defined interval of composition.

The composition boundaries have been chosen so that a design of experiment, detailed in Section 3.3.1, can be computed. The reduced experimental domain can be represented like a simplex, i.e. a mixture design in which the design points are arranged in a uniform way as described by Becker (Becker, 1978). Figure 33 displays the minimization of the experimental design in the range 0 – 20 wt.% for each alloying element in the copper-rich corner of the quaternary system.

In this regular tetrahedron, vertex, edges, faces and internal points respectively correspond to pure components (linear model), binary (quadratic model), ternary (special cubic model) and quaternary mixtures.

To summarize, four vertex points (A, B, C, D), six edge midpoints (E, F, J, H, I, J), four face-centre points (L, M, N) and one centroid points (O), which represent fifteen compositional points, are composing the mixture design (Table 10).

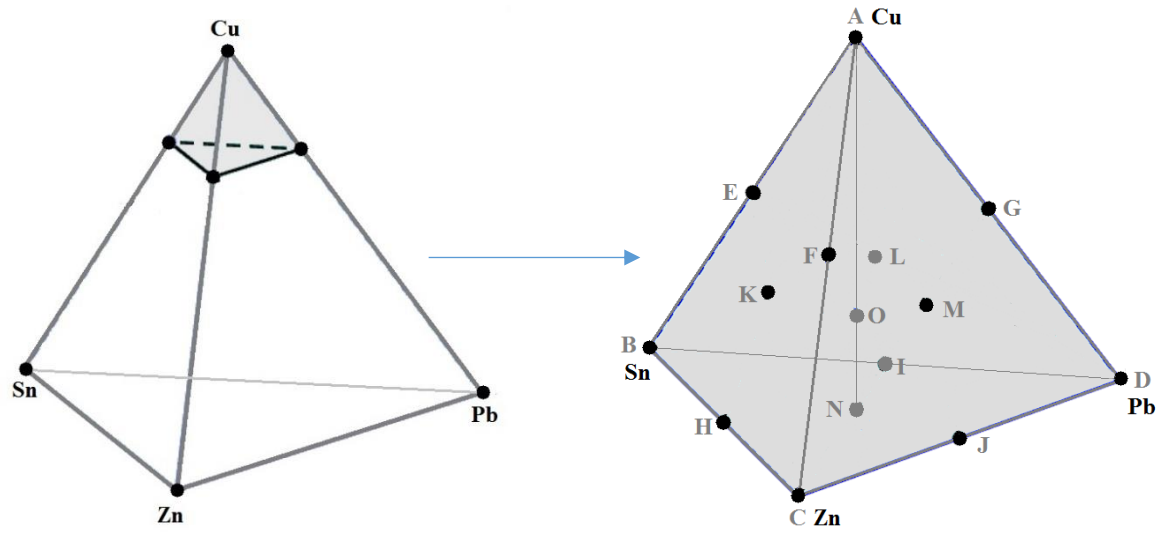

Figure 33: Experimental domain: a) full quaternary CuSnZnPb system with the composition ranges for each alloying element, b) final experimental domain as a reduced simplex

Material		*Simplex*	*Pseudo-Compositions*				*Compositions (wt.%)*			
Alloy	Comp.	*Position*	PC Cu	PC Sn	PC Zn	PC Pb	Cu	Sn	Zn	Pb
Cu	A	Vertice	1	0	0	0	100	0	0	0
CuSn	B	Vertice	0	1	0	0	80	20	0	0
CuZn	C	Vertice	0	0	1	0	80	0	20	0
CuPb	D	Vertice	0	0	0	1	80	0	0	20
CuSn	E	Half-edge	0.5	0.5	0	0	90	10	0	0
CuZn	F	Half-edge	0.5	0	0.5	0	90	0	10	0
CuPb	G	Half-edge	0.5	0	0	0.5	90	0	0	10
CuSnZn	H	Half-edge	0	0.5	0.5	0	80	10	10	0
CuSnPb	I	Half-edge	0	0.5	0	0.5	80	10	0	10
CuZnPb	J	Half-edge	0	0	0.5	0.5	80	0	10	10
CuSnZn	K	Face centre	0.33	0.33	0.33	0	86.67	6.67	6.67	0
CuSnPb	L	Face centre	0.33	0.33	0	0.33	86.67	6.67	0	6.67
CuZnPb	M	Face centre	0.33	0	0.33	0.33	86.67	0	6.67	6.67
CuSnZnPb	N	Face centre	0	0.33	0.33	0.33	80	6.67	6.67	6.67
CuSnZnPb	O	Central	0.25	0.25	0.25	0.25	85	5	5	5

Table 10: Selected alloys in the quaternary Cu-Pb-Sn-Zn system

3.2.2) Choice of moulds

Within the scope to apply different ranges of cooling rates, three materials with specific thermal properties have been tested:

- an industrial C40 steel (C 0.4%) which also contains manganese (0.72 wt.%), silicon and copper (0.15 wt.%), chromium (0.12 wt.%), vanadium and nickel (0.09 wt.%), and molybdenum (0.02 wt.%) (Figure 34a);

- a fired commercial clay (*C*), mainly composed by a oxidized ferric clayey matrix which is optically partially active (Figure 34b). The structural analysis confirm the presence of mullite ($3Al_2O_3$,$2SiO_2$). The angular inclusions are composed by quartz (SiO_2) of small dimensions (mainly inferior to 0.1 mm, maximum 0.3 mm), subordinate fragments of iron oxide (inferior to 0.8 mm) and occasional quarzite fragments (inferior to 1.0 mm). No mica has been detected.

- an industrial foundry sand (*S*), which is composed by synthetic quartz grains bounded with an organic agent. The metallographic observation of a polished cross-section of the material highlights a fine microstructure, composed by small ferritic (white) and perlitic (black) grains (Figure 34c).

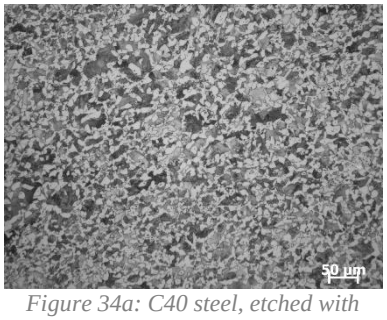

Figure 34a: C40 steel, etched with Nital 2% (LOM-BF, 200X)

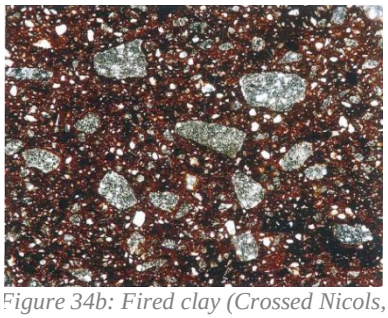
Figure 34b: Fired clay (Crossed Nicols, real dimensions 3.2x2.4mm, DISTAV)


Figure 34c: Sand (Stereo microscope, 180X)

The structural composition and the thermal properties of the three materials have been investigated at the DISTAV[4] (University of Genoa, Italy). The detail of these analysis is visible Appendix 1. Table 11 displays the main characteristics and thermal features.

	Mould characteristics		Thermal features of the material				
	Characteristic	**Preparation / Use**	**Material**	**Thermal behaviour**	**Density (g.cm-3)**	**Thermal conductivity ($W.m^{-1}.K^{-1}$)**	**Heat capacity ($J.m^{-3}.K^{-1}).10^6$**
Steel mould	Permanent Two-parts	As manufactured	C40	Conductive	7.845[(4)]	51.9 – 29.8[(5)] (0 – 1000°C)	3.8 – 6.0[(4)] (0 – 800°C)
Clay mould	Expandable Single-part	Moulding and Firing	Quartz, Mullite	Refractory	1.93 ± 0.05 (25°C)	1.25 ± 0.05 (25°C)	missing data
Sand mould	Expandable Single-part	As moulded	Synthetic quartz	Refractory	1.27 ± 0.10 (25°C)	0.41 ± 0.02 (25°C)	1.53 ± 0.08 (25°C)

Table 11: Description and thermal features of the three mould materials

[4] Dipartimento di Scienze della Terra, dell'Ambiente e della Vita
[5] From Brandes and Brook, 1992

The three moulds have been manufactured from these materials according to the same design (Figure 35) in order to produce cylindrical ingot of similar geometry (height 6.7 cm, diameter 2.0 cm) (Figure 36).

The metallic mould has been manufactured ad-hoc by lathing of a raw bar. The clay moulds have been modelled and fired at 900°C for 120 min (heating and cooling rates: 1°C/min) in order to eliminate the residual humidity which might be a serious issue during casting. In the same way, sand moulds have been manufactured by compacting the industrial sand into a frame in coir (Figures 37a, 37b and 37c).

A particular attention has been paid in the achievement of the thermocouple cavities, respectively positioned in contact with the melt (TC1), at 0.5 cm (TC2) and 1.0 cm (TC3).

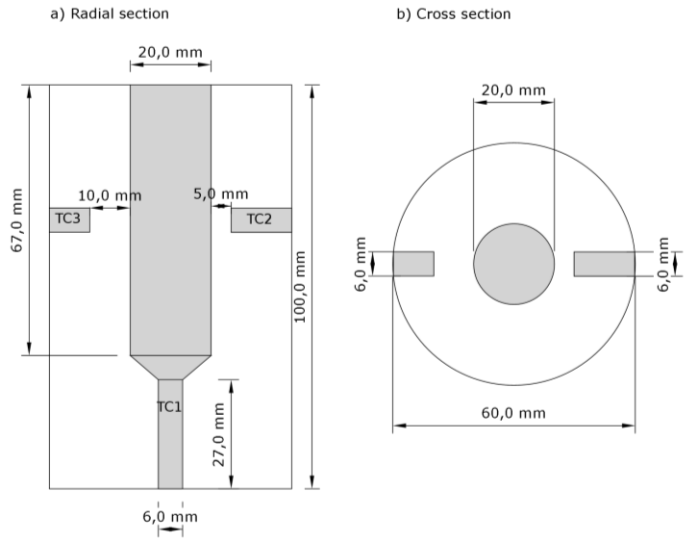

Figure 35: Dimensions of the moulds and thermocouple location: a) Radial section, b) Cross section (design by F. Castelli)

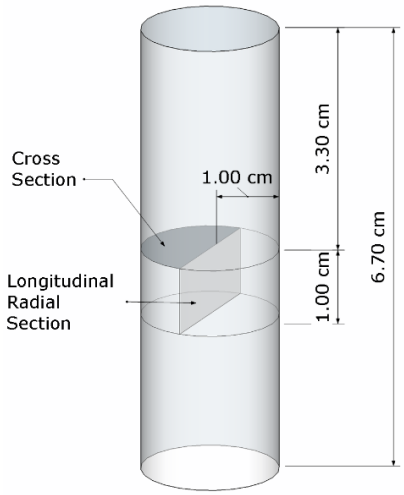

Figure 36: Dimensions of the ingot and sampling section

Figure 37a: Metallic mould

Figure 37b: Clay mould before firing treatment

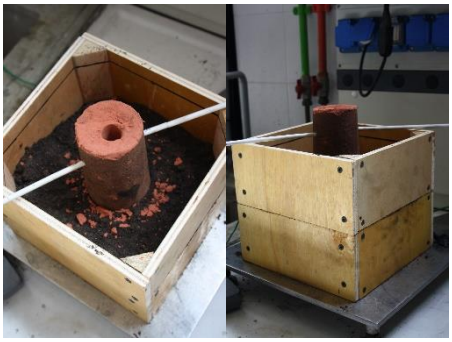

Figure 37c: Sand mould

3.2.3) Archaeological corpus

Archaeological context

The investigated archaeological artefacts come from a Bronze Age hoard discovered in 2003 in eastern France (Loyettes, Ain) (Figure 38).

The complete assemblage is composed by 69 axe-ingots from which 16 typological groups were identified (Delrieu et al., 2015). The classification in groups has been performed based on their shape and on the identification of recurrent superficial casting defects. All artefacts were supposed to be in an as-cast state, since their surface do not present any sign of finishing treatment.

This study is carried out in the framework of two multi-disciplinary projects directed by F. Delrieu and M. Gabillot respectively[6].

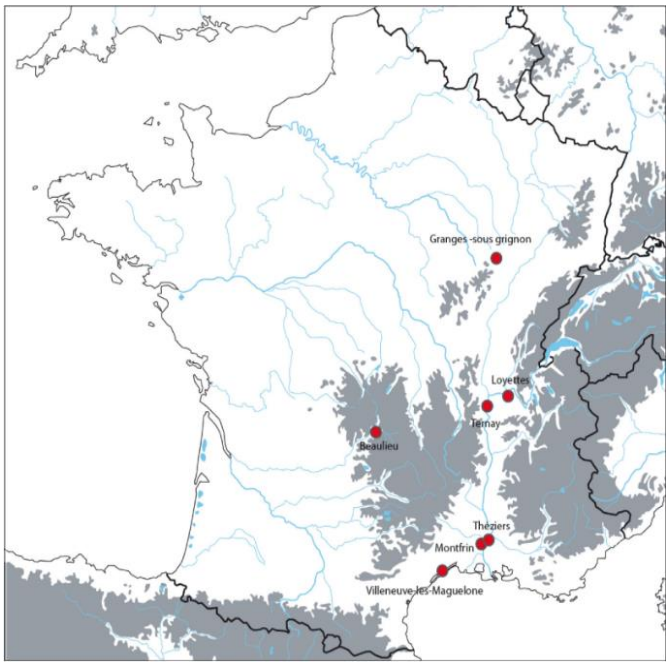

Figure 38: Localization of hoards from Bronze Age in France (Delrieu et al., 2015)

Selection of the corpus

Among the assemblage, 20 objects have been selected. Groups hearing high numbers of objects have been preferentially chosen in order to identify pattern of casting or groups of composition.

In this selected corpus, 8 axe-ingots belongs to group L8 (Figure 39a), 6 to group L10 (Figure 39b) and 3 to group M2 (Figure 39c). Other 2 specimens without classification have also been investigated. Table 12 details the samples features and the complete list of sample is visible in Appendix 2.

[6] **PCR Etude typologique, technologique et contextuelle du dépôt de l'âge du Bronze de Loyettes (Ain)**, 2013 – 2015, dir. F. Delrieu (SRA Rhône-Alpes, UMR5138); **PCR Territoires métallurgiques entre la Manche et les Alpes au milieu du deuxième millénaire avant notre ère,** 2016 – 2019, dir. M. Gabillot (CR CNRS, UMR 6298).

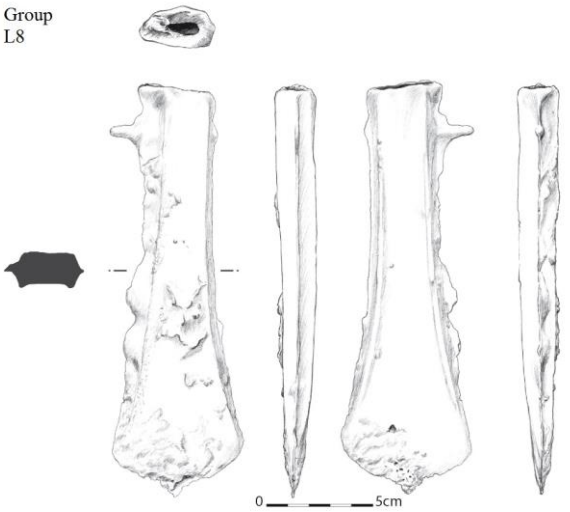

Figure 39a: Typological features of Group L8 (from Delrieu et al., 2015)

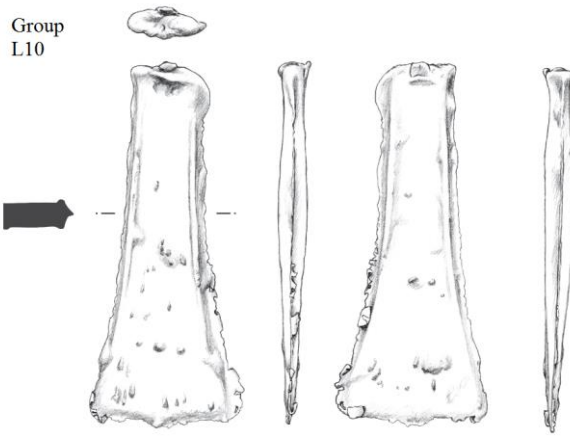

Figure 39b: Typological features of Group L10 (from Delrieu et al., 2015)

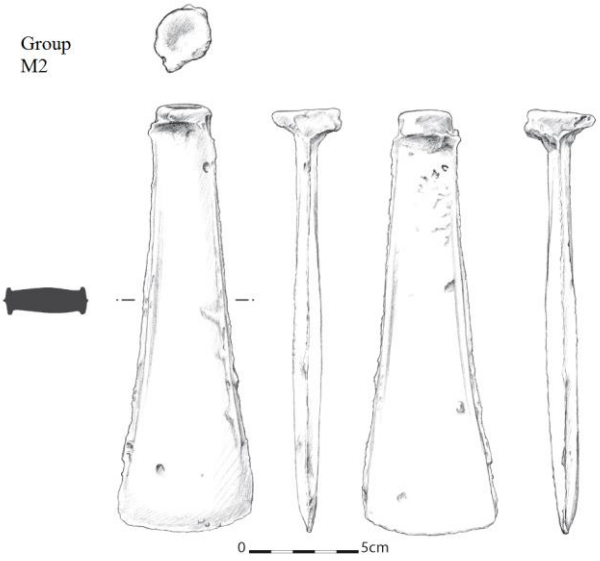

Figure 39c: Typological features of Group M2 (Delrieu et al., 2015)

Group	Object	Weight (kg)
L8	Loy 03	0.694
L8	Loy 04	0.675
L8	Loy 13	0.654
L8	Loy 14	0.674
L8	Loy 30	0.688
L8	Loy 36	0.690
L8	Loy 44	0.704
L8	Loy 47	0.676
L10	Loy 12	0.332
L10	Loy 16	0.354
L10	Loy 20	0.327
L10	Loy 42	0.332
L10	Loy 46	0.338
L10	Loy 57	0.323
M2	Loy 07	0.582
M2	Loy 59	0.559
M2	Ternay 561	Missing data

Table 12: Objects features

3.3) Techniques

3.3.1) Ingot casting and monitoring of the cooling

Experimental alloys have been prepared by pure metal melting into a graphite crucible and using an electric furnace for jewellery manufacture. The graphite acts as a reducing agent, which prevents oxidation and circumvents for the use of specific inert atmosphere for the casting. The use of pure metals allows the minimisation of the effect of trace elements.

Once the melt reaches the pouring temperature, it is cast into the corresponding mould and let solidified without any quenching stage.

The cooling of some samples has been monitored by three K-thermocouples (Chromel/Alumel) inserted in different positions in the moulds and connected to an elaboration system (CHROMA) (Figure 40), in order to perform a comparative investigation by numerical simulation through the ProCast software at the DIMI-UNIBS (Appendix 9).

Figure 40: Monitoring system

3.3.2) Control of the alloys composition

The mean chemical composition of each experimental alloy, as well as compositional changes along the dendrites, have been controlled.

The composition of each as-cast ingot has been systematically estimated by portative X-Ray Fluorescence (p-XRF) (Innov-X System, Delta Standard 2000 model, Olympus). A minimum of 3 measures has been carried on.

The percentage error between theoretical and experimental values was calculated with Equation 4:

$$\%Error = \frac{Experimental\ value - Theoretical\ value}{Theoretical\ value} . 100 \qquad \text{(Eq. 4)}$$

3.3.3) Thermal Analysis

The Differential Thermal Analysis (DTA) is a calorimetric technique, which measures the differences in energies released or absorbed of a material compared to an inert reference, and the changes in heat capacity as a function of temperature. The functioning of the instrument is well described in reference books (Brown and Gallagher, 1998).

Thermal analysis are widely used for the investigation of phase transitions in metallic systems, since they allow for the visualization of both I and II order phase transitions. Phase transitions of I order are melting and freezing, as well as allotropic transformations, while II order phase transitions are rather the disordered-ordered transitions and Curie transformations. The latter is visible as a deviation from the baseline due to specific heat variations of the system (Baricco, 2005).

3.3.3.i. Sample preparation

Samples with a weight between 0.5 g and 1.0 g were insert in tantalum crucibles suitable for the DTA. Crucibles were sealed under argon atmosphere in order to avoid any oxidation during the measurement.

3.3.3.ii. Experimental protocol

The analysis consists of recording the cooling curves at different rates from 1100 °C to 600 °C for the binary bronzes and from 1200 °C to 300 °C for the binary brasses. Each sample was submitted to several thermal cycles comprising a heating phase, fixed at 20 $K.min^{-1}$ for each cycle, and different cooling steps of 5, 10, 20 and 30$K.min^{-1}$. The sample CuSn8 was also submitted to a lower cooling rate (3 $K.min^{-1}$) in order to better follow the occurrence of the peritectic reaction. Table 13 details the thermal cycles applied to each sample.

System	*Sample*	*Temperature Range*	*Heating rates*	*Cooling rates*
Cu-Sn	CuSn3	1100°C – 600°C	20 $K.min^{-1}$	5; 10; 20; **30 $K.min^{-1}$**
	CuSn5	1100°C – 600°C	20 $K.min^{-1}$	5; 10; 20; **30 $K.min^{-1}$**
	CuSn8	1100°C – 600°C	20 $K.min^{-1}$	5; 10; 20; 30; **3 $K.min^{-1}$**
	CuSn10 I	1100°C – 600°C	20 $K.min^{-1}$	20; 30; **5 $K.min^{-1}$**
	CuSn10 II	1100°C – 600°C	20 $K.min^{-1}$	**10 $K.min^{-1}$**
	CuSn12	1100°C – 600°C	20 $K.min^{-1}$	5; 10; 20; **30 $K.min^{-1}$**
	CuSn14	1100°C – 600°C	20 $K.min^{-1}$	5; 10; 20; **30 $K.min^{-1}$**
	CuSn20	1100°C – 600°C	20 $K.min^{-1}$	5; 10; 20; **30 $K.min^{-1}$**
Cu-Zn	CuZn5	1200°C – 300°C	20 $K.min^{-1}$	3; 10; **30 $K.min^{-1}$**
	CuZn10	1200°C – 300°C	20 $K.min^{-1}$	3; 10; **30 $K.min^{-1}$**
	CuZn20	1200°C – 300°C	20 $K.min^{-1}$	3; 10; **30 $K.min^{-1}$**
	CuZn30	1200°C – 300°C	20 $K.min^{-1}$	3; 10; **30 $K.min^{-1}$**
	CuZn40	1200°C – 300°C	20 $K.min^{-1}$	3; 10; **30 $K.min^{-1}$**

Table 13: DTA procedure for thermal analysis. Values in bold correspond to the last cooling rates applied to the sample

3.3.3.iii. Data treatment

For binary alloys presenting a peritectic reaction, the DTA response is not easily understood. Ferro mentioned that during measurements in cooling, errors could be due to supercooling phenomenon (Ferro, 1982). In addition, parasite effects might appears due to metastable transformations, which are very frequent in peritectic systems.

Since the solidus temperature is more difficult to identify than the liquidus temperature, the use of derivative cooling curves allows for the visualization of a discontinuity toward then end of the solidification process (Figure 41). The attribution of the different peaks is performed according to the signal description displayed in Figure 42 (Boettinger et al, 2006; Ferro, 1982; Baricco, 2005).

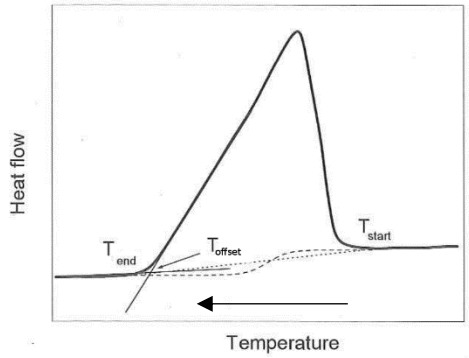

Figure 41: Identification of transition temperature (from Baricco, 2005)

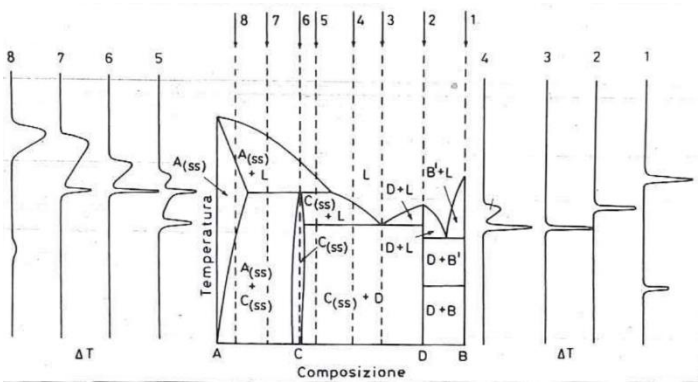

Figure 42: Correlation between cooling curves and phase diagrams (from Ferro, 1982)

The determination of the kinetic of phase transformation refers to the determination of the rate constant (k) and the activation energy of the transformation (E_a). This way, predictions about the transformation rate and the transformation mechanisms are possible.

The evolution of the solid fraction (α) with time, and with the lowering of temperature, is directly obtained through the DTA acquisition software. This value is between 0 (solidification beginning) and 1 (solidification end). We assume that the phase transformation can be described by the Johnson-Mehel-Avrami-Kolmogorov equation (JMAK), with k the reaction rate and n the Avrami coefficient or order of reaction (Eq. 5).

$$\alpha = 1 - e^{-[k(T)t]^n} \qquad \text{(Eq. 5)}$$

As a consequence, the solid fraction can be expressed under a logarithmic form (Eq. 6) and the Avrami plot can be displayed by plotting *ln(– ln (1 – α))* as a function of *ln(t).* The slope of the curve gives the Avrami coefficient (n) and the y-intercept value gives access to the constant of reaction (k).

$$\ln(-ln(1-\alpha)) = nln(k) + nln(t) \qquad \text{(Eq. 6)}$$

Using the Arrhenius form of the constant rate (Eq.7) and by plotting the *ln(k)* against the reciprocal temperature (*1/T*), the activation energy of the transformation and the pre-exponential factor can be respectively deduced from the curve slope (a) (Eq.8) and the y-intercept value (y_0) (Eq.9).

$$k(T) = k_0 e^{-Ea/T} \qquad \text{(Eq. 7)}$$

$$k_0 = e^a \qquad \text{(Eq. 8)} \qquad\qquad E_a = \frac{y_0}{R} \qquad \text{(Eq. 9)}$$

3.3.4) Construction of the D-Opt. Design

In the present work, a D-Optimal Design is carried out for its ability to describe complex systems combining variables of different types like mixtures and processes, as well as qualitative variables. As previously said, it provides the minimization of the determinant of the experimental matrix. This tool is essential for the determination of extrema (maximum, minimum and eventual saddle point) of a multivariate function and its optimization.

Calculations have been carried out through the statistical computing software R. This open source program is often updated by the worldwide statistical community and provides a large variety of statistical and graphical tools.

3.3.4.i. Identification of the variables: factors

During the first phase of experimental stabilization, the understanding of the system is essential. Six controllable factors have been identified, summarized in Table 14. They are separated in:

- quantitative mixture factors which correspond to the respective amounts of alloy elements into a defined composition range. The variables get the implicit restriction that the sum of all component must be 100%.
- the level of superheat, as quantitative process factor and which corresponds to the temperature interval between the melting temperature of the alloy and the pouring temperature.
- mould material, as qualitative process factor, that reflects the cooling rate applied to the molten metal during its solidification.

The pouring rate, which is the velocity at which the metal is poured into the mould, is also an important factor of which the experimental system does not allow the estimation; its variability is however reduced by carrying out casting with the same procedure and by a single operator.

Factors		C.	Uc.	Qt	Ql	M	P	Range
Weight percentage of copper (X_{Cu})	wt.% Cu	X		X		X		80 – 100
Weight percentage of tin (X_{Sn})	wt.% Sn	X		X		X		0 – 20
Weight percentage of zinc (X_{Zn})	wt.% Zn	X		X		X		0 – 20
Weight percentage of lead (X_{Pb})	wt.%Pb	X		X		X		0 – 20
Superheat (X_1)	°C	X		X			X	25 – 75
Material of the mould (S)		X			X		X	Steel/Clay/Sand
Pouring rate	L/min		X	X			X	-

Table 14: List of the factors of the system (C. = controllable, Uc. = uncontrollable, Qt = quantitative, Ql = qualitative, M = mixture, P = process)

- **Boundaries for mixture factors**

Compositions aforementioned are expressed under the form of pseudo-compositions that will be possible to compute. The compositions conversion from classical notation to pseudo-composition is visible Table 10.

- **Boundaries for process factors**

Regarding the factors of the process, boundaries have been defined on the basis of both the state of the art and pragmatic reasons.

For the parameter superheat, the lower limit corresponds to the first effect on castability, while the upper limit is settled by maximal temperature that can be reached by the casting furnace.

For the moulds, three materials have been chosen for their impact on cooling rate and their representativeness in both historical and industrial processes. Unlike the other parameters, this variable get the peculiarity of being purely qualitative. Therefore, a special model with the three levels S1 (Steel), S2 (Clay), S3 (Sand) is necessary.

3.3.4.ii. Identification of the variables: responses

The responses are used to give information on the investigated system. They correspond to the general condition of the system during the variations of parameters. A response can either be a continuous or a discrete value.

The chosen responses Y are listed in Table 15.

Cooling curves	Evolution of the temperature of the mould through time
Microstructure	Nature of the secondary phases
	Volume percentage of secondary phases
Macrostucture	Grain size, SDAS
	Semi-quantitative estimation of porosity (from + to +++)
Hardness	Macrohardness of the alloy

Table 15: List of the measured response

3.3.4.iii. Experimental matrix and model

At first, a full experimental matrix (A1) is built on the base of a full factorial experimental design that defines three levels for each experimental variable and which expresses all the possible combinations. This matrix, visible in Appendix 3, is composed by 135 samples, which also correspond to the number of experiments that would be required in a univariate methodology to investigate the system.

In order to verify the quality of the information provided by this matrix, a multiple regression is performed. The measurement of how much the variance of the estimated regression coefficient is increased due to collinearity can be estimated by the calculation of the inflation factors. An inflation factor is considered perfect if equal to 1. When it is comprised between 4 and 8, it is considered acceptable and an inflation factor above 8 translates the necessity of correction of the experimental matrix

From the results obtained, the inflation factor is calculated and estimated too high (1.00E+04). The quaternary mixture term (PCA*PCB*PCC*PCD) as well as the interaction terms between mixture variables and the quantitative experimental parameters (X1*PCA; X1*PCB; X1*PCC; X1*PCD) which present much smaller coefficient than the rest of the matrix, are rejected.

Therefore, the corrected experimental model proposed is the following (Eq. 10):

$$Y = \alpha_{PCA} X_{PCA} + \alpha_{PCB} X_{PCB} + \alpha_{PCC} X_{PCC} + \alpha_{PCD} X_{PCD} + \alpha_{PCA*PCB} X_{PCA*PCB}$$
$$+ \alpha_1 X_1 + \alpha_{S1} X_{S1} + \alpha_{S2} X_{S2} + \alpha_{PCA*PCC} X_{PCA*PCC} + \alpha_{PCA*PCD} X_{PCA*PCD} + \alpha_{PCB*PCC} X_{PCB*PCC}$$
$$+ \alpha_{PCC*PCD} X_{PCC*PCD} + \alpha_{PCC*PCD} X_{PCC*PCD} + \alpha_{PCA*PCB*PCC} X_{PCA*PCB*PCC}$$
$$+ \alpha_{PCA*PCB*PCD} X_{PCA*PCB*PCD} + \alpha_{PCA*PCC*PCD} X_{PCA*PCC*PCD} + \alpha_{PCB*PCC*PCD} X_{PCB*PCC*PCD} + \alpha_{11} X_1^2$$

(Eq.10)

with

α	18 coefficients
X_{PCA}, X_{PCB}, $X_{PCC,}$ X_{PCD}	4 terms related to the impact of pure pseudo-components (PC)
$X_{PCA*PCB}$, $X_{PCA*PCC}$, $X_{PCA*PCD}$, $X_{PCB*PCC}$, $X_{PCB*PCD}$, $X_{PCC*PCD}$	6 terms related to the impact of binary mixtures of PC
$X_{PCA*PCB*PCC}$, $X_{PCA*PCB*PCD}$, $X_{PCA*PCC*PCD,}$ $X_{PCB*PCC*PCD}$	4 terms related to the impact of ternary mixtures of PC
X1, $X1^2$	2 terms related to the linear and quadratic effect of the quantitative experimental parameter
X_{S1}, X_{S2}	2 terms related to the qualitative experimental variable

The previous corrections allow the compilation of a corrected experimental matrix (A2), with A2 = A1 (;18), visible in Appendix 3.

3.3.4.iv. Computation of the matrix

Once defined the experimental matrix, the algorithm of D-Opt Design can be applied. Since the model is composed by 18 coefficients, and that the D-Optimal Design requires at least the same quantity of experiments and coefficients, the lowest number of experiments will be 18.

At first instance, the computation of the determinant of the experimental matrix (Figure 43) shows that the maximum of information is given for 42 experiments. Beyond, the determinant values decreases and no extra information is provided. Then the computation of the inflation factor (Figure 44) shows that with 21 experiments, the quality of the information gathered is enough. Above, the inflation factor know some fluctuations but remains acceptable.

In the present work, a compromise is made between both quantity and quality of the information on one side, and available time of experiment on the other side, within the achievement of 35 experiments. The final optimized matrix is visible in Appendix 4.

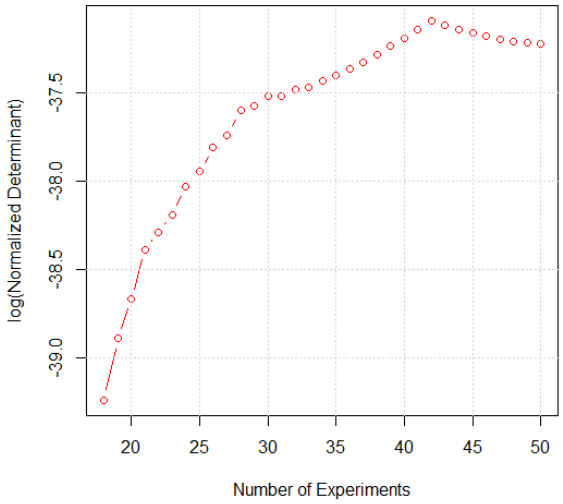

Figure 43: Determinant of the experimental matrix

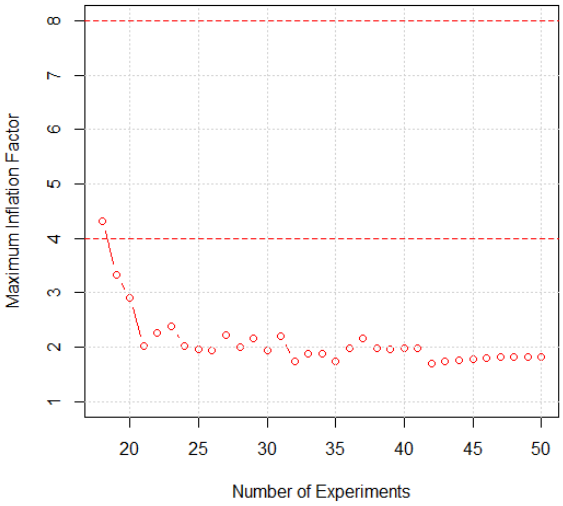

Figure 44: Inflation factor

The list of performed samples are visible in Appendix 5.

3.3.5) Metallography

Metallography corresponds to the determination of the structure and the constituent's features of metals or alloys, at both macroscopic and microscopic scales, and by means of a different examination tools.

In the case of cast materials, this science provides the description of the solidification structure, the examination of the phases and the metallic or non-metallic inclusions present in the matrix, as well as the solidification defects.

3.3.5.i. Sample preparation

The preparation was made according to the international standard ASTM E3-11.

- **Sampling**

The selection and the preparation of the metallographic sample is of high importance to obtain meaningful information and perform representative measurements.

Distinction has been made between experimental samples coming from laboratory castings and archaeological specimen sampled on historical artefacts.

- Samples coming from the DTA measurements have been mounted as it is, in graphite crucible, without any cutting steps;
- For experimental ingots, the central section has been sampled in order to avoid structural defects at edges;
- For the archaeological artefacts of Loyettes, micro-samples were taken from in three different areas. The first one is on the edge of the axe-ingot (distal part) while the second is on the top of the axe (proximal part).

- **Mounting and surface preparation**

All experimental samples have been hot mounted in phenolic resin (PF), while archaeological samples have been cold mounted in epoxy resin in order to avoid unwanted modification of the samples.

Standard procedures have been applied for the metallographic preparation of the sample surface. Mounted samples have been first grinded with abrasive SiC papers with a grit size from up to 1000 (18 µm) and then polished up to 1 µm.

3.3.5.ii. Instruments

A multiscale observation of the samples structure has been carried out through:

- **Stereo Microscope** (SM) Leica WILD M8 with magnification from 60 to 500X for the macroscopic observation of the grains;
- **Light-Optical Microscope** (LOM) Leica MEF4M with magnification from 25X to 1000X for the macroscopic observation of the grains as well as the microscopic observation of phases and inclusions;
- **Scanning Electron Microscope** (SEM) Zeiss EVO 40 with fixed magnification of 4000X and equipped with an EDS detector for quantitative measurements.

3.3.5.iii. Stereological techniques

Stereology correlates microscopic observations from a two-dimensional surface to the three-dimensional reality. The qualitative metallography gets its fundamental principle from it (Eq. 11) (Vander Voort, 2000):

$$V_V = A_A = P_P = L_L \qquad \text{(Eq. 11)}$$

where Vv = volume fraction, A_A = area fraction, P_P = point count, L_L = lineal fraction.

Qualitative metallography and stereological principles have been applied to the determination of the volume percent of each of the features of the matrix, the grain size and the repartition of the inclusions.

- **Grain size and Secondary Dendrite Arm Spacing (SDAS)**

Measurements was made according to the international standard ASTM E112.

For the description of microstructures with equiaxed grains, the linear intercept method is carried out by 3 readings by micrography and the average grain size is found by Equation 12.

$$D_{average} = {}^{L}/_{N} \qquad \text{(Eq.12)}$$

with $D_{average}$, the average grain diameter, L the line length and N the number of intercepted grains.

For microstructures with non-equiaxed grains, the grain length along the direction of heat transfer is measured by 10 readings for each micrography. The average grain size is presented.

Furthermore, along the radial cross-section, the length of each ingot's zone (chill R1, columnar R2 and central equiaxed R3) is measured by 10 readings for each micrography (Figure 45).

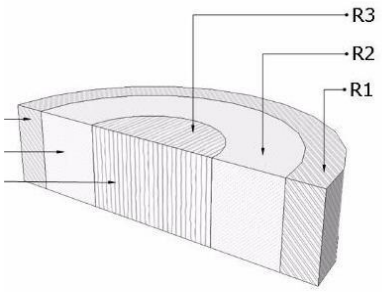

Figure 465: Identification of the different ingot's zones

Cast materials often present a non-annealed microstructure with dendritic pattern for which grains are not easily recognizable. In those cases, the Secondary Arm Dendrite Spacing (SDAS) is commonly used to describe the structure size.

According to Vandersluis and Ravindran, the most accurate method in terms of statistical significance consists in measuring the length L parallel to the primary arm and from center to center of the counted secondary arms (Figure 46). This way, the method is not influenced by the dendrite asymmetry. Despite the error that can be brought by the misestimating of the dendrite centers, the potential error in this approach is far outweighed by the inaccuracy of the other methods (Vandersluis and Ravindran, 2017).

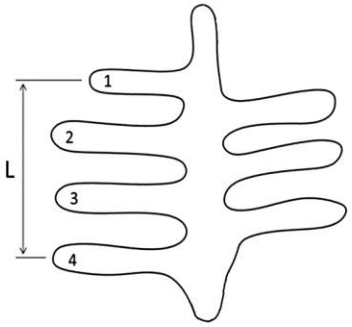

Figure 46: Determination of the SDAS (Vandersluis and Ravindran, 2017)

Thus, the secondary dendrite arm spacing is given by the Equation 13:

$$SDAS = \frac{L}{(N-1)} \qquad \text{(Eq. 13)}$$

In this work, the method has been used on 3 readings measured over 10 optical micrographs per each sample in order to have a good representativeness of the data.

- **Secondary phase and porosity volume percent's**

The volume percent of secondary phase and porosity are estimated with the software Image J on 10 pictures for each sample.

The data gathered are treated within a Principal Component Analysis (Section 3.3.8).

3.3.6) Hardness

By definition, hardness is the resistance of a material to permanent deformation when in contact with an indenter under load (Revankar, 2000).

This mechanical test is often performed in both industrial and archaeometric fields for its ease of execution since it does not require an elaborated sample preparation. Furthermore, studies show that this non-destructive and micro-invasive test presents a good reliability with other mechanical properties.

Different types of measurements are available as a function of the indenter shape.

In this work, Vickers macrohardness measurements are achieved within 5 measurements on the grinded surface of the samples for a load P = 10 kg and a dwell time t = 3 s.

3.3.7) Statistical treatment of data: Principal Component Analysis (PCA)

The PCA is a multivariate statistical tool that provides the dimensional reduction of a random multivariate sample, i.e. the minimization of the number of its variables by regrouping together the dependent ones. This corresponds to a change of space in which all the data of the set are projected on an axis that minimizes the loss of information carried. As PCA is an iterative process, once the first component is found, another one should be built in order to describe the remaining variability. A lower number of non-correlated, variables, called factors, is then identified and allows the description of the system into a new orthogonal space.

This way, correlations among the original variables and between these variables and factors may be clearly visualized, allowing the recognition of patterns of the system. The visualization of the results is carried on through the plot of both scores (reflecting the samples distribution) and loadings (reflecting the variables inter-correlations). The biplot permits to observe the distribution of the variables and the samples.

CHAPTER 4.

RESULTS AND DISCUSSION

4.1) Medium cooling rates (10^{-2} – 1 $K.s^{-1}$)

4.1.1) Control of the alloys composition

Tables 16 and 17 detail each sample composition with the respective relative error between theoretical and experimental values. Except for two samples of the Cu-Sn system (CuSn8 and CuSn10 II), the percent error is inferior to 10% and corresponds well to the expected compositions.

Sample	*Sn*	*% Error*
Cu Sn3	3.3 ± 0.2	10.0 %
Cu Sn5	5.4 ± 0.1	8.0 %
Cu Sn8	9.3 ± 0.2	**16.3 %**
Cu Sn10 I	10.8 ± 0.5	8.0 %
Cu Sn10 II	11.3 ± 0.4	**13.0 %**
Cu Sn12	12.5 ± 0.1	4.2 %
Cu Sn14	14.2 ± 0.3	1.4 %
Cu Sn20	20.4 ± 0.4	2.0 %

Table 16: Alloys composition for the Cu-Sn system

Sample	*Zn*	*% Error*
Cu Zn5	5.0 ± 0.3	0.0 %
Cu Zn10	10.6 ± 0 .5	6.0 %
Cu Zn20	20.7 ± 0.3	3.5 %
Cu Zn30	29.0 ± 0.5	-3.3 %
Cu Zn40	38.7 ± 0.3	-3.2 %

Table 17. Alloys composition for the Cu-Zn system

4.1.2) Cooling curves and kinetic investigation

Cooling curves are obtained by plotting the variation of DTA signal (expressed in µV/mg) against the temperature evolution (expressed in Celsius degrees).

4.1.2.1. Cu-Sn system

The experimental cooling curves for each bronze sample are presented in Figure 47.

Samples with the lowest tin amount (CuSn 3 and CuSn 5) present cooling curves with peaks bounded by rounded apices, characteristics of changes occuring within a definied temperature interval. The onset and offset are respectively interpreted as the liquidus and solidus of formartion of primary α grains from the liquid.

From sample CuSn 8 (Sn 9 wt.%) and for higher tin contents, two successive apices are visible which correspond to the passage through a two-phase domain. The onset of the first rounded tip represents the beginning of the fusional range and the biphasic (L+α) domain (liquidus) and ends at the sharp apex of the second signal (peritectic plateau).

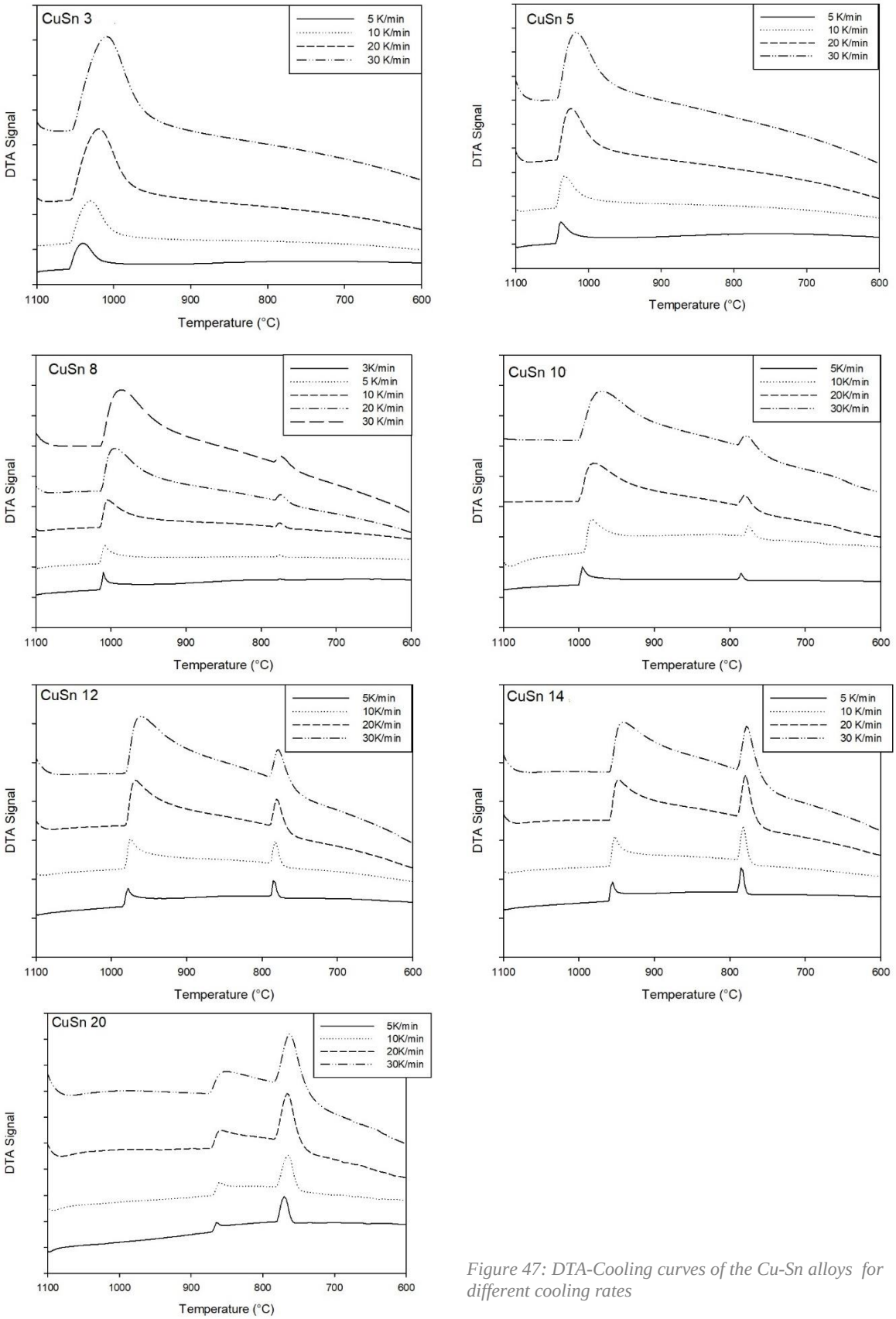

Figure 47: DTA-Cooling curves of the Cu-Sn alloys for different cooling rates

The determination of temperature of transformation is possible as described in the section 3.3.1. Raw values are visible in Appendix 7. It appears that the liquidus undergoes only a slight decrease of its value with the rise of the cooling rate. The second signal, which may correspond to the solidus knows a clear drop with the increase of cooling rate.

A kinetics investigation permits to follow the evolution of the solid fraction α as a function of both temperature and time, as well as the transformation rate (dα/dt) with time. The maximum value of transformation rate and the time of end of transformation are reported for each sample in Table X. When the cooling rate is increased, reactions occur faster and the total time of transformation is shortened. With respect to the first reaction, the peritectique solidification is much slower and shorter.

For low-tin bronze, only a single transformation is present, which is faster for highest cooling rates and as a consequence is earlier completed (Figures 48 and 49). This is the case for sample CuSn 3 and sample CuSn 5 which both provide the formation of the α-solid solution. The data of the samples CuSn 5 however present some inaccuracies and will be reconsidered in further works.

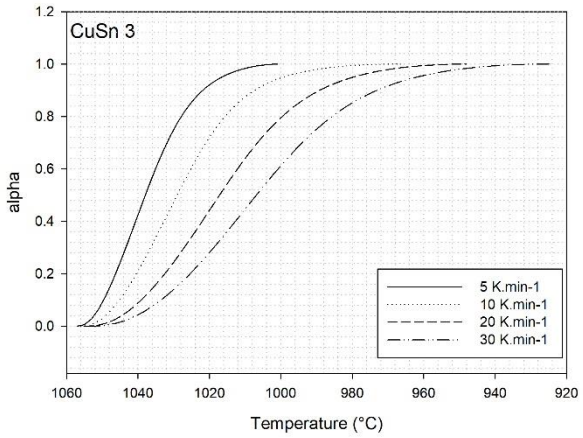

Figure 48: Evolution of the transformed fraction as a function of temperature (sample CuSn 3)

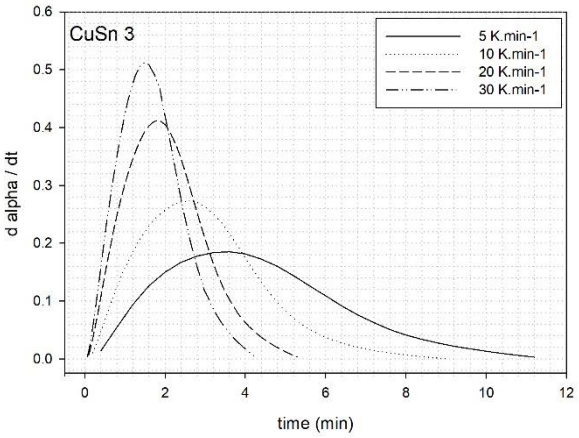

Figure 49: Evolution of the transformation rate with time (Sample CuSn 3)

For higher tin content (from sample CuSn 8), the slope change in the evolution of the transformed fraction indicates the occurrence of the peritectic solidification. From the plot of the transformation rate against time (Figures 50 and 51), it can be seen that this reaction appears in very different times according to the cooling rate, which also correspond to the level of undercooling of the sample.

From the sample CuSn 12, the peritectic transformation becomes as fast as the formation of the first crystals, and from sample CuSn 14 even faster.

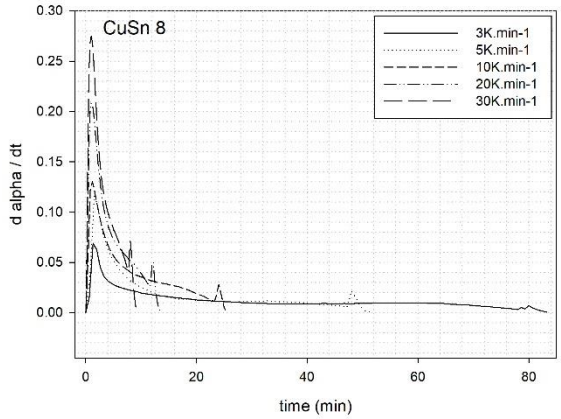

Figure 50: Evolution of the transformation rate with time (Sample CuSn 8)

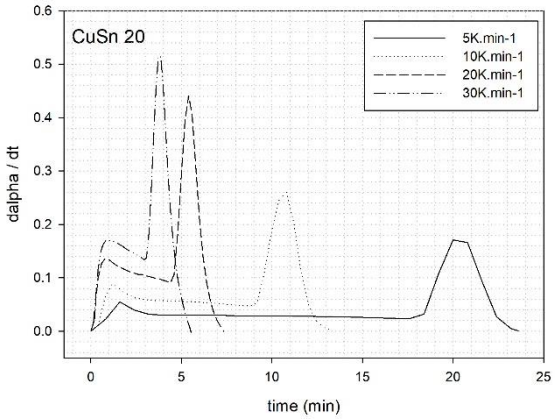

Figure 51: Evolution of the transformation rate with time (Sample CuSn 20)

The respective Avrami plot gives access to the order of reaction for each reaction in each sample (Figure 52 and 53).

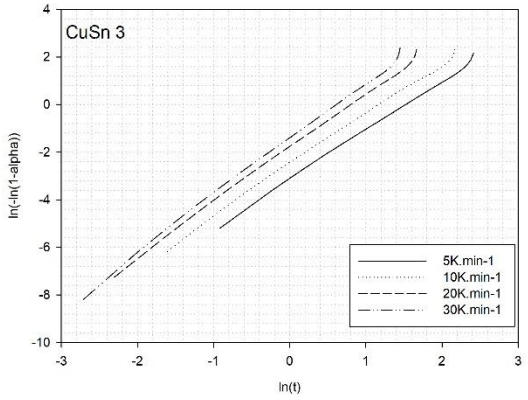

Figure 52: Avrami plot for single reaction (Sample CuSn 3)

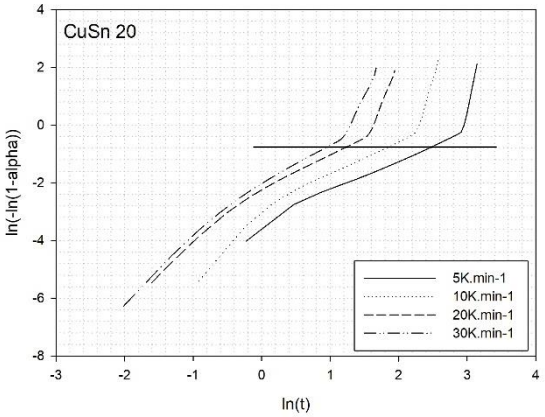

Figure 53: Avrami plot for two phase transformations (Sample CuSn 20)

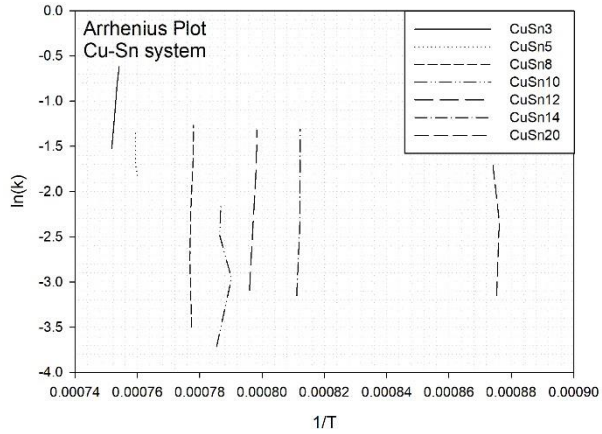

Figure 54: Arrhenius plot for the binary Cu-Sn system

Eventually, the slope of Arrhenius plot indicates the activation energy of the considered transformation (Figure 54). The data are reported in the Table 18.

For the single formation of the α solid-solution, the averaged order of reaction is 2, while it becomes 1 for the peritectic transformation. Only the orders of reaction and activation energies of the primary transformation (L → α) are reported.

Sample	*Cooling rate* β	*Reaction*	*Maximum rate of transformation* $(d\,\alpha_{max}/dt)$	*Time of transformation* (t)	*Reaction order (n)*	*Activation energy* (E_a)
CuSn 3	5 K.min^{-1}	L → α	0.19	10.4 min		
	10 K.min^{-1}	L → α	0.27	9.0 min	2.2 ± 0.1	2.4 .10^3 J.mol^{-1}
	20 K.min^{-1}	L → α	0.41	5.4 min		
	30 K.min^{-1}	L → α	0.51	4.3 min		
CuSn 5	5 K.min^{-1}	L → α	0.23	12.4 min		
	10 K.min^{-1}	L → α	0.17	16.4 min	1.8 ± 0.3	2.4.10^3 J.mol^{-1}
	20 K.min^{-1}	L → α	0.13	17.1 min		
	30 K.min^{-1}	L → α	0.63	3.5 min		
CuSn 8	3 K.min^{-1}	L → α	0.07	77.8 min		
		L + α → β	0.01	5.2 min		
	5 K.min^{-1}	L → α	0.12	46.9 min		
		L + α → β	0.02	4.9 min	1.1 ± 0.3	7.7 .10^3 J.mol^{-1}
	10 K.min^{-1}	L → α	0.13	23.1 min		
		L + α → β	0.03	2.6 min		
	20 K.min^{-1}	L → α	0.21	11.2 min		
		L + α → β	0.05	2.3 min		
	30 K.min^{-1}	L → α	0.27	7.4 min		
		L + α → β	0.07	1.8 min		
CuSn 10	5 K.min^{-1}	L → α	0.07	42.4 min		
		L + α → β	0.04	4.8 min		
	10 K.min^{-1}	L → α	0.13	21.1 min		
		L + α → β	0.05	3.5 min	0.7 ± 0.1	3.4 .10^3 J.mol^{-1}
	20 K.min^{-1}	L → α	0.17	10.6 min		
		L + α → β	0.08	2.0 min		
	30 K.min^{-1}	L → α	0.24	7.0 min		
		L + α → β	0.11	2.0 min		
CuSn 12	5 K.min^{-1}	L → α	0.07	38.8 min		
		L + α → β	0.08	4.6 min		
	10 K.min^{-1}	L → α	0.12	18.9 min		
		L + α → β	0.10	3.4 min		4.7 .10^3
	20 K.min^{-1}	L → α	0.18	9.5 min	1.4 ± 0.3	J.mol^{-1}
		L + α → β	0.14	2.2 min		
	30 K.min^{-1}	L → α	0.23	6.1 min		
		L + α → β	0.18	1.9 min		
CuSn 14	5 K.min^{-1}	L → α	0.07	34.4 min		
		L + α → β	0.10	3.2 min		
	10 K.min^{-1}	L → α	0.12	16.4 min		
		L + α → β	0.17	3.2 min	1.4 ± 0.4	9.1 .10^3 J.mol^{-1}
	20 K.min^{-1}	L → α	0.18	8.3 min		
		L + α → β	0.24	2.2 min		
	30 K.min^{-1}	L → α	0.21	5.4 min		
		L + α → β	0.27	2.4 min		
CuSn 20	5 K.min^{-1}	L → α	0.05	17.8 min		

		L + α → β	0.17	5.4 min		
	10 K.min^{-1}	L → α	0.09	9.0 min		
		L + α → β	0.26	4.1 min	1.4 ± 0.4	2.8 .10^{3} J.mol^{-1}
	20 K.min^{-1}	L → α	0.14	4.3 min		
		L + α → β	0.44	3.0 min		
	30 K.min^{-1}	L → α	0.17	3.0 min		
		L + α → β	0.51	2.5 min		

Table 18: Kinetics parameters for the Cu-Sn system

4.1.2.1. Cu-Zn system

The experimental curves of brass samples are presented in Figure 55.

From the sample CuZn 5 to the sample CuZn30, the cooling curves are characterised by a single peak more or less steep, which corresponds to the formation of the primary grains α. The peak's width is mainly due to the fact that brasses present a narrow interval of solidification for hypoperitectic compositions. Around 450°C, the slope of the baseline changes which main indicate a disordered-ordered transition in the α phase.

For the sample with the highest zinc content (CuZn 40), two main signals are noticeable. The onset and the offset of the first sharp peak respectively correspond to the liquidus and the solidus for the formation of the β primary phase. The second signal, around 850 °C, corresponds to the limite of solubility of zinc the the primary phase and provides the formation of secondary α grains. The slope change of the baseline around 450°C might correspond to the disordered-ordered transition of the β phase into a β' phase.

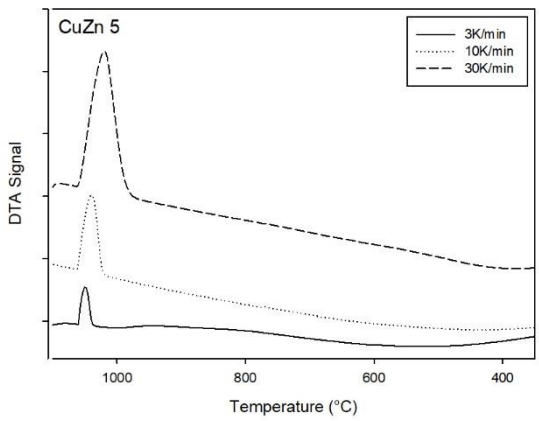

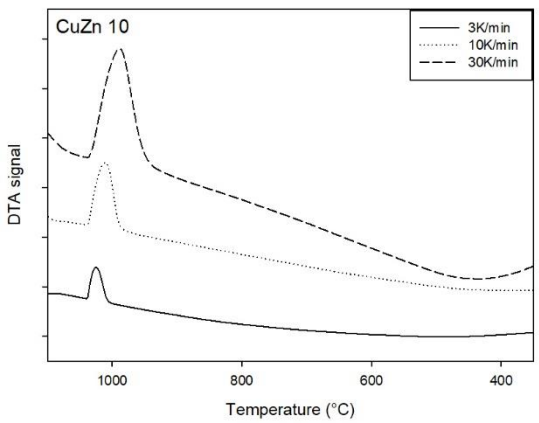

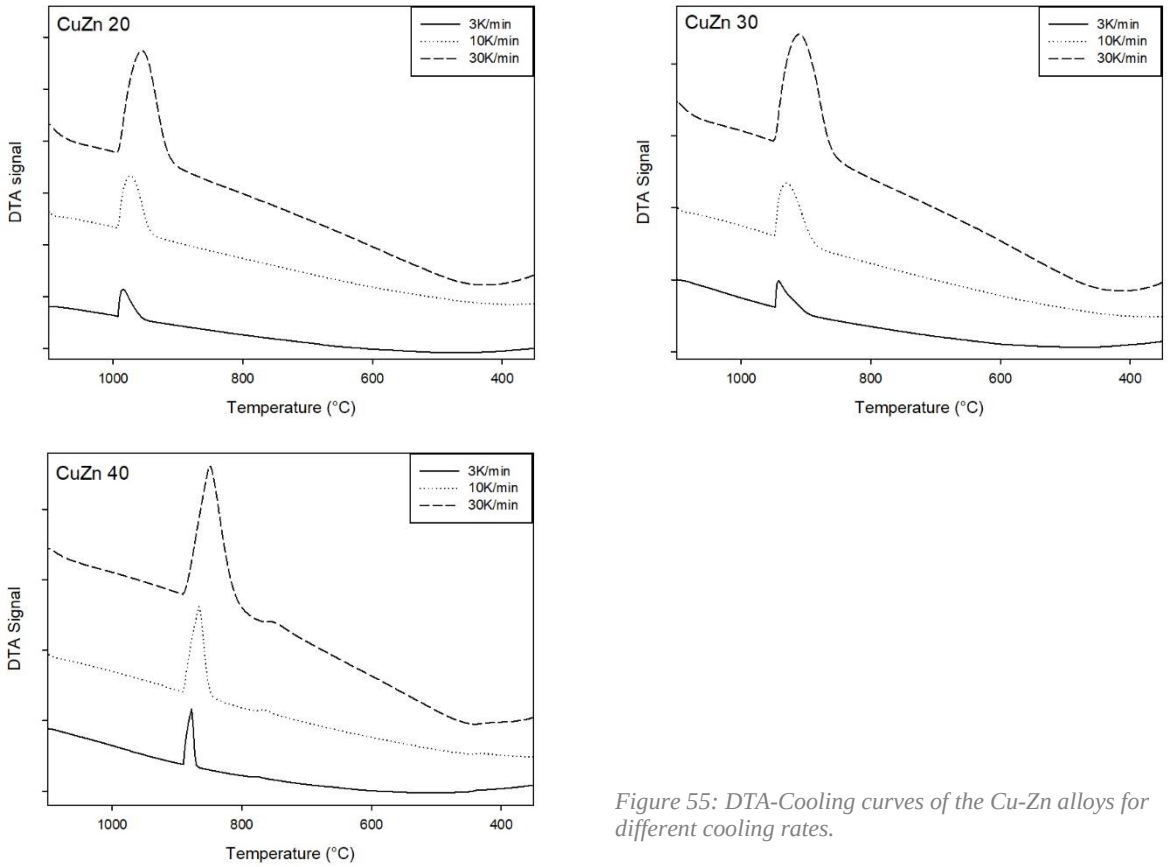

Figure 55: DTA-Cooling curves of the Cu-Zn alloys for different cooling rates.

The values of the liquidus are much lower than those predicted but do not show any meaningful variation for cooling rates between 3 and 30 $K.min^{-1}$. A decrease of the solidus temperatures has been noted with a rise of the cooling rate, and the occurrence of the peritectic transformation has been observed for alloys with a smaller zinc amount than expected by the equilibrium diagram. The raw values of characteristic points are visible in Appendix 7.

As previously investigated for the Cu-Sn, a kinetics study is performed in order to follow the evolution of the solidification as a function of cooling rate. The attention has been on the liquid-solid transition at high temperature. The maximum value of transformation rate and the time of end of transformation are reported for each sample in Table 19. Once again, when the cooling rate is increased, reactions occur faster and the total time of transformation is shortened.

For sample CuZn 5 to sample CuZn 30, the evolution of the solid fraction (α) as a function of both temperature and time, as well as the transformation rate (dα/dt) with time, can be followed (Figures 56 and 57).

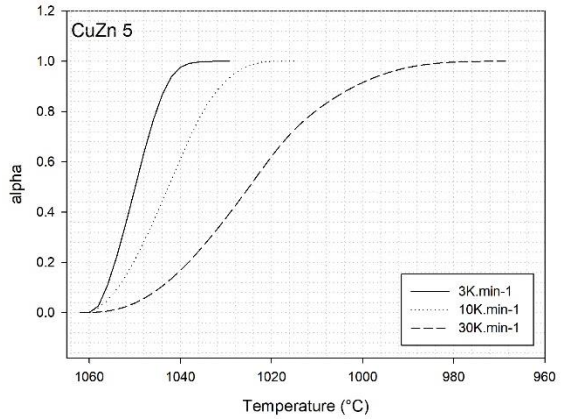

Figure 56: evolution of the transformed fraction with temperature decrease (Sample CuZn 5)

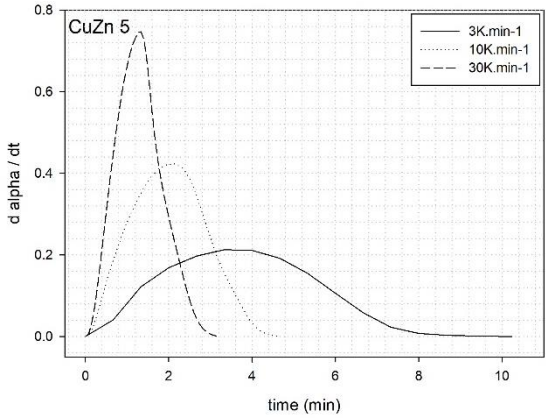

Figure 57: evolution of the transformation rate with time (Sample CuZn 5)

For the sample CuZn 40, however, the profile of the transformation rate is no more symmetrical and presents a sharp maximum for higher times after the solidification beginning (Figure 58 and 59). This phenomenon can be due to the narrow range of solidification of β-brasses, for which the liquidus and solidus are not easily identifiable.

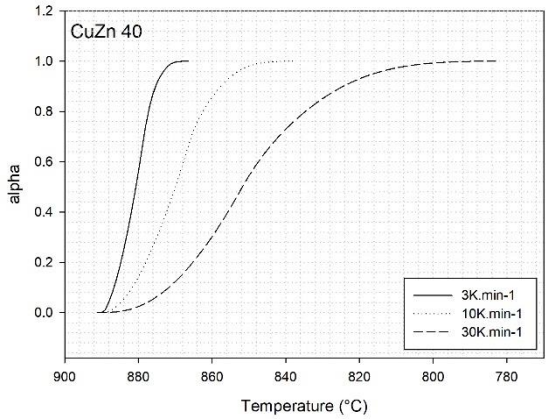

Figure 58: evolution of the transformed fraction with temperature decrease (Sample CuZn 40)

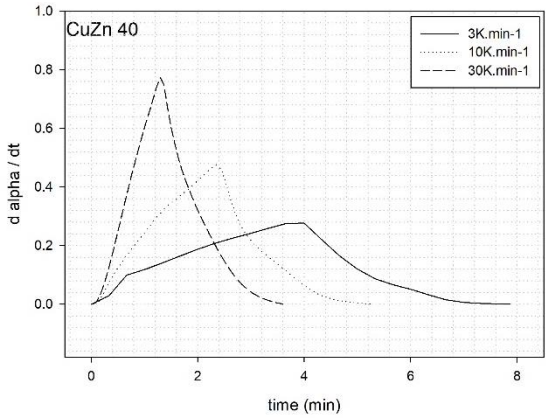

Figure 59: evolution of the transformation rate with time (Sample CuZn 40)

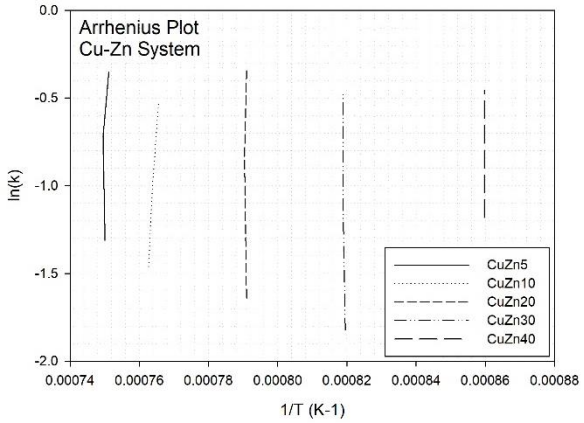

Figure 60: Arrhenius plot for the Cu-Zn system

Sample	*Cooling rate β*	*Reaction*	*Maximum rate of transformation ($d\alpha_{max}/dt$)*	*Time of transformation (t)*	*Reaction order (n)*	*Activation energy (E_a)*
CuZn 5	3 K.min-1	L → α	0.21	10.2 min		
	10 K.min-1	L → α	0.42	4.6 min	2.4 ± 0.2	$3.7 .10^4$
	30 K.min-1	L → α	0.75	3.1 min		$J.mol^{-1}$
CuZn 10	3 K.min-1	L → α	0.15	12.6 min		
	10 K.min-1	L → α	0.33	6.0 min	2.3 ± 0.5	$3.8 .10^4$
	30 K.min-1	L → α	0.61	3.8 min		$J.mol^{-1}$
CuZn 20	3 K.min-1	L → α	0.13	16.7 min		
	10 K.min-1	L → α	0.30	6.2 min	2.0 ± 0.4	$2.9 .10^4$
	30 K.min-1	L → α	0.63	3.1 min		$J.mol^{-1}$
CuZn 30	3 K.min-1	L → α	0.12	19.5 min		
	10 K.min-1	L → α	0.25	7.3 min	2.1 ± 0.5	$1.9 .10^4$
	30 K.min-1	L → α	0.53	3.7 min		$J.mol^{-1}$
CuZn 40	3 K.min-1	L → β	0.28	7.9 min		
	10 K.min-1	L → β	0.48	5.2 min	2.4 ± 0.2	*missing data*
	30 K.min-1	L → β	0.77	3.6 min		

Table 19: Kinetics parameters for the Cu-Zn system

4.1.3) Microstructural investigation

4.1.3.1) Cu-Sn system

The evolution of microstructures with tin content is presented in Figure 61.

The sample CuSn 3 (around 3 wt.% Sn) (Figure 61a) is composed by the single α primary phase, but a slight microsegregation of tin in copper is visible.

The sample CuSn 5 (around 5 wt.% Sn) (Figure 61b) is mainly composed by the monophasic primary phase α. The microsegregation is well noticeable at the dendrites scale. Despite of the low tin content in the alloy, the first nodules of secondary phase (α+δ) can be distiguished. This phase is however hardly quantificable due to its small dimensions.

From the sample CuSn 8 (Figures 61c, 61d, 61e), the eutectoid constituent (α+δ) is clearly observable in grey-blue in the interdendritic spaces which is in line with the previous cooling curves where the signal for the peritectic transformation was well visible.

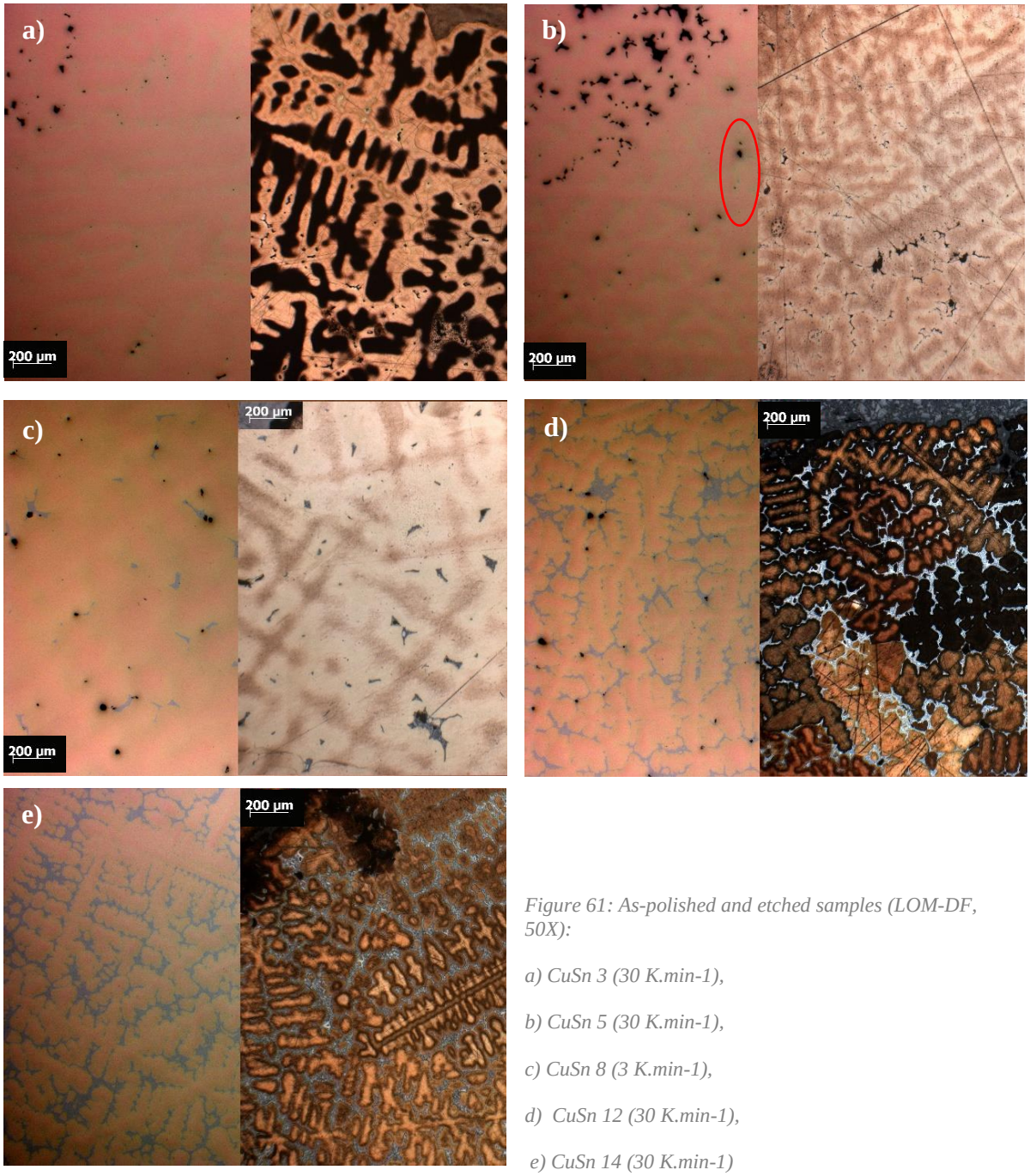

Figure 61: As-polished and etched samples (LOM-DF, 50X):

a) CuSn 3 (30 K.min-1),

b) CuSn 5 (30 K.min-1),

c) CuSn 8 (3 K.min-1),

d) CuSn 12 (30 K.min-1),

e) CuSn 14 (30 K.min-1)

Furthermore, two different cooling rates have been applied to the samples CuSn10 I (5 K.min-1) and CuSn10 II (10 K.min-1). According to the metallographic investigation, besides a finer microstructure for the CuSn10 II sample, the faster cooling rate also implies the formation of a higher quantity of peritectic and thereby of eutectoid constituent.

The comparison between the two samples is visible in Figure 62. This phenomenon is the direct consequence of the shift of the peritectic plateau towards lowest tin concentrations and the decrease of tin solubility in copper matrices with the increase of transformation kinetic.

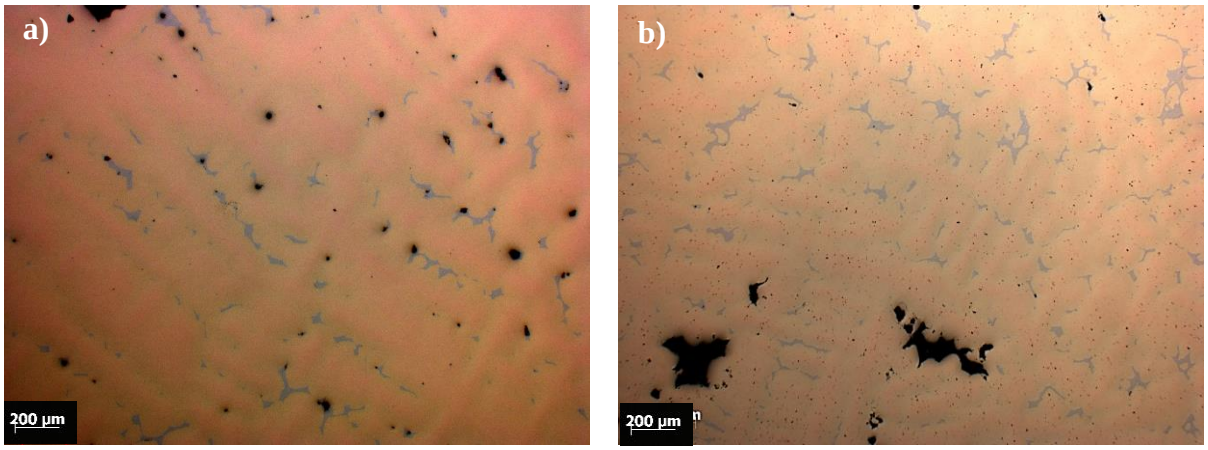

Figure 62: Samples CuSn 10 I (5 K/min) and II (10 K/min) (LOM, 50X),

The stereological analysis of the micrographs shows that the percentage of secondary phase increases with tin content (Table 20). This phase also appears for lower tin content that expected by equilibrium phase.

Sample	Last cooling rate applied	% vol. (α+δ)	SDAS
CuSn 3	30 K.min^{-1}	0.00%	123 ± 34
CuSn 5	30 K.min^{-1}	0.3 ± 0.1 %	92 ± 9
CuSn 8	3 K.min^{-1}	1.1 ± 0.6 %	224 ± 30
CuSn 10 I	5 K.min^{-1}	2.7 ± 1.4 %	254 ± 22
CuSn 10 II	10 K.min^{-1}	3.7 ± 1.4 %	172 ± 33
CuSn 12	30 K.min^{-1}	12.2 ± 1.8 %	112 ± 23
CuSn 14	30 K.min^{-1}	17.8 ± 2.1 %	111 ± 9
CuSn 20	30 K.min^{-1}	41.7 ± 2.3 %	42 ± 10

Table 20: Microstructural features of the Cu-Sn samples

On the basis of corresponding phase diagram (Fürtauer et al, 2013), a prediction of the final microstructure of these alloys in condition of equilibrium is possible, through the application of the lever rule which allows the mass fraction of each phase (Figure 63). In this computation, low-temperature transformations taking place under the temperature of 500°C, like the eutectoid transformation ($\delta \rightarrow \alpha + \varepsilon$), are not considered.

- For alloys with a tin content lower than 13.5 wt.%, the melt should solidify in a single α phase structure without the formation of any peritectic product ($W\alpha = 1$; $W\delta = 0$). At a cooling rate of 30K.min-1, a secondary phase (α+δ) has formed from a tin content of 9 wt.% (Sample CuSn8) and in higher proportions for the CuSn12 sample.

- For the alloy with a tin content of 14 wt.%, the peritectic transformation takes place and leads to the formation of a small amount of β-phase. However, with the temperature lowering, the solubility of tin in this peritectic phase decreases and this

element diffuses towards the surrounding α-solid solution. At ambient temperature, the resulting microstructure is monophasic (Wα = 1; Wδ =0); At a cooling rate of 30K.min-1, circa 18% of secondary phase has formed.

- For the high-tin alloy (20 wt.%), the α primary dendrites crystallize. At the peritectic temperature, these α crystals and the remaining liquid transform into the β-peritectic phase. With the temperature lowering, the solubility of tin in the β phase decreases and the element diffuses towards the α phase. A disordered-ordered transition takes place at 596 °C leading to the formation of the γ phase from the peritectic one. At 520°C, the eutectoid transformation brings to the formation of circa 39 % of the (α+δ) secondary phase from the γ phase. At a cooling rate of 30 $K.min^{-1}$, circa 42 % of secondary phase is formed.

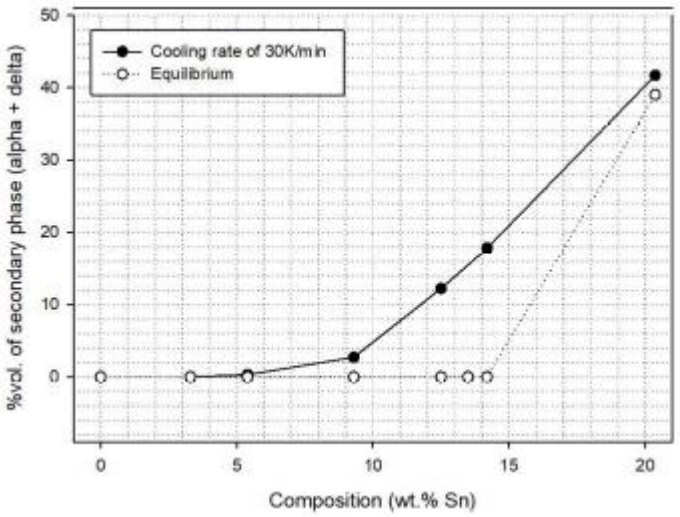

Figure 63: Evolution of secondary phase volume percent as a function of composition and cooling rate

4.1.3.2) Cu-Zn system

The microstructures of brass sample are divided in two typologies:

From the sample CuZn 5 to the sample CuZn30, the microstructure is dendritic monophasic composed by the α-solid solution. The segregation of the alloying elements is slightly visible (Fig. 64).

The sample CuZn 40 (38.7 wt.% Zn) however presents a biphasic microstructure of β primary phase (44.7 ± 0.7 wt.% Zn) in which the α phase has precipitated from the grain boundaries (36.5 ± 0.6 wt.% Zn) (Fig. 65).

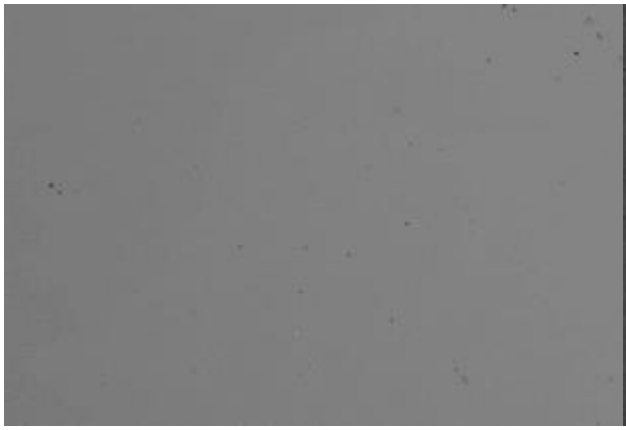

Figure 64: Sample CuZn5 (SEM, 300X)

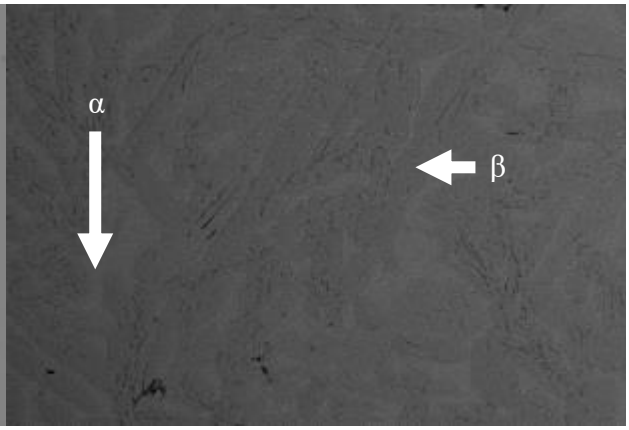

Figure 65: Sample CuZn 40 (SEM 300X)

The Wildmanstätten pattern of the α phase is due to the non-equilibrium cooling rate applied to the alloy (Fig.66).

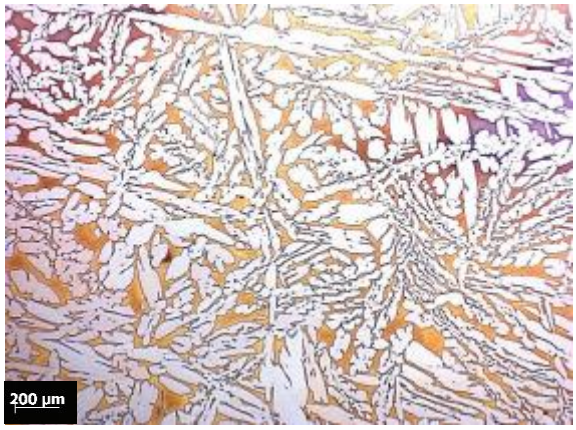

Figure 66: Micrograph of the etched sample CuZn40 (LOM-BF, 50X)

The stereological analysis of the micrographs shows that the percentage of secondary phase increases with zinc content (Table 21). This phase also appears for lower tin content that expected by equilibrium phase.

Sample	Last cooling rate applied	% vol. α	% vol. β
CuZn5	30 K.min-1	100%	0 %
CuZn10	30 K.min-1	100%	0 %
CuZn20	30 K.min-1	100%	0 %
CuZn30	30 K.min-1	100%	0 %
CuZn40	30 K.min-1	27.5 ± 1.2 %	72.5%

Table 21 Microstructural features of the brass samples:

4.2) Near-rapid cooling rates (1 – 10^3 $K.s^{-1}$)

4.2.1) Control of the alloys composition

Table 22 presents the average chemical compositions for each sample of the DoE.

Sample	*Alloy*	*Cu*	*Sn*	*Zn*	*Pb*	*Other*	
3 – 30	Cu	100.0 ± 0.1	-	-	-.	-	
20 – 34	Cu	99.7 ± 0.2	-	-	< 0.1	< 0.1	Si
6 – 50	Cu	99.9 ± 0.1	-	< 0.5	< 0.1	< 1.0	Si, Al
11 – 3	CuSn20	79.0 ± 0.1	21.0 ± 0.1	-	-	-	
19 – 8	CuSn20	78.9 ± 0.1	21.0 ± 0.1	-	-	< 0.1	Si, Ti
19 – 8R	CuSn20	78.4 ± 0.1	21.0 ± 0.1	-	< 0.1	0.1	Ti, Fe
17 – 16	CuSn20	78.7 ± 0.3	21.0 ± 0.3	-	< 0.1	< 0.5	Si, Ti
22 – 27	CuSn20	78.4 ± 0.4	21.4 ± 0.3	-	-	< 0.5	Si, Ti
DTA 20	CuZn20	79.5 ± 0.1	-	20.2 ± 0.1	-	-	
4 – 38	CuZn20	78.9 ± 0.2	-	20.7 ± 0.1	< 0.1	< 0.5	Si, Nb, Ni
12 – 93	CuZn20	79.6 ± 0.1	-	20.2 ± 0.1	-	< 0.1	Nb, Ni
2 – 58	CuPb20	79.8 ± 0.2	-	-	19.8 ± 0.3	< 1.0	Si, Al
2 – 58R	CuPb20	77.2 ± 0.1	-	-	21.9 ± 0.1	< 1.0	Si, Al
16 – 108	**CuPb20***	84.8 ± 0.1	-	-	15.0 ± 0.1	< 0.5	Si, W
14 – 82	CuSn10	89.8 ± 0.2	10.0 ± 0.1	-	< 0.1	< 0.5	Si, Ti
15 – 88	CuSn10	90.6 ± 0.1	9.3 ± 0.1	< 0.1	-	< 0.5	Si, Ti
Dhl	CuSn10	89.2 ± 0.4	10.3 ± 0.1	-	< 0.1	< 0.5	Si, Ti
13 – 102	CuSn10	89.3 ± 0.3	10.4 ± 0.2	-	< 0.1	< 0.5	Si
DTA 10	CuZn10	89.7 ± 0.1	-	10.1 ± 0.1	< 0.1	< 0.5	Si, Nb, Ni
8 – 68	CuZn10	89.3 ± 0.7	-	10.2 ± 0.2	-	1.0	Si, Nb, Ni
13 – 96	CuZn10	89.3 ± 0.1	-	10.5 ± 0.1	< 0.1	< 0.5	Si, Nb, Ni
1 – 109	CuPb10	88.8 ± 0.2	-	-	10.8 ± 0.4	< 0.5	Si, Al
1 – 109R	CuPb10	87.9 ± 0.1	-	-	11.6 ± 0.1	< 0.5	Si, Al
24 – 123	**CuPb10***	89.9 ± 0.8	-	-	8.7 ± 0.2	1.0	Si, Al
6 – 129	CuPb10	87.7 ± 0.8	-	-	11.2 ± 0.8	1.0	Si, Al
7 – 56	**CuSn10Zn10***	75.0 ± 0.4	12.3 ± 0.3	12.4 ± 0.2	< 0.1	< 0.5	Si, Ti, Nb, Ni
17 – 112	**CuSn10Zn10***	75.4 ± 0.2	12.4 ± 0.3	12.1 ± 0.1	< 0.1	< 0.1	Si, Nb, Ni
4 – 146	**CuSn10Pb10***	81.4 ± 0.6	10.3 ± 0.2	-	8.0 ± 1.1	< 1.0	Si, Ti
18 – 144	CuSn10Pb10	80.1 ± 0.2	9.9 ± 0.1	< 0.1	9.7 ± 0.1	< 0.5	Si, Ti
28 – 154	**CuSn10Pb10***	81.6 ± 0.4	10.1 ± 0.1		7.6 ± 0.2	< 1.0	Si, Ti, Al
1 – 6	**CuZn10Pb10***	88.8 ± 6.0	-	4.9 ± 2.9	6.1 ± 3.1	< 0.1	Si, Nb, Ni
14 – 100	CuZn10Pb10	80.7 ± 0.1	-	10.0 ± 0.1	9.2 ± 0.1	< 0.1	Si, Nb, Ni
9 – 73	CuSn6.7Zn6.7	86.8 ± 0.1	6.4 ± 0.2	6.7 ± 0.1	< 0.1	< 0.1	Si, Nb, Ni
15 – 101	CuSn6.7Zn6.7	86.5 ± 0.8	6.5 ± 0.3	6.6 ± 0.1	< 0.1	< 1.0	Si, Nb
7 – 164	CuSn6.7Pb6.7	85.8 ± 0.1	6.5 ± 0.2	-	7.3 ± 0.2	< 0.1	Al, Si, Ti
5 - 47	CuSn6.7Pb6.7	86.6 ± 0.1	6.4 ± 0.1	-	6.6 ± 0.1	< 0.1	Si
2 – 22	**CuZn6.7Pb6.7***	85.6 ± 0.2	-	6.0 ± 0.1	8.3 ± 0.2	< 0.5	Si, Nb, Ni
10 – 74	**CuZn6.7Pb6.7***	85.8 ± 0.1	< 0.5	7.2 ± 0.1	6.3 ± 0.1	< 0.5	Si, Ni
3 – 34	**CuSn6.7Zn6.7Pb6.7***	83.4 ± 2.4	5.1 ± 0.9	4.9 ± 0.5	6.5 ± 1.0	< 0.1	Si, Nb
11 – 89	CuSn6.7Zn6.7Pb6.7	80.4 ± 0.1	6.6 ± 0.1	6.5 ± 0.1	6.4 ± 0.1	< 0.1	Nb, Ni

Table 22: Average alloys composition, p-XRF measurements (in wt.%; average on 3 measurements; -: non detected)

The percentage error on each principal alloying element is presented Appendix 8.

The major part of specimens shows a relative error on the chemical composition lower to 10%. Specimens 16-108 (Cu Pb20), 1-6 (Cu Zn10 Pb10) and 3-34 (Cu Sn6.7 Zn6.7 Pb6.7) have lower contents in alloying elements than expected while specimens 2-22 (Cu Zn6.7 Pb6.7), 7-56 and 17-112 (Cu Sn6.7 Zn6.7) show higher contents in alloying elements.

4.2.2) Microstructure

4.2.2.1) Pure copper A

For this composition:

- two ingots have been cast in steel (samples 3-30 and 20-34), respectively with the highest (+ 75 °C) and lowest (+ 25 °C) levels of superheat;
- one ingot has been cast in clay (sample 6-50) with an intermediate level of superheat (+ 50 °C).

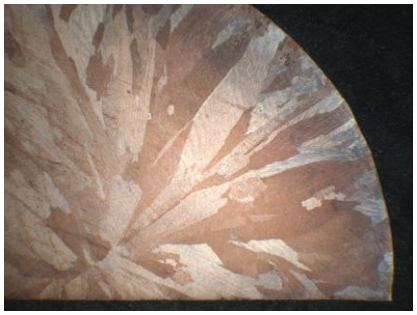

Figure 67: Sample 3-30 (Cu, Steel, +25°C)(Stereo, 9X)

Figure 68: Sample 20-34 (Cu, Steel, +75°C)(Stereo, 6X)

The ingots cast in steel show homogeneous microstructures and no structural defects can be observed. In both cases, two main zones are well visible in the radial section: the chill and columnar zones.

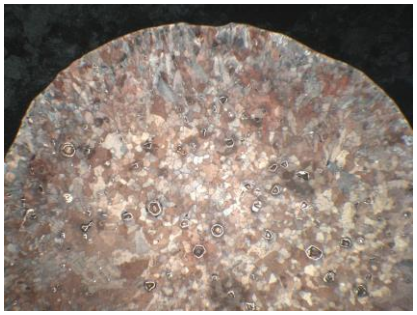

Figure 69: Sample 6-50 (Cu, Clay, +50°C)(Stereo, 6X)

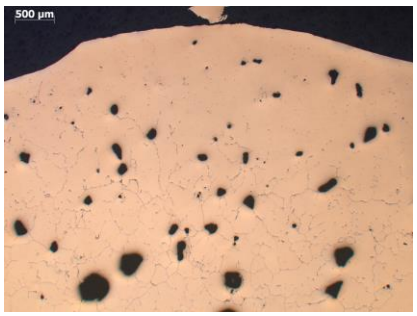

Figure 70: Sample 6-50 (Cu, Clay, +50°C)(LOM, 25X)

The ingot cast in clay presents a high quantity of rounded porosities (+++), which have larger dimensions in the ingot's center than in surface. Inclusions of copper oxide (Cu_2O) are present all over the radial section.

The etched surface shows an equiaxed microstructure in which dendrites are visible. Small chill and columnar zones are noticeable.

The grain size and porosity measurements are presented in Table 23. The difference of superheat between the two samples cast in steel mould do not have a significant impact on the specimen macrostructural features.

Composition	*Sample*	*Mould, Superheat*	*Porosity*	*SDAS (µm)*	*Average Grain Size (mm)*		*Length of ingot's zones (mm)*
Cu (A)	3 – 30	Steel, +25 °C	+	n.m.	*Chill*	0.9 ± 0.3	1.2 ± 0.5
					Columnar	4.2 ± 1.4	8.5 ± 0.6
					Equiaxed	0	0
	20 – 34	Steel, +75 °C	+	n.m.	*Chill*	0.6 ± 0.1	1.4 ± 0.3
					Columnar	4.9 ± 2.3	8.3 ± 0.5
					Equiaxed	0	0
	6 – 50	Clay, +50 °C	+++	80 ± 9	*Chill*	0.1 ± > 0.1	0.6 ± 0.1
					Columnar	0.9 ± 0.2	1.4 ± 0.4
					Equiaxed	0.2 ± > 0.1	7.0 ± 0.5

Table 23: Macroscopic measurements for the samples of composition A (n.m: non measurable)

4.2.2.2) Binary bronzes Cu – Sn

For this system, two compositions with respectively 20 wt. % and 10 wt. % of tin have been tested in the different moulds:

- Composition CuSn20
  Five ingots have been cast in the three different moulds with the same level of superheat (+ 75 °C): samples 11-3, 19-8 and 19-8R in steel, sample 17-16 in clay and sample 22-27 in sand.

- Composition CuSn10
  Four ingots have been cast in the three different moulds with the same level of superheat (+ 25 °C): sample 15-88 and 14-82 in steel, sample D_{hl} in clay and sample 13-102 in sand.

The nine specimens are composed by a dendritic primary phase made of solid solution α, and an eutectoid constituent in the interdendritic spaces.

The ingots cast in steel show a higher amount of secondary phase, than ingots cast in insulating moulds, which are similar between them. They also appear more heterogeneous, as shown by SDAS and secondary phase measurements (Table 24).

The sample 19-8 cast in steel also show few rounded porosities but wide shrinkage cavities in the ingot's center, whereas the samples cast in insulating mould only present rounded porosities due to gas. The volume percentage of porosity in the ingot cast in clay mould is significantly higher than in the ingot cast in sand mould. Even if the sample cast in clay mould seems to present a higher porosity due to gas, the difference is not significant.

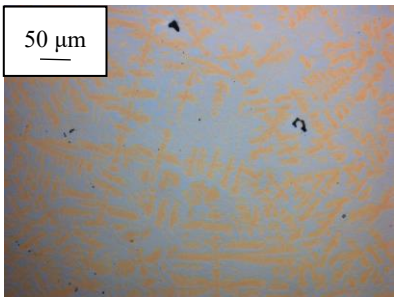

Figure 71: Sample 19-8 (CuSn20, Steel, +75 °C) (LOM, 200X)

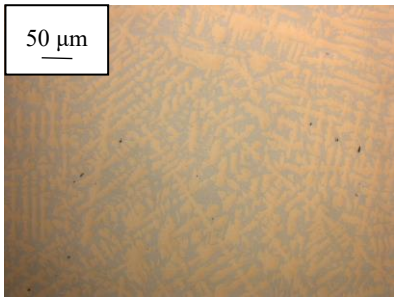

Figure 72: Sample 19-8R (CuSn20, Steel, +75 °C) (LOM, 200X)

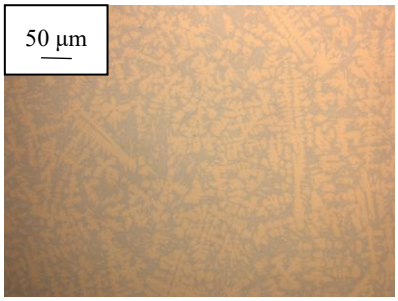

Figure 73: Sample 11-3 (CuSn20, Steel, +25 °C) (LOM, 200X)

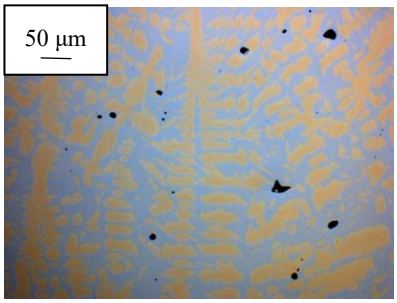

Figure 74: Sample 17-16 (CuSn20, Clay, +75 °C) (LOM, 200X)

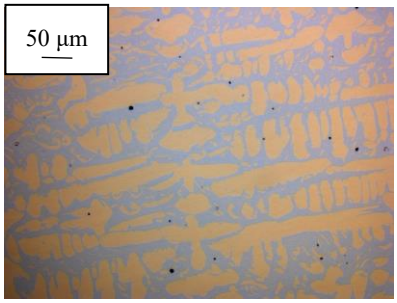

Figure 75: Sample 22-27 (CuSn20, Sand, +75 °C)(LOM, 25X)

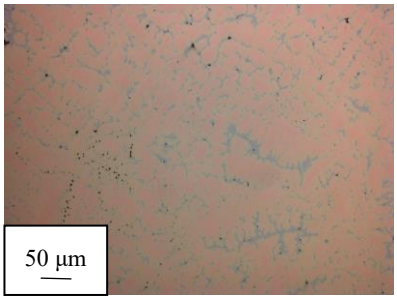

Figure 76: Sample 14 - 82 (CuSn10, Steel, +25 °C) (LOM, 200X)

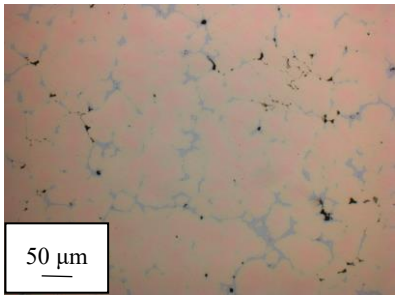

Figure 77: Sample Dhl (CuSn10, Clay, +25 °C)(LOM, 200X)

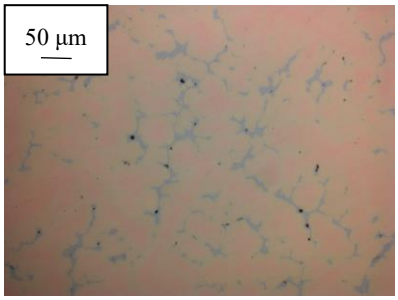

Figure 78: Sample 13 - 102 (CuSn10, Sand, +25 °C)(LOM, 200X)

The observation of the etched surfaces shows macrostructures significantly different according to the mould used for casting.

For the composition CuSn20, equiaxed grains of large dimensions compose the radial section of the ingot cast in sand (Figure 81) while the same section in the ingot cast in clay presents equiaxed grains of smaller dimensions with a small chill zone (Figure 80). The specimen cast in steel show the classical three-zones macrosctructure (Figure 79).

For the composition CuSn10, the three sections are composed by small equiaxed grains in which no columnar zone is visible (Figures 82 to 84).

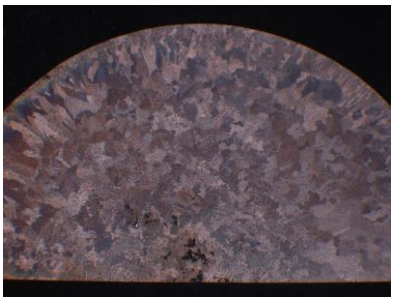

Figure 79: Sample 19-8 (Stereo, 6X)

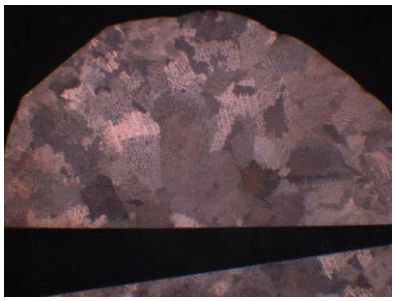

Figure 80: Sample 17-16 (Stereo, 6X)

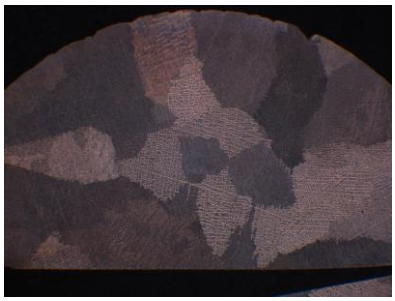

Figure 81: Sample 22-27 (Stereo, 6X)

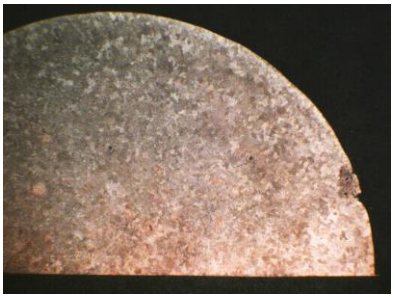

Figure 82: Sample 14-82 (Stereo, 6X)

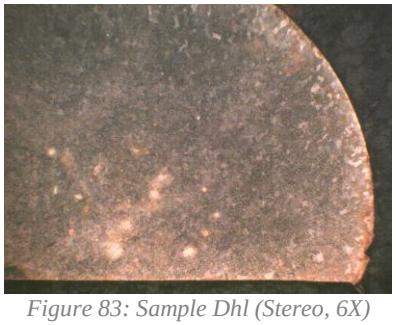

Figure 83: Sample Dhl (Stereo, 6X)

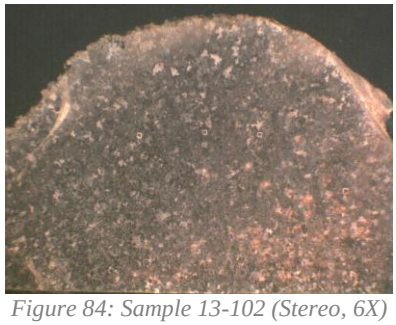

Figure 84: Sample 13-102 (Stereo, 6X)

Grain size measurements are presented Table 24. They confirm that more conductive the mould is, more the microstructure is fine and the interdendritic spacing is small. However, the more refractory the mould is, more the columnar zone in the radial section tends to disappear and the specimen is completely composed by equiaxed grains whose dimensions are deeply correlated with the cooling rate.

Composition	*Sample*	*Mould, Superheat*	*Porosity*	*SDAS (µm)*	*Secondary phase (vol. %)*	*Average Grain Size (mm)*		*Length of ingot's zones (mm)*
Cu Sn20 (B)	19 – 8	Steel, +75 °C	+	13 ± 3	49.7 ± 2.6	*Chill* *Columnar* *Equiaxed*	0.2 ± 0.1 0.9 ± 0.3 0.6 ± 0.2	0.5 ± 0.1 1.2 ± 0.3 8.1 ± 0.3
	19 – 8R	Steel, +75 °C	+	11 ± 2	44.4 ± 3.3	*Chill* *Columnar* *Equiaxed*	0.1 ± > 0.1 1.1 ± 0.3 0.5 ± 0.1	0.2 ± 0.1 1.6 ± 0.2 8.2 ± 0.1
	11 – 3	Steel + 25 °C	+	10 ± 3	44.7 ± 2.3	*Chill* *Columnar* *Equiaxed*	0.8 ± 0.2 0.7 ± 0.2 n.m.	0.5 ± 0.1 1.8 ± 0.2 7.7 ± 0.2
	17 – 16	Clay, +75 °C	++	17 ± 3	45.2 ± 2.3	*Chill* *Columnar* *Equiaxed*	0.5 ± 0.1 0.9 ± 0.3 0.6 ± 0.2	1.7 ± 0.3 0 7.6 ± 0.3
	22 – 27	Sand, +75°C	+	22 ± 4	43.5 ± 1.6	*Chill* *Columnar* *Equiaxed*	0 0 2.1 ± 0.4	0 0 10.0
Cu Sn10 (E)	14 – 82	Steel, +25 °C	+	16 ± 3	10.7 ± 2.0		n.m.	n.m.
	15 – 88	Steel, + 75 °C	+	12 ± 3	9.0 ± 1.6		n.m.	n.m.
	Dhl	Clay, +25 °C	+	30 ± 3	6.2 ± 1.1		n.m.	n.m.
	13 – 102	Sand, +25 °C	++	35 ± 3	5.3 ± 1.7		n.m.	n.m.

Table 24: Microscopic measurements for the samples of compositions B and E (n.m.: non measureable)

4.2.2.3) Binary brasses Cu – Zn

For this system, two compositions with respectively 20 wt. % and 10 wt. % of zinc have been tested in the three different moulds:

- Composition CuZn20
  Three ingots have been cast in the three different moulds and for different levels of superheat: sample DTA20 in steel (+25 °C), sample 4-38 in clay (+ 25 °C) and sample 12-93 in sand (+ 50°C);

- Composition CuZn10
  Three ingots have been cast in the three different moulds and for different levels of superheat: sample DTA10 in steel (+ 25°C), sample 8-68 in clay (+ 75 °C) and sample 13-96 in sand (+ 50°C).

The six samples are composed by the monophasic solid solution α in which microsegregation of zinc is slightly visible. Sections etching allows the observation of dendrites.

In each sample, small rounded porosities due to gas are homogeneously distributed on the observed-cross section. Only the ingot cast in the clay mould (CuZn20) shows some shrinkage cavities of large dimensions in the ingot's center.

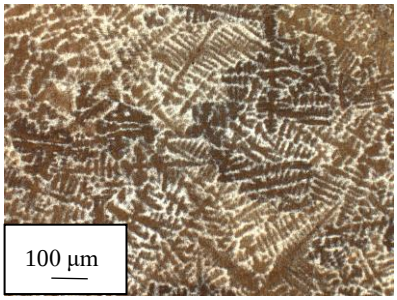

Figure 85: Sample DTA20 (CuZn20, Steel, +25 °C) (LOM, 100X)

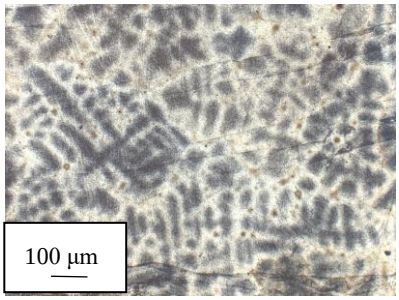

Figure 86: Sample 4-38 (CuZn20, Clay, +25 °C)(LOM, 100X)

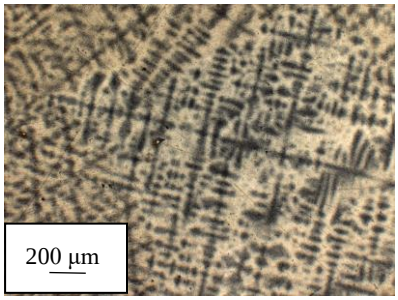

Figure 87: Sample 12-93 (CuZn20, Sand, +50 °C)(LOM, 50X)

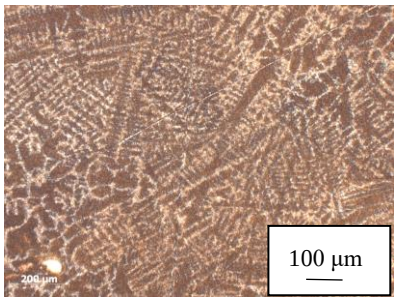

Figure 88: Sample DTA10 (CuZn10, Steelm +25 °C)(LOM, 100X)

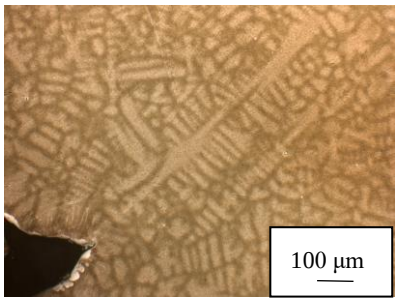

Figure 89: Sample 8-68 (CuZn10, Clay, + 75 °C)(LOM, 100X)

According to the mould used, the sections show very different macrostructures.

While the three zones (chill, columnar and equiaxed grains) are well visible for ingots cast in steel (DTA20 and DTA10), ingots cast in sand are rather composed by large equiaxed grains (12-93 and 13-96). In specimen cast in clay mould, the columnar zone can be discerned (4-38 and 8-68). Table 25 confirms that microstructure of the ingots cast in sand are coarser than those cast in steel and clay moulds.

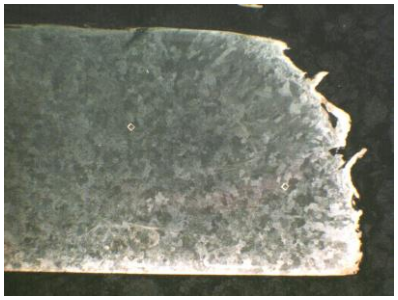

Figure 90: Sample DTA20 (Stereo, 6X)

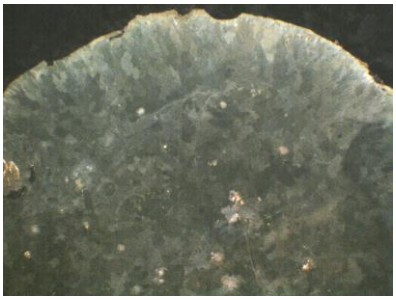

Figure 91: Sample 4-38 (Stereo, 6X)

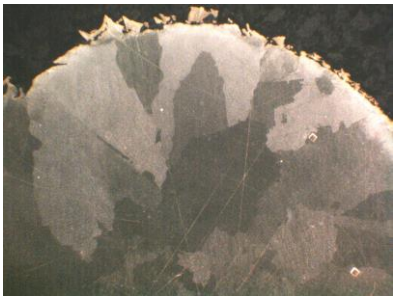

Figure 92: Sample 12-93 (Stereo, 6X)

Figure 93: Sample DTA10 (Stereo, 6X)

Figure 94: Sample 8-68 (Stereo, 6X)

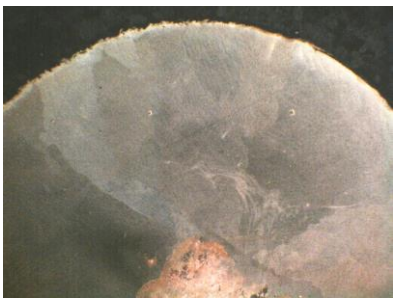

Figure 95: Sample 13-96 (Stereo, 6X)

Composition	*Sample*	*Mould, Superheat*	*Porosity*	*SDAS (µm)*	*Secondary phase (vol. %)*	*Average Grain Size (mm)*		*Length of ingot's zones (mm)*
Cu Zn20 (C)	DTA20	Steel, +75 °C	+	22 ± 2	0	*Chill* *Columnar* *Equiaxed*	0.3 ± 0.1 0.6 ± 0.1 0.3 ± 0.1	0.9 ± 0.2 1.4 ± 0.1 9.0 ± 0.2
	4-38	Steel, +75 °C	+	50 ± 3	0	*Chill* *Columnar* *Equiaxed*	0.1 ± > 0.1 0.7 ± 0.2 0.8 ± 0.1	0.4 ± 0.1 1.2 ± 0.1 9.8 ± 0.6
	12-93	Steel + 25 °C	+	68 ± 7	0	*Chill* *Columnar* *Equiaxed*	0 0 5.4 ± 1.5	0 0 10.0
Cu Zn10 (F)	DTA10	Steel, +25 °C	+	21 ± 5	0	*Chill* *Columnar* *Equiaxed*	0.5 ± 0.1 1.4 ± 0.4 0.8 ± 0.1	0.6 ± 0.1 1.6 ± 7.4 7.4 ± 0.2
	8-68	Clay + 75 °C	++	38 ± 5	0	*Chill* *Columnar* *Equiaxed*	0.2 ± 0.1 1.8 ± 0.3 1.1 ± 0.1	0.5 ± 0.1 0.9 ± 0.3 8.4 ± 0.5
	13-96	Sand, +50 °C	++	n.m.	0	*Chill* *Columnar* *Equiaxed*	0 0 5.5 ± 2.0	0 0 10.0

Table 25: Microscopic measurements for the samples of compositions C and F

4.2.2.4) Binary leaded copper Cu – Pb

For this system, two compositions with respectively 20 wt. % and 10 wt. % of lead have been tested in the different moulds:

- Composition CuPb20
  Three ingots have been cast: sample 2-58 and its replicate 2-58R in steel (+ 50°C) and sample 16-108 in sand (+ 75 °C).

- Composition CuPb10
  Four specimen have been cast for each mould and for specific level if superheat: sample 1-109 and its replicate 1-109R in steel (+ 25 °C), sample 24-123 in clay (+ 50 °C) and sample 6-129 in sand (+ 25°C).

Each specimen shows a copper-rich matrix with nodules of lead which are present in the intergranular spaces.

Samples cast in steel tend to present dendritic grains with partially recrystallized grains in some areas of the ingot.

Samples cast in insulatory moulds (clay and sand) tend to present granular microstructure over the whole radial section. Exception is done for the specimen 16-108, cast in sand, which also shows few dendritic grains and some partially recrystallized zones.

Figure 96: Sample 2-58 (CuPb20, steel, +50°C) (LOM, 100X)

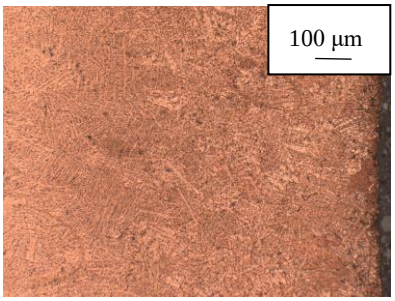

Figure 97: Sample 2-58R (CuPb20, steel, +50°C) (LOM, 100X)

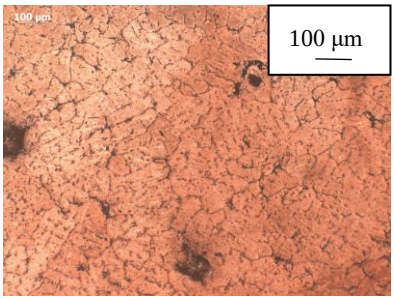

Figure 98: Sample 16-109 (CuPb20, sand, +75°C) (LOM, 100X)

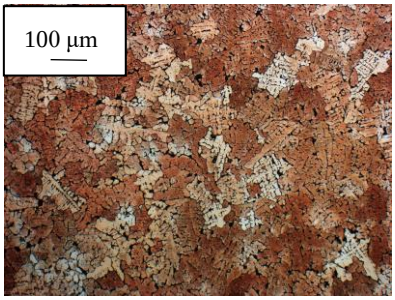

Figure 99: Sample 1-109 (CuPb10, steel, +25°C) (LOM, 100X)

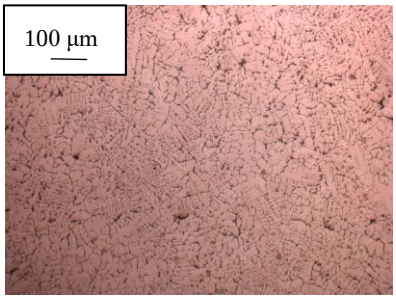

Figure 100: Sample 1-109R (CuPb10, steel, +25°C) (LOM, 100X)

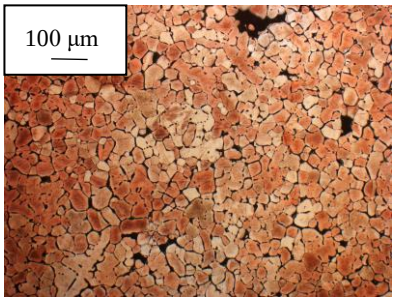

Figure 101: Sample 24-123 (CuPb10, Clay, +50°C) (LOM, 100X)

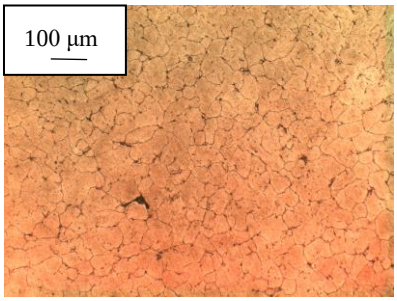

Figure 102: Sample 6-129 (CuPb10, Sand, +25°C) (LOM, 100X)

Even if no specific ingot zone can be identified, it can be noted that grains in border of ingot are smaller than in the center. This is particularly the case for samples cast in steel and in sand.

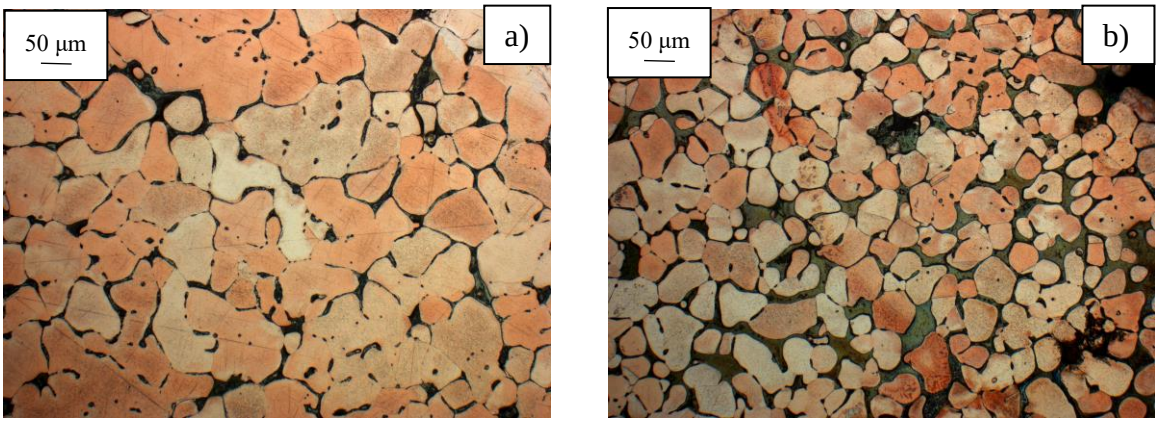

Figure 103: Sample 6-129 (LOM, 200X): a) center of the ingot, b) border of the ingot

Table 26 displays the quantitative microstructural features.

Composition	*Sample*	*Mould, Superheat*	*Porosity*	*SDAS*	*Average Grain Size (µm)*
CuPb20 (D)	2_58	Steel, +50 °C	+	6 ± 1	*Recryst.* 18.1 ± 6.0 *Dendrit.* 147.6 ± 19.0
	2_58R (26_60)	Steel, +50 °C	+	8 ± 1	*Recryst.* 13.3 ± 0.3 *Dendrit.* 101.1 ± 21.9
	16_108	Sand, +75 °C	+++	30 ± 2	*Recryst.* 50,1 ± 10,8 *Dendrit.* 271,4 ± 67,7
CuPb10 (G)	1_109	Steel, +25 °C	+	10 ± 1	*Recryst.* 68.5 ± 26.1 *Dendrit.* 166.2 ± 32.7
	1_109R	Steel, +25 °C	+	10 ± 1	*Recryst.* 29.6 ± 4.0 *Dendrit.* 107.7 ± 2.1
	6_129	Clay, +50 °C	+++	-	*Center* 36.3 ± 3.4 *Border* 36,3 ± 1,3
	24_123	Sand, +25 °C	++	-	*Center* 69.4 ± 3.7 *Border* 33.4 ± 4.1

Table 26: Metallographic measurements for the samples of compositions D and G

4.2.2.5) Ternary leaded bronze Cu – Sn – Pb

For this system, two compositions with respectively 10 wt. % and 6.7 wt. % of alloying elements have been tested in the three different moulds:

- Composition CuSn10Pb10
  Three ingots have been cast in the three different moulds and for different levels of superheat: sample 18-144 in steel (+ 75 °C), sample 4-146 in clay (+ 25 °C) and sample 28-154 in sand (+ 25 °C);

- Composition CuSn6.7Pb6.7
  Two ingots have been cast in steel (sample 7-164) and clay (sample 5-47) for the same level of superheat (+ 25°C).

The specimen show a typical biphasic microstructure composed by the primary solid solution α and the secondary phase in the interdendritic spaces. Lead nodules are also widely present in these spaces all over the section.

The microstructure is coarser for ingots cast in insulatory moulds than those cast in steel mould and characterized by a strong intern porosity (gas).

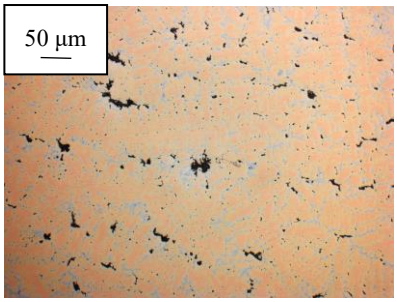

Figure 104: Sample 18-144 (CuSn10Pb100, Steel, +75 °C) (LOM, 200X)

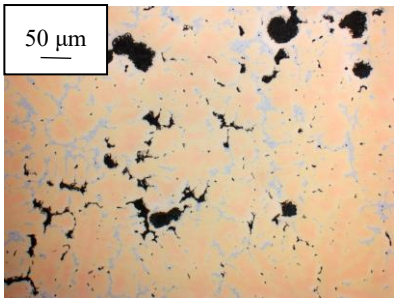

Figure 105: Sample 4-146 (CuSn10Pb10, Clay, +25°C) (LOM, 200X)

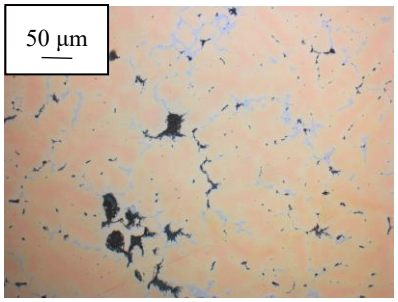

Figure 106: Sample 28-154 (CuSn10Pb10, Sand, +25 °C) (LOM, 200X)

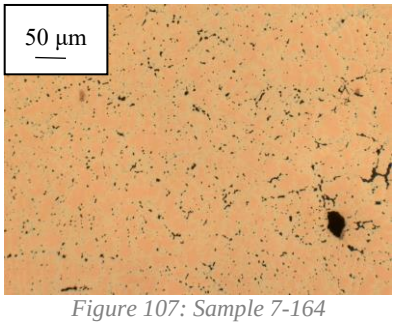

Figure 107: Sample 7-164 (CuSn6.7Pb6.7, Clay, +25 °C) (LOM, 200X)

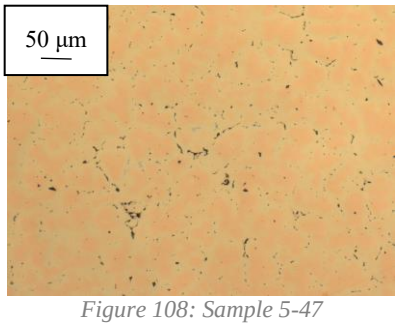

Figure 108: Sample 5-47 (CuSn6.7Pb6.7, Sand, +25 °C) (LOM, 200X)

The observation of the etched surfaces show that the specimens are composed by a dendritic primary microstructure with partially recrystallized grains.

The ingots cast in steel have a dendritic microstructure for which the determination grain size is not possible.

Only the specimen 28-154 show completely recrystallized grain in the ingots borders.

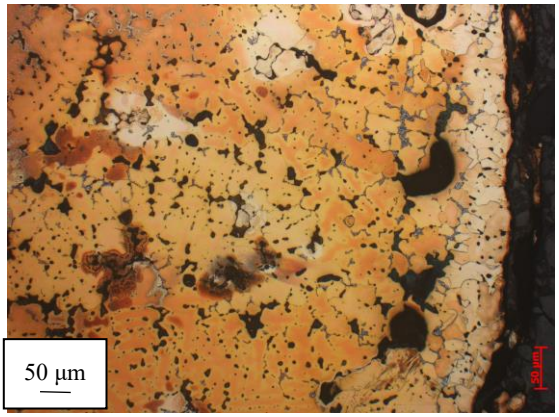

Figure 109: Sample 18-144 (LOM, 200X)

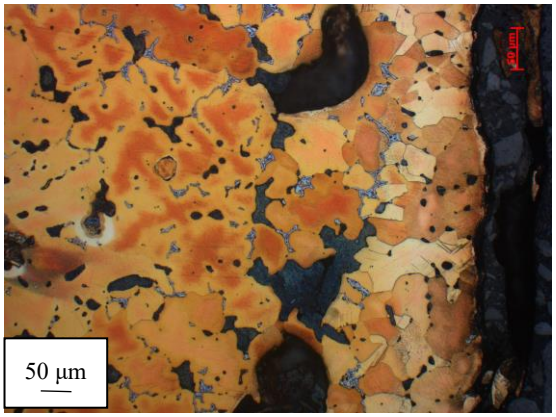

Figure 110: Sample 28-154 (LOM, 200X)

Table 27 reports the measurements on quantitative microstructural features.

Composition	*Sample*	*Mould, Superheat*	*Porosity*	*SDAS (µm)*	*Secondary phase (vol. %)*	*Average Grain Size (mm)*		*Length of ingot's zones (mm)*
Cu Sn10Pb10 (I)	18-144	Steel, +75 °C	+	15 ± 3	12.4 ± 5.0	*Chill* *Columnar* *Equiaxed*	0.1 ± > 0.1 0 0.3 ± 0.1	
	4-146	Clay, +25 °C	++	24 ± 5	6.2 ± 2.6	*Chill* *Columnar* *Equiaxed*	0.1 ± > 0.1 0 n.m.	
	28-154	Sand + 25 °C	+	30 ± 5	6.1 ± 2.7	*Recryst.* *Dendrit.*	0.08 ± 0.03 0.3 ± 0.1	-
Cu Sn6.7Pb6.7 (L)	7-164	Steel, +25 °C	+	13 ± 2	3.0 ± 1.2	*Chill* *Columnar* *Equiaxed*	0 0 n.m.	0 0 n.m.
	5-47	Clay, + 25 °C	++	21 ± 2	1.0 ± 0.4	*Dendrit partially recryst..*	0.1 ± > 0.1	-

Table 27: Metallographic measurements for the samples of compositions I and L (n.m.: non measurable)

4.2.2.6) Ternary leaded brass Cu – Zn – Pb

For this system, two compositions with respectively 10 wt. % and 6.7 wt. % of alloying elements have been tested in the three different moulds:

- Composition CuZn10Pb10
  Two ingots have been cast either in steel (sample 1-6), with the lowest superheat level (+ 25 °C), or in sand (sample 14-100) with an intermediate level of superheat (+ 50 °C);

- Composition CuZn6.7Pb6.7
  Two ingots have been cast either in steel (sample 2-22) with an intermediate level of superheat, or in clay (sample 10-74) for the highest level of superheat (+ 75°C).

The four specimen are composed the monophasic solid solution α with lead nodules in the interdendritic spaces.

The ingots cast in steel show dendritic grains in which the three characteristic ingots zone are visible. In the sample 1-6, a strong macrosegregation is visible in the ingot's center where the presence of non-alloyed copper is noticeable.

The ingot cast in clay has completely recrystallized grains.

The ingot cast in sand presents partially recrystallized grains and is composed by large equiaxed grains.

No specific porosity is observed, except for the sample cast in clay, which present an important porosity due to gas evacuation in the ingot center.

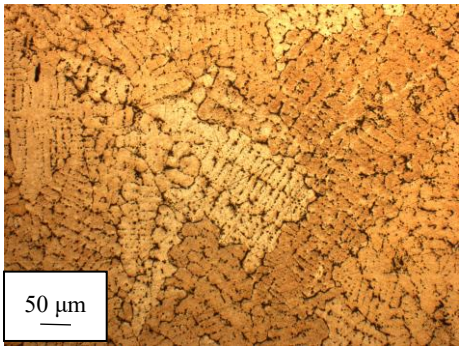

Figure 111: Sample 1-6 (CuZn10Pb10, Steel, +25 °C)(LOM, 200X)

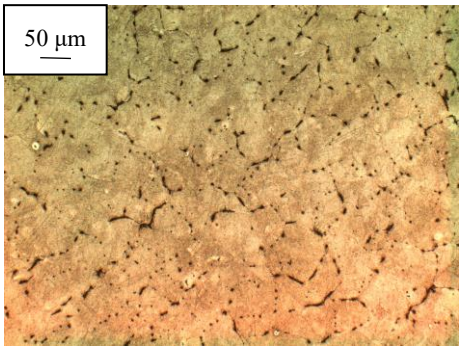

Figure 112: Sample 14-100 (CuZn10Pb10, Sand, +50 °C)(LOM, 200X)

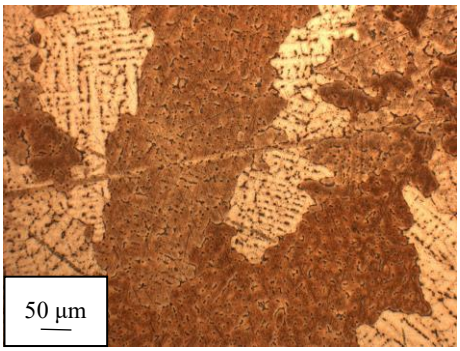

Figure 113: Sample 2-22 (CuZn6.7Pb6.7, Steel, + 50 °C) (LOM, 200X)

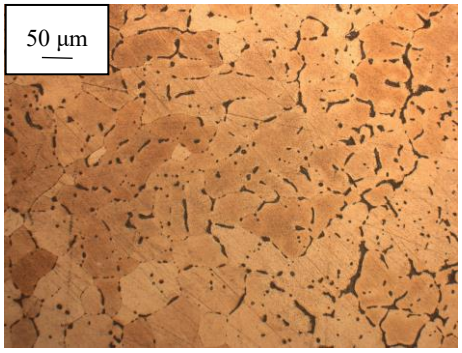

Figure 114: Sample 10-74 (CuZn6.7Pb6.7, Clay, +75 °C) (LOM, 200X)

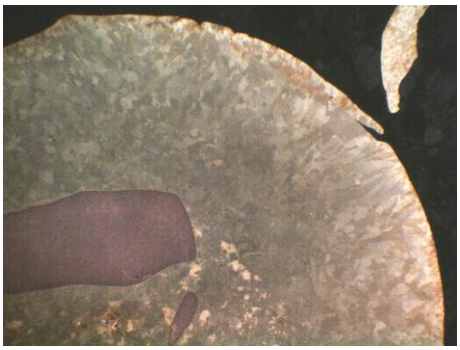

Figure 115: Sample 1-6 ((Stereo, 6X)

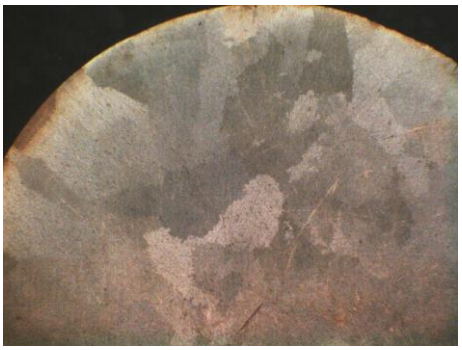

Figure 116: Sample 14-100 (Stereo, 6X)

Table 28 reports measurements on dendritic arms and grain size.

Composition	*Sample*	*Mould, Superheat*	*Porosity*	*SDAS (µm)*	*Secondary phase (vol. %)*	*Average Grain Size (mm)*		*Length of ingot's zones (mm)*
Cu Zn10Pb10 (J)	1-6	Steel, +25 °C	+	12 ± 1	0	*Chill* *Columnar* *Equiaxed*		0.3 ± 0.1 1.1 ± 0.3 9.6 ± 0.3
	14-100	Sand, +50 °C	+	28 ± 1	0	*Chill* *Columnar* *Equiaxed*	0 0 3.0 ± 0.5	0 0 10.0
Cu Zn6.7Pb6.7 (M)	2-22	Steel, +50 °C	+	17 ± 1	0	*Chill* *Columnar* *Equiaxed*	0.3 ± 0.1 0.4 ± 0.1 0.4 ± 0.1	0.5 ± 0.1 0.9 ± 0.1 8.8 ± 0.1
	10-74	Clay, + 75 °C	++	n.m.	0	*Recryst.*	47.3 ± 0.1	-

Table 28: Macroscopic measurements for the samples of compositions J and M (n.m.: non measurable)

4.2.2.7) Ternary gunmetal Cu – Sn – Zn

For this system, two compositions with respectively 10 wt. % and 6.7 wt. % of alloying elements have been tested in the three different moulds:

- Composition CuSn10Zn10
  Two ingots have been cast either in clay mould (sample 7_56) with an intermediate superheat level (+ 50 °C), or in sand (sample 17_112) with the highest level of superheat (+ 75 °C).

- Composition CuSn6.7Zn6.7
  Two ingots have been cast either in clay mould (sample 9_73) with the highest level of superheat (+ 75 °C), or in sand (sample 15-101) with an intermediate level of superheat (+ 50 °C).

The four specimen present a biphasic microstructure composed by primary dendrite of the solid solution α , and a secondary phase in the interdendritic spaces. No intern porosity is observed.

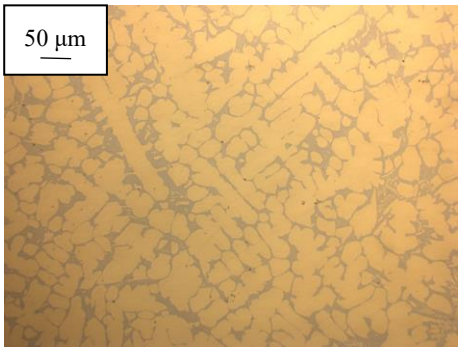

Figure 117: Sample 7-56
(CuSn10Zn10, Clay, +50°C)(LOM, 200X)

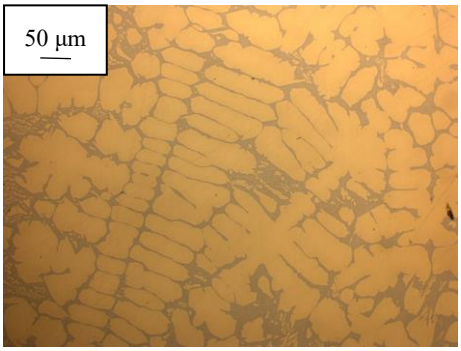

Figure 118: Sample 17-100
(CuSn10Zn10, Sand, +75°C) (LOM, 200X)

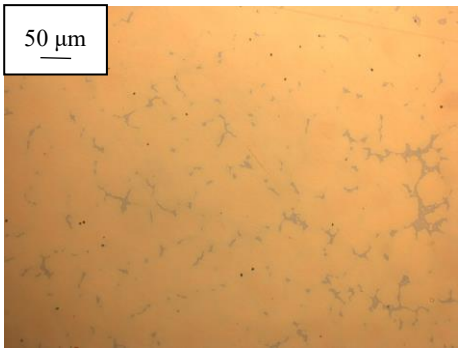

Figure 119: Sample 9-73
(CuSn6.7Zn6.7, Clay, +75 °C)(LOM, 200X)

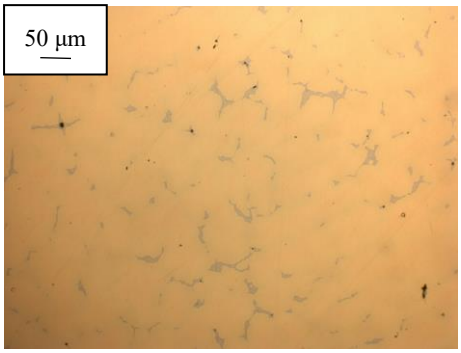

Figure 120: Sample 15-101
(CuSn6.7Zn6.7,Sand, +50°C) (LOM, 200X)

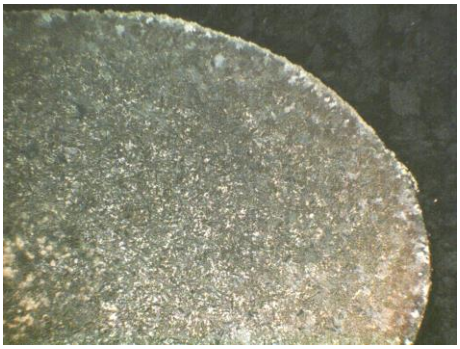

Figure 121: Sample 7-56 (Stereo, 6X)

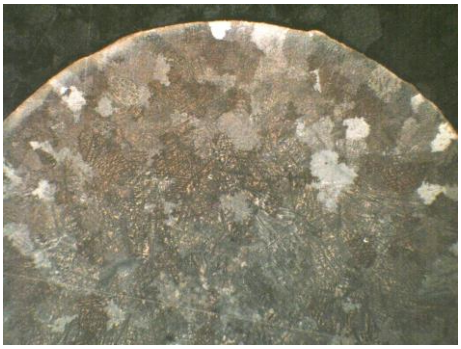

Figure 122: Sample 17-100 (Stereo, 6X)

Table 29 displays the quantitative microstructural features.

Composition	*Sample*	*Mould, Superheat*	*Porosity*	*SDAS (μm)*	*Secondary phase (vol. %)*	*Average Grain Size (mm)*		*Length of ingot's zones (mm)*
Cu Sn10Zn10 (H)	7-56	Clay, +50 °C	+	17 ± 1	28.2 ± 1.9	*Chill* *Columnar* *Equiaxed*		0.3 ± 0.1 1.1 ± 0.3 9.6 ± 0.3
	17-112	Sand, +75 °C	+	23 ± 2	27.9 ± 3.4	*Chill* *Columnar* *Equiaxed*	0 0 3.0 ± 0.5	0 0 10.0
Cu Sn6.7Zn6.7 (K)	9-73	Clay, +75 °C	+	31 ± 5	3.0 ± 0.9	*Chill* *Columnar* *Equiaxed*	0.6 ± 0.1 0.7 ± 0.1 0.4 ± 0.1	0.8 ± 0.1 0.9 ± 0.1 8.8 ± 0.1
	15-101	Sand, + 50 °C	++	35 ± 5	2.1 ± 0.6	*Recryst.*	47.3 ± 0.1	-

Table 29: Macroscopic measurements for the samples of compositions J and M (n.m.: non measurable)

4.2.2.8) Quaternary leaded gunmetal Cu – Sn – Zn – Pb

For this system, one composition has been selected, with 6.7 wt. % of each alloying element.

Two ingots have been cast, either in steel (sample 3-34) or in sand (sample 11-89) with respectively the highest (+ 75 °C) and the lowest level of superheat (+ 25°C).

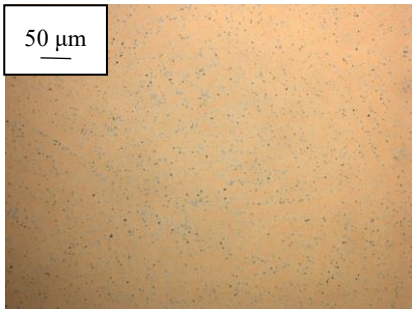

Figure 123: Sample 3-34 (CuSn6.7Zn6.7Pb6.7, Steel, +75 °C) (LOM, 200X)

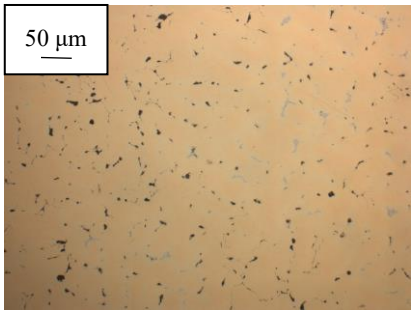

Figure 124: Sample 11-89 (CuSn6.7Zn6.7Pb6.7, Sand, +25 °C) (LOM, 200X)

The two specimens show biphasic microstructures composed by primary α dendrite and a secondary phase in the interdendritic spaces.

Lead is also present as nodules in these spaces.

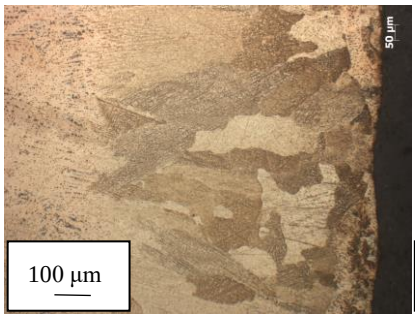

Figure 125: Sample 3-34 (CuSn6.7Zn6.7Pb6.7, Steel, +75 °C) (LOM, 100X)

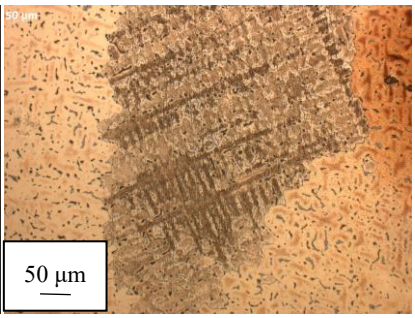

Figure 126: Sample 11-89 (CuSn6.7Zn6.7Pb6.7, Sand, +25 °C) (LOM, 100X)

While the three zones chill, columnar and equiaxed zones are visible on the specimen cast in steel, the ingot cast in sand is rather composed by large equiaxed grains.

Table 30 reports measurements on dendritic arms and grain size.

Composition	*Sample*	*Mould, Superheat*	*Porosity*	*SDAS (µm)*	*Secondary phase (vol. %)*	*Average Grain Size (mm)*	*Length of ingot's zones (mm)*
Cu Sn6.7Zn6.7Pb6.7 (N)	3-34	Steel, +75 °C	++	19 ± 1	5.9 ± 2.0	*Chill*	0.05 ± 0.01
						Columnar	0.3 ± 0.1
						Equiaxed	
	11-89	Sand, +25 °C	++	30 ± 1	3.8 ± 0.4	*Chill*	0
						Columnar	0
						Equiaxed	2.3 ± 0.2

Table 30: Macroscopic measurements for the samples of compositions N

4.2.3) Hardness

Tables 31, 32 and 33 respectively presents the hardness values of the DoE samples, replicate samples and samples of verification.

Composition		*Sample*	*Mould*	*Superheat*	*Hardness*
A	Cu 100	3 - 30	Steel	+ 25°C	57,7 ± 3,6
		20 - 34	Steel	+ 75°C	69,5 ± 3,5
		6 - 50	Clay	+ 50°C	39,9 ± 4,1
B	Cu Sn20	11 - 3	Steel	+ 25°C	248,7 ± 2,0
		19 - 8	Steel	+ 75°C	240,6 ± 1,2
		17 - 16	Clay	+ 75°C	228,7 ± 3,3
		22 - 27	Sand	+ 75°C	222,7 ± 4,7
C	Cu Zn20	4 - 38	Clay	+ 25°C	89,6 ± 3,5
		12 - 93	Sand	+ 50°C	82,6 ± 1,4
D	Cu Pb20	2 - 58	Steel	+ 50°C	49,8 ± 2,5
		16 - 108	Sand	+ 75°C	31,8 ± 7,8
E	Cu Sn10	13 - 102	Sand	+ 25°C	121,6 ± 0,5
		14 - 82	Steel	+ 25°C	120,2 ± 2,8
		15 - 88	Steel	+ 75°C	124,7 ± 3,3
F	Cu Zn10	8 - 68	Clay	+ 75°C	73,6 ± 3,7
		13 - 96	Sand	+ 50°C	82,6 ± 4,5
G	Cu Pb10	1 - 109	Steel	+ 25°C	51,8 ± 3,6
		6 - 129	Sand	+ 25°C	48,3 ± 3,8
		24 - 123	Clay	+ 50°C	49,4 ± 2,6
H	Cu Sn10 Zn10	7 - 56	Clay	+ 50°C	192,2 ± 3,9
		17 - 112	Sand	+ 75°C	204,3 ± 3,9
I	Cu Sn10 Pb10	4 - 146	Clay	+ 25°C	96,6 ± 4,2
		18 - 144	Steel	+ 75°C	108,7 ± 2,5
		28 - 154	Sand	+ 25°C	118,4 ± 3,7
J	Cu Zn10 Pb10	1 - 6	Steel	+ 25°C	55,1 ± 0,3
		14 - 100	Sand	+ 50°C	54,3 ± 0,2
K	Cu Sn6.7 Zn6.7	9 - 73	Clay	+ 75°C	74,9 ± 5,3
		15 - 101	Sand	+ 50°C	92,3 ± 1,9
L	Cu Sn6.7 Pb6.7	7 - 164	Steel	+ 25°C	91,0 ± 1,7
		5 - 47	Clay	**+ 25°C**	75,8 ± 3,1
M	Cu Zn6.7 Pb6.7	2 - 22	Steel	+ 50°C	57,1 ± 2,1
		10 - 74	Clay	**+ 75°C**	66,9 ± 2,8
N	Cu Sn6.7 Zn6.7 Pb6.7	3 - 34	Steel	+ 75°C	99,3 ± 0,7
		11 - 89	Sand	+ 25°C	84,1 ± 4,8

Table 31: Averaged hardness values with relative deviation standard of the DoE samples

Composition		Sample	Mould	Superheat	Hardness
B	Cu Sn20	19 - 8R	Steel	+ 75°C	239.9 ± 2,6
D	Cu Pb20	26 - 60 (2 - 58R)	Steel	+ 50°C	57,5 ± 3,3
G	Cu Pb10	1 - 109R	Steel	+ 25°C	51,1 ± 3,1

Table 32: Averaged hardness values with relative deviation standard of the replicate samples

Composition		Sample	Mould	Superheat	Hardness
C	Cu Zn20	DTA 20	Steel	+ 25°C	98,5 ± 0,9
E	Cu Sn10	D_{hl}	Clay	+ 25°C	*missing data*
F	Cu Zn10	DTA 10	Steel	+ 25°C	84,2 ± 3,1

Table 33: Averaged hardness values with relative deviation standard of the verification samples

As expected, alloying elements have a strong impact on hardness. While lead addition systematically makes the hardness of the alloy decrease, the addition of tin or zinc hardens the material.

For the same weight percentage, tin has however a stronger effect than zinc. Indeed tin atoms being much larger (118.7 u) than zinc atoms (65.4 u), the lattice deformation of copper is major with tin than zinc, even if the atomic fraction is lower. Furthermore, as said before, from 10 wt. % of tin in the matrix the hard secondary (α+δ) phase appears while brasses are composed by the solid solution (α) softer.

Since lead is insoluble in the copper matrix and segregates in the grain boundaries of the materials, it strongly affect the hardness of copper-based alloys.

Process parameters also have a slight effect on hardness values.

Materials cast in refractory mould is almost systematically softer than materials cast in steel mould. This can be due to the higher microporosity and grain size in clay and sand moulded ingots. In the case of bronze, the higher hardness of steel mould ingots is also due to the early formation of hard secondary phase (α+δ) with higher cooling rate.

Superheat seems to have a little effect on hardness as visible in samples 3-30 and 20-34 for pure copper, 11-3 and 19-8 for CuSn20, 14-82 and 15-88. A higher superheat seems to imply a higher hardness, but this point need to be further investigated to be concluded.

The influence of alloying elements and their contents in the alloy appears major than the influence of process parameters such as the mould material and the superheat.

4.2.4) Correlations between variables: Principal Component Analysis

The computation of the experimental matrix of responses Y is achieved over 5 principal components, with a total explained variance of 90.4 % (Figure 127). Appendix 9 details the experimental matrix.

The first two components are chosen for this analysis since they cover a cumulative explained variance of 63.9 %.

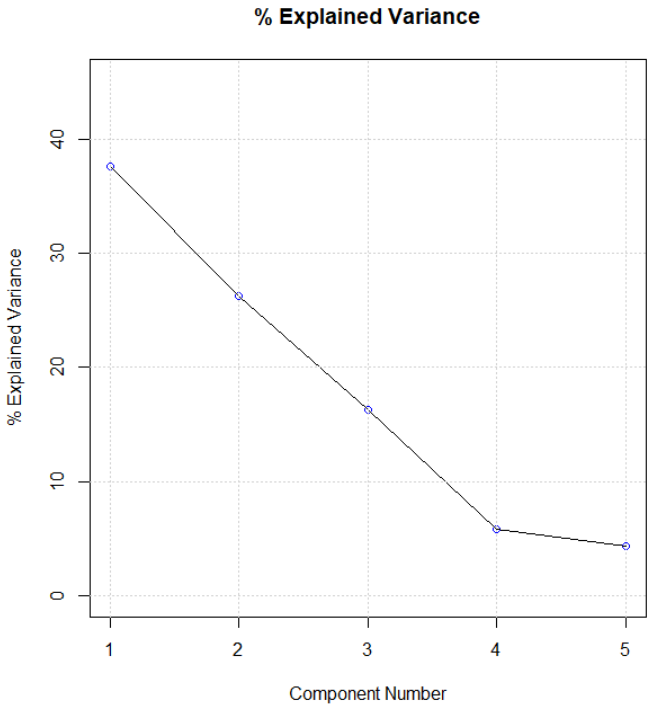

Figure 127: Explained variance for 5 principal components

On one hand, the loading plot allows the easy visualization and verification of correlations existing between the selected quantitative responses (Figure 128).

The following observations can be done:

- The deep correlation between the volume percentage of secondary phase and the hardness of the material is well visible according both first and second components (blue cluster). Indeed, the eutectoid constituent (α+δ), which composes the secondary phase, is harder than the α-solid solution and is responsible for the material hardness increase. These responses are correlated to the tin amount.

- The length of each ingot's zone is directly correlated to the respective average grain size according to both constituents, except for the equiaxed area whose average grain size is rather connected to the average size of recrystallized grains. This can be explained by two phenomena:

  1) The presence of recrystallized grains, and if any mechanic deformation is applied, always implies a complete equiaxed microstructure. These responses are correlated to the lead amount;

  2) The length of the equiaxed zone can be connected to other parameters, like the length of the two other zones (chill and columnar), as seen in black on the loading plot (opposite correlation), or the amount of some alloying elements, like lead.

– The Secondary Dendrite Arm Spacing seems to be correlated with the average grain size of both recrystallized and equiaxed grains. Indeed the presence of recrystallized grain corresponds to a better diffusion of alloying elements in the copper-matrix, a dissolution of the secondary phase in the interdendritic spaces and a lower microsegregation of the solid solution. These responses are correlated to the amount of lead, which acts as grain refiner and favours the formation of equiaxed grains. A correlation with the zinc amount is also visible, since this element is completely soluble in the α-solid solution for the considered composition range (0 – 20 wt. %).

As a result of grain refinement, the dendrites are larger since no secondary phase is present to act as dendrite refiner. The opposite correlation of SDAS with secondary phase, and thus hardness, is confirmed in Figure 128.

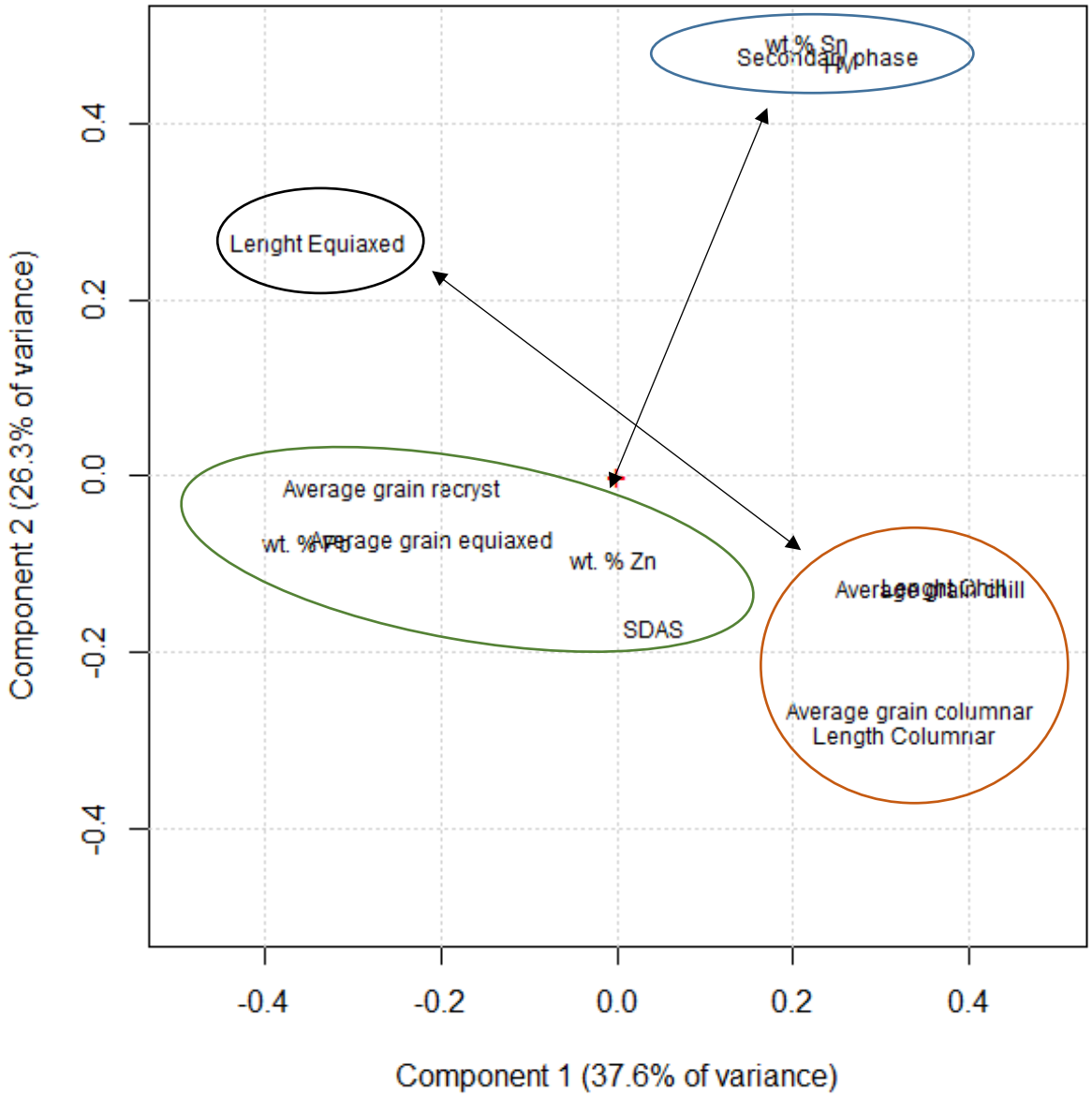

Figure 128: Loading plot (63.9 % of total explained variance)

On a second hand, the score plots are used in order to visualize correlations existing between the considered samples in relation with the two main components (Figure 129).

The clusters of composition are well identifiable. This means that the samples of same composition (i.e. same alloy family) show similar properties;

However, exceptions are visible and which can be explained by:

- A compositional gap due to experimental variability between the samples of a same alloy family: case of samples 10-74 and 2-22 (Cu Sn6.7 Pb6.7);
- Different microstructural features: case of 13-96 (CuZn10), and 6-50 (Cu).

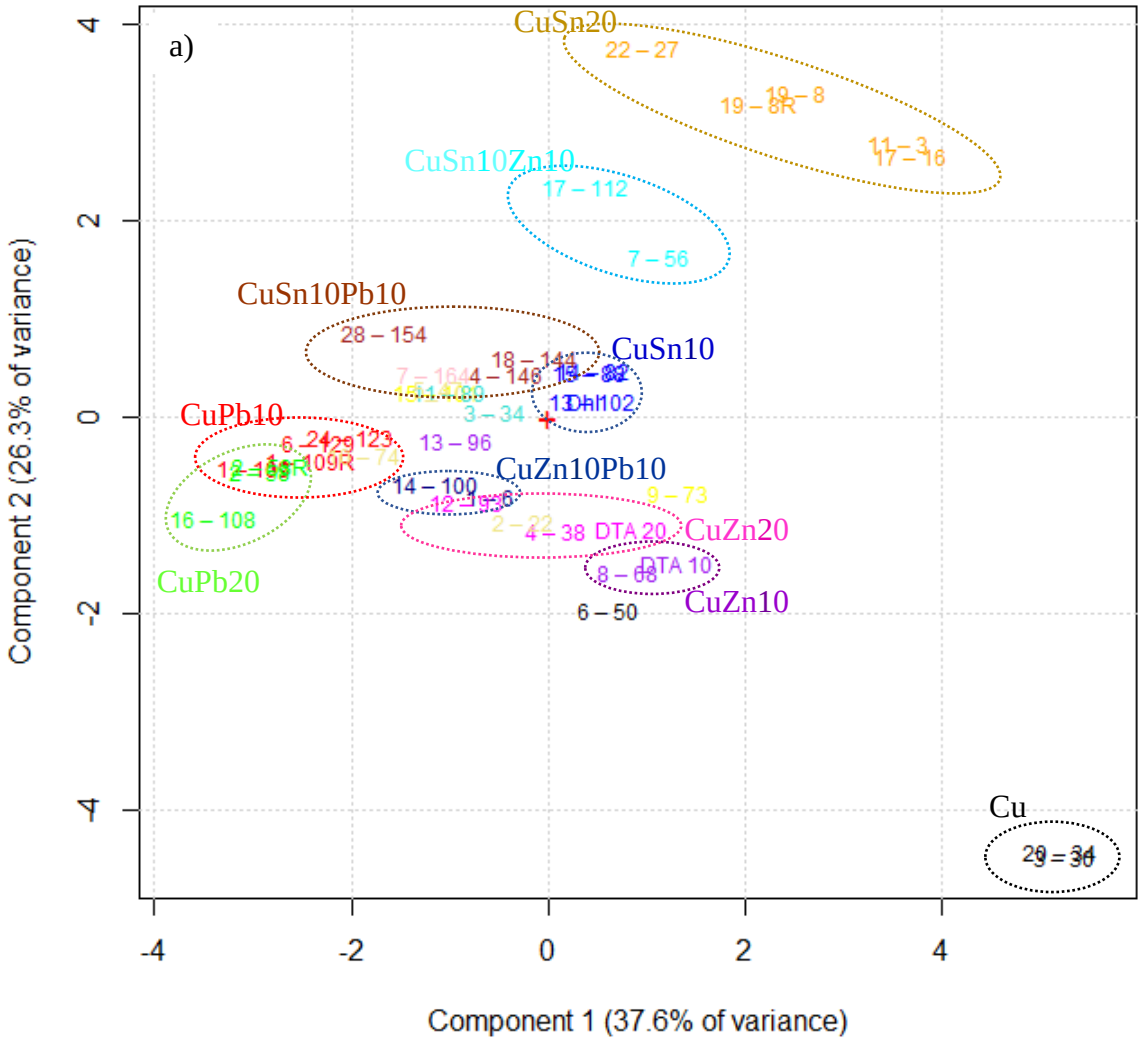

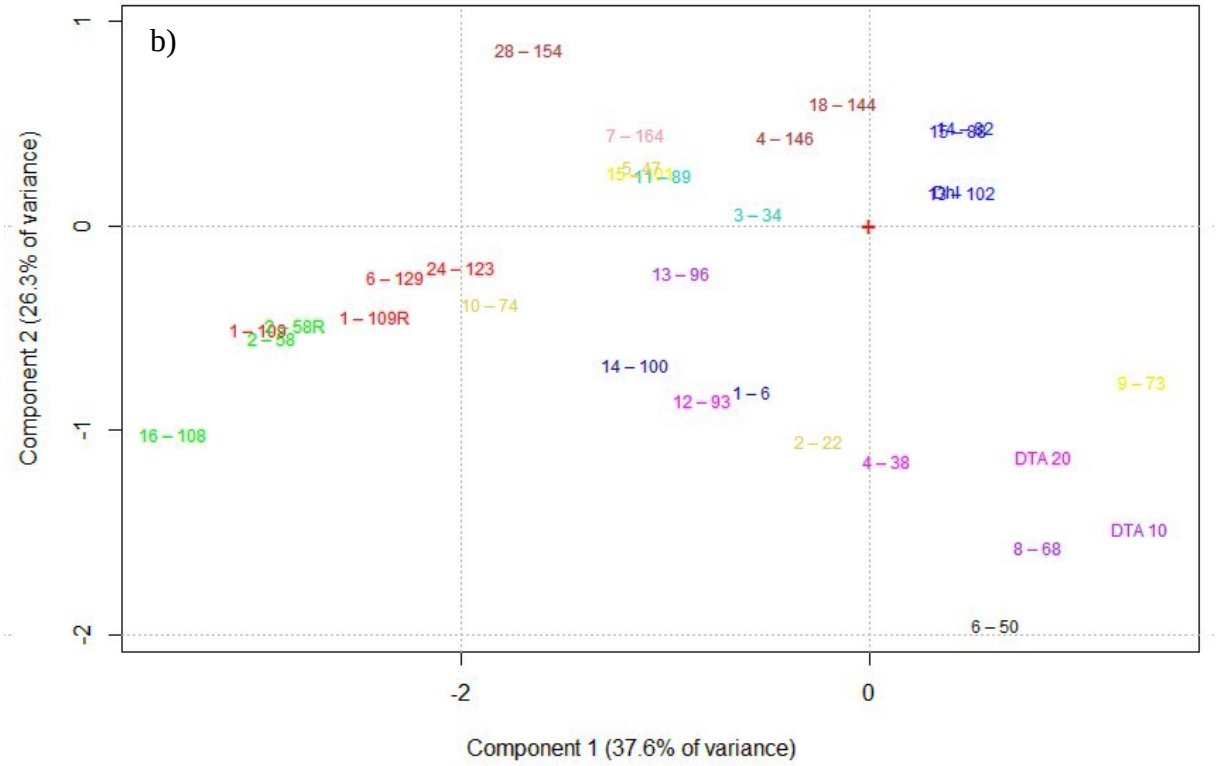

Figure 129: Score plot (63.9 % of total explained variance) in correlation with the alloys family. a) *Full plot, b) Zoom*

Black = Cu; Orange = CuSn20; Blue = CuSn10; Pink = CuZn20; Violet = CuZn10; Green = CuPb20; Red =CuPb10; Brown = CuSn10Pb10; Pale pink = CuSn6.7Pb6.7; Delft Blue = CuZn10Pb10; Beige = CuZn6.7Pb6.7; Light blue = CuSn10Zn10 and CuSn6.7Zn6.7Pb6.7; Yellow = CuSn6.7Zn6.7.

4.2.5) Predictive models: Experimental Design Modelling

As explained in previous sections, the model of experimental design is composed by 18 terms: 6 terms related to the binary mixtures, 2 terms related to the qualitative variables, 4 related to the ternary mixtures, and 2 terms related to the linear and quadratic effect of the quantifiable variable.

As a reminder of equation 10:

$$Y = \alpha_{PCA} X_{PCA} + \alpha_{PCB} X_{PCB} + \alpha_{PCC} X_{PCC} + \alpha_{PCD} X_{PCD} + \alpha_{PCA*PCB} X_{PCA*PCB}$$

$$+ \alpha_1 X_1 + \alpha_{S1} X_{S1} + \alpha_{S2} X_{S2} + \alpha_{PCA*PCC} X_{PCA*PCC} + \alpha_{PCA*PCD} X_{PCA*PCD} + \alpha_{PCB*PCC} X_{PCB*PCC}$$

$$+ \alpha_{PCC*PCD} X_{PCC*PCD} + \alpha_{PCC*PCD} X_{PCC*PCD} + \alpha_{PCA*PCB*PCC} X_{PCA*PCB*PCC}$$

$$+ \alpha_{PCA*PCB*PCD} X_{PCA*PCB*PCD} + \alpha_{PCA*PCC*PCD} X_{PCA*PCC*PCD} + \alpha_{PCB*PCC*PCD} X_{PCB*PCC*PCD} + \alpha_{11} X_1^2$$

4.2.5.1) Hardness

The model is computed with the experimental matrix A3 and hardness as response Y.

The examination of the linear regression, residuals in fitting and statistical parameters shows low residues in fitting for every samples (Figures 130a and 130b).

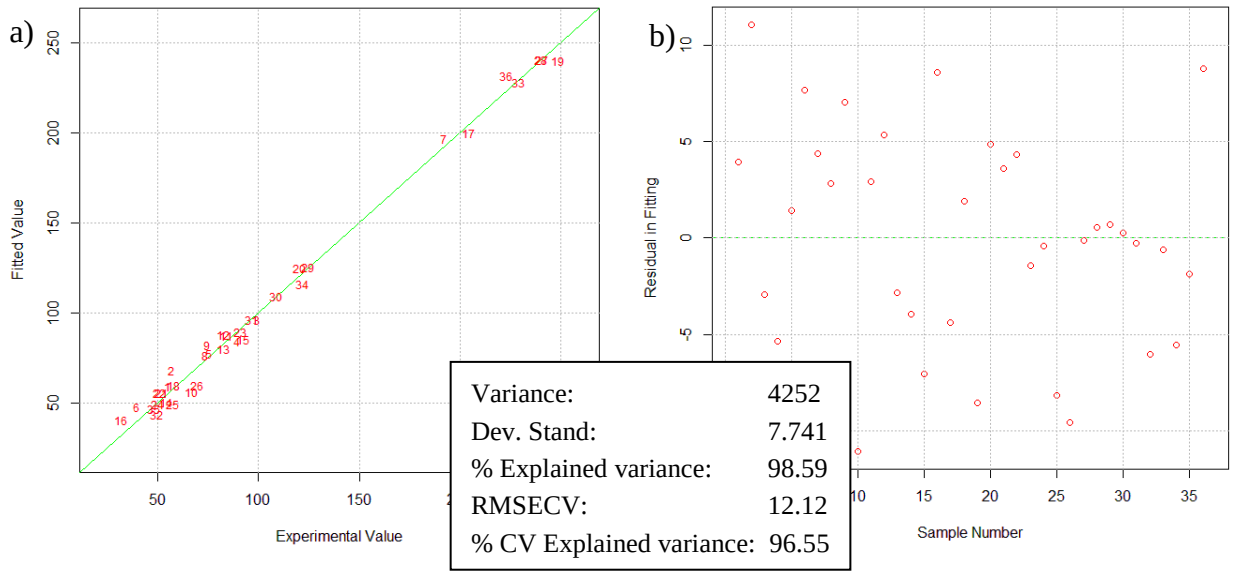

Figure 130: Linear regression: a) Experimental vs. Fitted Values, b) Residuals in fitting

The computation of the coefficients, with the respective statistical significance, is presented Figure 131.

The first four components correspond to the response of each pseudo-component (PC) as if pure. In this case, PCB (CuSn20) is the hardest component, followed by PCC (CuZn20), PCA (Cu) and finally PCD (CuPb20).

Coefficients 5 and 18 are relative to the level of superheat. It clearly appears that these coefficients are not significant, and that hardness is not affected by these process variables.

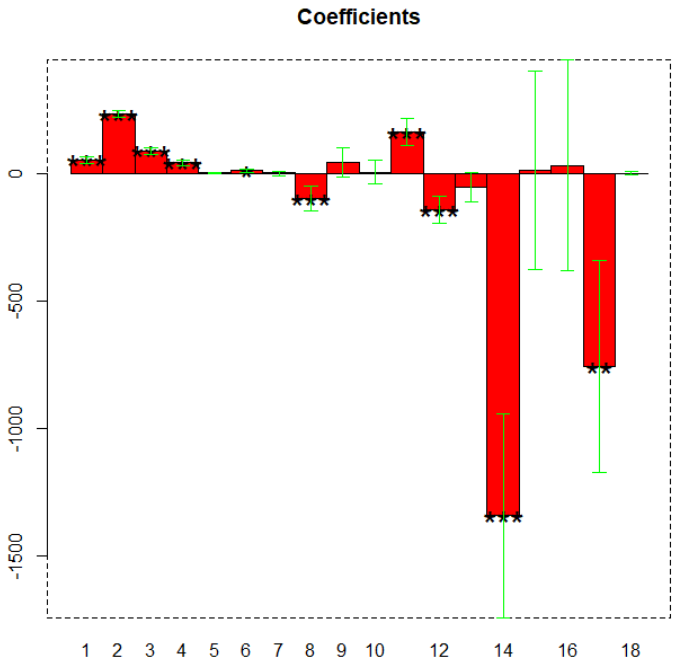

Figure 131: Coefficient for the computation

Coefficients 6 and 7 correspond to the qualitative variable of the mould and are by definition relative to the third implicit variable (S3 = use of a sand mould). It appears that the coefficient 6 (S1 = use of a steel mould) can be considered slightly significant[7] (*) with respect to the two others (Table 34). However, the coefficient 7 (S2 = use of a clay mould) does not present significant effect with respect to the coefficient S3.

Coefficient	*Significance*	*Value*	*Effect*
S1	*	8.9987	+ 9.0

Table 34: Coefficients value and relative effect for the binary mixtures

Among the coefficients of binary mixtures, only the coefficients 8 (PCA*PCB), 11 (PCB*PCC) and 12 (PCB*PCD) are significant effect (***). This means that the interaction between the corresponding pseudo-components have a non-unneglectable impact on hardness. The effect values are calculated by dividing the coefficient value by the square of components number (Table 35).

Coefficient	*Significance*	*Value*	*Effect*
PCA*PCB	***	-99.2564	- 25
PCB*PCC	***	160.9443	+ 40
PCB*PCD	***	-143.7264	- 36

Table 35: Coefficients value and relative effect for the binary mixtures

Among the coefficients of ternary mixtures, only the coefficients 14 (PCA*PCB*PCC) and 17 (PCB*PCC*PCD) have a significant effect (respectively *** and **) (Table 36).

Coefficient	*Significance*	*Value*	*Effect*
PCA*PCB*PCC	***	-1339.8223	-50
PCB*PCC*PCD	**	-757.8015	-28

Table 36: Coefficients value and relative effect for the ternary mixtures

An expression for the predictive model of hardness:

$$HV = 50.9X_{PCA} + 231.4X_{PCB} + 87.9X_{PCC} + 40.4X_{PCD} + 0.2X_1 + 9.0X_{S1} - 3.4X_{S2}$$
$$- 99.3X_{PCA*PCB} + 41.4X_{PCA*PCC} + 4.3X_{PCA*PCD} + 160.9X_{PCB*PCC} - 143.7X_{PCC*PCD}$$
$$-55.2X_{PCC*PCD} - 1339.8X_{PCA*PCB*PCC} + 10.4X_{PCA*PCB*PCD} + 29.6X_{PCA*PCC*PCD}$$
$$-757.8X_{PCB*PCC*PCD} - 0.1X_1^2 \qquad \text{(Eq. 14)}$$

The statistical features of the coefficients are visible in Appendix 10.

[7] Significance: * = p < 0.05; ** = p < 0.01; *** = p < 0.01

The predictive model is tested and confirmed by three experiments of verification (Figure 132 and Table 37). It shows good results of prediction, whose standard deviation is coherent.

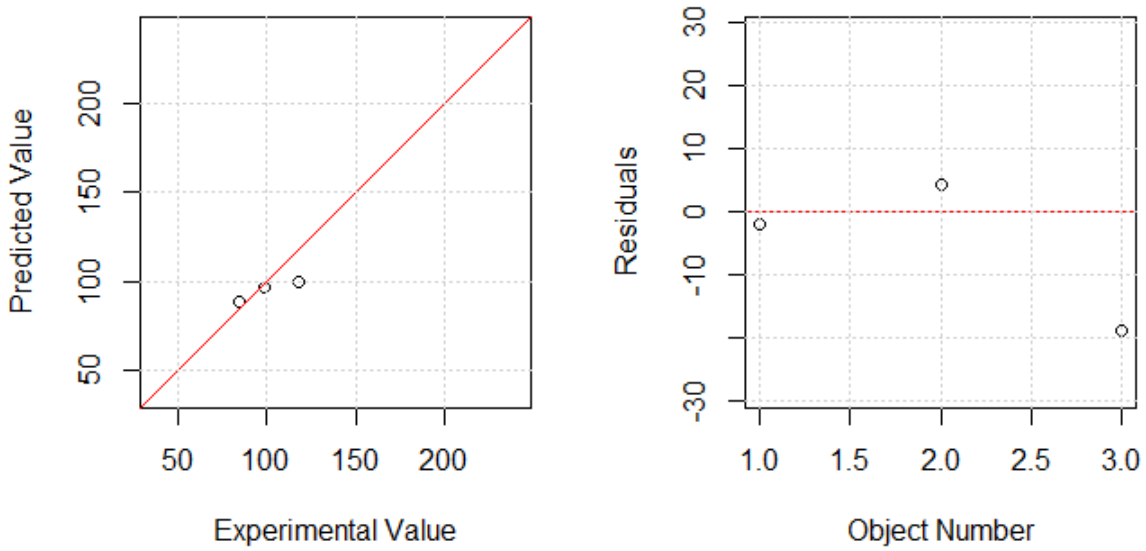

Figure 132: Prediction plots

Sample	*Experimental Value*	*Predicted Value*	*Δx^2*	*Standard deviation*
DTA20	98.50	96.62472	3.516675078	
DTA10	84.20	88.46810	18.21667761	11.1
28-154	118.40	99.67020	350.805408	

Table 37: Experiments of verification

4.2.5.2) Secondary phase

The model is computed with the experimental matrix A3 and the volume percentage of secondary phase as response Y.

The linear regression shows very low residues in fitting for every samples (Figure 133a and 133b), as well as the standard deviation.

As seen through the PCA, the hardness is strongly correlated with the formation of secondary phase. It explains that the coefficient computation for the secondary phase is similar to the computation of the hardness model.

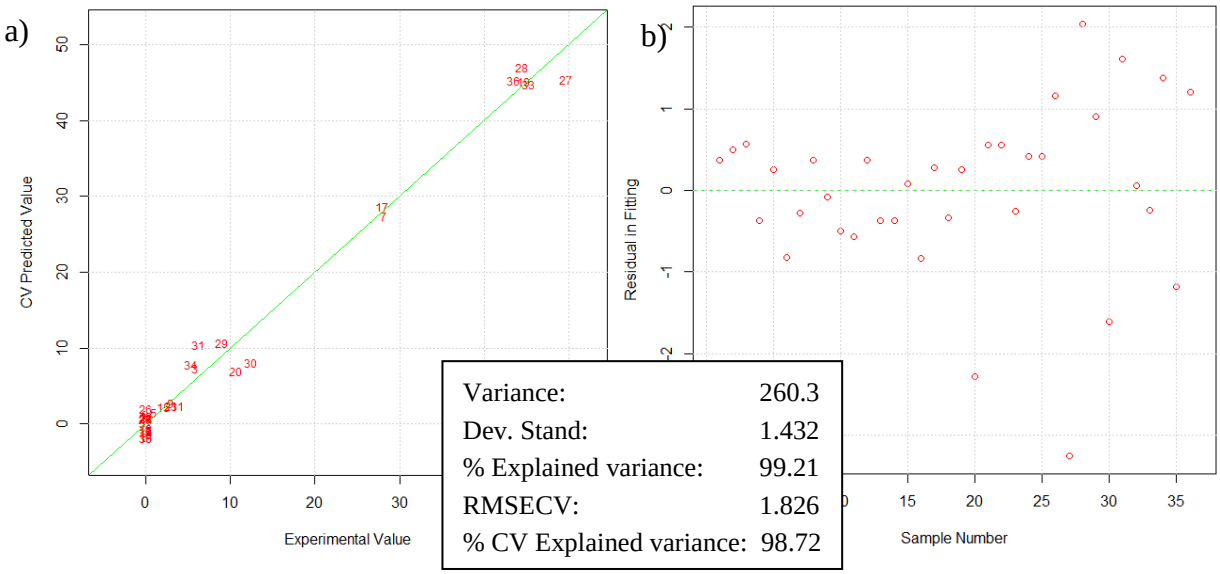

Figure 133: Prediction plots

The computation of the coefficients, with the respective statistical significance, is presented Figure 134.

The first four components correspond to the response of each pseudo-component (PC) as if pure. In this case, PCB (CuSn20) is the component favouring the formation of secondary phase. The other three components do not have any effect.

Coefficients 5 and 18 are relative to the level of superheat. It clearly appears that these coefficients are not significant, and that the formation of secondary phase is not affected by these process variables.

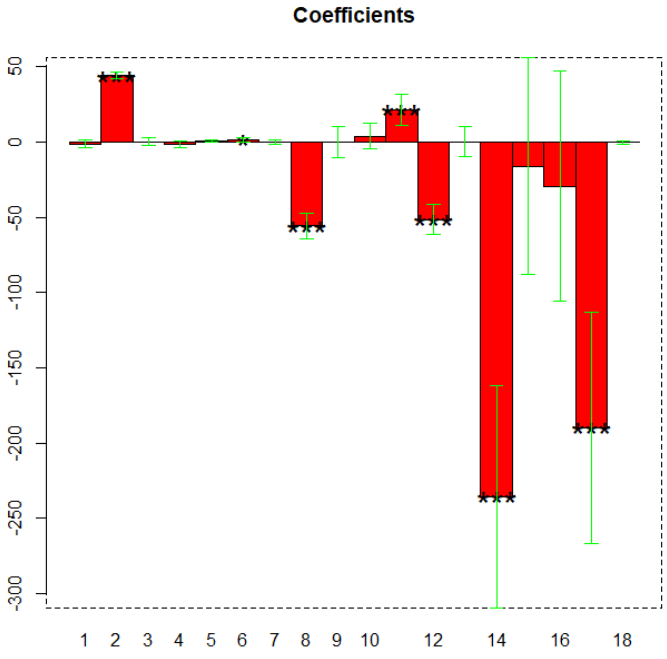

Figure 134: Coefficient for the computation

Coefficients 6 and 7 correspond to the qualitative variable of the mould and are by definition relative to the third implicit variable (S3 = use of a sand mould). It appears that the coefficient 6 (S1 = use of a steel mould) can be considered slightly significant (*) with respect to the two others (Table 38). However, the coefficient 7 (S2 = use of a clay mould) does not present significant effect with respect to the coefficient S3.

Coefficient	*Significance*	*Value*	*Effect*
S1	*	1.73704	+ 1.7

Table 38: Coefficients value and relative effect for the binary mixtures

Among the coefficients of binary mixtures, only the coefficients 8 (PCA*PCB), 11 (PCB*PCC) and 12 (PCB*PCD) are significant effect (***). The effect values are calculated by dividing the coefficient value by the square of components number (Table 39).

Coefficient	*Significance*	*Value*	*Effect*
PCA*PCB	***	-55.58207	-13.9
PCB*PCC	***	21.54605	5.4
PCB*PCD	***	-51.54526	-12.9

Table 39: Coefficients value and relative effect for the binary mixtures

Among the coefficients of ternary mixtures, only the coefficients 14 (PCA*PCB*PCC) and 17 (PCB*PCC*PCD) have a significant effect (respectively *** and **) (Table 40).

Coefficient	*Sgnificance*	*Value*	*Effect*
PCA*PCB*PCC	***	-235.52495	-8.723146296
PCB*PCC*PCD	**	-189.86584	-7.032068148

Table 40: Coefficients value and relative effect for the ternary mixtures

An expression for the predictive model of the volume percentage of secondary phase:

$$vol.\%\ 2nd\ phase = -1.1X_{PCA} + 44.2X_{PCB} + 0.4X_{PCC} - 1.3X_{PCD} + 0.7X_1 + 1.7X_{S1} + 0.2X_{S2}$$
$$- 55.6X_{PCA*PCB} + 0.1X_{PCA*PCC} + 4.1X_{PCA*PCD} + 21.5X_{PCB*PCC} - 51.5X_{PCC*PCD} + 0.4X_{PCC*PCD}$$
$$-235.5X_{PCA*PCB*PCC} - 15.9X_{PCA*PCB*PCD} - 29.2X_{PCA*PCC*PCD} - 189.9X_{PCB*PCC*PCD} + 0.3X_1^2$$

(Eq. 15)

The statistical features of the coefficients are visible in Appendix 10.

The predictive model is tested and confirmed by four experiments of verification (Figure 135 and Table 41). It shows good results of prediction, whose standard deviation is coherent.

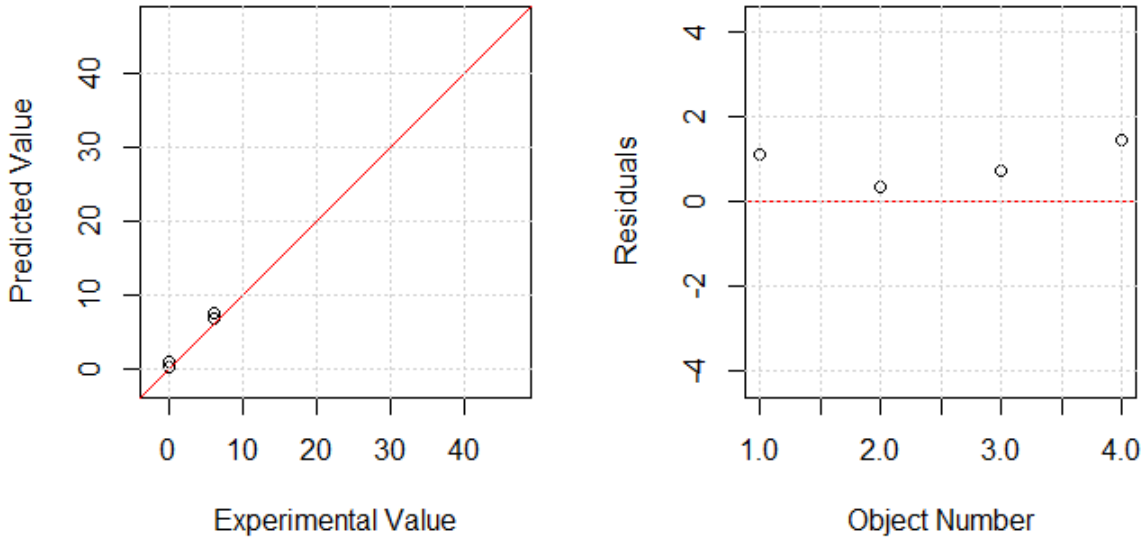

Figure 135: Prediction plots

Sample	*Experimental Value*	*Predicted Value*	*Δx^2*	*Standard deviation*
DTA20	0	1.1162774	1.246075234	1.0
DTA10	0	0.3717564	0.138202821	
Dhl	6.2	6.9258227	0.526818592	
28-154	6.1	7.5635246	2.141904255	

Table 41: Experiments of verification

4.2.5.3) Secondary Dendrite Arm Spacing

The model is computed with the experimental matrix A3 and the secondary dendrite arm spacing as response Y. Experiments for which the SDAS has not been quantified are not taken into consideration.

The linear regression shows very low residues in fitting for every samples (Figure 136a and 136b), as well as the standard deviation.

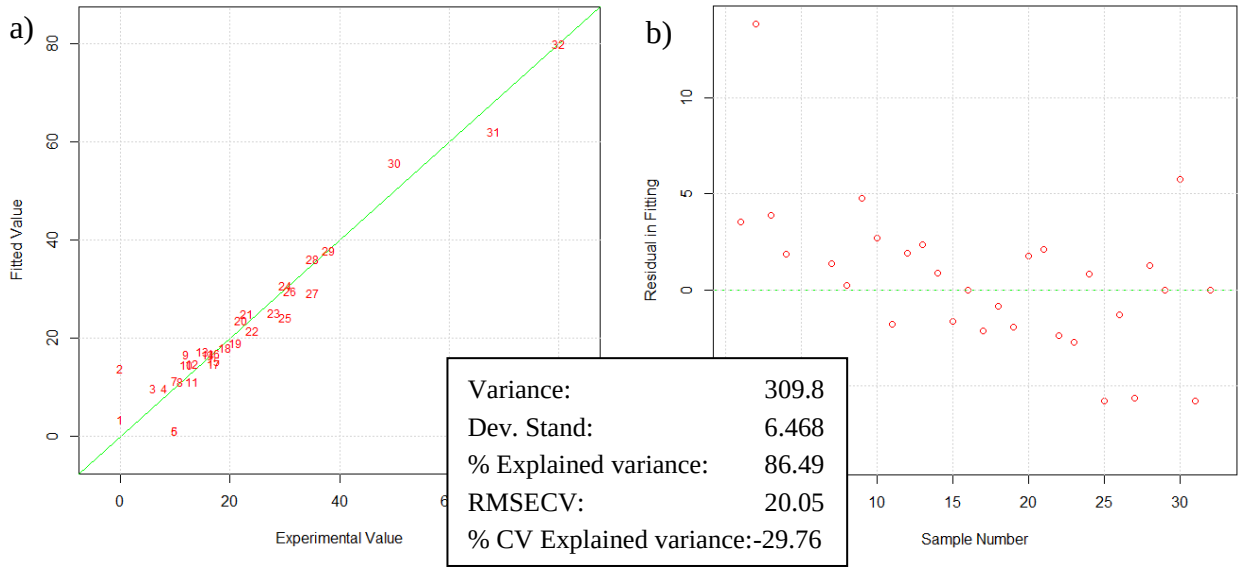

Figure 136: Prediction plots

The computation of the coefficients, with the respective statistical significance, is presented Figure 137.

The first four components correspond to the response of each pseudo-component (PC) as if pure. In this case, PCA (Cu) is the component favouring the biggest SDAS, followed by PCC (CuZn20). The two other components, PCB (CuSn20) and PCD (CuPb20), are still significant but have smaller effects..

Once again, coefficients 5 and 18 are relative to the level of superheat. It clearly appears that these coefficients are not significant, and that the SDAS is not affected by these process variables.

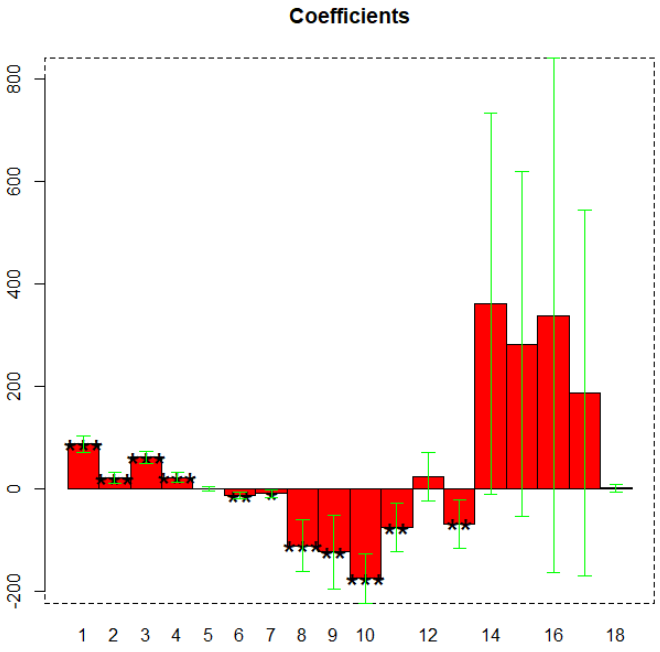

Figure 137: Coefficient for the computation

Coefficients 6 and 7 correspond to the qualitative variable of the mould and are by definition relative to the third implicit variable (S3 = use of a sand mould). It appears that the coefficient 6 (S1 = use of a steel mould) is significant (**) with respect to the third: using a still mould decreases the SDAS. The coefficient 7 (S2 = use of a clay mould) can be considered as slightly significant (*) with respect to the coefficient S3. Table 42 displays the variable's effects.

Coefficient	*Significance*	*Value*	*Effect*
S1	**	-12.53576	- 12.5
S2	*	-8.38902	- 8.3

Table 42: Coefficients value and relative effect for the binary mixtures

Every coefficients of binary mixtures show a significant effect on SDAS except the coefficient 12 (PCB*PCD). Coefficients 8 (PCA*PCB), 9 (PCA*PCC) and 10 (PCA*PCD) have the biggest significance (***), while the coefficients 11 (PCB*PCC) and 13 (PCC*PCD) are less significant (**). The effect values are calculated by dividing the coefficient value by the square of components number (Table 43).

Coefficient	*Significance*	*Value*	*Effect*
PCA*PCB	***	-110.84109	-27.7
PCA*PCC	***	-122.96100	-30.7
PCA*PCD	***	-173.94684	-43.5
PCB*PCC	**	-75.23320	-18.8
PCC*PCD	**	-68.08332	-17.0

Table 43: Coefficients value and relative effect for the binary mixtures

No coefficients of ternary mixtures appears significant to the secondary dendrite arm spacing.

An expression for the predictive model of the volume percentage of secondary phase:

$$SDAS = 88.4X_{PCA} + 22.0X_{PCB} + 62.2X_{PCC} + 22.4X_{PCD} - 0.1\,X_1 - 12.5X_{S1} - 8.32X_{S2}$$
$$- 110.8X_{PCA*PCB} - 123.0X_{PCA*PCC} - 173.9X_{PCA*PCD} - 75.2X_{PCB*PCC} + 23.6X_{PCC*PCD}$$
$$+361.4X_{PCA*PCB*PCC} + 282.8X_{PCA*PCB*PCD} + 339.0X_{PCA*PCC*PCD} + 187.8X_{PCB*PCC*PCD} + 1.9X_1^2$$
$$-68.1X_{PCC*PCD} \quad \text{(Eq. 16)}$$

The statistical features of the coefficients are visible in Appendix 10.

The predictive model is tested and confirmed by four experiments of verification (Figure 138 and Table 44). Results of prediction are less accurate that those of the previous models.

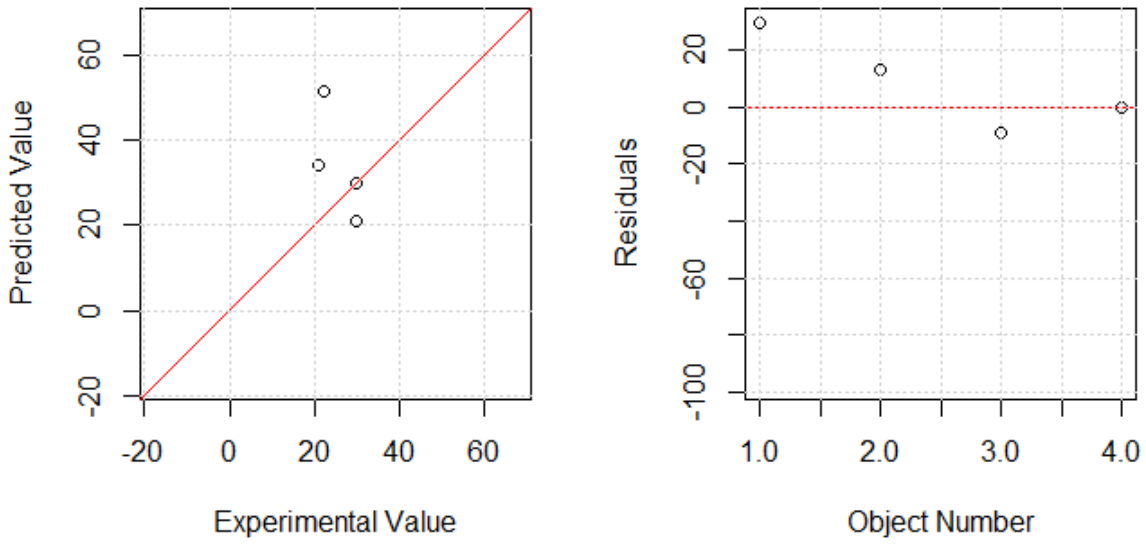

Figure 138: Prediction plots

Sample	*Experimental Value*	*Predicted Value*	*Δx^2*	*Standard deviation*
DTA20	22	51.62464	877.6192951	16.8
DTA10	21	33.96458	168.0803346	
Dhl	30	21.00525	80.90552756	
28-154	30	30.01805	0.000325802	

Table 44: Experiments of verification

4.3) The archaeological corpus of Loyettes

4.3.1) Alloys composition

The chemical composition of each sample's alloy has been estimated by SEM-EDS measurements on the polished cross-section. Table 45 displays the average composition on 5 measures in weight percentage (wt.%).

Group	*Sample*	*Cu*	*Sn*	*Other*	
L8	Loy 03	96.4 ± 0.2	1.5 ± 0.1	2.0 ± 0.1	Fe, S
	Loy 04	98.0 ± 0.1	0.9 ± 0.2	1.1 ± 0.1	Fe, S
	Loy 13	94.6 ± 0.2	1.6 ± 0.2	3.9 ± 0.2	Fe, S
	Loy 14	96.7 ± 0.1	1.3 ± 0.1	2.0 ± 0.2	Fe, S
	Loy 30	95.8 ± 0.4	2.3 ± 0.4	1.9 ± 0.1	Fe, S
	Loy 36	95.9 ± 0.3	1.5 ± 0.1	2.6 ± 0.2	Fe, S
	Loy 44	94.9 ± 0.3	1.8 ± 0.4	3.4 ± 0.1	S
	Loy 47	97.0 ± 0.3	3.0 ± 0.3	< 0.5	
L7	Loy 45	97.8 ± 0.6	1.6 ± 0.2	< 1.0	Fe, S, Mo
L10	Loy 12	99.1 ± 0.4	0.8 ± 0.3	< 0.5	Pb
	Loy 20	98.0 ± 0.1	1.6 ± 0.1	< 0.5	S
	Loy 16	97.8 ± 0.4	1.6 ± 0.2	< 1.0	Fe, S
	Loy 42	97.8 ± 0.5	2.0 ± 0.2	< 1.0	Mo, S
	Loy 46	98.5 ± 0.2	1.3 ± 0.2	< 0.5	S
	Loy 57	97.2 ± 0.2	1.2 ± 0.2	1.6 ± 0.1	Fe, S
L18	Loy 58	92.6 ± 0.2	4.6 ± 0.2	2.8 ± 0.1	Fe, S
Ternay	561	99.2 ± 0.5	0.8 ± 0.1	< 0.5	S
M2	Loy 07	98.8 ± 0.2	1.2 ± 0.1		
	Loy 59_1	96.8 ± 0.2	1.4 ± 0.2	1.8 ± 0.3	Fe, S, Mo
	Loy 59_2	97.1 ± 0.7	1.2 ± 0.2	1.7 ± 0.7	Fe, S, Mo

Table 45: Chemical composition of ingot alloys (SEM-EDS measurements, wt.%)

The whole corpus is composed by binary bronze alloys, which contain tin between 0.8 and 4.6 wt.%. For these 20 ingots, a cluster of composition is visible for tin content inferior to 2.0 wt.%, as displayed in Figure 140. Two samples, Loy47 from group L8 and Loy58 from group L18, show tin content particularly high, 3.0 and 4.6 wt:% respectively.

Figure 139 details the composition for each group of typology. It appears that ingots from the groups T and L18 have respectively tin content lower (0.8 ± 0.1 wt.%) and much higher (4.6 ± 0.2 wt.%) than the cluster of composition. However, the two ingots from the group M2 have similar compositions. Finally, the compositions of group L10 are relatively homogeneous, while the ingots from the group L8 present a disparate distribution of tin content.

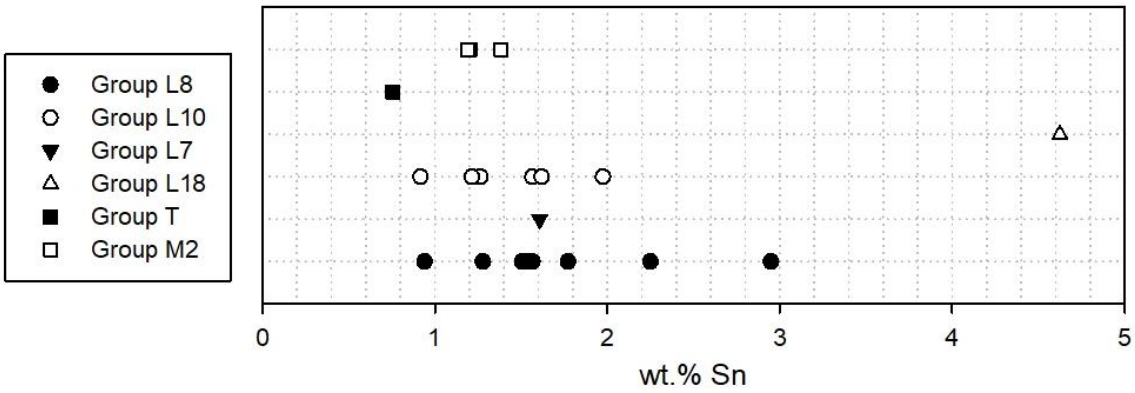

Figure 139 : Composition of artefacts in function of typological group

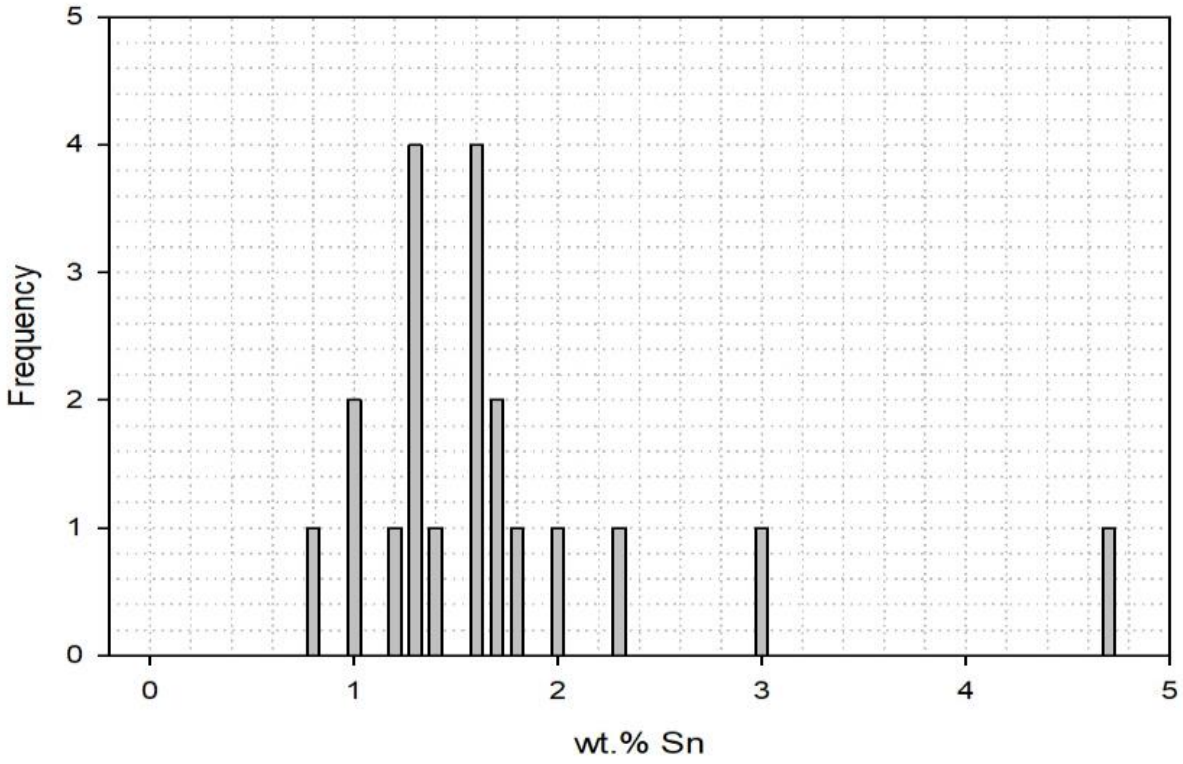

Figure 140: Tin ubiquity in the selected corpus (20 objects)

4.3.2) Microstructural investigation

For each sample, the metallographic investigation has concerned the observation of the metallic matrix and inclusions, the determination of the grain typology (dendritic or recrystallized) and the structure's granulometry (respectively average grain size or SDAS). Grains are considered as dendritic when the microsegregation is sufficient to allow the determination of the SDAS.

The characterization of corrosion layers was not carried out during this study.

4.3.1.1) Group L8

Each sample of the group is composed by the solid solution α, where microsegregation of tin is more or less visible according to the global amount of this element in the alloy.

Rounded dark inclusions, composed by mixed sulphur of copper and iron, are regularly distributed over the observed surface of every specimen. For samples Loy 13 and Loy 44, larger light-grey inclusions with irregular shapes are occasionally observed. They are composed by high-iron content (90 at.%) mixed with copper.

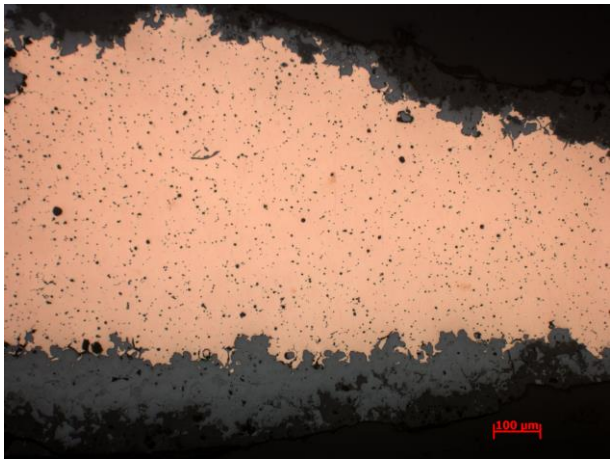

Figure 141: Matrix with inclusions of iron and copper sulphur (Sample Loy 14, LOM-BF, 100X)

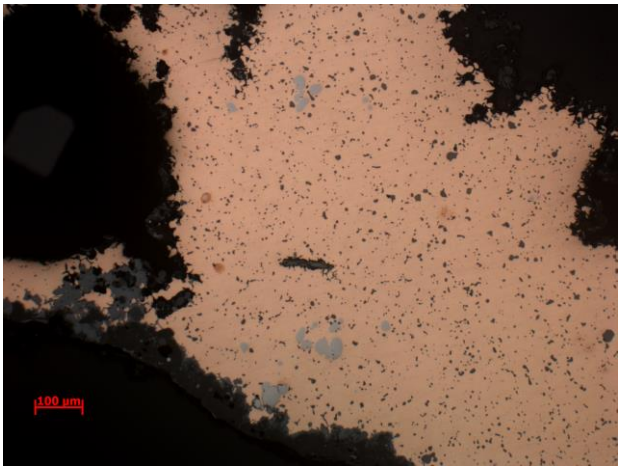

Figure 142: Matrix with inclusions of iron and copper sulphur (dark inclusions) and iron mixed with copper inclusions (light grey inclusions) (Sample Loy 13, LOM-BF, 100X)

Three typologies of grains have been identified: only dendritic grains, (Figure 144), completely recrystallized grains (Figure 143) and both typologies (Figure 145). Stereological measurements are displays in Table 46.

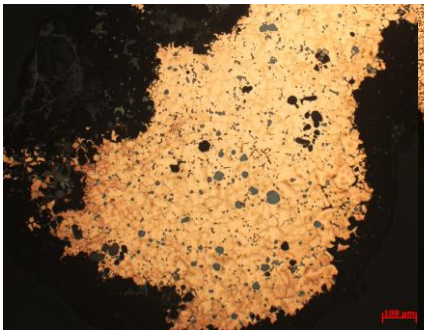

Figure 143: Recrystallized grains (Sample Loy 13, etched , LOM-BF, 100X)

Figure 144: Dendritic microstructure (Sample Loy 30, etched, LOM-BF, 100X)

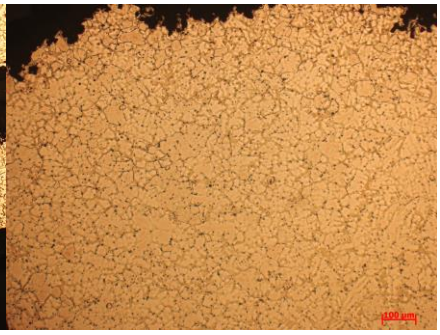

Figure 145: Dendritic and recrystallized microstructure (Sample Loy03, etched, LOM-BF, 100X)

Sample	Secondary phase (% vol.)	Grain Typology	Average grain diameter (µm)	Average SDAS (µm)
Loy 03	-	D + R	29.9 ± ± 2.1	16.4 ± 0.4
Loy 04	-	D + R	49.7 ± 6.1	16.9 ± 1.7
Loy 13	-	R	22.8 ± 4.9	-
Loy 14	-	R	37.7 ± 10.7	-
Loy 30	-	D	-	7.5 ± 1.2
Loy 36	-	R	35.8 ± 2.0	-
Loy 44	-	D + R	34.6 ± 3.8	12.0 ± 2.4
Loy 47	-	D	-	22.0 ± 7.9

Table 46: Metallographic features of the samples of the Group L8. Grain typology: D = dendritic, R = recrystallized

4.3.1.2) Group L10

Like previously, each sample of the Group L10 is composed by the solid solution α, where microsegregation of tin is more or less visible according to the global amount of this element in the alloy.

The rounded dark inclusion of iron and copper sulphur are noticeable in every sample (Figure 146). In this group, only the sample Loy 42 also shows the presence of small rounded white inclusions, identified as tin oxides (cassiterite), only visible through SEM observation.

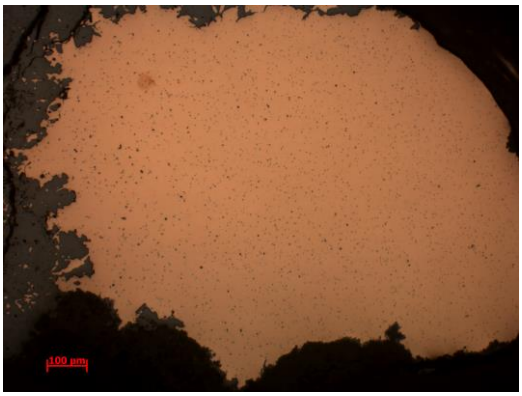

Figure 146: Matrix with inclusions of iron and copper sulphur (Sample Loy 16, LOM-BF, 100X)

Microstructures have been identified according the same three typologies as previously seen: dendritic (Figure 148), recrystallized grains (Figure 147) and mixed (Figure 149).

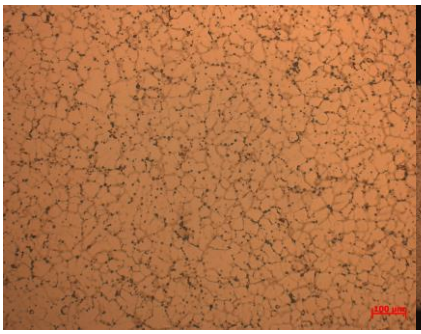

Figure 147: Recrystallized grains (Sample Loy 57, etched , LOM-BF, 100X)

Figure 148: Dendritic microstructure (Sample Loy 20, etched, LOM-BF, 100X)

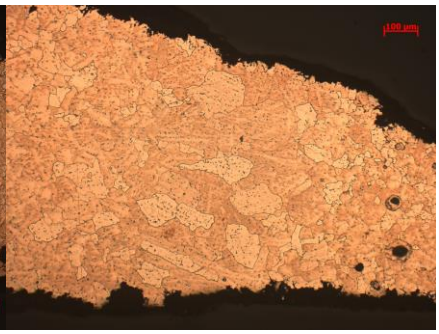

Figure 149: Dendritic and recrystallized microstructure (Sample Loy 12, etched, LOM-BF, 100X)

Stereological measurements are displays in Table 47.

Sample	Secondary phase (% vol.)	Grain Typology	Average grain diameter (µm)	Average SDAS (µm)
Loy 12	-	D + R	43.4 ± 12.6	12.2 ± 2.2
Loy 16	-	D	-	19.8 ± 1.9
Loy 20	-	D	-	7.0 ± 1.4
Loy 42	-	D + R	42.6 ± 4.2	16.1 ± 1.4
Loy 46	-	R	28.0 ± 3.8	-
Loy 57	-	R	37.4 ± 7.7	-

Table 47: Metallographic features of the samples of the Group L10. Grain typology: D = dendritic, R = recrystallized

4.3.1.3) Group M2

The three samples are composed by the solid solution α without secondary phase.

The same inclusions made of sulphur of iron and copper are observable (Figure 150), even for the sample Ternay which is not part of the Loyettes corpus (Figure 151).

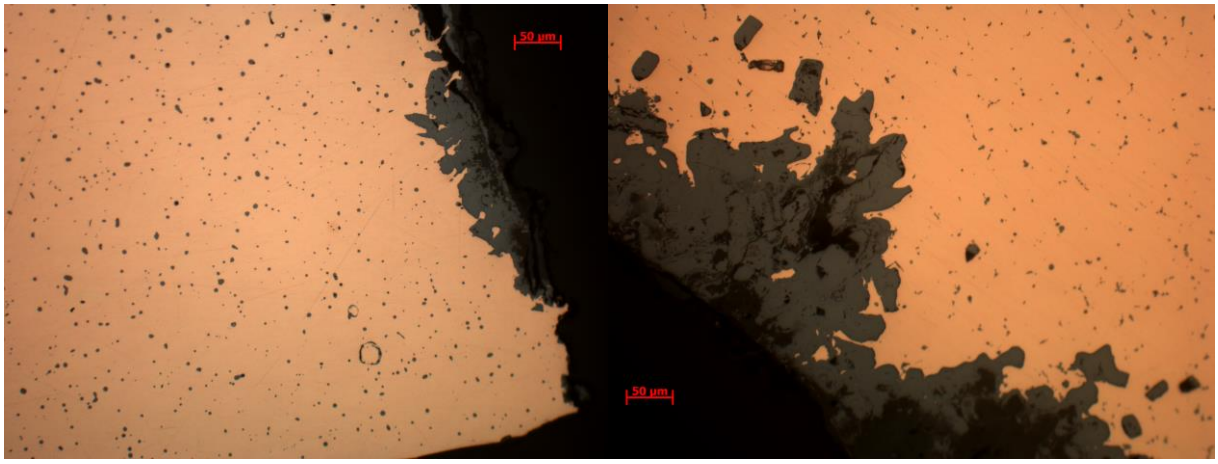

Figure 150: atrix with inclusions of iron and copper sulphur (Sample Loy 59, LOM-BF, 200X)

Figure 151: Matrix with inclusions of iron and copper sulphur (Sample Ternay, LOM-BF, 200X)

Furthermore, the three microstructure typologies previously stabilized are identified (Figures 152 to 154).

Figure 152: Recrystallized grains (Sample Loy 07, etched , LOM-BF, 200X)

Figure 153: Dendritic microstructure (Sample Ternay, etched, LOM-BF, 100X)

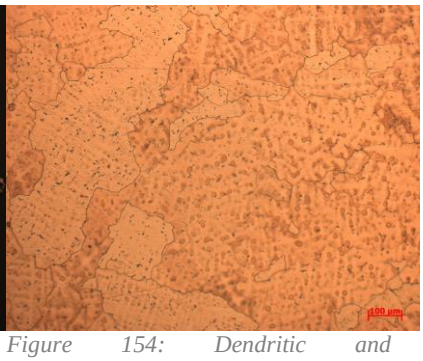

Figure 154: Dendritic and recrystallized microstructure (Sample Loy 59, etched, LOM-BF, 100X)

Stereological measurements are displays in Table 48.

Sample	Secondary phase (% vol.)	Grain Typology	Average grain diameter (µm)	Average SDAS (µm)
Loy 59	-	D + R	32.0 ± 3.7	13.9 ± 1.6
Loy 07	-	R	17.9 ± 1.5	-
Ternay	-	D	-	24.2 ± 1.3

Table 48: Metallographic features of the samples of the Group M2. Grain typology: D = dendritic, R = recrystallized

4.3.1.4) Non-classified

These two samples are composed by a solid solution α in which microsegregation is well-visible. It is particularly the case of the sample L18 – Loy58, which is rich in tin (Figure 143).

Sulphur of iron and copper are homogenously distributed over the observed surfaces, and the presence of tin oxides is noted for both samples.

While the microstructure of the sample Loy 58 is entirely composed by recrystallized grains (Figure 155), the sample Loy 45 show a mixed microstructure (Figure 156)

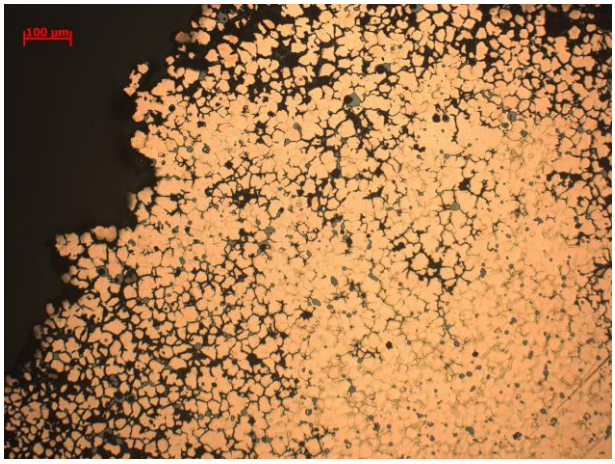

Figure 155: Recrystallized grains (Sample Loy 58, etched , LOM-BF, 100X)

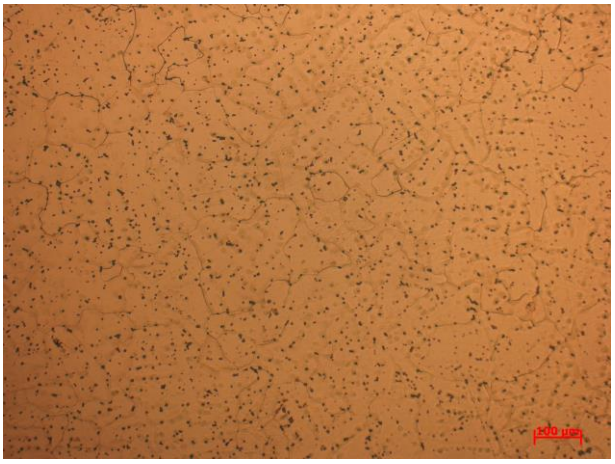

Figure 156: Dendritic and recrystallized microstructure (Sample Loy 45, etched, LOM-BF, 100X)

Stereological measurements are displays in Table 49.

Sample	Secondary phase (% vol.)	Grain Typology	Average grain diameter (µm)	Average SDAS (µm)
L7 - Loy 45	-	R	24.7 ± 5.5	-
L18 - Loy 58	-	D + R	46.4 ± 9.6	23.2 ± 1.1

Table 49: Metallographic features of the samples of the non-classified specimens. Grain typology: D = dendritic, R = recrystallized

4.3.3) Discussion about the manufacturing process

Thanks to the investigation of archaeologists, it has been possible to divide the large corpus of Loyettes in several groups based on the macrostructural features of each artefact.

The systematic and accurate presence or absence of specific cavities or blisters on the ingots surface permits to assume the use of permanent moulds, which can undergo up to a dozen of casting cycles. In a first assumption, it can be think that stone or metal moulds may have been used for the manufacturing of Loyettes ingots.

The raw external state, the dendritic microstructure and the presence of non-deformed inclusions confirm the as-cast state of these artefacts and that no finishing treatment has been applied.

As seen during the experiments of DoE, recrystallized grains on the material's edges can be observed if the alloys is composed by grain refiner elements (lead nodules, inclusions, etc.) and if a refractory mould is used. This way, the heat removal is delayed and the material can reach recrystallization temperature in these areas.

In conclusion, stone moulds are preferentially assumed for the production of the corpus.

It can be reasonable to think that several moulds have been filled simultaneously from the same melt and multivariate analysis is performed in order to identify correlations of composition between the artefacts of the selected corpus.

However, no clear cluster can be identified for the score plot (Figure 157), and further analysis on a larger corpus should be done.

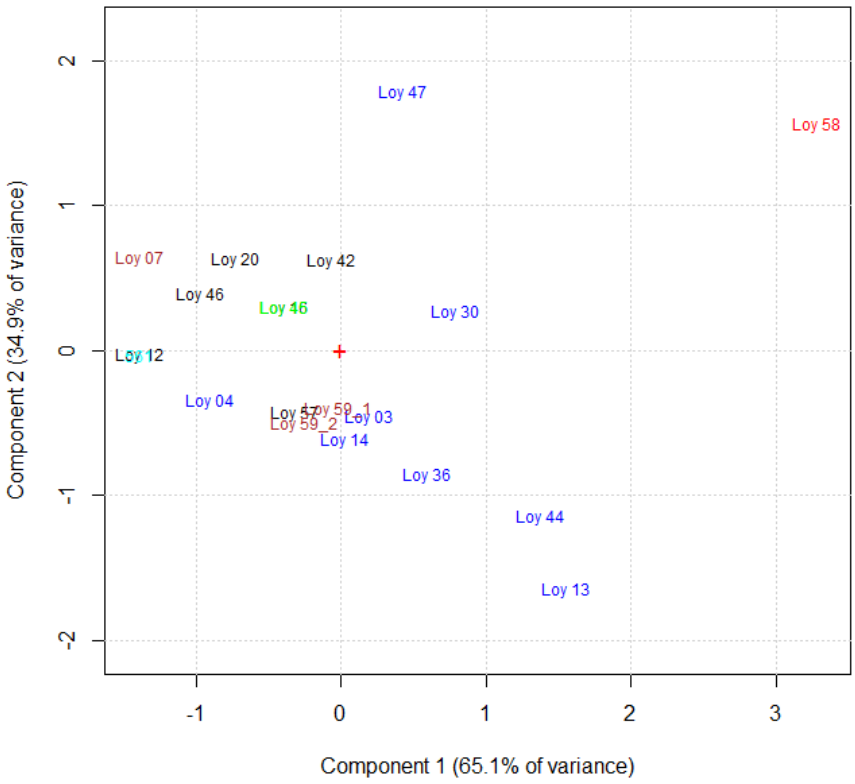

Figure 157: Score plot (100% of total explained variance)

CONCLUSIONS

This Ph.D work started from the statement that copper and its alloys, as well as casting practices are of major importance for both archaeometric studies and researches in the field of material sciences.

The empirical origins of actual knowledge on the non-equilibrium behaviour of ancient copper alloys, like bronze and brass, during casting processes have implied the necessity of gathering quantitative data upon the impact of different velocities of solidification on the cast object's features.

A multi-technical methodology based on a multivariate approach has been built in order to firstly investigate different scales of cooling rate (i.e. medium, near rapid), and secondly the impact of different variables of process (i.e. alloys composition, superheat, mould material) on the macro and microstructure, as well as on macrohardness.

It has been shown through a DTA investigation that the phase transformation temperatures in the binary Cu-Sn and Cu-Zn systems decrease when cooling rate is raised, even for reduced departures from equilibrium (max. 30 $K.min^{-1}$).

While the microstructure of Cu-Zn alloys is not significantly modified by the application of medium cooling rates, the microstructures of Cu-Sn alloys are more affected. It has been noticed that the peritectic transformation can occur from a tin content of 5 wt.% at $30K.min^{-1}$.

The kinetics investigation has confirmed that higher values of cooling rates permit to reduce the times of reaction, which becomes faster.

From casting experiments and on the basis of the metallographic investigation carried out, different conclusions can be drawn:

- The thermal properties of the material used as casting mould have the main influence among other factors on the removal of heat from the melt and then on the cooling rate values;

- The range of cooling rates generated by common mould used in casting processes is wide enough to significantly modify the structural features on as-cast ingots;

- The level of superheat (from +25 °C to + 75 °C) does not have a significant effect on the cooling rate and thus on any microstructural feature, or hardness.

- Ingots cast in conductive mould have a tendency towards the formation of stronger shrinkage cavities and to be more heterogeneous in the secondary phase repartition and grain size.

- The use of the steel mould tends to favour the formation of three zones in the ingot: the chill, columnar and equiaxed zones, whose lengths are directly linked to the alloy composition, the amount of interdendritic phases and the presence of defects like porosities;

- The use of the clay mould tends to avoid the formation of the columnar zone, which is rarely observed. Thus, alloys cast in clay mould mainly present an equiaxed macrostructure with small grains in the chill zone;

- The use of the sand mould tends to form ingots with large equiaxed grains.

From a methodologic point of view, in spite of the variability of as-cast ingots, the computation of a D-optimal design permits to generate sustainable models which predict the hardness, the volume percentage of secondary phase that form during solidification and the secondary dendrite arm spacing of several copper-based alloys on the basis of their composition and process parameters. However, further investigations should deal with the reproduction of the experimental ingots that have shown the highest composition gap between the expected alloys composition and the experiment in order to reduce the experimental variability.

The numerical simulation performed has allowed the extraction of some data about the cooling rate applied, the time of solidification and the mould thermal behaviour for lower temperatures. The correlation with experimentation is however limited by the determination of non-steady values of thermal dependent features of mould materials during casting and the estimation of the heat transfer coefficient. A certain variability in the mould manufacturing stage should also be considered.

The archaeometric investigation of the Loyettes corpus (as-cast axe ingots) has highlighted the main microstructural features of these artefacts.

The selected assemblage consists of by binary bronzes having a chemical composition mainly between 1 and 2 wt.% of tin. Some objects are richer in tin (4.6 wt.%).

The as-cast state of those ingots is confirmed by the dendritic microstructure of each of them and by the presence of non-deformed inclusions. The presence of recrystallized grains can be correlated to the refractory behaviour of the casting mould, with the presence of inclusions, which favour the grain refinement.

Each sample presents a large quantity of inclusions that are dispersed in the copper-rich matrix. On the basis of their chemical composition, four typologies of inclusions have been identified:

- round-dark mixed sulphides of copper and iron (respectively 30 at.%, 50 at.% and 8 at.%), present in every samples. Selenium has also been detected in some of them (< 1 at.%).
- high-iron (90 at.%) inclusions mixed with copper (10 at.%), only visible in two samples (Loy 13 and Loy 44 from Group L8). These inclusions are rather light-grey and larger with irregular shapes ;
- tin oxides (Figure), well-known as cassiterite (SnO_2), have been identified for two samples (Loy 42 from Group L8 and sample Loy 07 from M2). These inclusions have extremely small dimensions and are only visible at high magnification;
- silicon-rich inclusions, also identified in two samples (Loy 47 from group L8 and Loy 07 from group M2).

These inclusions have important dimensions and irregular shapes. The occurrence of inclusion in the microstructure of archaeologic artefacts can bring a lot of information about the manufacturing process, since they are directly correlated with the ores from which the alloying element have been reduced, or from the smelting process itself.

Thus, the presence of mixed iron and copper sulphurs is very common since they derive from the copper-rich ore used for the production of copper (chalcopyrite $CuFeS_2$). Furthermore, in case of thermos-mechanical treatment, these inclusions have the particularity to deform with the whole matrix and rather adopt long sharp shapes in the elongation direction. Here, the rounded shape confirm the as-cast conditions of the whole corpus.

The presence of silicon can be explained either as a part of the original ore, or as a deliberate addition (fayalite Fe_2SiO_4) aiming to ease the slagging stage of chalcopyrite. Indeed, this element rather reacts with iron and allow the separation of copper and iron.

Finally, tin oxide inclusions can be interpreted as elements coming from the tin-rich ore. For the low tin contents considered in this study, it can be assumed that tin was not produced from smelting processes but rather added in the copper-rich matrix in the form of oxides.

APPENDIX

APPENDIX 1 – CHARACTERIZATION OF THE MOULD MATERIALS

A1.1. PETROGRAPHIC ANALYSIS - Composition of the fired clay

Prof. R. CABELLA - DISTAV

The petrographic observation shows that the material is composed by two main components (Figures 1 - 3):

1. An oxidized red clayey matrix mainly composed by iron and which is partially optically active. Angular inclusions made of quartz of fine dimensions (average < 0.1 mm, max 0.3 mm) are well noticeable with iron oxides fragments (dimensions < 0.8 mm) and occasionally some quartzite fragments (dimensions < 1mm). No mica crystals are visible.
2. Angular[1] and subangular[2] fragments relatively frequent (c. 30 %) (average dimensions < 0.5 mm, max 0.7 mm). They are made of a light clayey matrix (kaolinitic, appears grey under nicols prism and is partially optically active) and relatively abundant quartz inclusions (dimensions <0.1 mm)

Vacuoles are relatively rare. No signs of advanced vitrification due to high-temperature fired are visible.
The refractory features of the clay is due to the numerous inclusions of quartz and kaolinite fragments.

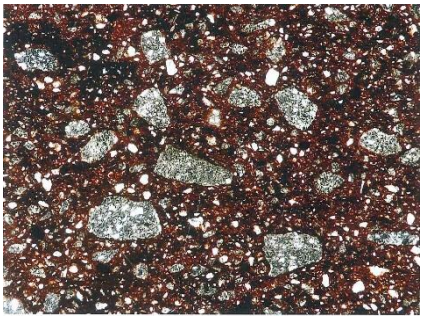

Figure 1: Microscopic observation with crossed nicols (real dimensions: 3.2 x 2.4 mm)

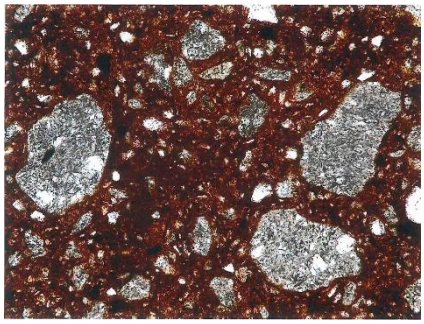

Figure 2: Microscopic observation with parallel nicols (real dimensions 1.3 x 1.0 mm)

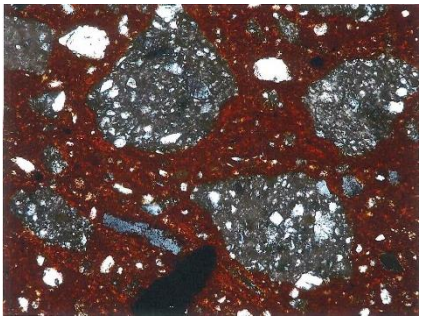

Figure 3: Microscopic observation with crossed nicols (real dimensions 1.3 x 1.0 mm)

[1] sharp edges separated by small depressions
[2] incipient rounding of the most pronounced edges

A1.2. X-RAY DIFFRACTION ANALYSIS (DISTAV) - Structural composition of the raw clay, the fired clay and the sand

Prof. C. CARBONE - DISTAV

XRD investigation shows that:

- the crude clay is composed by a matrix of kaolinite, illite, and sillimanite with the presence of quartz;
- the fired clay is only composed by mullite and kaolinite
- the sand is composed by quartz and calcite. The unidentified signal might be related to the presence of an organic bounding agent.

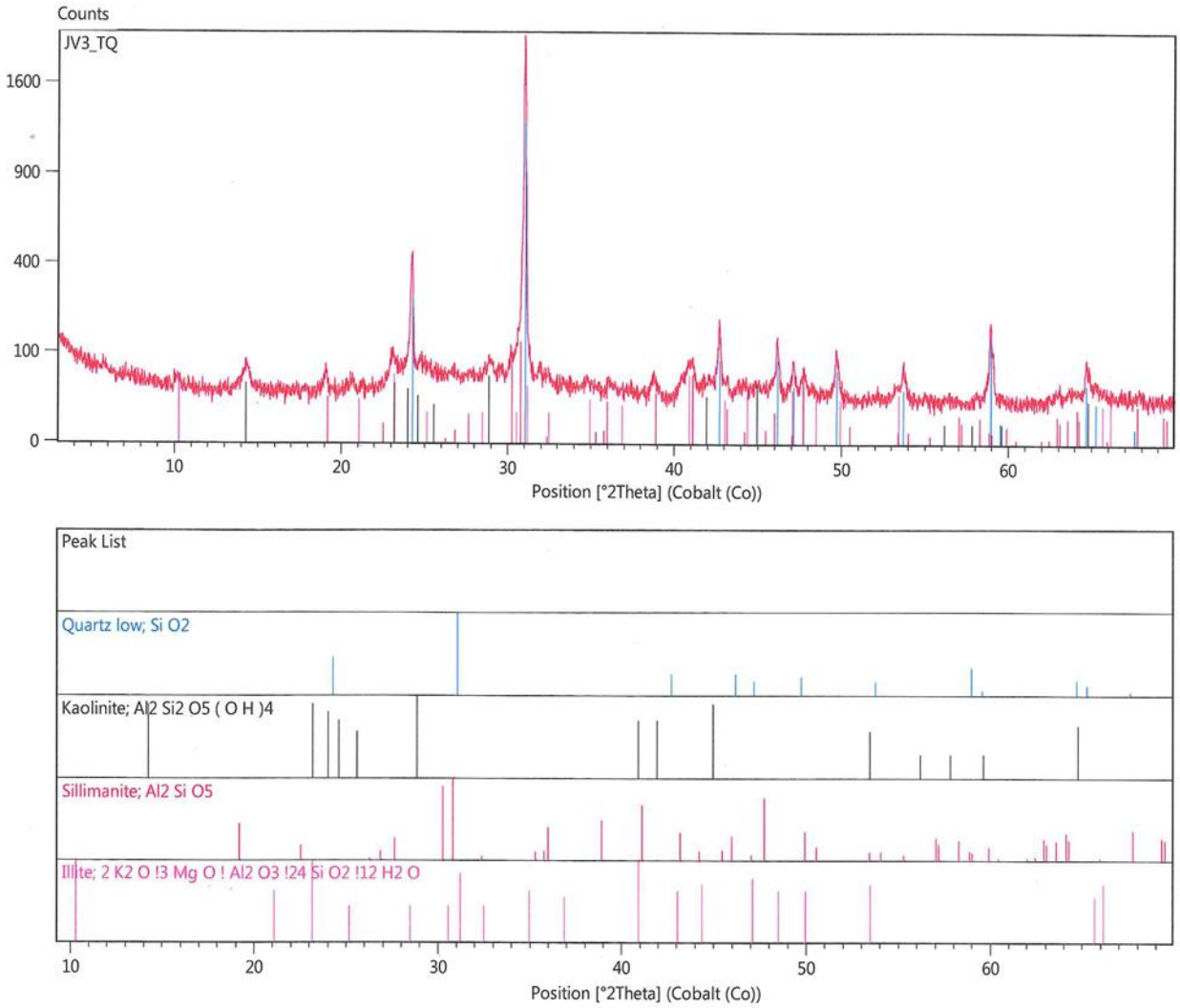

Figure 4: Crude clay

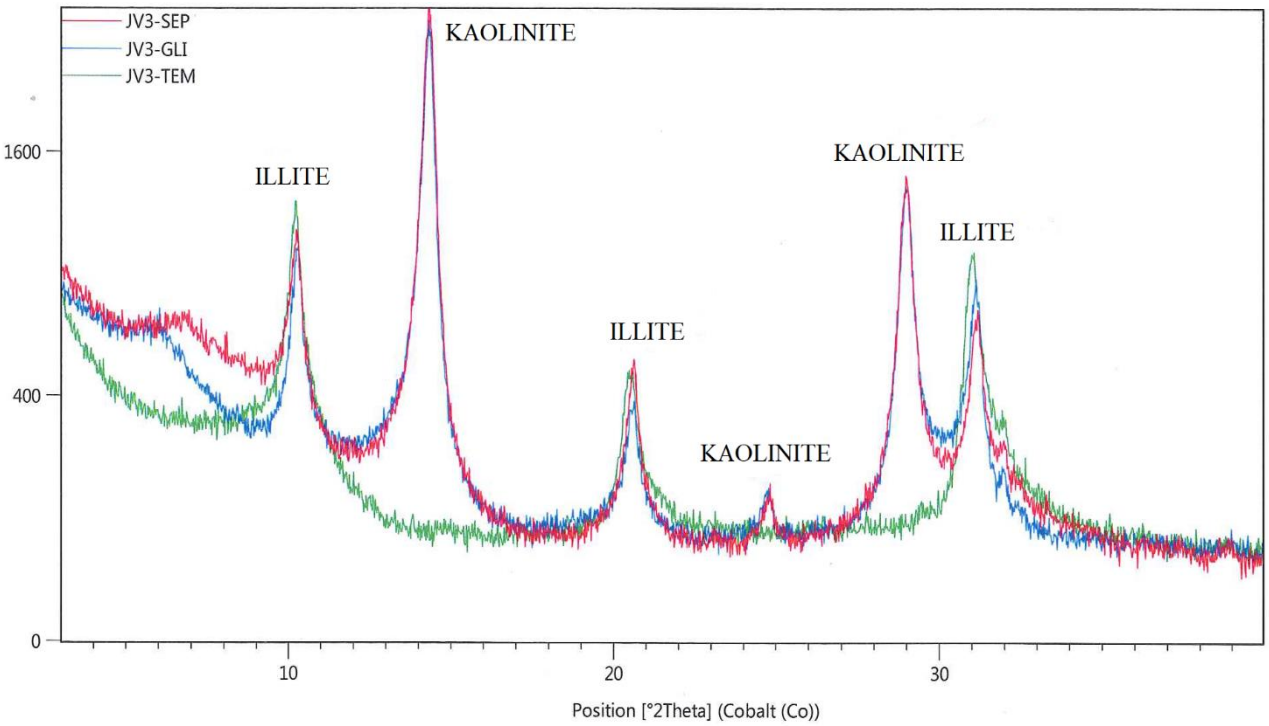

Figure 6: Crude clay

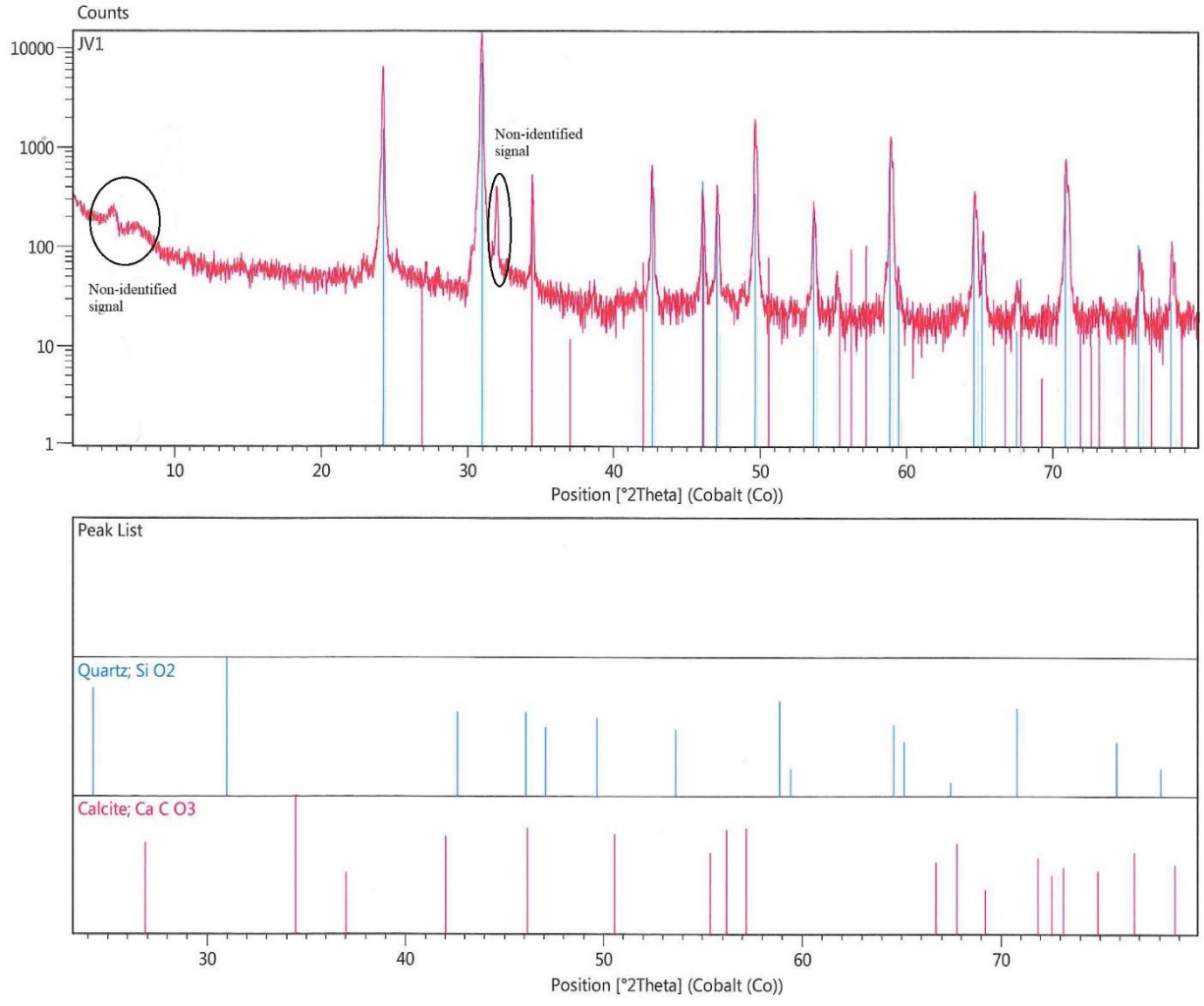

Figure 5: Sand

A1.3. NEEDLE PROBE ANALYSIS (DISTAV) - Determination of the thermal properties of the fired clay and the sand at ambient temperature

Prof. M. VERDOYA - DISTAV

Sample/ Measure	*Mass m (g)*	*Height h (cm)*	*Diameter d (cm)*	*Radius r (cm)*	*Area A (cm^2)*	*Volume V (cm^3)*	*Density ρ ($g.cm^{-3}$)*	*Thermal conductivity λ ($W.m^{-1}.K^{-1}$)*	*Volume heat capacity Cp ($J\ m^{-3}K^{-1}).10^6$*	*Thermal diffusivity α ($m^2s^{-1}).10^{-6}$*
Clay/1	7.1	0.7	2.5	1.3	5.0	3.6	2.0	1.2 ± 0.2	-	-
Clay/2	6.8	0.7	2.5	1.3	4.9	3.5	1.9	1.3 ± 0.2	-	-
Clay/3	14.4	1.8	2.3	1.2	4.2	7.4	1.9	-	-	-
Sand/1								0.43	1.62	0.27
Sand/2								0.38	1.42	0.27
Sand/3								0.42	1.53	0.27
Sand/4								0.43	1.58	0.27
Sand/5	47.76	2.95		2.01		37.52	1.27	0.40	1.41	0.28
Sand/6								0.39	1.54	0.25
Sand/7								0.41	1.58	0.26
Sand/8								0.42	1.58	0.27
Sand/9								0.41	1.53	0.27
Sand/10								0.02	0.08	0.01
Average								**0.37 ± 0.12**	**1.39 ± 0.46**	**0.24 ± 0.08**

Table 1: Needle probe results on the clay and the sand materials

A1.4. DIFFERENTIAL SCANNING CALORIMETRY – Evolution of the heat capacity of the sand with increase of temperature

Prof. S. DELSANTE - DCCI

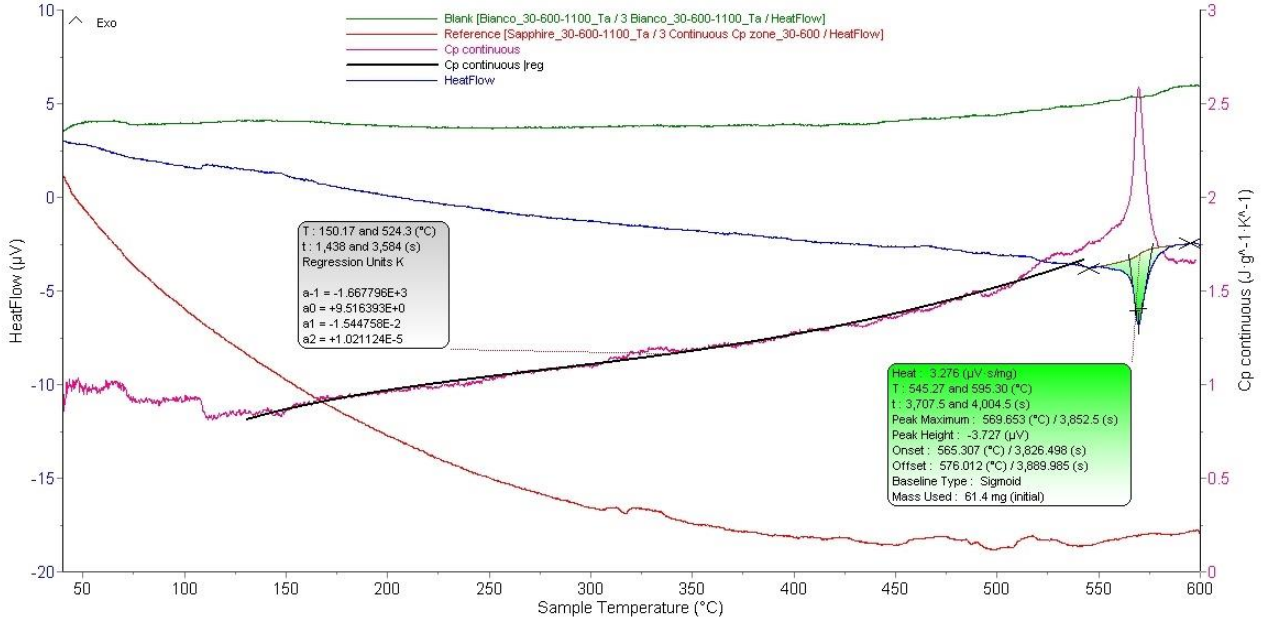

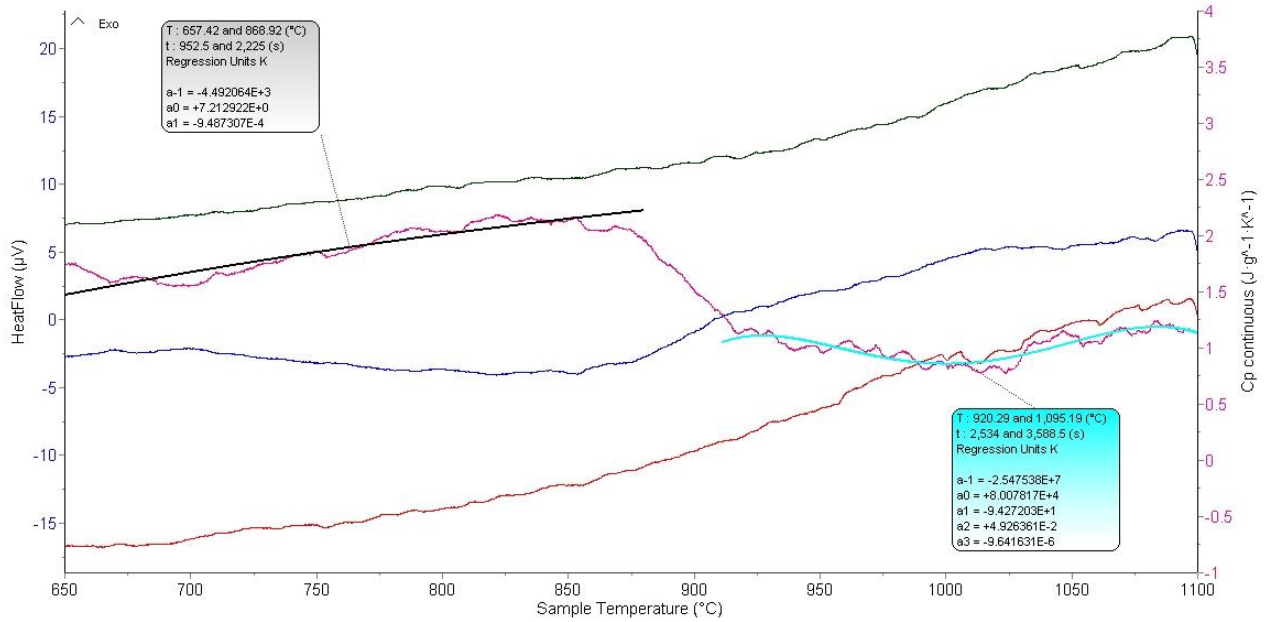

Temperature (°C)	a^{-1}	a^0	a^1	a^2	a^3	*Average Cp* $(J\ m^{-3}K^{-1}).10^6$
150.2 – 524.3	-1.67E+03	9.52E+00	-1.54E-02	1.02E-05	-	**1.24**
657.4 – 868.9	-4.49E+03	7.21E+00	-9.49E-04	-	-	**1.85**
920.3 – 1095.2	-2.55E+07	8.01E+04	-9.43E+01	4.93E-01	-9.64E-06	**2.82**

APPENDIX 2 – INVESTIGATED CORPUS OF LOYETTES

Gp L8 - LOY 03

Gp L8 - LOY 04

Gp L8 - LOY 14

Gp L8 - LOY 13

Gp L8 - LOY 30

Gp L8 - LOY 36

Gp L8 - LOY 44

Gp L8 - LOY 47

Gp L10 - LOY 12

Gp L10 - LOY 16

Gp L10 - LOY 20

Gp L10 - LOY 42

Gp L10 - LOY 46

Gp L10 - LOY 57

Gp M2 – LOY 07

Gp M2 – LOY 59

Gp L18 – LOY 58

Gp L7 – LOY 45

APPENDIX 3 – FULL (A1) + REDUCED (A2) MATRIXES

N	A	B	C	D	X1	X2 S1	X2 S2	A*B	A*C	A*D	B*C	B*D	C*D	A*B*C	A*B*D	A*C*D	B*C*D	A*B*C*D	X1²	X1*A	X1*B	X1*C	X1*D
1	1	0	0	0	-1	1	0	0	0	0	0	0	0	0	0	0	0	0	1	-1	0	0	0
2	0	1	0	0	-1	1	0	0	0	0	0	0	0	0	0	0	0	0	1	0	-1	0	0
3	0	0	1	0	-1	1	0	0	0	0	0	0	0	0	0	0	0	0	1	0	0	-1	0
4	0	0	0	1	-1	1	0	0	0	0	0	0	0	0	0	0	0	0	1	0	0	0	-1
5	0.5	0.5	0	0	-1	1	0	0.25	0	0	0	0	0	0	0	0	0	0	1	-0.5	-0.5	0	0
6	0.5	0	0.5	0	-1	1	0	0	0.25	0	0	0	0	0	0	0	0	0	1	-0.5	0	-0.5	0
7	0.5	0	0	0.5	-1	1	0	0	0	0.25	0	0	0	0	0	0	0	0	1	-0.5	0	0	-0.5
8	0	0.5	0.5	0	-1	1	0	0	0	0	0.25	0	0	0	0	0	0	0	1	0	-0.5	-0.5	0
9	0	0.5	0	0.5	-1	1	0	0	0	0	0	0.25	0	0	0	0	0	0	1	0	-0.5	0	-0.5
10	0	0	0.5	0.5	-1	1	0	0	0	0	0	0	0.25	0	0	0	0	0	1	0	0	-0.5	-0.5
11	0.33	0.33	0.33	0	-1	1	0	0.12	0.12	0	0.12	0	0	0.04	0	0	0	0	1	-0.33	-0.33	-0.33	0
12	0.33	0.33	0	0.33	-1	1	0	0.12	0	0.12	0	0.12	0	0	0.04	0	0	0	1	-0.33	-0.33	0	-0.33
13	0.33	0	0.33	0.33	-1	1	0	0	0.12	0.12	0	0	0.12	0	0	0.04	0	0	1	-0.33	0	-0.33	-0.33
14	0	0.33	0.33	0.33	-1	1	0	0	0	0	0.12	0.12	0.12	0	0	0	0.04	0	1	0	-0.33	-0.33	-0.33
15	0.25	0.25	0.25	0.25	-1	1	0	0.06	0.06	0.06	0.06	0.06	0.06	0.02	0.02	0.02	0.02	0.004	1	-0.25	-0.25	-0.25	-0.25
16	1	0	0	0	0	1	0	0	0	0	0	0	0	0	0	0	0	0	0	-1	0	0	0
17	0	1	0	0	0	1	0	0	0	0	0	0	0	0	0	0	0	0	0	0	-1	0	0
18	0	0	1	0	0	1	0	0	0	0	0	0	0	0	0	0	0	0	0	0	0	-1	0
19	0	0	0	1	0	1	0	0	0	0	0	0	0	0	0	0	0	0	0	0	0	0	-1
20	0.5	0.5	0	0	0	1	0	0.25	0	0	0	0	0	0	0	0	0	0	0	-0.5	-0.5	0	0
21	0.5	0	0.5	0	0	1	0	0	0.25	0	0	0	0	0	0	0	0	0	0	-0.5	0	-0.5	0
22	0.5	0	0	0.5	0	1	0	0	0	0.25	0	0	0	0	0	0	0	0	0	-0.5	0	0	-0.5
23	0	0.5	0.5	0	0	1	0	0	0	0	0.25	0	0	0	0	0	0	0	0	0	-0.5	-0.5	0
24	0	0.5	0	0.5	0	1	0	0	0	0	0	0.25	0	0	0	0	0	0	0	0	-0.5	0	-0.5
25	0	0	0.5	0.5	0	1	0	0	0	0	0	0	0.25	0	0	0	0	0	0	0	0	-0.5	-0.5
26	0.33	0.33	0.33	0	0	1	0	0.12	0.12	0	0.12	0	0	0.04	0	0	0	0	0	-0.33	-0.33	-0.33	0
27	0.33	0.33	0	0.33	0	1	0	0.12	0	0.12	0	0.12	0	0	0.04	0	0	0	0	-0.33	-0.33	0	-0.33
28	0.33	0	0.33	0.33	0	1	0	0	0.12	0.12	0	0	0.12	0	0	0.04	0	0	0	-0.33	0	-0.33	-0.33
29	0	0.33	0.33	0.33	0	1	0	0	0	0	0.12	0.12	0.12	0	0	0	0.04	0	0	0	-0.33	-0.33	-0.33
30	0.25	0.25	0.25	0.25	0	1	0	0.06	0.06	0.06	0.06	0.06	0.06	0.02	0.02	0.02	0.02	0.004	0	-0.25	-0.25	-0.25	-0.25
31	1	0	0	0	1	1	0	0	0	0	0	0	0	0	0	0	0	0	1	-1	0	0	0
32	0	1	0	0	1	1	0	0	0	0	0	0	0	0	0	0	0	0	1	0	-1	0	0
33	0	0	1	0	1	1	0	0	0	0	0	0	0	0	0	0	0	0	1	0	0	-1	0
34	0	0	0	1	1	1	0	0	0	0	0	0	0	0	0	0	0	0	1	0	0	0	-1
35	0.5	0.5	0	0	1	1	0	0.25	0	0	0	0	0	0	0	0	0	0	1	-0.5	-0.5	0	0
36	0.5	0	0.5	0	1	1	0	0	0.25	0	0	0	0	0	0	0	0	0	1	-0.5	0	-0.5	0
37	0.5	0	0	0.5	1	1	0	0	0	0.25	0	0	0	0	0	0	0	0	1	-0.5	0	0	-0.5
38	0	0.5	0.5	0	1	1	0	0	0	0	0.25	0	0	0	0	0	0	0	1	0	-0.5	-0.5	0
39	0	0.5	0	0.5	1	1	0	0	0	0	0	0.25	0	0	0	0	0	0	1	0	-0.5	0	-0.5
40	0	0	0.5	0.5	1	1	0	0	0	0	0	0	0.25	0	0	0	0	0	1	0	0	-0.5	-0.5
41	0.33	0.33	0.33	0	1	1	0	0.12	0.12	0	0.12	0	0	0.04	0	0	0	0	1	-0.33	-0.33	-0.33	0
42	0.33	0.33	0	0.33	1	1	0	0.12	0	0.12	0	0.12	0	0	0.04	0	0	0	1	-0.33	-0.33	0	-0.33
43	0.33	0	0.33	0.33	1	1	0	0	0.12	0.12	0	0	0.12	0	0	0.04	0	0	1	-0.33	0	-0.33	-0.33
44	0	0.33	0.33	0.33	1	1	0	0	0	0	0.12	0.12	0.12	0	0	0	0.04	0	1	0	-0.33	-0.33	-0.33
45	0.25	0.25	0.25	0.25	1	1	0	0.06	0.06	0.06	0.06	0.06	0.06	0.02	0.02	0.02	0.02	0.004	1	-0.25	-0.25	-0.25	-0.25
46	1	0	0	0	-1	0	1	0	0	0	0	0	0	0	0	0	0	0	1	-1	0	0	0
47	0	1	0	0	-1	0	1	0	0	0	0	0	0	0	0	0	0	0	1	0	-1	0	0
48	0	0	1	0	-1	0	1	0	0	0	0	0	0	0	0	0	0	0	1	0	0	-1	0
49	0	0	0	1	-1	0	1	0	0	0	0	0	0	0	0	0	0	0	1	0	0	0	-1
50	0.5	0.5	0	0	-1	0	1	0.25	0	0	0	0	0	0	0	0	0	0	1	-0.5	-0.5	0	0
51	0.5	0	0.5	0	-1	0	1	0	0.25	0	0	0	0	0	0	0	0	0	1	-0.5	0	-0.5	0

52	0.5	0	0	0.5	-1	0	1	0	0	0.25	0	0	0	0	0	0	0	0	1	-0.5	0	0	-0.5
53	0	0.5	0.5	0	-1	0	1	0	0	0	0.25	0	0	0	0	0	0	0	1	0	-0.5	-0.5	0
54	0	0.5	0	0.5	-1	0	1	0	0	0	0	0.25	0	0	0	0	0	0	1	0	-0.5	0	-0.5
55	0	0	0.5	0.5	-1	0	1	0	0	0	0	0	0.25	0	0	0	0	0	1	0	0	-0.5	-0.5
56	0.33	0.33	0.33	0	-1	0	1	0.12	0.12	0	0.12	0	0	0.04	0	0	0	0	1	-0.33	-0.33	-0.33	0
57	0.33	0.33	0	0.33	-1	0	1	0.12	0	0.12	0	0.12	0	0	0.04	0	0	0	1	-0.33	-0.33	0	-0.33
58	0.33	0	0.33	0.33	-1	0	1	0	0.12	0.12	0	0	0.12	0	0	0.04	0	0	1	-0.33	0	-0.33	-0.33
59	0	0.33	0.33	0.33	-1	0	1	0	0	0	0.12	0.12	0.12	0	0	0	0.04	0	1	0	-0.33	-0.33	-0.33
60	0.25	0.25	0.25	0.25	-1	0	1	0.06	0.06	0.06	0.06	0.06	0.06	0.02	0.02	0.02	0.02	0.004	1	-0.25	-0.25	-0.25	-0.25
61	1	0	0	0	0	0	1	0	0	0	0	0	0	0	0	0	0	0	0	-1	0	0	0
62	0	1	0	0	0	0	1	0	0	0	0	0	0	0	0	0	0	0	0	0	-1	0	0
63	0	0	1	0	0	0	1	0	0	0	0	0	0	0	0	0	0	0	0	0	0	-1	0
64	0	0	0	1	0	0	1	0	0	0	0	0	0	0	0	0	0	0	0	0	0	0	-1
65	0.5	0.5	0	0	0	0	1	0.25	0	0	0	0	0	0	0	0	0	0	0	-0.5	-0.5	0	0
66	0.5	0	0.5	0	0	0	1	0	0.25	0	0	0	0	0	0	0	0	0	0	-0.5	0	-0.5	0
67	0.5	0	0	0.5	0	0	1	0	0	0.25	0	0	0	0	0	0	0	0	0	-0.5	0	0	-0.5
68	0	0.5	0.5	0	0	0	1	0	0	0	0.25	0	0	0	0	0	0	0	0	0	-0.5	-0.5	0
69	0	0.5	0	0.5	0	0	1	0	0	0	0	0.25	0	0	0	0	0	0	0	0	-0.5	0	-0.5
70	0	0	0.5	0.5	0	0	1	0	0	0	0	0	0.25	0	0	0	0	0	0	0	0	-0.5	-0.5
71	0.33	0.33	0.33	0	0	0	1	0.12	0.12	0	0.12	0	0	0.04	0	0	0	0	0	-0.33	-0.33	-0.33	0
72	0.33	0.33	0	0.33	0	0	1	0.12	0	0.12	0	0.12	0	0	0.04	0	0	0	0	-0.33	-0.33	0	-0.33
73	0.33	0	0.33	0.33	0	0	1	0	0.12	0.12	0	0	0.12	0	0	0.04	0	0	0	-0.33	0	-0.33	-0.33
74	0	0.33	0.33	0.33	0	0	1	0	0	0	0.12	0.12	0.12	0	0	0	0.04	0	0	0	-0.33	-0.33	-0.33
75	0.25	0.25	0.25	0.25	0	0	1	0.06	0.06	0.06	0.06	0.06	0.06	0.02	0.02	0.02	0.02	0.004	0	-0.25	-0.25	-0.25	-0.25
76	1	0	0	0	1	0	1	0	0	0	0	0	0	0	0	0	0	0	1	-1	0	0	0
77	0	1	0	0	1	0	1	0	0	0	0	0	0	0	0	0	0	0	1	0	-1	0	0
78	0	0	1	0	1	0	1	0	0	0	0	0	0	0	0	0	0	0	1	0	0	-1	0
79	0	0	0	1	1	0	1	0	0	0	0	0	0	0	0	0	0	0	1	0	0	0	-1
80	0.5	0.5	0	0	1	0	1	0.25	0	0	0	0	0	0	0	0	0	0	1	-0.5	-0.5	0	0
81	0.5	0	0.5	0	1	0	1	0	0.25	0	0	0	0	0	0	0	0	0	1	-0.5	0	-0.5	0
82	0.5	0	0	0.5	1	0	1	0	0	0.25	0	0	0	0	0	0	0	0	1	-0.5	0	0	-0.5
83	0	0.5	0.5	0	1	0	1	0	0	0	0.25	0	0	0	0	0	0	0	1	0	-0.5	-0.5	0
84	0	0.5	0	0.5	1	0	1	0	0	0	0	0.25	0	0	0	0	0	0	1	0	-0.5	0	-0.5
85	0	0	0.5	0.5	1	0	1	0	0	0	0	0	0.25	0	0	0	0	0	1	0	0	-0.5	-0.5
86	0.33	0.33	0.33	0	1	0	1	0.12	0.12	0	0.12	0	0	0.04	0	0	0	0	1	-0.33	-0.33	-0.33	0
87	0.33	0.33	0	0.33	1	0	1	0.12	0	0.12	0	0.12	0	0	0.04	0	0	0	1	-0.33	-0.33	0	-0.33
88	0.33	0	0.33	0.33	1	0	1	0	0.12	0.12	0	0	0.12	0	0	0.04	0	0	1	-0.33	0	-0.33	-0.33
89	0	0.33	0.33	0.33	1	0	1	0	0	0	0.12	0.12	0.12	0	0	0	0.04	0	1	0	-0.33	-0.33	-0.33
90	0.25	0.25	0.25	0.25	1	0	1	0.06	0.06	0.06	0.06	0.06	0.06	0.02	0.02	0.02	0.02	0.004	1	-0.25	-0.25	-0.25	-0.25
91	1	0	0	0	-1	0	0	0	0	0	0	0	0	0	0	0	0	0	1	-1	0	0	0
92	0	1	0	0	-1	0	0	0	0	0	0	0	0	0	0	0	0	0	1	0	-1	0	0
93	0	0	1	0	-1	0	0	0	0	0	0	0	0	0	0	0	0	0	1	0	0	-1	0
94	0	0	0	1	-1	0	0	0	0	0	0	0	0	0	0	0	0	0	1	0	0	0	-1
95	0.5	0.5	0	0	-1	0	0	0.25	0	0	0	0	0	0	0	0	0	0	1	-0.5	-0.5	0	0
96	0.5	0	0.5	0	-1	0	0	0	0.25	0	0	0	0	0	0	0	0	0	1	-0.5	0	-0.5	0
97	0.5	0	0	0.5	-1	0	0	0	0	0.25	0	0	0	0	0	0	0	0	1	-0.5	0	0	-0.5
98	0	0.5	0.5	0	-1	0	0	0	0	0	0.25	0	0	0	0	0	0	0	1	0	-0.5	-0.5	0
99	0	0.5	0	0.5	-1	0	0	0	0	0	0	0.25	0	0	0	0	0	0	1	0	-0.5	0	-0.5
100	0	0	0.5	0.5	-1	0	0	0	0	0	0	0	0.25	0	0	0	0	0	1	0	0	-0.5	-0.5
101	0.33	0.33	0.33	0	-1	0	0	0.12	0.12	0	0.12	0	0	0.04	0	0	0	0	1	-0.33	-0.33	-0.33	0
102	0.33	0.33	0	0.33	-1	0	0	0.12	0	0.12	0	0.12	0	0	0.04	0	0	0	1	-0.33	-0.33	0	-0.33
103	0.33	0	0.33	0.33	-1	0	0	0	0.12	0.12	0	0	0.12	0	0	0.04	0	0	1	-0.33	0	-0.33	-0.33

104	0	0.33	0.33	0.33	-1	0	0	0	0	0	0.12	0.12	0.12	0	0	0	0.04	0	1	0	-0.33	-0.33	-0.33
105	0.25	0.25	0.25	0.25	-1	0	0	0.06	0.06	0.06	0.06	0.06	0.06	0.02	0.02	0.02	0.02	0.004	1	-0.25	-0.25	-0.25	-0.25
106	1	0	0	0	0	0	0	0	0	0	0	0	0	0	0	0	0	0	0	-1	0	0	0
107	0	1	0	0	0	0	0	0	0	0	0	0	0	0	0	0	0	0	0	0	-1	0	0
108	0	0	1	0	0	0	0	0	0	0	0	0	0	0	0	0	0	0	0	0	0	-1	0
109	0	0	0	1	0	0	0	0	0	0	0	0	0	0	0	0	0	0	0	0	0	0	-1
110	0.5	0.5	0	0	0	0	0	0.25	0	0	0	0	0	0	0	0	0	0	0	-0.5	-0.5	0	0
111	0.5	0	0.5	0	0	0	0	0	0.25	0	0	0	0	0	0	0	0	0	0	-0.5	0	-0.5	0
112	0.5	0	0	0.5	0	0	0	0	0	0.25	0	0	0	0	0	0	0	0	0	-0.5	0	0	-0.5
113	0	0.5	0.5	0	0	0	0	0	0	0	0.25	0	0	0	0	0	0	0	0	0	-0.5	-0.5	0
114	0	0.5	0	0.5	0	0	0	0	0	0	0	0.25	0	0	0	0	0	0	0	0	-0.5	0	-0.5
115	0	0	0.5	0.5	0	0	0	0	0	0	0	0	0.25	0	0	0	0	0	0	0	0	-0.5	-0.5
116	0.33	0.33	0.33	0	0	0	0	0.12	0.12	0	0.12	0	0	0.04	0	0	0	0	0	-0.33	-0.33	-0.33	0
117	0.33	0.33	0	0.33	0	0	0	0.12	0	0.12	0	0.12	0	0	0.04	0	0	0	0	-0.33	-0.33	0	-0.33
118	0.33	0	0.33	0.33	0	0	0	0	0.12	0.12	0	0	0.12	0	0	0.04	0	0	0	-0.33	0	-0.33	-0.33
119	0	0.33	0.33	0.33	0	0	0	0	0	0	0.12	0.12	0.12	0	0	0	0.04	0	0	0	-0.33	-0.33	-0.33
120	0.25	0.25	0.25	0.25	0	0	0	0.06	0.06	0.06	0.06	0.06	0.06	0.02	0.02	0.02	0.02	0.004	0	-0.25	-0.25	-0.25	-0.25
121	1	0	0	0	1	0	0	0	0	0	0	0	0	0	0	0	0	0	1	-1	0	0	0
122	0	1	0	0	1	0	0	0	0	0	0	0	0	0	0	0	0	0	1	0	-1	0	0
123	0	0	1	0	1	0	0	0	0	0	0	0	0	0	0	0	0	0	1	0	0	-1	0
124	0	0	0	1	1	0	0	0	0	0	0	0	0	0	0	0	0	0	1	0	0	0	-1
125	0.5	0.5	0	0	1	0	0	0.25	0	0	0	0	0	0	0	0	0	0	1	-0.5	-0.5	0	0
126	0.5	0	0.5	0	1	0	0	0	0.25	0	0	0	0	0	0	0	0	0	1	-0.5	0	-0.5	0
127	0.5	0	0	0.5	1	0	0	0	0	0.25	0	0	0	0	0	0	0	0	1	-0.5	0	0	-0.5
128	0	0.5	0.5	0	1	0	0	0	0	0	0.25	0	0	0	0	0	0	0	1	0	-0.5	-0.5	0
129	0	0.5	0	0.5	1	0	0	0	0	0	0	0.25	0	0	0	0	0	0	1	0	-0.5	0	-0.5
130	0	0	0.5	0.5	1	0	0	0	0	0	0	0	0.25	0	0	0	0	0	1	0	0	-0.5	-0.5
131	0.33	0.33	0.33	0	1	0	0	0.12	0.12	0	0.12	0	0	0.04	0	0	0	0	1	-0.33	-0.33	-0.33	0
132	0.33	0.33	0	0.33	1	0	0	0.12	0	0.12	0	0.12	0	0	0.04	0	0	0	1	-0.33	-0.33	0	-0.33
133	0.33	0	0.33	0.33	1	0	0	0	0.12	0.12	0	0	0.12	0	0	0.04	0	0	1	-0.33	0	-0.33	-0.33
134	0	0.33	0.33	0.33	1	0	0	0	0	0	0.12	0.12	0.12	0	0	0	0.04	0	1	0	-0.33	-0.33	-0.33
135	0.25	0.25	0.25	0.25	1	0	0	0.06	0.06	0.06	0.06	0.06	0.06	0.02	0.02	0.02	0.02	0.004	1	-0.25	-0.25	-0.25	-0.25

APPENDIX 4 – FINAL EXPERIMENTAL MATRIX (A3)

N	A	B	C	D	X1	S1	S2	A*B	A*C	A*D	B*C	B*D	C*D	A*B*C	A*B*D	A*C*D	B*C*D	X1²	**Sample**
1	1	0	0	0	-1	1	0	0	0	0	0	0	0	0	0	0	0	1	**3_30**
2	0	1	0	0	-1	1	0	0	0	0	0	0	0	0	0	0	0	1	**11_3**
5	0.5	0.5	0	0	-1	1	0	0.25	0	0	0	0	0	0	0	0	0	1	**14_82**
6	0	0	0.5	0.5	-1	1	0	0	0	0	0	0	0.25	0	0	0	0	1	**1_6**
7	0.5	0	0	0.5	-1	1	0	0	0	0.25	0	0	0	0	0	0	0	1	**1_109**
12	0.33	0.33	0	0.33	-1	1	0	0.1089	0	0.1089	0	0.1089	0	0	0.035937	0	0	1	**7_164**
19	0	0	0	1	0	1	0	0	0	0	0	0	0	0	0	0	0	0	**2_58**
22	0.33	0	0.33	0.33	0	1	0	0	0.1089	0.1089	0	0	0.1089	0	0	0.035937	0	0	**2_22**
31	1	0	0	0	1	1	0	0	0	0	0	0	0	0	0	0	0	1	**20_34**
32	0	1	0	0	1	1	0	0	0	0	0	0	0	0	0	0	0	1	**19_8**
34	0	0.33	0.33	0.33	1	1	0	0	0	0	0.1089	0.1089	0.1089	0	0	0	0.035937	1	**3_34**
35	0.5	0.5	0	0	1	1	0	0.25	0	0	0	0	0	0	0	0	0	1	**15_88**
38	0	0	1	0	-1	0	1	0	0	0	0	0	0	0	0	0	0	1	**4_38**
39	0	0.5	0	0.5	1	1	0	0	0	0	0	0.25	0	0	0	0	0	1	**18_144**
47	0.33	0	0.33	0.33	-1	0	1	0	0.1089	0.1089	0	0	0.1089	0	0	0.035937	0	1	**5_47**
50	1	0	0	0	0	0	1	0	0	0	0	0	0	0	0	0	0	0	**6_50**
54	0	0.5	0	0.5	-1	0	1	0	0	0	0	0.25	0	0	0	0	0	1	**4_146**
56	0	0.5	0.5	0	0	0	1	0	0	0	0.25	0	0	0	0	0	0	0	**7_56**
67	0.5	0	0	0.5	0	0	1	0	0	0.25	0	0	0	0	0	0	0	0	**24_123**
68	0.5	0	0.5	0	1	0	1	0	0.25	0	0	0	0	0	0	0	0	1	**8_68**
73	0.33	0.33	0.33	0	1	0	1	0.1089	0.1089	0	0.1089	0	0	0.035937	0	0	0	1	**9_73**
74	0.33	0.33	0	0.33	1	0	1	0.1089	0	0.1089	0	0.1089	0	0	0.035937	0	0	1	**10_74**
77	0	1	0	0	1	0	1	0	0	0	0	0	0	0	0	0	0	1	**17_16**
89	0	0.33	0.33	0.33	-1	0	0	0	0	0	0.1089	0.1089	0.1089	0	0	0	0.035937	1	**11_89**
93	0	0	1	0	0	0	0	0	0	0	0	0	0	0	0	0	0	0	**12_93**
95	0.5	0.5	0	0	-1	0	0	0.25	0	0	0	0	0	0	0	0	0	1	**13_102**
96	0.5	0	0.5	0	0	0	0	0	0.25	0	0	0	0	0	0	0	0	0	**13_96**
97	0.5	0	0	0.5	-1	0	0	0	0	0.25	0	0	0	0	0	0	0	1	**6_129**
99	0	0.5	0	0.5	-1	0	0	0	0	0	0	0.25	0	0	0	0	0	1	**28_154**
100	0	0	0.5	0.5	0	0	0	0	0	0	0	0	0.25	0	0	0	0	0	**14_100**
101	0.33	0.33	0.33	0	0	0	0	0.1089	0.1089	0	0.1089	0	0	0.035937	0	0	0	0	**15_101**
108	0	0	0	1	1	0	0	0	0	0	0	0	0	0	0	0	0	1	**16_108**
112	0	0.5	0.5	0	1	0	0	0	0	0	0.25	0	0	0	0	0	0	1	**17_112**
122	0	1	0	0	1	0	0	0	0	0	0	0	0	0	0	0	0	1	**22_27**

APPENDIX 5 – LIST OF THE EXPERIMENTAL DESING SAMPLES

A5.1. SAMPLES OF EXPERIMENTAL DESIGN

Composition		*Sample*	*Mould*	*Superheat*	*Melting point*	*Pouring Temp.*
A	Cu 100	3 - 30	Steel	+ 25°C	1083 °C	1110 °C
		20 - 34	Steel	+ 75°C	1083 °C	1150 °C
		6 – 50	Clay	+ 50°C	1083 °C	1133 °C
B	Cu Sn20	11-3	Steel	+ 25°C	910 °C	935 °C
		19-8	Steel	+ 75°C	910 °C	985 °C
		17-16	Clay	+ 75°C	910 °C	985 °C
		22-27	Sand	+ 75°C	910 °C	985 °C
C	Cu Zn20	4-38	Clay	+ 25°C	1000 °C	1025 °C
		12-93	Sand	+ 50°C	1000 °C	1050 °C
D	Cu Pb20	2-58	Steel	+ 50°C	1000 °C	1050 °C
		16-108	Sand	+ 75°C	1000 °C	1075 °C
E	Cu Sn10	13-102	Sand	+ 25°C	1011 °C	1036 °C
		14-82	Steel	+ 25°C	1011 °C	1036 °C
		15-88	Steel	+ 75°C	1011 °C	1086 °C
F	Cu Zn10	8-68	Clay	+ 75°C	1045 °C	1120 °C
		13-96	Sand	+ 50°C	1045 °C	1095 °C
G	Cu Pb10	1-109	Steel	+ 25°C	1020 °C	1045 °C
		6-129	Sand	+ 25°C	1020 °C	1045 °C
		24-123	Clay	+ 50°C	1020 °C	1070 °C
H	Cu Sn10 Zn10	7-56	Clay	+ 50°C	880 °C	930 °C
		17-112	Sand	+ 75°C	880 °C	955 °C
I	Cu Sn10 Pb10	4-146	Clay	+ 25°C	964 °C	989 °C
		18-144	Steel	+ 75°C	964 °C	1039 °C
J	Cu Zn10 Pb10	1-6	Steel	+ 25°C	1000 °C	1025 °C
		14-100	Sand	+ 50°C	1000 °C	1050 °C
K	Cu Sn6.7 Zn6.7	9-73	Clay	+ 75°C	983 °C	1058 °C
		15-101	Sand	+ 50°C	983 °C	1033 °C
L	Cu Sn6.7 Pb6.7	7-164	Steel	+ 25°C	1000 °C	1025 °C
		5-47	Clay	+ 75°C	1000 °C	1075 °C
M	Cu Zn6.7 Pb6.7	2-22	Steel	+ 50°C	1025 °C	1075 °C
		10-74	Clay	+ 25°C	1025 °C	1050 °C
N	Cu Sn6.7 Zn6.7 Pb6.7	3-34	Steel	+ 75°C	c. 1010 °C	1085 °C
		11-89	Sand	+ 25°C	c. 1010 °C	1035 °C

A5.2. REPLICATE SAMPLES

Composition		*Sample*	*Mould*	*Superheat*	*Melting point*	*Pouring Temp.*
B	Cu Sn20	19-8	Steel	+ 75°C	910 °C	985 °C
D	Cu Pb20	26-60	Steel	+ 50°C	1000 °C	1050 °C
G	Cu Pb10	1-109	Steel	+ 25°C	1020 °C	1045 °C

A5.3. VERIFICATION SAMPLES

Composition		*Sample*	*Mould*	*Superheat*	*Melting point*	*Pouring Temp.*
C	Cu Zn20	DTA 20	Steel	+ 25°C	1000 °C	1025 °C
E	Cu Sn10	D-hl	Clay	+ 25°C	1011 °C	1036 °C
F	Cu Zn10	DTA 10	Steel	+ 25°C	1045 °C	1065 °C
i	Cu Sn10 Pb10	28-154	Sand	+ 25°C	964 °C	989 °C

APPENDIX 6 – TRANSITION TEMPERATURES IDENTIFIED BY DTA

A6.1. THE CU-SN SYSTEM

Sample	*Equilibrium liquidus*[3]	*3K/min*	*5K/min*	*10K/min*	*20K/min*	*30K/min*
CuSn 3	≈ 1060	-	1057.0	1055.5	1054.0	1052.8
CuSn 5	≈ 1045	-	1043.7	1043.8	1042.4	-
CuSn 8	≈ 1015	1013.2	1014.1	1013.6	1012.3	1012.1
CuSn 10	≈ 995	-	1000.0	992.3	998.4	997.8
CuSn 12	≈ 975	-	983.2	981.2	979.6	979.5
CuSn 14	≈ 950	-	959.7	958.2	958.0	958.0
CuSn 20	≈ 900	-	869.3	868.2	871.1	872.6

Sample	*Attribution*	*Equilibrium*[1]	*3K/min*	*5K/min*	*10K/min*	*20K/min*	*30K/min*
CuSn 3	solidus	≈ 1010	-	1009.8	990.1	973.7	949.2
CuSn 5	solidus	≈ 975	-	975.5	970.3	966.8	957.7
CuSn 8		≈ 900	983.4	967.8	780.1	781.3	782.3
	peritectic	798	778.0	778.9			
CuSn 10		≈ 860		788.5	780.6	788.9	788.5
CuSn 12		≈ 830	-	788.0	788.1	788.5	788.8
CuSn 14	peritectic	798	-	789.0	788.9	789.0	788.7
CuSn 20	peritectic	798	-	779.6	779.2	781.2	781.6

Table 2: Modification of the transformations temperature with an increase of the cooling rate

[3] From Fürtauer et al, 2013

A6.2. THE CU-ZN SYSTEM

Sample	*Equilibrium Liquidus*	*Liquidus at 3 K.min^{-1}*	*Liquidus at 10 K.min^{-1}*	*Liquidus at 30 K.min^{-1}*
CuZn 5	1077 °C	1060 °C	1061 °C	1058 °C
CuZn 10	1059 °C	1038 °C	1036 °C	1033 °C
CuZn 20	1019 °C	991 °C	992 °C	991 °C
CuZn 30	967 °C	947 °C	948 °C	948 °C
CuZn 40	899 °C	890 °C	890 °C	890 °C

Sample	*Equilibrium Solidus*	*Solidus at 3 K.min^{-1}*	*Solidus at 10 K.min^{-1}*	*Solidus at 30 K.min^{-1}*
CuZn 5	1065 °C	1039 °C	1022 °C	983 °C
CuZn 10	1041 °C	1005 °C	988 °C	945 °C
CuZn 20	988 °C	951 °C	941 °C	912 °C
CuZn 30	924 °C	896 °C	881 °C	858 °C
CuZn 40	893 °C	871 °C	847 °C	805 °C

Sample	*Equilibrium*			
CuZn 30	**Peritectic $L + \alpha \rightarrow \beta$**	**at 3 K.min^{-1}**	**at 10 K.min^{-1}**	**at 30 K.min^{-1}**
	-	-	892 °C	890 °C
CuZn 40	**Peritectic $L + \alpha \rightarrow \beta$**	**at 3 K.min^{-1}**	**at 10 K.min^{-1}**	**at 30 K.min^{-1}**
	902 °C			
	$\beta \rightarrow \alpha + \beta$	**at 3 K.min^{-1}**	**at 10 K.min^{-1}**	**at 30 K.min^{-1}**
	786 °C	783 °C	779 °C	770 °C
	$\alpha + \beta \rightarrow \alpha + \beta'$	**at 3 K.min^{-1}**	**at 10 K.min^{-1}**	**at 30 K.min^{-1}**
	454 °C	438 °C	444 °C	450 °C

Table 3: Modification of the transformations temperature with an increase of the cooling rate

APPENDIX 7 – PERCENTAGE ERROR ON THE COMPOSITION OF DOE SAMPLES

Sample	*Alloy*	*% Error Cu*	*% Error Sn*	*% Error Zn*	*% Error Pb*
3 – 30	Cu	0.0 %	-	-	-
20 – 34	Cu	- 0.3 %	-	-	-
6 – 50	Cu	- 0.1 %	-	-	-
11 – 3	CuSn20	- 1.3 %	0.0 %	-	-
19 – 8	CuSn20	- 1.4 %	5.0 %	-	-
19-8R	CuSn20	*missing data*			
17 – 16	CuSn20	- 1.6 %	5.0 %	-	-
22 – 27	CuSn20	- 2.0 %	7.0 %	-	-
DTA 20	CuZn20	- 0.6 %	-	1.0 %	-
4 – 38	CuZn20	- 1.4 %	-	3.5 %	-
12 – 93	CuZn20	- 0.5 %	-	1.0 %	-
2 – 58	CuPb20	- 0.3 %	-	-	- 1.0 %
26 – 60	CuPb20	3.5 %	-	-	9.5 %
16 – 108	CuPb20	6.0 %	-	-	**- 25.0 %**
14 – 82	CuSn10	- 0.2 %	0.0 %	-	-
15 – 88	CuSn10	0.7 %	- 7.0 %	-	-
Dhl	CuSn10	- 0.9 %	3.0 %	-	-
13 – 102	CuSn10	- 0.8 %	4.0 %	-	-
DTA 10	CuZn10	- 0.3 %	-	1.0 %	-
8 – 68	CuZn10	- 0.8 %	-	2.0 %	-
13 – 96	CuZn10	- 0.8 %	-	5.0 %	-
1 – 109	CuPb10	- 1.3 %	-	-	8.0 %
1-109R	CuPb10	*missing data*			
24 – 123	CuPb10	- 0.1 %	-	-	**- 13.0 %**
6 – 129	CuPb10	- 2.6 %	-	-	**12.0 %**
7 – 56	CuSn10Zn10	- 6.3 %	**23.0 %**	**24.0 %**	-
17 – 112	CuSn10Zn10	- 5.7 %	**24.0 %**	**21.0 %**	-
4 – 146	CuSn10Pb10	1.8 %	3.0 %	-	**- 20.0 %**
18 – 144	CuSn10Pb10	0.1 %	- 1.0 %	-	- 3.0 %
28 – 154	CuSn10Pb10	2.0 %	1.0 %	-	**- 24.0 %**
1 – 6	CuZn10Pb10	**11.0 %**	-	**- 51.0 %**	**- 39.0 %**
14 – 100	CuZn10Pb10	0.9 %	-	0.0 %	- 8.0 %
9 – 73	CuSn6.7Zn6.7	0.2 %	- 4.5 %	0.0 %	-
15 – 101	CuSn6.7Zn6.7	- 0.1 %	- 3.0 %	- 1.5 %	-
7 – 164	CuSn6.7Pb6.7	*missing data*			
5 - 47	CuSn6.7Pb6.7	0.0 %	- 4.5 %	-	- 1.5 %
2 – 22	CuZn6.7Pb6.7	- 1.2 %	-	**- 10.4 %**	**23.9 %**
10 – 74	CuZn6.7Pb6.7	- 0.9 %	-	7.5 %	- 6.0 %
3 – 34	CuSn6.7Zn6.7Pb6.7	4.3 %	**- 23.9 %**	**- 26.9 %**	- 3.0 %
11 – 89	CuSn6.7Zn6.7Pb6.7	0.5 %	- 1.5 %	- 3.0 %	- 4.5 %

Table 4: Percentage error on the chemical composition of as-cast specimens

APPENDIX 8 – PCA MATRIX

Sample	Alloy	wt.%Sn	wt.%Zn	wt.%Pb	HV	2nd ph.	SDAS	Lenght Chill	Average grain chill	Length Columnar	Average grain columnar	Lenght Equiaxed	Average grain equiaxed	Average grain recryst
1 – 109	CuPb10	0.00	0.00	10.80	51.80	0.00	10.00	0.00	0.00	0.00	0.00	10.00	166.20	68.50
1 – 109R	CuPb10	0.00	0.00	11.60	51.10	0.00	10.00	0.00	0.00	0.00	0.00	10.00	107.70	29.60
1 – 6	CuZn10Pb10	0.00	4.90	6.10	55.10	0.00	12.00	0.33		1.11		9.60		0.00
10 – 74	CuZn6.7Pb6.7	0.00	7.20	6.30	66.90	0.00		0.00	0.00	0.00	0.00	10.00	0.00	47.30
11 – 3	CuSn20	21.00	0.00	0.00	248.70	44.70	10.00	0.80	0.80	1.80	0.70	7.70		0.00
11 – 89	CuSn6.7Pb6.7	6.60	6.50	6.40	84.10	3.80	30.00	0.00	0.00	0.00	0.00	10.00	2.30	0.00
12 – 93	CuZn20	0.00	20.20	0.00	82.60	0.00	68.00	0.00	0.00	0.00	0.00	10.00	5.40	0.00
13 – 102	CuSn10	10.40	0.00	0.00	121.60	5.30	35.00							
13 – 96	CuZn10	0.00	10.50	0.00	82.60	0.00		0.00	0.00	0.00	0.00	10.00	5.50	0.00
14 – 100	CuZn10Pb10	0.00	10.00	9.20	54.30	0.00	28.00	0.00		0.00		10.00	3.00	0.00
14 – 82	CuSn10	10.00	0.00	0.00	120.20	10.70	16.00							
15 – 101	CuSn6.7Zn6.7	6.50	6.60	0.00	92.30	2.10	35.00	0.00	0.00	0.00	0.00	10.00	0.00	47.30
15 – 88	CuSn10	9.30	0.00	0.00	124.70	9.00	12.00							
16 – 108	CuPb20	0.00	0.00	15.00	31.80	0.00	30.00	0.00	0.00	0.00	0.00	10.00	271.40	50.10
17 – 112	CuSn10Zn10	12.40	12.10	0.00	204.30	27.90	23.00	0.00	0.00	0.00	0.00	10.00	3.00	0.00
17 – 16	CuSn20	21.00	0.00	0.00	228.70	45.20	17.00	1.70	0.50	0.00	0.90	7.60	0.60	0.00
18 – 144	CuSn10Pb10	9.90	0.00	9.70	108.70	12.40	15.00		0.10				0.30	
19 – 8	CuSn20	21.00	0.00	0.00	240.60	49.70	13.00	0.50	0.20	1.20	0.90	8.10	0.60	0.00
19 – 8R	CuSn20	21.00	0.00	0.00	239.90	44.40	11.00	0.20	0.10	1.60	1.10	8.20	0.50	0.00
2 – 22	CuZn6.7Pb6.7	0.00	6.00	8.30	57.10	0.00	17.00	0.50	0.30	0.90	0.40	8.80	0.40	0.00
2 – 58	CuPb20	0.00	0.00	19.80	49.80	0.00	6.00	0.00	0.00	0.00	0.00	10.00	147.60	18.10
2 – 58R	CuPb20	0.00	0.00	21.90	57.50	0.00	8.00	0.00	0.00	0.00	0.00	10.00	101.10	13.30
20 – 34	Cu	0.00	0.00	0.00	69.50	0.00		1.40	0.60	8.30	4.90	0.00	0.00	0.00
22 – 27	CuSn20	21.40	0.00	0.00	222.70	43.50	22.00	0.00	0.00	0.00	0.00	10.00	2.10	0.00
24 – 123	CuPb10	0.00	0.00	8.70	49.40	0.00	0.00	0.00	0.00	0.00	0.00	10.00	0.00	36.30
28 – 154	CuSn10Pb10	10.10	0.00	7.60	118.40	6.10	30.00	0.00	0.00	0.00	0.00	10.00	0.30	80.00
3 – 30	Cu	0.00	0.00	0.00	57.70	0.00		1.20	0.90	8.50	4.20	0.00	0.00	0.00
3 – 34	CuSn6.7Zn6.7Pb6.7	5.10	4.90	6.50	99.30	5.90	19.00	0.10	0.05	0.90	0.30	9.00		0.00
4 – 146	CuSn10Pb10	10.30	0.00	8.00	96.60	6.20	24.00		0.10		0.00			
4 – 38	CuZn20	0.00	20.70	0.00	89.60	0.00	50.00	0.40	0.10	1.20	0.70	9.80	0.80	0.00
5_47	CuSn6.7Pb6.7	6.40	0.00	6.60	75.80	1.00	21.00	0.00	0.00	0.00	0.00	10.00	0.10	0.00
6 – 129	CuPb10	0.00	0.00	11.20	48.30	0.00	0.00	0.00	0.00	0.00	0.00	10.00	0.00	51.40
6 – 50	Cu	0.00	0.00	0.00	39.90	0.00	80.00	0.60	0.10	1.40	0.90	7.00	0.20	0.00
7 – 164	CuSn6.7Pb6.7	6.50	0.00	7.30	91.00	3.00	13.00	0.00	0.00	0.00	0.00			
7 – 56	CuSn10Zn10	12.30	12.40	0.00	192.20	28.20	17.00	0.30		1.10		9.60		0.00
8 – 68	CuZn10	0.00	10.20	0.00	73.60	0.00	38.00	0.50	0.20	1.80	1.80	8.40	1.10	0.00
9 – 73	CuSn6.7Zn6.7	6.40	6.70	0.00	74.90	3.00	31.00	0.80	0.60	0.90	0.70	8.80	0.40	0.00
Dhl	CuSn10	10.30	0.00	0.00		6.20	30.00							
DTA 10	CuZn10	0.00	10.10	0.00	84.20	0.00	21.00	0.60	0.50	1.60	1.40	7.40	0.80	0.00
DTA 20	CuZn20	0.00	20.20	0.00	98.50	0.00	22.00	0.90	0.30	1.40	0.60	9.00	0.30	0.00

APPENDIX 9 – PARAMETERS OF THE DOE COEFFICENTS

A9.1. HARDNESS MODEL

Coefficient	*Value*	*Standard Deviation*	*Significance*
α_{Cu}	50.9141	5.843	0.0000
α_{Sn}	231.4409	5.418	0.0000
α_{Zn}	87.9263	6.137	0.0000
α_{Pb}	40.3632	5.154	0.0001
α_{1}	0.1566	1.932	0.9539
α_{S1}	8.9987	3.543	0.1153
α_{S2}	-3.3523	3.827	0.5958
α_{CuSn}	-99.2564	22.196	0.0002
α_{CuZn}	41.3980	27.036	0.2651
α_{CuPb}	4.3012	21.747	0.8839
α_{SnZn}	160.9443	26.144	0.0004
α_{SnPb}	-143.7264	25.969	0.0000
α_{ZnPb}	-55.1759	26.472	0.1727
α_{CuSnZn}	-1339.8223	189.927	0.0014
α_{CuSnPb}	10.3656	185.285	0.9312
α_{CuZnPb}	29.6398	196.527	0.9604
α_{SnZnPb}	-757.8015	197.488	0.0013
$\alpha_{X1}{}^{2}$	-0.1436	3.472	0.9838

Table 5: Parameters of the coefficients for the predictive model of hardness

A9.2. SECONDRY PHASE MODEL

Coefficient	*Value*	*Standard Deviation*	*Significance*
α_{Cu}	-1.07355	1.1544	0.3586
α_{Sn}	44.21183	1.1794	0.0000
α_{Zn}	0.37390	0.9392	0.6929
α_{Pb}	-1.32282	0.9811	0.1860
α_{1}	0.74452	0.5396	0.1762
α_{S1}	1.73704	0.8509	0.0486
α_{S2}	0.24687	0.7278	0.7364
α_{CuSn}	-55.58207	6.7794	0.0000
α_{CuZn}	-0.08318	4.0171	0.9836
α_{CuPb}	4.05580	3.7532	0.2871
α_{SnZn}	21.54605	3.4978	0.0000
α_{SnPb}	-51.54526	12.6057	0.0002
α_{ZnPb}	0.41309	3.4587	0.9056
α_{CuSnZn}	-235.52495	22.5814	0.0000
α_{CuSnPb}	-15.91395	46.2808	0.7330
α_{CuZnPb}	-29.19913	31.9030	0.3662
α_{SnZnPb}	-189.86584	49.1403	0.0004
$\alpha_{X1}{}^{2}$	-0.25015	0.5253	0.6368

Table 6: Parameters of the coefficients for the predictive model of secondary phase volume percentage

A9.3. SDAS MODEL

Coefficient	*Value*	*Standard Deviation*	*Significance*
α_{Cu}	88.38902	99.226	0.3797
α_{Sn}	21.95655	6.754	0.0027
α_{Zn}	62.22863	13.485	0.0001
α_{Pb}	22.41702	6.842	0.0025
α_{1}	-0.05566	2.031	0.9783
α_{S1}	-12.53576	5.147	0.0206
α_{S2}	-8.38902	5.796	0.1575
α_{CuSn}	-110.84109	199.677	0.5827
α_{CuZn}	-122.96100	232.708	0.6009
α_{CuPb}	-173.94684	200.696	0.3925
α_{SnZn}	-75.23320	31.989	0.0250
α_{SnPb}	23.59800	26.980	0.3883
α_{ZnPb}	-68.08332	35.212	0.0621
α_{CuSnZn}	361.43098	481.658	0.4585
α_{CuSnPb}	282.78806	329.999	0.3979
α_{CuZnPb}	338.97796	612.210	0.5836
α_{SnZnPb}	187.83968	131.422	0.1626
α_{X1^2}	1.87610	6.104	0.7606

Table 7: Parameters of the coefficients for the predictive model of secondary phase volume percentage

APPENDIX 10 – ESTIMATION OF THE COOLING RATE

The numerical simulation has been tested for the cooling of a binary tin bronze (CuSn10) in the three moulds and for a superheat of 75°C. Six points of calculation have been selected: three into the mould walls (Figure 9) and three others inside the cast ingot (Figure 7).

A10.1. TEMPERATURE DECREASE INSIDE THE CAST INGOT

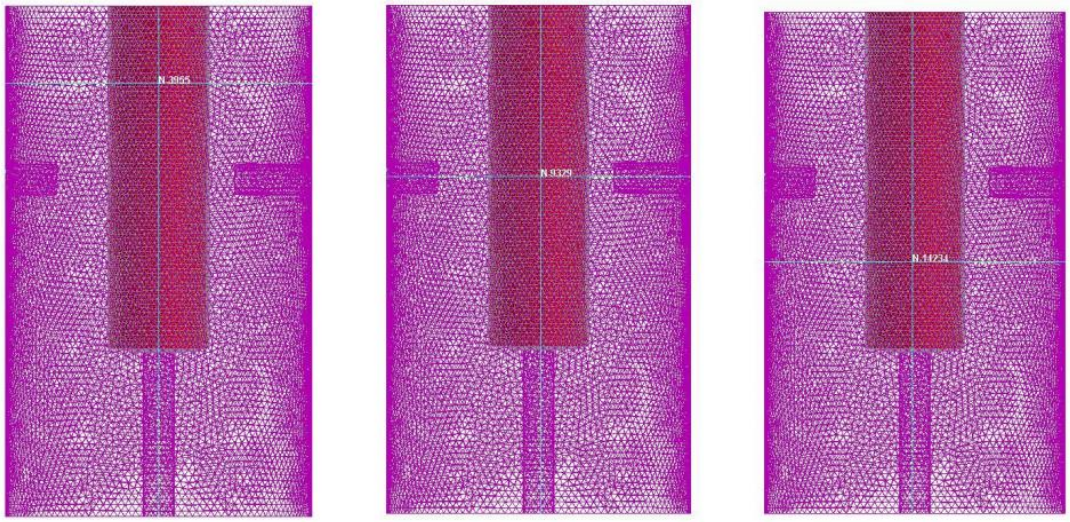

Figure 7: Points of simulation in the sample: the top, the middle and the bottom of the cast cylinder.

The computed cooling curves (Figure 8) show that, for a same mould and same superheat level, the three points of measurement inside the cylinder do not present significant differences in their thermal behaviour. This can be explained by the small dimensions of the ingot and its simple geometry.

Therefore, the temperature gradient along the vertical axe of the mould can be neglected and an unidirectional solidification in the radial direction can be assumed.

Furthermore, from these curves, it is well visible that the cooling rates implied by each mould is different one from the other. Thus, the higher cooling rate is produced, as expected, by the metallic mould, while the sand mould let the melt solidify more slowly.

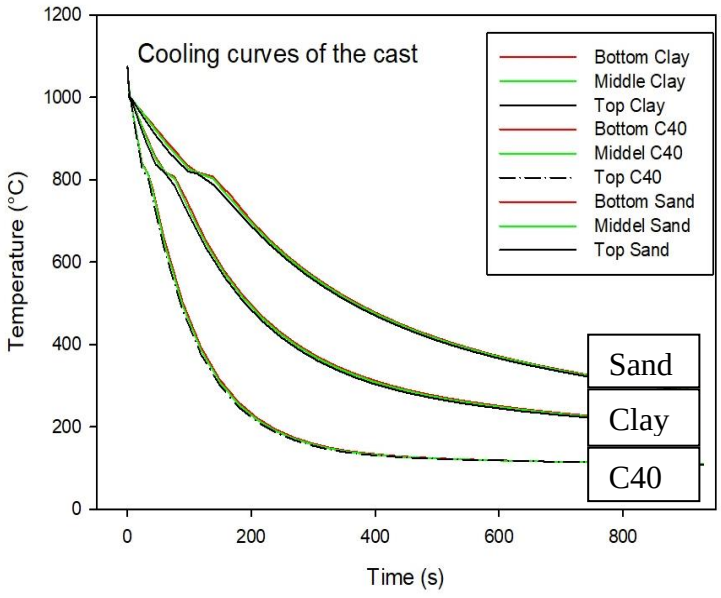

Figure 8: Computed cooling curves of the different points inside the cast and for the three mould materials

From Figure 69, three stages of cooling can be identified, and the values of cooling features are visible Table 21:

1. **Cooling of the liquid**, between the pouring temperature and the solidus temperature. A first estimation of the cooling rate applied to the molten metal can be made by computing the slope of the cooling curve between these temperatures

2. **Phase transformation**, between the liquidus and solidus temperatures. The time interval between the beginning and the end of solidification gives the time of solidification.

3. **Cooling of the solid,** below the solidus temperature to room temperature.

Mould	*Cooling rate ($K.s^{-1}$)*	*Time of solidification (s)*	*Solid-state cooling*
C40 Steel	8.1	30.4	$T = 116.0 + 1028\ e^{(-1.11.10^{-2}\ t)}$
Clay	3.6	57.0	$T = 213.9 + 902.8\ e^{(-5.77.10^{-3}\ t)}$
Sand	1.6	129.9	$T = 254.7 + 870.9\ e^{(-3.42.10^{-3}\ t)}$

Table 8: Estimation of the cooling rate, time of solidification and the solid cooling law from the data of Numerical Simulation

A10.2. TEMPERATURE DECREASE INTO THE MOULD WALLS

The chosen points correspond to the positions of the three thermocouple's tips.

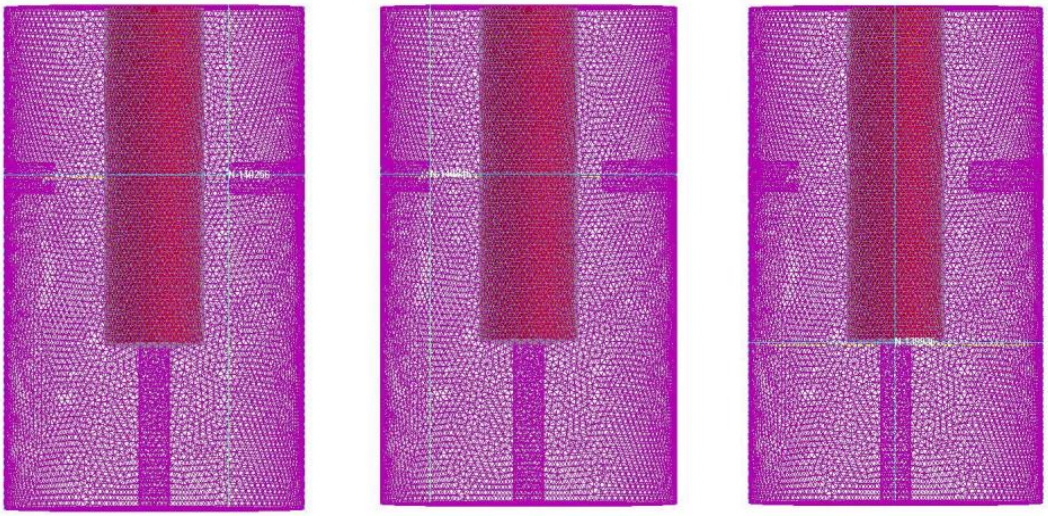

Figure 9: Points of simulation in the mould: TC2 (0.5 cm from the melt), TC3 (1.0 cm from the melt), TC1 (in contact with the melt).

The computed cooling curves (Figure 10) show that these three points very different behaviour between each other during the lowering of temperature.

While the point in contact with the melt (TC1) undergoes for each mould a strong temperature variation, the points inside the mould (TC2 and TC3) are subject to a progressive temperature change.

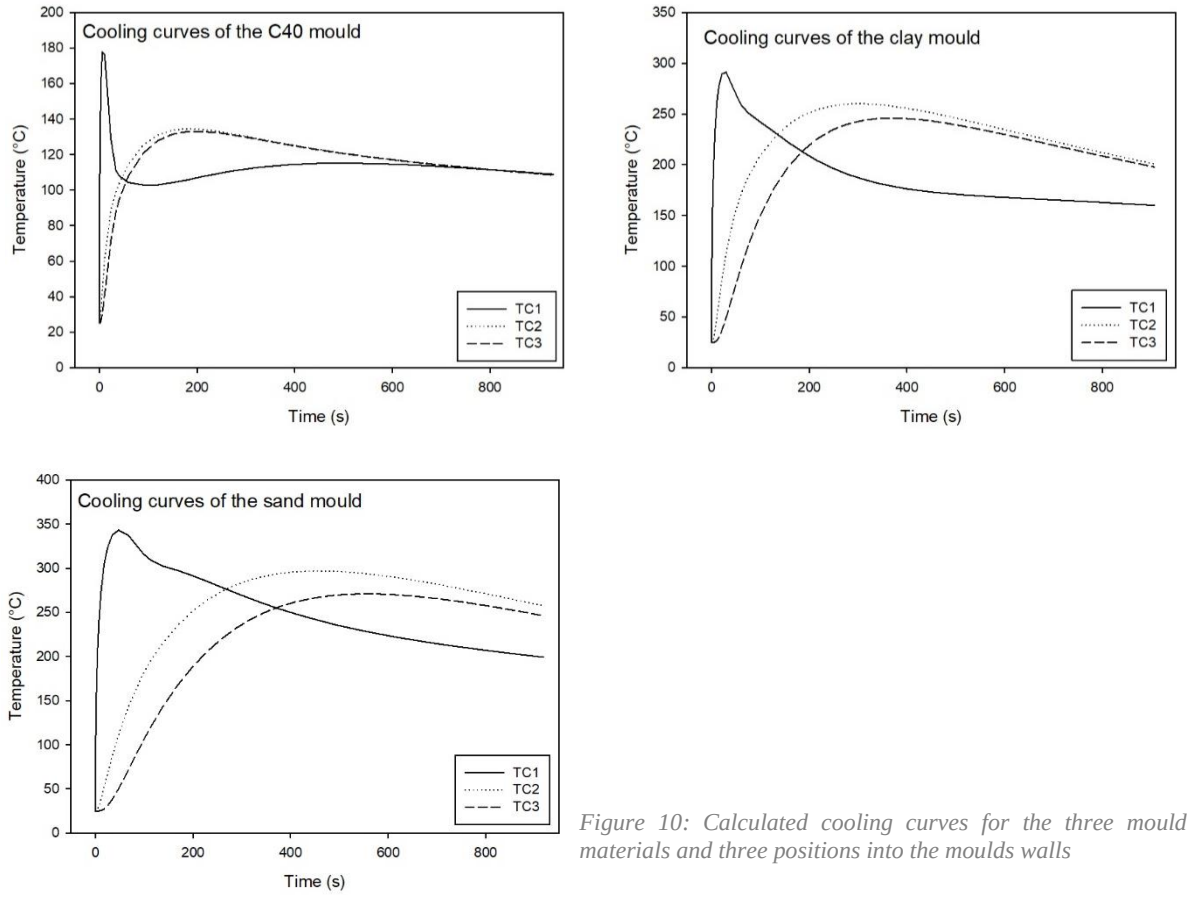

Figure 10: Calculated cooling curves for the three mould materials and three positions into the moulds walls

Confrontations with experimental measurement of temperature with time for each mould and each thermocouple are visible in the following Figures 11, 12 and 13.

In the case of the steel mould, the numerical results are coherent with experiment. The lower temperature values found for the intern thermocouple (TC1) can be explained by the instrumental limit of the CHROMA system for recording very fast temperature changes.

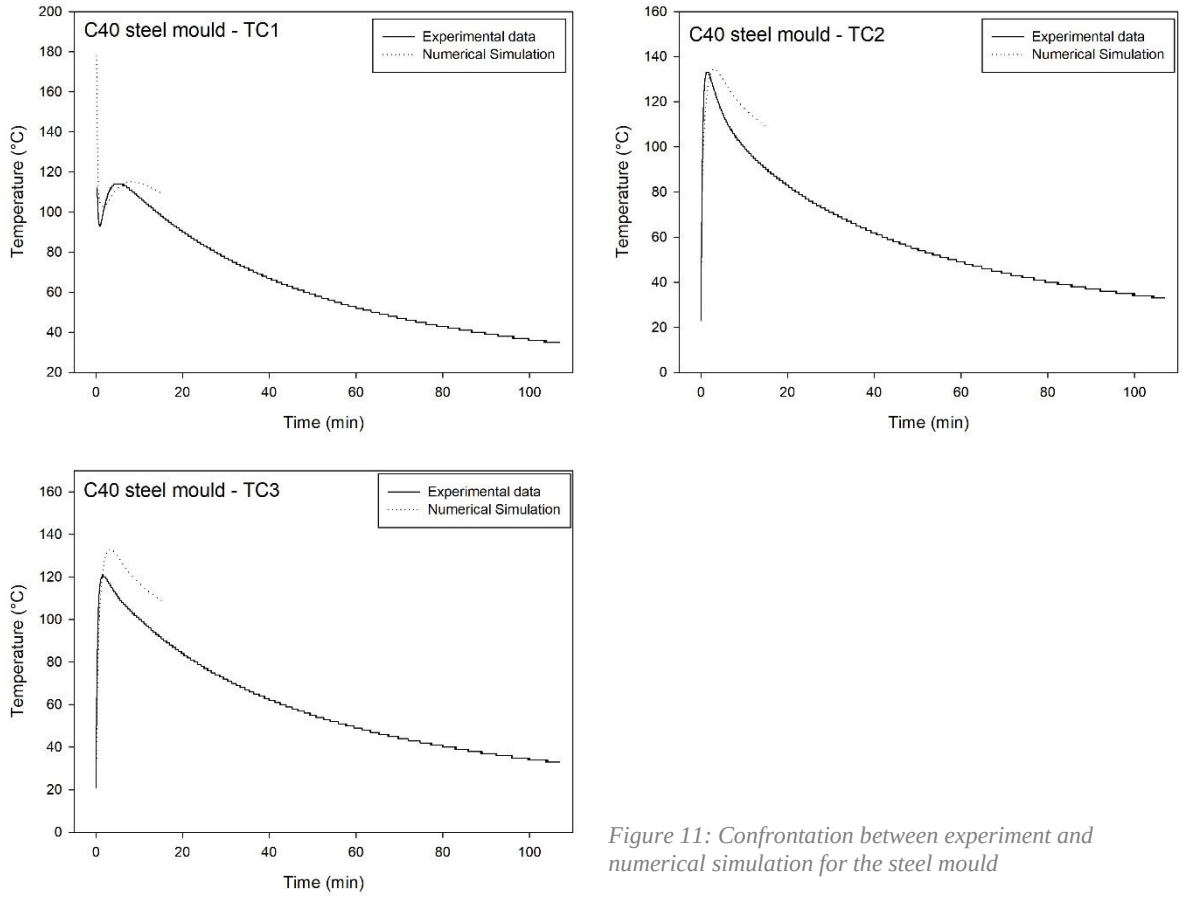

Figure 11: Confrontation between experiment and numerical simulation for the steel mould

In the case of the clay mould, experimental data of the thermocouple 2 are not available due to a dysfunction during casting experiment. The difference between numerical simulation and experimental cooling curves is clear. Indeed numerical simulation lets think that the cooling is more continuous than the experimental curves.

This deviation could be explained on one side by the use of standard values of thermal properties for sand material that differ from the experimental material used for casting. This could lead to a divergence in the estimation of the interfacial gap between mould walls and solidified alloy.

Finally, an inaccuracy in the determination of the experimental position of the thermocouple in the mould is also possible.

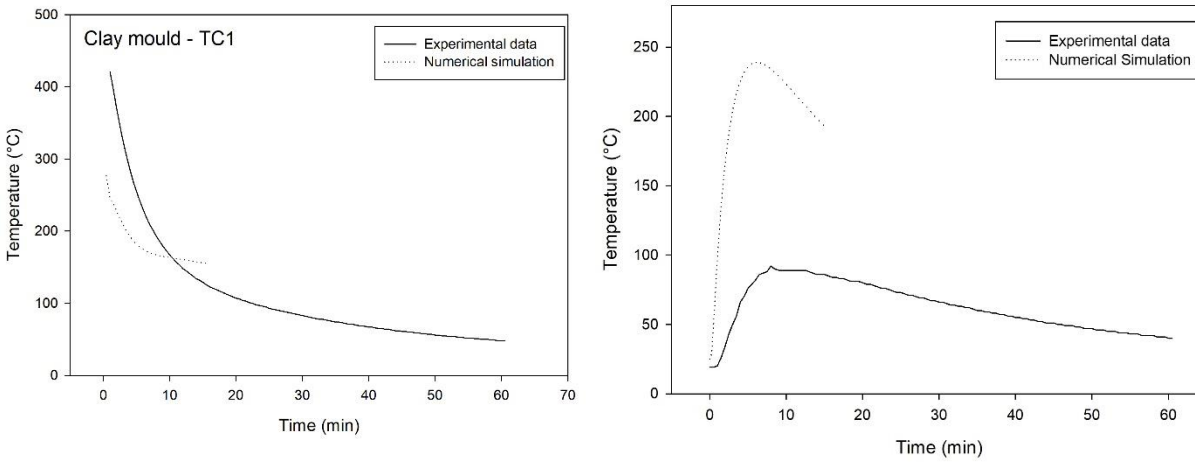

Figure 12: Confrontation between experiment and numerical simulation for the clay mould

For casting experimentation sand mould, the same observation can be made.

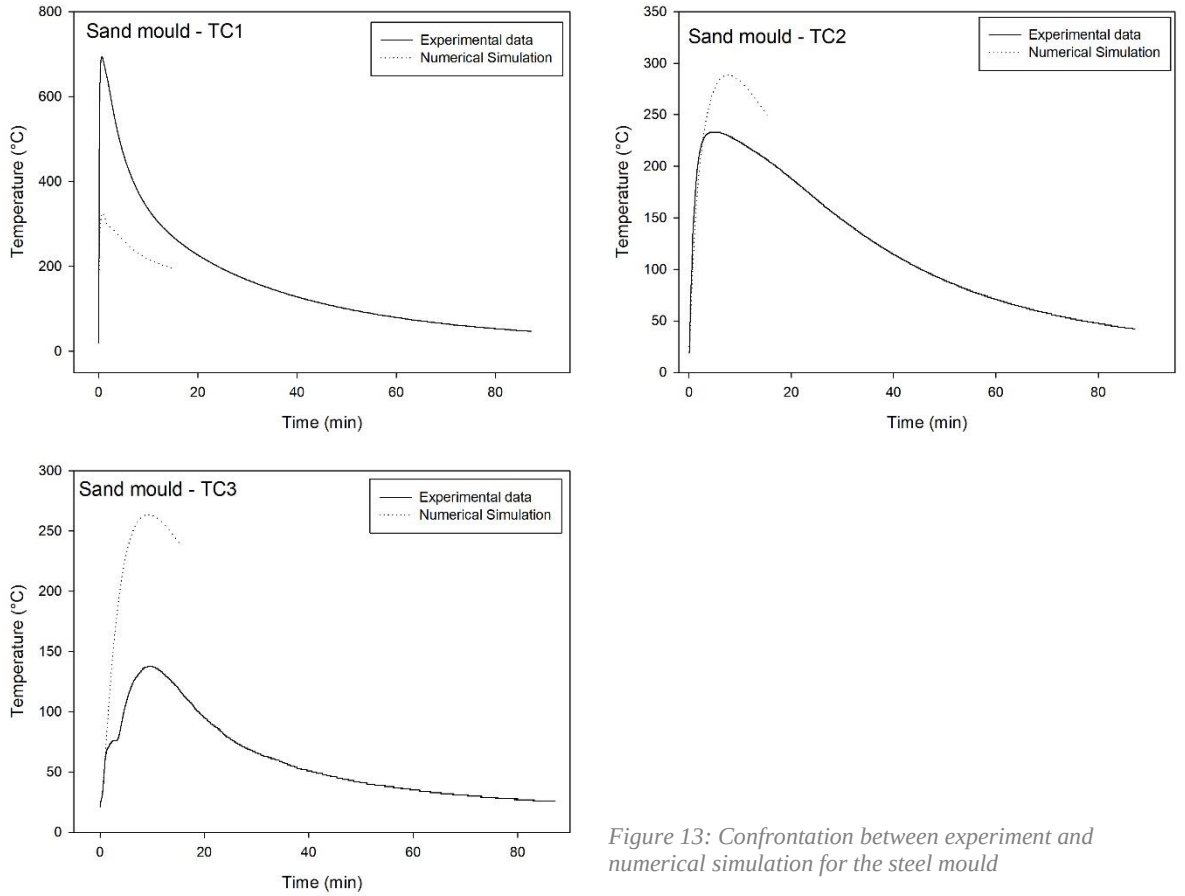

Figure 13: Confrontation between experiment and numerical simulation for the steel mould

REFERENCES

- **S. AKAMATSU, M. PLAPP**, Eutectic and peritectic solidification patterns, Current Opinion in Solid State and Materials Science 20, (2016), pp. 46 – 54.

- **D. ASHKENAZI, S. BUNIMOVITZ, A. STERN**, Archaeometallurgical investigation of thirteenth-twelfth centuries BCE bronze objects from Tel Beth-Shemesh, Israel, Journal of Archaeological Science: Reports 6 (2016), pp. 170 – 181.

- **ASM Handbook**, Glossary of terms, Vol.15 Casting, (1992), pp. 1 – 12.

- **ASTM E3-11**. Standard Guide for Preparation of Metallographic Specimens.

- **ASTM E112-12**. Standard Test Methods for Determining Average Grain Size.

- **N. AYER, S. MARTIN, R.L. DWYNER, L. GACE, L. LAURIN**, Environmental performance of copper alloy Net-pens: life cycle assessment of Atlantic salmon grow-out in copper alloy and nylon net pens, Aquaculture 453, (2016), pp. 93 – 103.

- **M. BARICCO,** Tecniche di Analisi Termica. In R. MONTANARI (ed.) Tecniche sperimentali per la caratterizzazione dei materiali, dal laboratorio alla produzione, Associazione Italiana di Metallurgia, 2005), pp. 31 – 62.

- **N. BECKER**, Models and Designs for experiments with Mixtures, Austral. J. Statist., 20 (3), (1978), pp. 195 – 208.

- **T. BEENTJES**, The casting of western sculpture during the XIXth century: sand casting *versus* lost wax casting, Proceedings Métal à ciel ouvert, La sculpture métallique d'extérieur du XIX^{e} au début du XX^{e} siècle, Outdoor metallic sculpture from the XIXth to the early XXth century, 15es journées d'études de la SFIIC, 4 & 5 décembre 2014, Paris, pp. 120 – 129.

- **A. BENCOMO, R. BISBAL, R. MORALES**, Simulation of the aluminium alloy A356 solidification cast in cylindrical permanent molds, Revista Matéria, Vol. 13, N°2, (2008), pp. 294 – 303.

- **T. BERTHOUD, S. CLEUZIOU, L.P. HURTEL, M. MENU, C. VOLFOVSKY**, Cuivres et alliages en Iran, Afghanistan, Oman au cours des IVe et IIIe millénaires, Pal2orient, Vol. 8, N°2, pp. 39 – 54.

- **H. BILONI, W.J. BOETTINGER**, Solidification. In (eds.) R.W. Cahn, P. Haasen, Physical Metallurgy, Fourth, revised and enhanced edition, Vol.1, Elsevier, (1996), pp. 669 – 842.

- **W.J.J. BOETTINGER, U.R. KATTNER, K.W. MOON, J.H. PEREPEZKO**, DTA and Heat-Flux DSC Measurements of Alloy Melting and Freezing, National Institut of Standards and Technology, Special Publication 960-15, Washington (2006).

- **V. BONGIORNO, J. VERNET, P. PICCARDO**, La statuaire funéraire contemporaine du Cimetière Monumental de Staglieno de Gênes, Italie. In M. Pernot (Ed.) Quatre mille ans d'histoire du cuivre, Presses Universitaires de Bordeaux, Ausonius Editions, (2017), pp. 291 – 309.

- **E.A. BRANDES, G.B. BROOK**, Smithells Metals Reference Book, Seventh Edition, (1992).

- **P.J. BRAY, A.M. POLLARD**, A new interpretative approach to the chemistry of copper-alloy objects: source, recycling and technology, Antiquity 86 (2012), pp. 853 – 867.
- **M.E. BROWN, P.K. GALLAGHER**, Handbook of Thermal Analysis and Calorimetry, Vol. 1 Principles and Practices, Elsevier, (1998).
- **J. CAMPBELL**, Castings practice. The 10 rules of castings, Elsevier, (2004).
- **J. CAMPBELL**, Complete Casting Handbook: Metal Casting Processes, Metallurgy, Techniques and Design, Elsevier, (2011).
- **T. CAPARROS, R. NALLIER, Y, FRANEL, H. GUY, M.-F. GLEIZE**, Un ensemble exceptionnel de vestiges métallurgiques de l'âge du bronze final à Aubervilliers (Seine-Saint-Denis), Bulletin de l'Association pour la Promotion des Recherches sur l'Age du Bronze 7 (2010), pp. 38 – 50.
- **M. CASTELLE, Y. COQUINOT, D. BOURGARIT**, Casting cores of French bronze statues of the 16th and 17th centuries: identification of regional practices and artistic choices, Microchemical Journal, (2015).
- **C. CERT**, Les moules de métallurgistes dans les Pyrénées, Bulletin de la Société Préhistorique Française 97, 4, (2000), pp. 595 – 608.
- **D.J. CHAKRABARTI, D.E. LAUGHLIN**, The Cu-Pb (Copper-Lead) System, Bulletin of Alloy Phase Diagram 5, 5, (1984), pp. 503 – 510.
- **Y.A. CHANG, J.P. NEUMANN, A. MIKULA, D. GOLDBERG**, Cu-Pb-Sn. In Monograph Series 6, Phase Diagrams and Thermodynamic Properties of Ternary Copper-Metallic Systems, (1979a), pp. 631 – 642.
- **Y.A. CHANG, J.P. NEUMANN, A. MIKULA, D. GOLDBERG**, Cu-Pb-Zn. In Monograph Series 6, Phase Diagrams and Thermodynamic Properties of Ternary Copper-Metallic Systems, (1979b), pp. 643 – 651.
- **S. CHATTOPADHYAY, S. SRIKANTH**, The Cu-Pb-Sn (Copper-Lead-Tin) System, Journal of Phase Equilibria 15, 5, (1994), pp. 553 – 557.
- **C. CHEVILLOT**, Les bronzes à travers l'histoire, Proceedings Métal à ciel ouvert, La sculpture métallique d'extérieur du XIX^{e} au début du XX^{e} siècle, Outdoor metallic sculpture from the XIXth to the early XXth century, 15es journées d'études de la SFIIC, 4 & 5 décembre 2014, Paris, pp. 8 – 13.
- **C. CICUTTI, R. BOERI,** On the relationship between primary and secondary dendrite arm spacing in continuous casting products, Scripta Materialia, 45, (2001), pp. 1455 – 1460.
- **H.-B. CUI, J.-J. GUO, Y.-Q. SU, H.-S. DING, S.-P. WU, W.-S. BI, D.-M. XU, H.-Z. FU**, Microstructure evolution of Cu-Pb monotectic alloys during directional solidification, Transactions of Nonferrous Metals Society of China 16, (2006), pp. 783 – 790.
- **U.A. DABADE, R.C. BHEDASGAONKAR**, Casting Defect Analysis using Design of Experiments (DoE) and Computer Aided Casting Simulation Technique, Procedia CIRP 7, (2013), pp. 616 – 621.
- **J. DANKO, M. HOLTZER,** The state of art and of world's casting production, Metalurgija 45, 4, (2006), pp. 333 – 340.

- **V. DEBUT, M. CARVALHO, E. FIGUEIREDO, J. ANTUNES, R. SILVA**, The sound of bronze: Virtual resurrection of a broken medieval bell, Journal of Cultural Heritage 19, (2016), pp. 544 – 554

- **F. DELRIEU, H. GANDOIS, C, LE CARLIER DE VESLUD, M. MELIN, WITH COLLABORATION OF V. BARDEL, F. CATTIN, M. GABILLOT**, Un nouvel assemblage de haches-lingots dans la vallée du Rhône : le dépôt de Loyettes (Ain), Bulletin de l'Association pour la Promotion des Recherches sur l'Age du Bronze 13 (2015), pp.41 – 49.

- **I. DE RYCK, A. ADRIAENS, F. ADAMS**, An overview of Mesopotamian bronze metallurgy during the 3rd millennium BC, Journal of Cultural Heritage 6, (2005), pp. 261 – 268.

- **Q.Z. DIAO, H.L TSAI**, Modelling of Solute Redistribution in the Mushy Zone during Solidification of Aluminium-Copper Alloys, Metallurgical Transactions A, Vol. 22A, (1993), pp. 963 – 973.

- **N. DOLIC, J. MEDVED, P. MRVAR, F. UNKIC**, Influence of cooling rates on temperatures phase transitions and on microstructure of aluminium alloy EN AW-5083, Mat-wiss.u. Werkstofftech, 43, No. 11, (2012), pp. 957 – 964.

- **J. DUBOS**, Fondeur 'art aujourd'hui, Technè, 18, (2003), pp. 49 – 56.

- **P. EFSTATHIOU, M. ANAGNOSTAKOU, E. KOUSKOUNI, C. PETROPOULOU, K. KARAGEORGOU, Z. MANOLIDOU, S. PAPANIKOLAOU, M. TSERONI, E. LOGOTHETIS, V. KARYOTI**, Implementation of antimicrobioal copper in neonatal intensive care unit. Antimicrob Resist Infect Control 2 (Suppli 1) :O68, (2013).

- **M. EL BEALY, B.G. THOMAS,** Prediction of Dendrite Arm Spacing for Low Alloy Steel Casting Processes, Metallurgical and Materials Transactions B, Vol. 27B, (1996), pp. 689 – 693.

- **Z. EL MORR, M.PERNOT**, Middle Bronze Age metallurgy in the Levant: evidence from the weapons of Byblos, Journal of Archaeological Science, 38, (2011), pp. 2613 – 2624.

- **R. FERRO, S. DELFINO**, Equilibri di fase in sistemi eterogenei. In Principi ed Applicazioni di Calorimetria ed Analisi Termica, G. della Gatta and A. Lucci, ed. Piccin, (1982), pp. 51 – 70.

- **M.C. FLEMINGS**, Solidification processing. In R.W. Cahn, P. Haasen, E.J. Kramer, (eds) Materials Science and Technology Vol. 15, Processing of Metals and Alloys, VHC, (1991), pp. 2 – 56.

- **S.C. FLOOD, J.D. HUNT,** Columnar to Equiaxed Transition. In ASM Handbook, Vol. 15 Casting, (2004), pp. 130 – 136.

- **G. FORM, J. WALLACE**, Solidification of Metals: General principles, Modern Casting 37 (1960).

- **E. FORMIGLI**, Le tecniche del colore nella statuaria antica in bronzo. In E. Formigli (ed.) Colore e luce nella statuaria antica in bronzo, "L'ERMA" di Bretschneiger, (2013), Roma, pp. 1 – 23.

- **H. FREDRIKSSON**, Interpretation and Use of Cooling Curves (Thermal Analysis). In ASM Handbook Vol. 15, Casting, (2004), pp. 182 – 185.

- **H. FREDRIKSSON, U. ÅKERLIND**, Materials Processing during Casting, John Wiley & Sons Ltd, (2006).

- **M. FRIEDMAN**, Bangladesh Metal Casting, Five Techniques, The University Press Limited, (2001), pp. 21.
- **S. FÜRTAUER, D. LI, D. CUPID, H. FLANDORFER**, The Cu-Sn phase diagram, Part I: New experimental results, Intermetallics 34 (2013), pp. 141 – 147.
- **G.G. GNESIN**, Revisiting the history of materials science: on the origin of metallurgical technologies in the Bronze Age, Powder Metallurgy and Metal Ceramics, Vol. 52, Nos 7 – 8, (2013), pp. 477 – 488.
- **M. GOODWAY**, History of Casting. In ASM Handbook, Vol.15 Casting, (2004), pp.15 – 23.
- **V.K. GOUDA, G.I. YOUSSEF, N.A. ABDEL GHANY**, Characterization of Egyptian bronze archaeological artifacts, Surface and Interface Analysis 44, (2012), pp. 1338 – 1345.
- **M.P. GROOVER**, Fundamentals of Modern Manufacturing, Materials, Processes and Systems, 4th Edition, John Wiley & Sons. Inc. (2010).
- **B. GUISSANI, M. MARELLI, S. RECCHIA, F. COLPANI, I ANGELINI, G. ARTIOLI,** Tracing the provenance of ancient copper objects: A multivariate data analysis approach, Proceedings of the 2nd International Conference on Archaeometallurgy in Europe, Aquileia, Italy, (2007), pp. 17 – 21.
- **D. HANSON, W.T. PELL-WALPOLE**, Chill-cast tin bronzes, Edward Arnold & Co, London, (1951).
- **W. HELLER**, Copper-Based Alloys, Material Science & Technology, Vol. 8, (2006), pp. 277 – 246.
- **M. HILLERT**, Solidification and Casting of Metals, The Metals Society, London, (1979).
- **K. HO, R.D. PEHLKE**, Metal-Mold Interfacial Heat Transfer, Metallurgical Transactions B, (1985), pp. 585 – 594.
- **R.A. HORTON**, Investment Casting. In ASM Handbook Vol 15 Casting, ASM International, (2004), pp. 253 – 269.
- **V.A. HOSSEINI, S.G. SHABESTARI, R. GHOLIZADEH,** Study on the effect of cooling rate on the solidification parameters, microstructure, and mechanical properties of LM13 alloy using cooling curve thermal analysis technique, Material Design, 50, (2013), pp. 7–14.
- **Y.C. HUANG, S.W. CHEN, C.Y. CHOU, W. GIERLOTKA**, Liquidus projection and thermodynamic modelling of Sn-Zn-Cu ternary system, Journal of Alloys and Compounds 477, (2009), pp. 283 – 290.
- **S. HURST**, Metal Casting: Appropriate technology in the small foundry, ITDG Publishing, London, (1996).
- **G.M. INGO, T. DE CARO, C. RICCUCI, E. ANGELINI, S. GRASSINI, S. BALBI, P. BERNARDINI, D. SALVI, L. BOUSSELMI, A. ÇILINGIROĞLU, M. GENER, V.K. GOUDA, O. AL JARRAH, S. KHOSROFF, Z. MAHDJOUB, Z. AL SAAD, W. EL-SADDIK, P. VASSILIOU**, Large scale investigation of chemical composition, structure and corrosion mechanism of bronze archaeological artefacts from Mediterranean basin, Applied Physics A 83, (2006), pp. 513 – 520.
- **T. JANTZEN, P.J. SPENCER**, Thermodynamic assessments of the Cu-Pb-Zn and Cu-Sn-Zn systems, Calphad 22, 3, (1998), pp. 417 – 434.

- **H. JONES**, A perspective on the development of rapid solidification and nonequilibrium processing and its future, Materials Science and Engineering, A304 – 306, (2001), pp. 11 – 19.

- **D.P. KANICKI**, Casting Advantages, Applications and Market Size. In ASM Handbook, Vol.15 Casting, (2004), pp. 37 – 45.

- **C.H. KONRAD, M. BRUNNER, K. KYRGYZBAEV, R. VÖLKL, U. GLATZEL**, Determination of heat transfer coefficient and ceramic mold material parameters for alloy IN738LC investment castings, Journal of Materials Processing Technology, 211, (2011), pp. 181 – 186.

- **B. KOROJY, L. EKBOM, H. FREDRIKSSON**, Microsegregation and Solidification Shrinkage of Copper-Lead Base alloys, Advances in Materials Science and Engineering, (2009).

- **E. LAMOUCHE**, Fondeurs, artistes et artisans du bronze à Rome : 1585 – 1625, Ph.D Thesis, Ecole Doctorale en Sciences de l'Homme et de la Société, Université de Picardie Jules Verne, (2013).

- **R. LEARDI**, Experimental design in chemistry: A tutorial, Analytica Chimica Acta, 2009, 652 / 1-2, 161 – 172.

- **H. LECHTMAN**, Arsenic Bronze: Dirty Copper or Chosen Alloy ? A View from the Americas, Journal of Field Archaeology, Vol. 23, N° 4, (1996), pp. 477 – 514.

- **G. LESOULT**, Fundamentals of Growth. In ASM Handbook Vol. 15 Casting, ASM International, (2004), pp. 109 – 158.

- **D. LI, P. FRANKE, S. FÜRTAUER, D. CUPID, H. FLANDORFER**, The Cu-Sn phase diagram part II: New thermodynamic assessment, Intermetallics 34, (2013), pp. 148 – 158.

- **S.M. LIANG, H.M. HSIAO, R. SCHMID-FETZER**, Thermodynamic assessment of the Al–Cu–Zn system, part I: Cu–Zn binary system, CALPHAD: Computer Coupling of Phase Diagrams and Thermochemistry 51, (2015), pp. 224 – 232.

- **A. LUCCI**, Analisi cinetiche isoterme e non isoterme di trasformazioni e reazioni allo stato solido. In Principi ed Applicazioni di Calorimetria ed Analisi Termica, G. della Gatta and A. Lucci, ed. Piccin, (1982), pp. 127 – 145

- **M.A. MARTORANO, J.D.T. CAPOCCHI**, Dendrite structure control in directionally solidified bronze casting, Int. J. Cast Metals Res., 13, (2000), pp. 49 – 57.

- **N.D. MEEKS**, Tin-rich surface on bronze – Some experimental and archaeological considerations, Archaeometry 28, 2 (1986), pp. 133 – 162.

- **J. MIETTINEN,** Thermodynamic-kinetic simulation of solidification in binary fcc copper alloys with calculation of thermophysical properties, Computational Materials Science, 22, (2001), pp. 240 – 260.

- **J. MIETTINEN, P. DOCHEVA, G. VASSILEV**, Thermodynamic description of the Cu-Pb-Sn system at the Cu-Pb side, CALPHAD : Computer Coupling of Phase Diagrams and Thermochemistry 34, (2010a), pp. 415 – 420.

- **J. MIETTINEN, V. GANDOVA, G. VASSILEV**, Thermodynamic description of the Cu–Pb–Zn system, CALPHAD: Computer Coupling of Phase Diagrams and Thermochemistry 34, (2010b), pp. 377 – 383.

- **A.P. MIODOWNIK**, Cu-Zn (Copper-Zinc). In (eds) P.R. Subramanian, D.J. Chakrabarti, D.E. Laughlin, Monograph Series on Alloy Phase Diagrams, Vol. 10 Phase Diagrams of Binary Copper Alloys, (1994), pp. 487 – 496.

- **J.F. MOREAU**, Le chaudron en alliage de cuivre: échanges d'un nouveau type entre l'Europe et le Nord-Est de l'Amérique du Nord à l'époque moderne. In M. Pernot (ed.) Quatre mille ans d'histoire du cuivre, Presses Universitaires de Bordeaux, Ausonius Editions, (2017), pp. 181 – 196.

- **J.S. PARK, C.W. PARK, K.J. LEE**, Implication of peritectic composition in historical high-tin bronze metallurgy, Materials Characterization 60 (2009), pp. 1268 – 1275.

- **J.H. PEREPEZKO,** Nucleation Kinetics. In ASM Handbook, Vol. 15 Casting, (2004), pp. 101 – 108.

- **M. PERNOT**, Un trajectoire bien particulière. In M. Pernot (ed.) Quatre mille ans d'histoire du cuivre, Presses Universitaires de Bordeaux, Ausonius Editions, (2017), pp. 15 – 20.

- **M. PERNOT**, La place de la technique dans les sociétés anciennes, Cahiers d'Epistémé, Vol. 1 Histoire et éthique des sciences et des techniques, Presses Universit2 Bordeaux 1, (2006), pp. 7 – 25.

- **M. PERNOT**, L'organisation de l'atelier du bronzier. In C. Mordant, M. Pernot, V. Rychner (eds.) L'atelier du bronzier en Europe du XXe au VIIIe siècle avant notre ère. Actes du colloque international Bronze '96, Neuchâtel et Dijon. Tome II : Du minerai au métal, du métal à l'objet. Paris, CTHS, (1998), pp. 107 – 116.

- **P. PICCARDO, R. AMENDOLA, A. ADOBATI, C. FALETTI**, Studio della fluidità di leghe a base rame, La Metallurgia Italiana, (2009), pp. 31 – 38.

- **P. PICCARDO, M. PERNOT**, Studio analitico e strutturale di alcuni vasi celtici in bronzo. Metallurgia Italiana, 11, (1997) pp. 43–52.

- **A.M. POLLARD, P. BRAY, C. GOSDEN, A. WILSON, H.HAMEROW**, Characterising copper-based metals in Britain in the first millennium AD: a preliminary quantification of metal flow and recycling, Antiquity 89 (2015), pp. 697 – 713.

- **M. QUARANTA, E. CATELLI, S. PRATI, G. SCIUTTO, R. MAZZEO**, Chinese archaeological artefacts: Microstructure and corrosion behaviour of high-leaded bronzes, Journal of Cultural Heritage 15, (2014), pp. 283 – 291.

- **M. RADIVOJEVIĆ, T. REHREN, J. KUZMANOVIĆ-CVETKOVIĆ, M. JOVANOVIĆ, J.P. NORTHOVER**, Tainted ores and the rise of tin bronzes in Eurasian, c. 6500 years ago, Antiquity 87 (2013), pp. 1030 – 1045.

- **G. REVANKAR**, Introduction to Hardness Testing. In ASM Handbook Vol.8, Mechanical Testing and Evaluation, (2000), pp. 197 – 202.

- **KH. RI, V.G. KOMKOV, E.KH. RI,** Effect of Alloying Elements on the Physico-mechanical Properties of Copper and Tin Bronze, Russian Metallurgy, (2014), pp. 750 – 755.

- **B.W. ROBERTS, C.P. THRONTON, V.C. PIGOTT**, Development of metallurgy in Eurasia, Antiquity, 83 (2009), pp. 1012 – 1022.
- **C. ROLLEY**, La coulée des grands bronzes d'après les sources antiques, Techné 18, (2003), pp. 14 -18.
- **X. SANG, K. DU, H. YE**, An ordered structure of Cu3Sn in Cu–Sn alloy investigated by transmission electron microscopy, Journal of Alloys and Compounds, 469, (2009), pp. 129 – 136.
- **N. SAUNDERS, A.P. MIODOWNIK**, The Cu-Sn (Copper-Tin) System, Bulletin of Alloys Phase Diagrams, Vol. 11, No 3, (1990), pp. 278 – 287.
- **J.S. SCHEY**, Introduction to Manufacturing Processes, Mcgraw Hill series in Mechanical Engineering, (2002).
- **R.F. SCHMIDT, D.G SCHMIDT**, Selection and Application of Copper Alloy Casting. In ASM Handbook Vol. 2, Properties and Selection: Nonferrous Alloys and Special Purpose Materials, ASM International, (2000), pp. 1150 – 1180.
- **R.F. SCHMIDT, D. G. SCHMIDT, M. SAHOO**, Copper and Copper Alloys, In: ASM Handbook Vol 15 Casting, ASM International, (2004), pp. 771 – 785.
- **J.N. SILVA, D.J. MOUTINHO, A.L. MOREIRA, I.L. FERREIRA, O.L. ROCHA,** Determination of heat transfer coefficients at metal-mold interface during horizontal unsteady-state directional solidification of Sn-Pb alloys, Materials Chemistry and Physics, Vol. 130, 1-2, (2011), pp. 179 – 185.
- **P.H. SMITH, T. BEENTJES**, Nature and Art, Making and Knowing: Reconstructing Sixteenth-Century Life-Casting Techniques, Renaissance Quarterly, Vol. 63, No. 1, (2010), pp. 128 – 179.
- **D.M. STEFANESCU, R. RUXANDA**, Fundamentals of Solidification. In ASM Handbook, Vol 9, Metallography and Microstructures, ASM International, (2004), pp. 71 – 92.
- **Z. TAŞLIÇUKUR, G.S. ALTUĞ, Ş. POLAT, Ş.H. ATAPEK, E. TÜREDI**, A microstructural study on CuSn10 bonze produced by sand and investment casting techniques, Metal 12, (2012).
- **H.F. TAYLOR, J. WULFF, C. FLEMINGS**, Foundry Engineering, Wiley, New-York, (1959).
- **C.P. THORNTON**, Of brass and bronze in prehistoric Southwest Asia, in S. La Niece, D. Hook & P. Craddock (ed.) Metals and mining: studies in archaeometallurgy: 123-35. London: Archetype, (2007).
- **H.E. TROIANI, A. BARUJ**, In situ optical microscopy study of a phase transformation induced by the dezincification of beta Cu–Zn, Materials Science and Engineering A 454–455 (2007) pp. 441–445
- **P.E.A. TURCHI, M. SLUITER, F.J. PINSKI, D.D. JOHNSON, D.M. NICHOLSON, G.M. STOCKES, J.B. STAUNTON**, First-Principles Study of Phase Stability in Cu-Zn Substitutional Alloys, Physical Review Letters 67, 13, (1991), pp. 1779 – 1782.
- **R.F. TYLECOTE**, The early history of metallurgy in Europe, Longman Archaeology Series, London and New-York, (1987).
- **R.F. TYLECOTE**, A History of Metallurgy, Second Edition, Maney for the Institute of Materials, (1992).

- **D.E.T. TYLER,** Introduction to Copper and Copper Alloys. In ASM Handbook Vol. 2, Properties and Selection: Nonferrous Alloys and Special Purpose Materials, ASM International, (2000), pp. 216 – 240.

- **G.F. VANDER VOORT**, Introduction to Stereological Principles. In Practical Guide to Image Analysis, ASM International, (2000), pp. 15 – 34.

- **G.F. VANDER VOORT**, Atlas of Time-Temperature Diagrams for Non Ferrous Alloys, ASM International, (1991), pp 63 – 136.

- **E. VANDERSLUIS, C. RAVINDRAN,** Comparison of Measurement Methods for Secondary Dendrite Arm Spacing, Metallography, Microstructure and Analysis, 6, (2017), pp. 89 – 94.

- **T. VENTURA, S. TERZI, M. RAPPAZ, A.K. DAHLE,** Effects of solidification kinetics on microstructure formation in binary Sn-Cu solder alloys, Acta Materialia, 59, (2011), PP. 1651 – 1658.

- **G.O. VERRAN, R.P.K. MENDES, L.V.O. DALLA VALENTINA**, DOE applied to optimization of aluminium alloy die castings, Journal of Materials Processing Technology, Volume 200, Issues 1-3, (2008), pp. 120 – 125.

- **C. VILARINHO, D. SOARES, F. CASTRO**, Contribution to the knowledge of the Cu-Sn-Zn system for compositions close to brass alloys, Journal of Alloys and Compounds 379, (2004), pp. 161 – 165.

- **P. VILLARS, A. PRINCE, H. OKAMOTO**, Handbook of Ternary Alloy Phase Diagrams, Vol 8 Cu-Mg-Si – Ga-Hg-Te, ASM International, (1997).

- **M. VIQUAR MOHIUDDIN, S. F. HUSSAINY, A. KRISHNAIAH, P. LAXMINARAYANA, S. SUNDARRAJAN**, Experimental Study of Sand Mold Process Parameters on Al-Alloy Sand Casting using DoE, Journal of Mechanical and Civil Engineering, Vol. 11, Issue 6, Ver. VI, (2014), pp. 1 – 6.

- **L. WEBLEY, S. ADAMS**, Material Genealogies: Bronze Moulds and their Castings in Later Bronze Age Britain, Proceedings of the Prehistoric Society 0, (2016), pp. 1 – 19.

- **C.E. WEST, T.E. GRUBACH**, Permanent Mould Casting. In: ASM Handbook Vol 15 Casting, ASM International, (2004), pp. 275 – 285.

- **J.Jr., WORKMAN**, The state of multivariate thinking for scientists in industry: 1980 – 2000, Chemometrics and Intelligent Laboratory Systems, **60**, (2002), 13 – 23.

- **L.Y. ZHANG, Y.H. JIAMG, Z. MA, S.F. SHAN, Y.Z. JIA, C.Z. FAN, W.K. WANG,** Effect of cooling rate on solidified microstructure and mechanical properties of aluminium-A356 alloy, Journal of Materials Processing Technology, 207, (2008), PP. 107 – 111.

ACKNOWLEDGEMENTS

Firstly, I would like to express my sincere gratitude to my advisor **Prof. Paolo PICCARDO** for the continuous support during my Ph.D studies and related researches, for his motivation and patience all along these three years.

My sincere thanks also go to **Prof. Carla MARTINI** from the Department of Industrial Engineering at the University of Bologna and **Prof. Annalisa POLA** from the Department of Mechanical and Industrial Engineering, at the University of Brescia for having accepted with caring the role of external referees. Their observations and advices have brought new perspectives to this work.

Besides advisor and referees, I would like to express my gratitude to:

- **Prof. Riccardo LEARDI** from the Pharmacy Department at the University of Genoa (UNIGE – DIFAR) for the development of the multivariate methodology and his constant availability;

- **Ph.D Lorenzo MONTESANO** and **Dr. Eng. Marialaura TOCCI** from the Department of Mechanical and Industrial Engineering, at University of Brescia (UNIBS) for the tests of numerical simulation and DSC measurements;

- **Prof. Roberto CABELLA**, **Prof. Cristina CARBONE** and **Prof. Massimo VERDOYA** from the Department of Earth, Environment and Life Sciences (UNIGE – DISTAV) for the characterization of the casting moulds;

- **Ph.D Maréva GABILLOT** from the UMR ARTeHis of the University of Bourgogne for having us involved in her PRC project and **Fabien DELRIEU** from the Direction of Cultural Affairs of Auvergne-Rhône-Alpes (DRAC) for having put to our disposition the corpus of Loyettes;

- **Dr. Daniele MACCIÒ** from the Department of Chemistry and Industrial Chemistry at the University of Genoa (UNIGE – DCCI), for the DTA measurements;

- **Prof. Simona DELSANTE** from the Department of Chemistry and Industrial Chemistry at the University of Genoa (UNIGE – DCCI), for her availability in DSC and XRD analysis.

This Ph.D work is the achievement of five years of inspiring work in the research group of Metallurgy and Materials at the DCCI. Many thanks to my colleagues and friends **Valeria BONGIORNO, Giorgia GHIARA, Simone ANELLI, Andrea PECUNIA, Roberto SPOTORNO** for the every-day life in lab.

A very special gratitude goes to **Caterina BO**, **Filippo CASTELLI** and **Luca SITÀ** for their technical advices and practical help, particularly for the construction of the moulds necessary to these numerous casting experiments.

Also to **Enrico PUZO** for its permanent availability, his technical support and his trust for letting me work in his office.

.. and of course, so many thanks to my parents, my brother and family, to my friends from both France and Italy, and to Filo: thank you for your presence and you support, no matter the kilometres between us.

Thanks for all your encouragement!